Modelling precessing binary black hole systems

by

Serguei Ossokine

A thesis submitted in conformity with the requirements
for the degree of Doctor of Philosophy
Graduate Department of Astronomy and Astrophysics
University of Toronto

Abstract

Modelling precessing binary black hole systems

Serguei Ossokine
Doctor of Philosophy
Graduate Department of Astronomy and Astrophysics
University of Toronto
2015

Gravitational waves are one of the most exciting predictions of General Relativity. Due to their compactness, binary black hole (BBH) systems are likely sources for gravitational waves detectable by ground-based interferometric detectors such as Advanced LIGO. Distinguishing a true signal from noise requires accurate models of gravitational waves from BBH systems. In the last decade, numerical relativity has been instrumental in generating these models. The Spectral Einstein Code (`SpEC`) developed by the SXS Collaboration has been used to investigate many aspects of BBH systems. Generically, the spins of the black holes in the binary are misaligned with the orbital angular momentum, causing the orbital plane and the spins to precess. Such systems are of particular importance as they exhibit interesting dynamics and large modulations of the gravitational waveform.

In this thesis, we explore the problem of modelling precessing BBH by extending the capabilities of `SpEC` both in the construction of initial data and in dynamical evolution. We thereafter compare numerical relativity results to Post-Newtonian theory to assess the accuracy of precessing dynamics in Post-Newtonian theory.

We begin this dissertation by examining the problem of robustly constructing initial data for high mass ratio, high spin precessing BBH. We discuss many technical improvements that now enable the construction of constraint-satisfying initial data for a much larger region of the parameter space.

Next, we discuss the implementation of an important technical improvement that permits the evolution of arbitrarily precessing BBH systems; in particular, those where

the orientation of the orbital plane changes by more than 90 degrees.

We then compare the results of precessing BBH simulations done with `SpEC` to PN theory. We find generally good agreement between PN and NR precession dynamics, supporting the creation of phenomenological waveforms constructed using rotated non-precessing waveforms.

Finally, we examine a case of transitional precession in NR, where the total angular momentum changes drastically during the inspiral, and once more find good agreement with PN predictions.

"Nothing in life is to be feared, it is only to be understood. Now is the time to understand more, so that we may fear less. "

-Marie Curie

Dedication

This thesis is dedicated to my mother.

Эта диссертация посвящена моей маме.

Acknowledgements

First, I would like to thank my supervisor Harald Pfeiffer for his guidance and seemingly inexhaustible patience during the course of this Ph.D. His knack for finding interesting projects and answering my incessant questions has been invaluable. I would also like to thank Charles Dyer for teaching me General Relativity and inspiring me to pursue a Ph.D. in the field. Norm Murray has my thanks for serving on my Ph.D committee and asking insightful questions for me to ponder during committee meetings.

In the last 6 years I had the pleasure of collaborating with many wonderful people from the SXS collaboration. I thank Mike Boyle and Larry Kidder for answering the many questions I had about everything, especially PN theory. Mark Scheel and Béla Szilágyi have provided a wealth of knowledge about how `SpEC` actually functions. I thank Dan Hemberger for his assistance on many issues and his willingness to help on every difficulty I have encountered.

I have also been fortunate to be surrounded by many knowledgable post-docs at CITA who have always had the door open for many questions: Kipp Cannon, Tony Chu, Francois Foucart, Prayush Kumar and Aaron Zimmerman.

Greg Chambers, Sesh Chari and Dustin Yu: thank you for keeping me sane throughout the whole process, your friendship allowed me the much needed respite from the Ph.D. world.

I would like to thank my family for their unwavering support and believing in me even when I did not myself.

Finally, none of this would have been possible without my partner in crime Emma Lloyd. I love you.

Contents

List of Tables

List of Figures

Chapter 1

Introduction

About a century ago, Albert Einstein published his seminal work on General Relativity. It revolutionized the way gravity is viewed and today forms a cornerstone of modern physics. In this framework, gravity is represented by the curvature of spacetime as embodied by the Riemann curvature tensor. The relationship between the matter content and curvature is given by the Einstein Field equations, which relate the Ricci tensor $R_{\alpha\beta}$ to the stress energy tensor $T_{\alpha\beta}$:

$$R_{\alpha\beta} - \frac{1}{2} R g_{\alpha\beta} = 8\pi T_{\alpha\beta}. \tag{1.1}$$

Two of the most striking predictions of general relativity are the existence of black holes and gravitational radiation. Black holes are regions of spacetime which are causally disconnected from the rest of spacetime by an event horizon. The famous "no hair theorem" [128] asserts that black holes in equilibrium are completely characterized by mass m, spin $\vec{S}$ and charge Q. The most common scenario for black hole formation is gravitational collapse of a star, when the core of the star is so massive that not even neutron degeneracy pressure is enough to support it against collapse.

Gravitational radiation is a propagating perturbation in spacetime itself. Gravitational waves carry energy and angular momentum and only couple weakly to matter, which means that they are largely unaffected by circumstances that make electromagnetic observations difficult (e.g. scattering by dust). This implies that gravitational waves preserve more information about the source and thus may allow us to receive information not available via EM observations. Of course, the weak coupling to matter also makes gravitational waves incredibly difficult to detect. However, we already possess indirect evidence for their existence. Indeed, the 1993 Nobel Prize in Physics was awarded to Russell A. Hulse and Joseph H. Taylor, Jr. for observations of the change in orbital

period of a binary pulsar system (known as the Hulse-Taylor binary) [184, 178]. The prediction of the decay of the orbital period due to the emission of gravitational waves matches the observations spectacularly. Since then, several other systems with pulsars have confirmed this result (see [185] and references therein).

In the next year, advanced laser-interferometric detectors Advanced LIGO and Virgo will begin operating. It is expected that binary black hole (BBH) systems will be some of the primary sources of signals for these detectors. Due to the weakness of the gravitational wave signal, one must employ matched filtering techniques to distinguish signals from the noise. Matched filtering requires template waveforms for comparison with the incoming signal. This necessitates extremely accurate modelling of binary black hole systems. Some of the leading approaches are semi-analytical approximants such as the Post-Newtonian (PN) expansion (see e.g. [25] and references therein) and Effective One Body (EOB) theory (see [62] and references therein). However, to accurately describe the highly dynamic final orbits and coalescence, one must solve the full two-body problem of GR numerically. Today, many groups have successfully simulated binary black holes, and many facets of the BBH problem have been explored (see [103, 147, 94, 126, 83] for reviews).

Lately, *precessing* systems have become of particular interest. In these systems, the interaction between the spins of the black holes and the orbital angular momentum causes the orbital plane and the spins to precess. This precession is reflected in the gravitational wave signal. It changes the direction of dominant emission of gravitational waves and affects the phasing of the binary. In the past, only non-precessing templates have been used to search for signals. However, several studies have indicated that neglecting precession (for BH and NSBH binaries) can significantly impact detection and parameter estimation for Advanced LIGO [88, 50, 59]. Thus, generating accurate precessing waveforms that can be used to assess the accuracy, or to inform semi-analytic approximants, is of prime importance. The SXS collaboration has recently released a catalogue of simulations done with the `SpEC` code [1]. This code has been used to successfully explore many aspects of binary black hole dynamics, but much work remains to be done to explore the full parameter space of precessing binaries.

`SpEC` is a multi-domain pseudo-spectral code that is capable of efficiently solving elliptic and hyperbolic partial differential equations. For binary black holes, it utilizes a first order formulation of the Einstein Field Equations (see Section 1.3). Employing spectral methods gives the ability to simulate very long inspirals [174]. `SpEC` is also capable of simulating black hole - neutron star and neutron star - neutron star compact binaries.

The goal of this thesis is two-fold. The first is to improve and extend our ability to simulate precessing binary black hole systems in full numerical relativity. The second is to use numerical relativity simulations to explore the dynamics of precessing binaries, and to compare them to predictions of Post-Newtonian theory, in order to assess their accuracy.

Thus, this dissertation focuses on several topics associated with modelling precessing binary black hole systems:

i) In Chapter 2 we discuss many enhancements to the initial data solver in the `SpEC` code. These additions allow robust creation of initial data for high mass ratio ($q \gtrsim 10$), high spin ($\chi \gtrsim 0.9$) precessing binaries. We also introduce and test a new method to control linear momentum in initial data that eliminates spurious gravitational wave mode mixing during the inspiral. Finally, we explore other applications of the new code, such as hyperbolic encounters.

ii) Chapter 3 describes a new technique that allows the simulation of arbitrarily precessing binaries in `SpEC` and in particular those where the change of the orientation of the binary is $\gtrsim 90^\circ$. These cases are particularly interesting, as they feature the largest modulations of the gravitational waveform. The techniques described here have been used for simulations in [130] and other publications since.

iii) Chapters 4 and 5 are concerned with results of numerical simulations of precessing binaries and their comparison to semi-analytic approximations. In Chapter 4, we introduce a framework to compare the dynamics of precessing binaries from the SXS catalogue and Post-Newtonian theory. We find good agreement despite any gauge issues that may be involved. In Chapter 5, we concentrate on a new numerical relativity simulation of a system undergoing transitional precession - an extremely dynamical regime where the angular momentum of the binary changes direction dramatically during the inspiral. This behaviour has been observed previously in Post-Newtonian theory [11], but never before simulated in full numerical relativity. We apply the formalism of Chapter 4 to this case and once again recover good agreement between Post-Newtonian theory and numerical relativity, even for this unusual regime.

iv) In Chapter 6, we summarize the results and discuss possible future work.

The material from Chapter 2 has been submitted to *Classical and Quantum Gravity* [137]. The material of Chapter 3 is published in [138]. Finally, the material of Chapter 4 is based on [136].

In the rest of the introduction we briefly summarize the steps towards simulating binary black hole systems numerically. For brevity we focus in particular on the techniques used in the `SpEC` code.

1.1 3+1 decomposition

To evolve the Einstein field equations numerically, it is natural to recast them in 3+1 form. In this formulation, the initial data is prescribed on a hypersurface and evolution equations are used to evolve the geometric quantities forward in time. We assume that the spacetime manifold $\mathcal{M}$ is globally hyperbolic and thus admits a foliation. We denote by t a regular scalar field defined on $\mathcal{M}$ such that each spacelike hypersurface Σ_t is a level set of t, i.e.

$$\Sigma_t = \{p \in \mathcal{M},\ t(p) = t\},\ \forall t \in \mathbb{R}. \tag{1.2}$$

In this chapter, we reserve Greek letters to denote space-time indices (0,1,2,3) while Latin letters represent spatial indices (1,2,3). The 4-dimensional metric with signature $(-,+,+,+)$ is denoted by $g_{\mu\nu}$; ∇ is the compatible connection. Meanwhile, we use γ_{ij} and D_i to indicate the metric and its compatible connection in a hypersurface Σ.

The vector field $\nabla^\mu t = g^{\mu\nu}\nabla_\mu t$ is normal to the hypersurface. Renormalizing, we define the unit normal to Σ_t as:

$$n^\mu \equiv (-g^{\alpha\beta}\nabla_\alpha t \nabla_\beta t)^{-1/2}\nabla^\mu t \equiv \alpha^{-1}\nabla^\mu t, \tag{1.3}$$

where α is the lapse function that determines the interval of proper time for observers travelling along the normal vector n^μ. We define the time-vector field

$$t^\mu = \alpha n^\mu + \beta^\mu, \tag{1.4}$$

where the shift β^μ is an arbitrary spatial vector. The integral curves of t^μ will have the same spatial coordinates on different hypersurfaces. In standard adapted coordinates $\{t, x^i\}$, the time-vector has components $(1,0,0,0)$. Given a time vector t^μ, Eq. (1.4) shows that the lapse and shift are (up to a minus sign) simply the projections of t^μ along the normal and into the hypersurface respectively.

In adapted coordinates, the spacetime metric can be written as:

$$ds^2 = -\alpha^2 dt + \gamma_{ij}(dx^i + \beta^i dt)(dx^j + \beta^j dt). \tag{1.5}$$

This equation can be interpreted as $ds^2 = -(\text{proper time between hypersurfaces})^2 + (\text{proper distance within each hypersurface})^2$ [22].

The geometric information is carried by two tensors: the induced metric $\gamma_{\mu\nu}$ and the extrinsic curvature $K_{\mu\nu}$. The induced metric determines the curvature within each hypersurface, while the extrinsic curvature tensor $K_{\mu\nu}$ describes how the hypersurface Σ_t bends inside the manifold $\mathcal{M}$. They are given explicitly by

$$\gamma_{\mu\nu} = g_{\mu\nu} + n_\mu n_\nu, \tag{1.6}$$

$$K_{\mu\nu} = -\frac{1}{2}\mathcal{L}_n g_{\mu\nu}. \tag{1.7}$$

To obtain Einstein's equations in 3+1 form, one performs projections along the normal n^μ and into the hypersurface Σ [22, 9, 80]. The field equations can be written as $G_{\mu\nu} = 8\pi T_{\mu\nu}$, where $G_{\mu\nu} \equiv R_{\mu\nu} - \frac{1}{2}Rg_{\mu\nu}$ is the Einstein tensor. There are 3 non-trivial projections that can be done. First, entirely along the unit normal: $n^\mu n^\nu G_{\mu\nu}$; secondly, a mixed projection $\gamma^\mu_\rho n^\nu g_{\mu\nu}$. These projections give the famous Hamiltonian and momentum constraint equations respectively:

$$R + K^2 + K_{\mu\nu}K^{\mu\nu} = 16\pi\rho, \tag{1.8}$$

$$D_\mu(K^{\alpha\mu} - \gamma^{\alpha\mu})K = 8\pi S^\alpha, \tag{1.9}$$

where $K \equiv K^\mu_\mu$ is the mean curvature and $\rho \equiv n_\mu n_\nu T^{\mu\nu}$ and $S^\alpha \equiv -\gamma^{\mu\alpha}n^\nu T_{\mu\nu}$ represent matter terms. These equations involve only the geometric quantities defined on the hypersurface Σ_t. In the rest of this chapter, we will always work only with vacuum solutions, so we set $\rho = 0$ and $S^\alpha = 0$.

Switching for convenience to adapted coordinates, Eqs. (1.8) and (1.9) are given by:

$$R + K^2 + K_{ij}K^{ij} = 0, \tag{1.10}$$

$$D_j(K^{ij} - \gamma^{ij}K) = 0. \tag{1.11}$$

Finally, performing a full projection of the Einstein field equations into Σ_t gives the evolution of the extrinsic curvature tensor:

$$\partial_t K_{ij} = \alpha(R_{ij} - 2K_{ik}K^k{}_j + KK_{ij}) - D_iD_j\alpha + \beta^k\partial_k K_{ij} + K_{ik}\partial_j\beta^k + K_{jk}\partial_i\beta^k. \quad (1.12)$$

The evolution of the spatial metric γ_{ij} is purely kinematic and is the definition of extrinsic curvature:

$$\partial_t\gamma_{ij} = -2\alpha K_{ij} + D_{(i}\beta_{j)}. \quad (1.13)$$

Just like Maxwell's equations, the Einstein field equations have split into the constraint equations Eqs. (1.10) and (1.11), and the evolution equations Eqs. (1.12) and (1.13). Once constraint-satisfying initial data for γ_{ij} and K_{ij} is found on the initial hypersurface, the evolution equations determine them for all time. Notice that in order to solve the evolution equations, we also need to choose the lapse α and the shift β^i, which amount to the choice of coordinates.

1.2 Construction of initial data

The construction of initial data amounts to solving Eqs. (1.10) and (1.11) on the initial hypersurface. Two immediate complications arise. The first is to rewrite Eqs. (1.10) and (1.11) as elliptic equations, which involves choosing which data is free. The second is to choose the free data to describe a physical situation of interest. Fortunately, there are several standard techniques which have been employed extensively in the literature (see e.g. [22, 80] for detailed descriptions) that address both of these issues. The techniques all start with the conformal decomposition of the form

$$\gamma_{ij} = \psi^4\tilde{\gamma}_{ij}, \quad (1.14)$$

where ψ is a spatially dependent scalar function, called the *conformal factor*; and $\tilde{\gamma}_{ij}$ is the conformal metric. The goal is to derive an equation for the conformal factor so that it is solvable with choice of the conformal metric. Using Eq. (1.14), we can rewrite the Hamiltonian constraint, Eq. (1.8), as

$$8\tilde{D}^2\psi - \psi\tilde{R} + \psi^5K^2 + \psi^5K_{ij}K^{ij} = 0, \quad (1.15)$$

where $\tilde{D}$ is the covariant derivative compatible with the conformal metric $\tilde{\gamma}_{ij}$. Given a choice of $\tilde{\gamma}_{ij}$ (which determines $\tilde{R}$), Eq. (1.15) is an equation for the conformal factor. Of course, the extrinsic curvature K_{ij} must satisfy the momentum constraint. It is beneficial

to decompose the extrinsic curvature tensor into trace and trace-free parts:

$$K_{ij} = A_{ij} + \frac{1}{3}\gamma_{ij}K. \tag{1.16}$$

Defining $A^{ij} = \psi^{10}\tilde{A}^{ij}$ and $K = \tilde{K}$, we can rewrite the momentum and Hamiltonian constraints as

$$\tilde{D}_j\tilde{A}^{ij} - \frac{2}{3}\psi^6\tilde{\gamma}^{ij}\tilde{D}_jK = 0, \tag{1.17}$$

$$8\tilde{D}^2\psi - \psi\tilde{R} - \frac{2}{3}\psi^5K^2 + \psi^{-7}\tilde{A}_{ij}\tilde{A}^{ij} = 0. \tag{1.18}$$

There are standard ways to proceed from here. The technique adapted by most groups is the *transverse traceless* decomposition [187]. By employing the analytic solutions of the momentum constraint due to Bowen and York [28], one can reduce the problem to the solution of the Hamiltonian constraint for the conformal factor. A decomposition of the conformal factor into an analytic singular piece, and a well-behaved solution u, allows u to be determined without any special treatment of the black holes. This *puncture* initial data is easily extendable to cases with more than two black holes [36].

In this thesis, we focus on an alternative approach known as the Extended Conformal Thin Sandwich (XCTS) method [150]. It allows for a natural choice of "free" data that corresponds to a quasi-equilibrium situation. We define $\tilde{u}_{ij} \equiv \partial_t\tilde{\gamma}_{ij}$ and choose $\tilde{\gamma}^{ij}\tilde{u}_{ij} = 0$ to determine $\tilde{u}_{ij}$ completely. From Eq. (1.13), it follows that

$$\tilde{A}^{ij} = \frac{1}{2\tilde{\alpha}}((\tilde{\mathbb{L}}\beta)^{ij} - \tilde{u}^{ij}), \tag{1.19}$$

where $\tilde{\alpha} = \psi^6\alpha$ is the conformal lapse. We have also introduced the longitudinal operator,

$$(\mathbb{L}\beta)^{ij} \equiv D^i\beta^j + D^j\beta^i - \frac{2}{3}\gamma^{ij}D_k\beta^k. \tag{1.20}$$

This operator has the conformal scaling $(\mathbb{L}\beta)^{ij} = \psi^{-4}(\tilde{\mathbb{L}}\beta)^{ij}$ and the conformal version of the operator is given by Eq. (1.20) with all quantities now associated with the conformal metric.

The momentum and Hamiltonian constraints are now recast as equations for the shift

β^i and the conformal factor ψ:

$$\tilde{D}_j\left(\frac{1}{2\tilde{\alpha}}(\tilde{\mathbb{L}}\beta)^{ij}\right) - \tilde{D}_j\left(\frac{1}{2\tilde{\alpha}}\tilde{u}^{ij}\right) - \frac{2}{3}\psi^6\tilde{D}^i K = 0, \tag{1.21}$$

$$\tilde{D}^2\psi - \frac{1}{8}\psi\tilde{R} - \frac{1}{12}\psi^5 K^2 + \frac{1}{8}\psi^{-7}\tilde{A}^{ij}\tilde{A}_{ij} = 0. \tag{1.22}$$

In addition, the lapse function is fixed via the evolution equation for K:

$$\tilde{D}^2(\alpha\psi) = \alpha\psi\left(\frac{7}{8}\psi^{-8}\tilde{A}_{ij}\tilde{A}^{ij} + \frac{5}{12}\psi^4 K^2 + \frac{1}{8}\tilde{R}\right) - \psi^5\partial_t K + \psi^5\beta^i\tilde{D}_i K. \tag{1.23}$$

In this formulation, the free data are the Lagrangian-type pairs $(\tilde{\gamma}_{ij}, \tilde{u}_{ij})$ and $(K, \partial_t K)$.

Consider a system of binary black holes in a quasi-circular orbit in a coordinate system that co-rotates with the binary. Then, the system should appear time-independent up to corrections due to radiation of gravitational waves that carry away energy and angular momentum. In such a corotating system, it is natural to choose [146]

$$\tilde{u}_{ij} = \partial_t K = 0. \tag{1.24}$$

More formally, we assume the existence of an approximate helical Killing vector ξ^μ, which generates the circular orbit. The corotating frame can then be chosen by setting $t^\mu \propto \xi^\mu$. In such a frame, we expect the partial derivatives of the metric to vanish approximately.

Given a choice for $\tilde{\gamma}_{ij}$ and K (for example $\tilde{\gamma}_{ij} = \delta_{ij}$ and $K = 0$), Eqs. (1.21) to (1.23) above can be solved, if the boundary conditions have been provided. These boundary conditions must be imposed at spatial infinity[1] and are determined by the requirement that the hypersurface is asymptotically flat. For binary black holes, the boundary conditions must also include a treatment of the singularities. For the XCTS system, the standard approach is to use *excision*, where the region inside black holes is removed from the computational domain. In this case, the boundary conditions on the excised surfaces for the lapse and shift ensure that these surfaces are apparent horizons, and also determine the physical properties (mass, spin) of the black holes. The details of how the boundary conditions can be chosen are found in [57].

[1] In practice, at a timelike artificial boundary of the computational domain far away from the black holes.

1.3 Evolution

With the initial data constructed in Sec. 1.2 in hand, one might hope that the evolution in time can be done by simply integrating the ADM evolution equations Eqs. (1.12) and (1.13). Unfortunately, this is not the case, as this system turns out to be ill-posed and small perturbations grow exponentially as the evolution progresses. There are several approaches to curing this instability. One can make a gauge choice that eliminates problematic terms, or introduce new auxiliary variables, or recast the evolution equations in strongly hyperbolic form.

In practice, several of these approaches are combined to yield stable evolution schemes. The most popular scheme is BSSNOK formulation [21, 165, 131], which is used by the majority of numerical relativity groups today (see e.g. [95] for an overview of many numerical relativity codes). BSSNOK recasts the ADM equations by using a conformal rescaling of the spatial metric and the traceless part of the extrinsic curvature, and then promoting the contracted Christoffel symbols to a new evolved field. By exploiting the Hamiltonian constraint, the equations are brought to a strongly hyperbolic form [160], guaranteeing well-posedness. However, in this work, we describe instead the Generalized Harmonic (GH) approach, which was originally used by Pretorius [153] for the first stable evolution of the binary black hole spacetime. In particular, we focus on the first order formulation due to Lindblom et al [108], introduced below.

The starting point of the GH approach is to abandon the 3+1 view and return to the full 4-dimensional Einstein equations. In vacuum, they can be written as

$$-\frac{1}{2}g^{\mu\nu}\partial_\mu\partial_\nu g_{\alpha\beta} + \nabla_{(\alpha}\Gamma_{\beta)} + g^{\mu\nu}g^{\rho\sigma}(\partial_\rho g_{\mu\alpha}\partial_\sigma g_{\nu\beta} - \Gamma_{\alpha\mu\rho}\Gamma_{\beta\nu\sigma}) = 0. \tag{1.25}$$

Here, $\Gamma_\mu \equiv g^{\alpha\beta}\Gamma_{\mu\alpha\beta}$ is the trace of the Christoffel symbol $\Gamma_{\alpha\beta\gamma}$, and

$$\nabla_\alpha\Gamma_\beta = \partial_\alpha\Gamma_\beta - g^{\mu\nu}\Gamma_{\mu\alpha\beta}\Gamma_\nu. \tag{1.26}$$

The first 2 terms on the left-hand side of Eq. (1.25) contain second derivatives of the metric. If we could eliminate the term given by Eq. (1.26), Eq. (1.25) would become a non-linear wave equation. One way of achieving this is to make a gauge choice $\Gamma_\beta = 0$, such that $\nabla_\alpha\Gamma_\beta = 0$. The choice $\Gamma_\beta = 0$ is equivalent to the requirement that the coordinates satisfy the covariant scalar homogeneous wave equation:

$$g_{\mu\nu}\nabla^\rho\nabla_\rho x^\nu = -\Gamma_\mu = 0, \tag{1.27}$$

also known as *harmonic* coordinates. These coordinates have been used for many applications in general relativity, ranging from a convenient gauge choice for the Post-Newtonian expansion [25], to a rigorous formulation of the Cauchy problem of General Relativity (see [78] for a review).

We can generalize Eq. (1.27) to satisfy the wave equation *with a source*:

$$g_{\mu\nu}\nabla^{\rho}\nabla_{\rho}x^{\nu} = -\Gamma_{\mu} = H_{\mu}, \tag{1.28}$$

where $H_{\mu}(x^{\alpha}, g_{\alpha\beta})$ is an arbitrary *gauge source* function. If $H_{\mu} = 0$, one recovers standard harmonic coordinates. In GH coordinates, the field equations Eq. (1.25) are given by (e.g. [108]):

$$g^{\mu\nu}\partial_{\mu}\partial_{\nu}g_{\alpha\beta} = -2\nabla_{(\alpha}H_{\beta)} + 2g^{\mu\nu}g^{\rho\sigma}(\partial_{\rho}g_{\mu\alpha}\partial_{\sigma}g_{\nu\beta} - \Gamma_{\alpha\mu\rho}\Gamma_{\beta\nu\sigma}). \tag{1.29}$$

They must also be supplemented with the constraint

$$C_{\alpha} \equiv H_{\alpha} + \Gamma_{\alpha}. \tag{1.30}$$

Of course, the condition that $C_{\alpha} = 0$ is equivalent to the definition of GH gauge Eq. (1.28).

In principle, the 2nd order formulation Eq. (1.29) can be integrated directly for the spacetime metric $g_{\alpha\beta}$. However, in practice, this system is still not numerically stable. In his seminal work [153], Pretorius modified Eq. (1.29) by adding multiples of the constraints to achieve a stable evolution.

Instead, `SpEC` recasts Eq. (1.29) as a first-order system. To do so, new variables are defined to represent the derivatives of the metric:

$$\Phi_{i\mu\nu} \equiv \partial_i g_{\mu\nu}, \tag{1.31}$$

$$\Pi_{\mu\nu} \equiv -n^{\alpha}\partial_{\alpha}g_{\mu\nu}. \tag{1.32}$$

Choosing these auxiliary variables lets the same techniques used previously for scalar fields [97] to bring the system to first-order form. The use of Eq. (1.31) introduces a new constraint function:

$$C_{i\alpha\beta} = \partial_i g_{\alpha\beta} - \Phi_{i\alpha\beta}. \tag{1.33}$$

It turns out that this constraint grows exponentially during numerical evolution. To prevent the runaway growth, multiples of $C_{i\alpha\beta}$ are added to the evolution system, parametrized by constraint damping parameters $\gamma_0, \gamma_1, \gamma_2$. The resulting equations are given by [108]

$$\begin{aligned}
\partial_t g_{\mu\nu} &- (1+\gamma_1)\beta^k \partial_k g_{\mu\nu} = -\alpha \Pi_{\mu\nu} - \gamma_1 \beta^i \Phi_{i\mu\nu}, && (1.34)\\
\partial_t \Pi_{\mu\nu} &- \beta^k \partial_k \Pi_{\mu\nu} + \alpha \gamma^{ki} \partial_k \Phi_{i\mu\nu} - \gamma_1\gamma_2 \beta^k \partial_k g_{\mu\nu} \\
&= 2\alpha g^{\rho\sigma}\left(\gamma^{ij}\Phi_{i\rho\mu}\Phi_{j\sigma\nu} - \Pi_{\rho\mu}\Pi_{\sigma\nu} - g^{\alpha\beta}\Gamma_{\mu\rho\alpha}\Gamma_{\nu\sigma\beta}\right) - 2\alpha\nabla_{(\mu}H_{\nu)} \\
&\quad -\frac{1}{2}\alpha n^\rho n^\sigma \Pi_{\rho\sigma}\Pi_{\mu\nu} - \alpha n^\rho \Pi_{\rho i}\gamma^{ij}\Phi_{j\mu\nu} \\
&\quad +\alpha\gamma_0\left[2\delta^\rho{}_{(\mu}n_{\nu)} - g_{\mu\nu}n^\rho\right](H_\rho + \Gamma_\rho) - \gamma_1\gamma_2\beta^i\Phi_{i\mu\nu}, && (1.35)\\
\partial_t \Phi_{i\mu\nu} &- \beta^k\partial_k\Phi_{i\mu\nu} + \alpha\partial_i\Pi_{\mu\nu} - \alpha\gamma_2\partial_i g_{\mu\nu} \\
&= \frac{1}{2}\alpha n^\rho n^\sigma \Phi_{i\rho\sigma}\Pi_{\mu\nu} + \alpha\gamma^{jk}n^\rho\Phi_{ij\rho}\Phi_{k\mu\nu} - \alpha\gamma_2\Phi_{i\mu\nu}. && (1.36)
\end{aligned}$$

This system is symmetric hyperbolic and thus is guaranteed to be well-posed. It has also proven robust in numerical evolution.

One can relate the choice of gauge via H_μ to the lapse and shift introduced in Section 1.1. Because Eq. (1.28) is an evolution equation for the coordinates, we expect it to yield evolution equations for the lapse and shift. Indeed, we get:

$$\begin{aligned}
\partial_t\alpha - \beta^k\partial_k\alpha &= -\alpha(H_t - \beta^i H_i + \alpha K), && (1.37)\\
\partial_t\beta^i - \beta^k\partial_k\beta^i &= \alpha\gamma^{ij}[\alpha(H_j + \gamma^{kl}\Gamma_{jkl}) - \partial_j\alpha]. && (1.38)
\end{aligned}$$

Simple conditions on the gauge source functions (e.g. harmonic coordinates $H_\mu = 0$) yield complicated evolution equations for the lapse and shift. Conversely, simple conditions on the lapse and shift (e.g. geodesic coordinates $\alpha = 1$, $\beta^i = 0$) yield a complicated expression for H_μ. It should be emphasized that in this formulation, H_μ is a fixed algebraic function and not an evolved field.

In `SpEC`, the gauge source function H_μ is chosen to minimize the changes of the lapse and shift at the start of the numerical simulation. H_μ is then rolled off smoothly to the damped harmonic gauge:

$$H_\alpha = \mu_0\left[\ln\left(\frac{\sqrt{\gamma}}{\alpha}\right)\right]^2\left[\ln\left(\frac{\sqrt{\gamma}}{\alpha}\right)n_\alpha - \alpha^{-1}\gamma_{\alpha i}\beta^i\right], \quad (1.39)$$

where μ_0 is an arbitrary coefficient and γ is the determinant of the spatial metric γ_{ij} [109, 175, 173].

To evolve the system in Eqs. (1.34,1.35,1.36), boundary conditions are required on the artificial timelike boundary of the computational domain, as well as on the apparent horizons of the black holes. The prescription used in `SpEC` can be found in [108, 109].

Chapter 2

Improvements to the construction of binary black hole initial data

2.1 Chapter overview[1]

Construction of binary black hole initial data is a prerequisite for numerical evolutions of binary black holes. This chapter reports improvements to the binary black hole initial data solver in the Spectral Einstein Code, to allow robust construction of initial data for mass-ratio above 10:1, and for dimensionless black hole spins above 0.9, while improving efficiency for lower mass-ratios and spins. We implement a more flexible domain decomposition, adaptive mesh refinement and an updated method for choosing free parameters. We also introduce a new method to control and eliminate residual linear momentum in initial data for precessing systems,and demonstrate that it eliminates gravitational mode mixing during the evolution. Finally, the new code is applied to construct initial data for hyperbolic scattering and for binaries with very small separation.

2.2 Introduction

Almost a century ago the existence of gravitational waves was first predicted [70]. Gravitational radiation offers an exciting new observational window [161, 96] and the enticing possibility of multimessenger astronomy. With the second generation of gravitational wave detectors poised to come online [87, 3, 181], it is more important than ever to model the likely sources of gravitational waves. Some of the most promising are binary

[1]The material herein is based on Serguei Ossokine, Francois F. Foucart, Harald P. Pfeiffer, Michael Boyle, and Béla Szilágyi. *Improvements to the construction of binary black hole initial data.* In prep, 2015. Submitted to CQG.

black holes, with predicted detection rates of $0.4 - 1000$ per year for Advanced LIGO [4]. To detect such systems, matched filtering techniques must be used in order to extract the signal from the noise [71]. This requires accurate models of binary black hole inspiral, merger and ringdown. A vast amount of work has been done in this direction in full numerical relativity which is necessary to describe the very dynamic plunge and merger regimes (see e.g. [103, 147, 94, 126, 83] for overviews of the field).

While many groups now successfully simulate binary black hole systems [143, 15, 7, 8, 95], much of the vast 7-dimensional parameter space consisting of the mass ratio q and the dimensionless spins $\boldsymbol{\chi}_{A,B}$ remains unexplored. Most of the attention has been focused on binaries close to equal mass ($q \lesssim 8$) and modest spin ($\chi_{A,B} \lesssim 0.8$) (although see [113, 170, 162, 183, 45, 166]) For stellar mass black hole binaries, one can expect mass ratios $\lesssim 15$ and arbitrary spin magnitudes and orientations, which leads to precession of the spins and the orbital plane. Precessing, high mass-ratio binaries have interesting dynamics, causing large modulations of the gravitational waveform. One can expect even higher mass ratios ($q \simeq 30$) for neutron star-black hole (NSBH) binaries (see [167] a BH-Wolf-Rayet system with BH mass $30M_{\odot}$). At high mass ratios, BBH systems can be used as proxies for NSBH systems(e.g. [73]). One would thus like to simulate high-mass ratio BBH systems.

Intermediate mass black holes (IMBH) with masses $m = 10^2 - 10^4 M_{\odot}$ have been hypothesised to exist to complete the BBH mass hierarchy (e.g., the review [53]). Searches for IMBH have been performed and several candidates have been identified (see e.g. [127, 142] for recent observations). Higher mass ratio ($10 \lesssim q \lesssim 100$) systems may serve as models for binaries containing an IMBH and a stellar mass black hole or neutron star. Advanced era gravitational wave detectors might be able to observe gravitational waves from such systems, with a detection rate of up to 10 events per year for stellar-mass - IMBH binaries [4]. It is thus important to explore these systems in numerical relativity.

The first step to numerically evolving a binary black hole spacetime is the construction of appropriate data on the initial hypersurface [55]. This involves the solution of the elliptic constraint equations with free data that corresponds to a binary in quasi-equilibrium, ideally allowing for arbitrary masses, spins and velocities of the two black holes. The Spectral Einstein Code (`SpEC`) [1] includes a BBH initial data solver [145] based on the extended conformal thin sandwich equations [188, 150], incorporating quasi-equilibrium black hole boundary conditions [56, 57, 49]. This solver has been used to construct BBH for a wide range of configurations [130]. Construction of BBH with increasing mass-ratio, increasing spin magnitudes and the desire to construct initial data for highly spinning BBH with arbitrary spin axes have necessitated a variety of improvements to the initial

data code compared to its original presentation [145, 57, 148, 118, 38].

This chapter summarizes these improvements and extends the original code even further, in anticipation of future desire to study even more generic BBH systems. Specifically, here, we present:
(i) Flexible domain-decomposition to allow a wider range of mass-ratios, spins and separations.
(ii) Adaptive mesh-refinement to enhance computational efficiency and to ensure robust numerical convergence for mass-ratios $q \gtrsim 5$ and dimensionless spins $\gtrsim 0.9$.
(iii) Improved updating formulae for iterative determination of the free parameters. These formulas allow one to achieve very high spins and mass ratios, for example an equal-mass binary with aligned spins of 0.9999, and a $q = 50$ single-spinning binary with spin of 0.95 on the large black hole.
(iv) Building on previous work [75, 93], we control of the ADM linear momentum to avoid drifts of the center of mass in BBH evolutions. This eliminates gravitational mode mixing due to the motion of the centre of mass with respect to a fixed extraction sphere.
(v) Control of the center of mass.

This chapter is organized as follows. In Sec. 2.3 we describe in detail the numerical enhancements and additions to the code. In Sec. 2.4 we present the results of initial data construction for several challenging configurations as well as an exploratory evolution of a new data set that demonstrates that the control of linear momentum in initial data leads to the elimination of gravitational wave mode mixing. Finally we summarize the results in Sec. 3.5 and introduce the construction of initial data for closely separated binaries and binaries on hyperbolic orbits as applications of the techniques developed in this work.

2.3 Numerical techniques

The main task of constructing initial data is twofold: first, to solve the elliptic constraint equations on the initial hypersurface; and then, to ensure that the solution represents the astrophysical situation of interest (in our case, a black-hole binary in quasi-equilibrium). In `SpEC`, the former is achieved by using a pseudo-spectral multidomain method; see [145]. The number of subdomains is kept fixed, but the resolution of each subdomain is dynamically adjusted to obtain low truncation error. To enforce quasi-equilibrium conditions, `SpEC` employs the extended conformal thin sandwich (XCTS) formalism [150]. Before solving the conformal thin-sandwich equations, various free parameters must be chosen - for example, the sizes of the excision regions, and certain other parameters that affect the

location, spin or motion of the black holes. The free parameters differ from the physical parameters one desires to control, such as the masses and spins of the black holes, or the linear momentum $\mathbf{P}_{\rm ADM}$ of the initial data hypersurface. Therefore, iterative root-finding is needed, as described in Buchman et al [38]. To minimize the computational cost associated with many iterations of high resolution solves, we adopt a hybrid approach. The resolution of the domain and the free parameters are adjusted simultaneously based on the current estimated truncation error and the differences between the desired and obtained physical quantities.

In the remainder of this section, we describe in detail the improvements to the initial data code.

2.3.1 Domain decomposition

Figure 2.1 indicates the geometry of the domain-decomposition employed here. There are two inner spherical shells (thick black circles labeled A and B), which are surrounded by a set of cylinders (light blue) that are aligned with the axis connecting the two black holes.

Along the axis of the cylinders there are three subdomains with rectangular cross-section (indicated in green). One of these is located between the two excision spheres, and is a truncated square pyramid. The other two are rectangular blocks. In earlier work [145] the two inner spherical shells were restricted to have the *same* outer radius, and all cylinders were restricted to have the same inner radius. This restriction results in a comparatively larger shell around the smaller black hole (B). For very unequal mass systems, $m_B \ll m_A$, in particular, it may be preferable to have a smaller outer radius of shell B, roughly comparable with the sphere of influence of black hole B. This would maximize the agreement of the geometry of the domain decomposition with the structure of the solution. Therefore, here, we allow unequal radii of the two inner shells, as indicated in Fig. 2.1. This has the largest impact when we consider small separations in initial data (for example, for studying remnant properties) where the old domain decomposition requires a larger separation between the two black holes than the new domain-decomposition in order for the solver to converge.

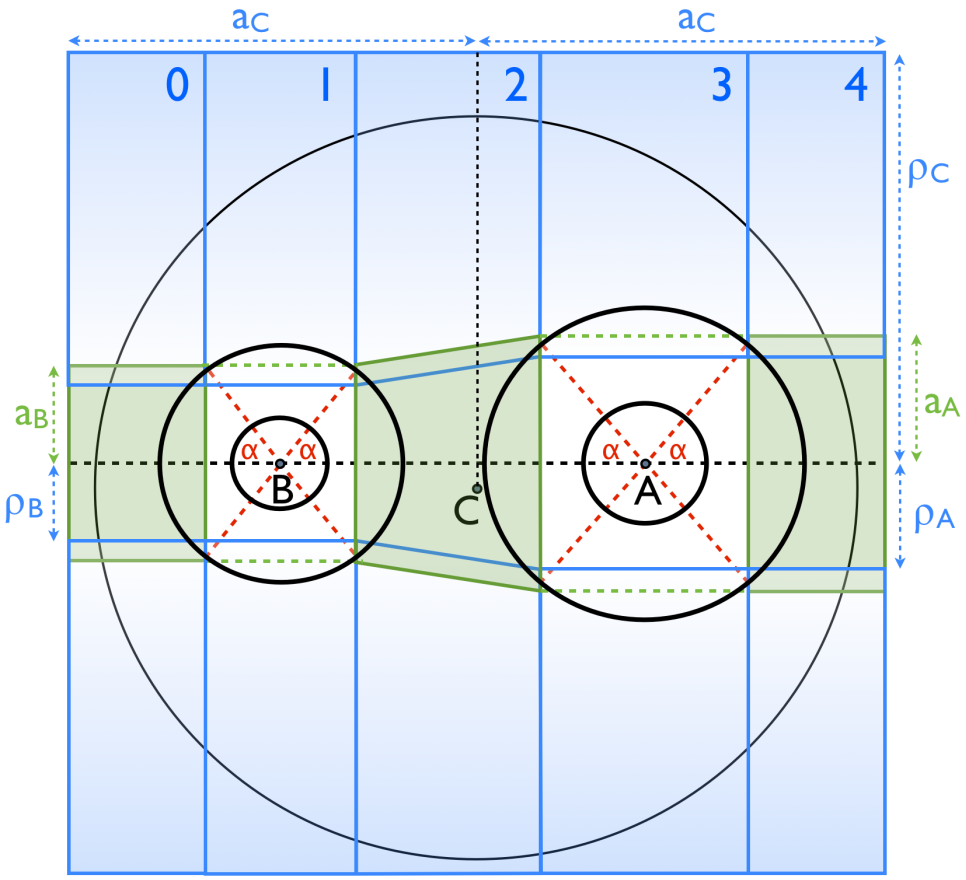

Figure 2.1: Schematic of the domain decomposition for the initial data solver. The thick black circles denote the inner and outer boundaries of the inner spherical shells (labeled A and B next to their centers). The blue shaded regions represent five open cylinders with axis along the line connecting A and B. The green solidly filled regions represent three domains with square cross-section. The thin black circle represents the inner boundary of the outer spherical shell, with center indicated by the letter C. Dashed lines are guides to the eye, to indicate the dimensions of the various subdomains.

The new domain-decomposition uses several parameters from which the placement and dimension of each subdomain follow unambiguously. We begin by specifying the inner and outer spherical shells:

- The centres of the inner spherical shells, $\mathbf{c}_{\mathrm{A}}$ and $\mathbf{c}_{\mathrm{B}}$, and of the outer spherical shell, $\mathbf{c}_{\mathrm{C}}$. Note that $\mathbf{c}_{\mathrm{C}}$ is not required to lie on the line connecting $\mathbf{c}_{\mathrm{A}}$ and $\mathbf{c}_{\mathrm{B}}$.
- The inner and outer radii of the inner spherical shells and the outer spherical shell, r_{A}, r_{B}, r_{C}, and R_{A}, R_{B}, R_{C}.

The remaining parameters $\alpha, f_{\mathrm{cyl}}, f_{\mathrm{block}}$, and f_{C} determine the relative sizes of the cylinders and rectangular blocks:

- The rectangular blocks and cylinders end on planes orthogonal to the axis connecting the centers of the excision spheres. The location of these planes is determined by the parameter α, through the requirement that these planes intersect the inner spherical shells A and B in circles of radius $R_{A,B}\sin\alpha$. The opening angle of these circles as viewed from the center of the spheres is chosen to have the same value for all four planes.
- The inner radii of the cylinders are determined by the parameter f_{cyl} via

$$\rho_{A,B} = f_{\mathrm{cyl}} R_{A,B} \sin\alpha. \tag{2.1}$$

  Note that $f_{\mathrm{cyl}} < 1$ is required for the cylinders 1 and 3 to cover all volume outside the spheres A and B.

- The size of the blocks orthogonal to the line connecting the two spheres is determined by the parameter f_{block},

$$a_{A,B} = f_{\mathrm{block}} R_{A,B} \sin\alpha. \tag{2.2}$$

  The multiplier f_{block} must satisfy $f_{\mathrm{block}} > f_{\mathrm{cyl}}$ to ensure that the blocks cover the entire open region within cylinders 0, 2, and 4.

- The multipler f_{C}, which measures how much larger the outer size of the cylinders is compared to the inner edge of the outer spherical shell:

$$a_{\mathrm{C}} = \rho_{\mathrm{C}} = f_{\mathrm{C}} r_C. \tag{2.3}$$

  To ensure complete overlap between the cylinders and the sphere C, $f_{\mathrm{C}} > 1 + C_{\perp}/r_{\mathrm{C}}$, with $C_{\perp}$ being the distance from point C to the axis of the cylinders.

The value of $f_{\rm block}$ will determine the relative size of the face of the blocks to the inner spheres: If $f_{\rm block} > 1$, then the edge of the block will be entirely outside the inner spherical shell. Conversely, if $f_{\rm block} < 1/\sqrt{2}$, then the face of the rectangular block is completely contained within the inner spherical shell. These considerations will impact which subdomain (sphere of cylinder) will provide boundary data for the blocks.

Our standard values for the grid-internal geometry coefficients are $\alpha = 45°$, $f_{\rm cyl} = 0.95$, $f_{\rm block} = 1.05$, and $f_{\rm C} = 1.1$. We have found these choices to be robust for a wide variety of component masses, spins and separations.

2.3.2 Adaptive mesh refinement

An important factor in efficiently generating high-accuracy initial data is the choice of resolution in each of the subdomain used in our domain decomposition (see Fig. 2.1). Typically, we want our representation of the solution to have about the same accuracy in all subdomains. Unfortunately, we do not know a priori what resolution is needed in a given subdomain to reach a target accuracy. Furthermore, the optimal resolution varies significantly with the physical parameters of the binary. The old initial data solver [145, 57] used hard-coded resolutions, tuned to equal-mass low spin BBH. For unequal mass systems, rapidly spinning black holes, and/or widely separated binaries the old resolutions are less efficient and can even prevent convergence of the elliptic solver when a high accuracy is requested.

To generate initial data, we generally go through multiple intermediate solves, progressively improving the accuracy of the solution while converging towards the desired binary parameters. So instead of predetermining the resolution which will be used in each subdomain at each level of refinement, we can use the preceding numerical solution to predict the optimal resolution in each subdomain to reach a target accuracy. This significantly improves the efficiency of the initial data solver, with computing times decreased by about an order of magnitude for challenging configurations. And it also allows us to push the binary parameters to more extreme values.

Our multi-domain spectral solver represents the solution in each subdomain as a tensor-product of basis-functions. Depending on the topology of the subdomain, the basis functions are Chebyshev polynomials, and/or Fourier series, and/or spherical harmonics (see [145] for details). Following Szilágyi [173], for a given subdomain and a given basis function, we define the power P_i in the i-th mode by the root-mean-square value of all the coefficients of the i-th mode across all spectral coefficients of the other basis-functions. For instance, in a spherical shell with spectral expansion

of the form $u(r,\theta,\phi) = \sum_{i=0}^{N_r-1} \sum_{l\leq L,|m|\leq l} \tilde{u}_{ilm} T_i(r) Y_{lm}(\theta,\phi)$, the radial power would be $P_i = \left(\frac{1}{N_{\theta\phi}} \sum_{l\leq L,|m|\leq l} |\tilde{u}_{ilm}|^2\right)^{1/2}$, where $N_{\theta\phi} = (L+1)^2$ represents the number of angular coefficients[2].

For the expected spectral convergence, P_i should decay exponentially as a function of i [29, 145], i.e. $\log_{10} P_i$ when plotted vs. i should be a straight line. The slope f' of this line represents the decrease in the magnitude of the spectral coefficients when going from mode i to mode $i+1$. We estimate f' using Eq. (53) of Szilágyi [173].The current truncation error of the spectral expansion is approximated as the highest retained coefficient [29].

Given the current estimate of the error as ϵ and the estimate of the convergence rate as f', we can reach a target accuracy ϵ^* by adding

$$\Delta N = -\frac{\epsilon - \epsilon^*}{f'} \tag{2.4}$$

modes to the spectral expansion (recall $f' < 0$ and a higher accuracy means a lower ϵ).The answer is rounded up so that $\Delta N > 1$ if the current accuracy is worse than the target accuracy, and we set $\Delta N = 0$ if $\epsilon < \epsilon^*$, i.e. the resolution is not allowed to decrease. For the configuration q3 from Table 2.1 the resolution was allowed to decrease without noticeable impact on the convergence behaviour, cf. Figure 2.7.

The outer spherical shell needs comparatively small angular resolution ~ 10, and sometimes AMR yields the same resolution at neighbouring E_{DT}. Because the ADM-quantities are exclusively evaluated in the outer spherical shell (cf. Sec. 2.3.4 below), this would result in apparent non-convergence of ADM linear and angular momentum. Therefore, we increase the angular resolution of the outer sphere by one extra grid-point in the θ direction and the corresponding two extra grid-points in the ϕ direction, whenever AMR triggers an adjustment to the domain decomposition.

2.3.3 Iterative determination of free parameters

When constructing initial data, we wish to achieve desired masses M_A^*, M_B^* and desired black hole spin vectors $\boldsymbol{\chi}_A^*$ and $\boldsymbol{\chi}_B^*$. The free data, however, is instead given by the radii and angular frequencies of the apparent horizons $r_{A,B}$ and $\boldsymbol{\Omega}_{A,B}^H$, which we write as

$$\underline{\mathbf{u}} = (r_A, r_B, \boldsymbol{\Omega}_A^H, \boldsymbol{\Omega}_B^H). \tag{2.5}$$

[2]For spherical harmonic basis-functions, the top two modes are filtered [145] and are therefore not included in the data P_i.

Therefore, one needs to determine values of the free parameters that result in the desired physical parameters. Thus we must solve the system of equations

$$\underline{\mathbf{F}} = (M_A - M_A^*, M_B - M_B^*, \boldsymbol{\chi}_A - \boldsymbol{\chi}_A^*, \boldsymbol{\chi}_B - \boldsymbol{\chi}_B^*) = 0. \tag{2.6}$$

The standard approach to the problem would be to use Newton's method; however, evaluating the Jacobian J_n is too expensive numerically as every evaluation of the function $\underline{\mathbf{F}}$ requires an elliptic solve. We instead use the following approach: make an initial guess $\underline{\mathbf{u}}_0$ based on the Kerr expressions for both black holes,

$$M_{A,B} = r_{A,B}/(1 + \sqrt{1 - 4r_{A,B}^2 \boldsymbol{\Omega}_{A,B}^2}), \tag{2.7}$$

$$\boldsymbol{\chi}_{A,B} = -2r_{A,B}\boldsymbol{\Omega}_{A,B}^H, \tag{2.8}$$

and perform an elliptic solve for $\underline{\mathbf{F}}_0$. We then construct an analytic Jacobian J_0 by using Eqs. (2.7,2.8) to evaluate the partial derivatives, and update the initial guess by $\underline{\mathbf{u}}_1 = \underline{\mathbf{u}}_0 - J_0^{-1}\underline{\mathbf{F}}_0$. After this we update the Jacobian using Broyden's method [152]:

$$J_k = J_{k-1} + \frac{1}{\|\underline{\boldsymbol{\Delta}\mathbf{u}}_k\|}\underline{\mathbf{F}}(\underline{\mathbf{u}}_k)\underline{\boldsymbol{\Delta}\mathbf{u}}_k^T, \tag{2.9}$$

where $\underline{\boldsymbol{\Delta}\mathbf{u}}_k = \underline{\mathbf{u}}_k - \underline{\mathbf{u}}_{k-1}$. This corresponds to the "secant" approximation for a function of one variable. Finally we set

$$\underline{\mathbf{u}}_{k+1} = \underline{\mathbf{u}}_k - J_k^{-1}\underline{\mathbf{F}}_k. \tag{2.10}$$

The major advantage of this approach lies in the use of numerical information in the update of the Jacobian. This is important in the regime where the simple analytic Jacobian becomes inadequate. Broyden's method is applied to the intrinsic physical properties of each black hole, i.e. the eight parameters listed in (2.5). We also control more general properties of the binary, such as the total linear momentum and the position of its centre of mass. As discussed in Sec. 2.3.5 this is done with explicit updating formulae that are applied simultaneously at every step of Broyden's method.

We are now faced with two intertwined iterations: AMR to tune grid-sizes to a desired truncation error; and root-finding to adjust free parameters to achieve the desired physical masses, spins, etc. When the physical parameters are still far away from the desired values, very stringent AMR resolution would waste computing time, so we aim to tighten the AMR resolution while simultaneously decreasing root-finding errors. We do so by using an overall truncation error target E_{DT} for AMR. We start with a large

value for E_{DT}, corresponding to a small grid-size. As root-finding residuals decrease, we will decrease E_{DT}. We proceed as follows: At iteration $k = 0, 1, 2, \ldots$, we compute two measures of progress in root finding: First, the residual $\mathcal{R}_k$ which quantifies how close the physical parameters are to their desired values. $\mathcal{R}_k$ is simply the rms error in the physical parameters:

$$\mathcal{R}_k = \sqrt{\frac{1}{5}\left(\frac{(\Delta M_A)^2 + (\Delta M_B)^2}{M^2} + \Delta\boldsymbol{\chi}_A^2 + \Delta\boldsymbol{\chi}_B^2 + \frac{\boldsymbol{P}_{ADM}^2}{M^2}\right)}. \tag{2.11}$$

Second, the improvement $\mathcal{I}_k$ that indicates how quickly root-finding converges, defined as

$$\mathcal{I}_k = \max_{Q^i}\left(\frac{Q^i_{k-3}Q^i_{k-2}}{Q^i_{k-1}Q^i_k}\right)^{1/2}, \quad k \geq 3, \tag{2.12}$$

where $Q^i = \{\Delta M_A, \Delta M_B, \|\Delta\boldsymbol{\chi}_A\|, \|\Delta\boldsymbol{\chi}_B\|, \|\boldsymbol{P}_{ADM}\|\}$.

We monitor 2 conditions:

1. $\mathcal{I}_k \leq \epsilon_{\mathcal{I}}$,
2. $\mathcal{R}_k \leq \epsilon_{\mathcal{R}} E_{DT}$,

where E_{DT} is the desired truncation error, and $\epsilon_{\mathcal{R}}$ and $\epsilon_{\mathcal{I}}$ are tunable parameters. The first condition assures that the resolution is increased if the root-finding convergence becomes "flat" (e.g., due to the inability to measure the masses accurately enough at the current resolution). The second condition ensures AMR resolution is sufficiently high to ensure the physical parameters can be computed more accurately than the current $\mathcal{R}_k$, with $\epsilon_{\mathcal{R}}$ being a safety factor. If either condition is satisfied and we have already reached our termination truncation error then the initial data construction is completed. Otherwise, we divide E_{DT} by a factor of 10 and continue with the next itertion. For all cases we have encountered, the choices $\epsilon_{\mathcal{R}} = 10^2$ and $\epsilon_{\mathcal{I}} = 1.5$ have proven to be robust.

2.3.4 Calculation of asymptotic quantities

Accurate knowledge of the total energy, linear momentum and angular momentum of the constructed initial data sets aid their characterization. Even more important, accurate control of the total linear momentum is essential to avoid a drift of the center of mass of the binary during long evolutions, cf. Fig. 2.6.

We define the linear and angular momenta on a slice Σ intersecting spatial infinity on the surface S_∞ using the Arnowitt-Deser-Misner (ADM) prescription. Our initial data

satisfy the asymptotic gauge conditions [186]

$$\frac{\partial \tilde{\gamma}_{ij}}{\partial x^j} = O(r^{-3}), \tag{2.13}$$
$$\gamma^{ij} K_{ij} = O(r^{-3}), \tag{2.14}$$

needed to remove ambiguities in the definition of the ADM angular momentum, as well as the boundary condition $g_{\mu\nu} = \eta_{\mu\nu}$ on S_∞. The old code [145, 149] directly evaluated the resulting surface integrals at infinity [12, 186],

$$P^i_{\rm ADM} = \frac{1}{8\pi} \oint_{S_\infty} (K^{ij} - K\gamma^{ij})\, dS_j, \tag{2.15}$$
$$J^{\rm ADM}_i = \frac{1}{8\pi} \oint_{S_\infty} \epsilon_{ijk} x^j (K^{kl} - K\gamma^{kl})\, dS_l, \tag{2.16}$$

using extrapolation in powers of $1/r$ to infinite radius [149]. $P^{\rm ADM}$ is then found to be a combination of $1/r^2$ terms of K^{ij}, and $J^{\rm ADM}$ a combination of $1/r^3$ terms. The old technique, therefore, is very sensitive to small errors in K^{ij} in the outermost sphere of our computational domain (the outer boundary is typically located at $r_{\rm out} \sim 10^{10} M$) and particularly to the presence of constraint violating modes in that sphere. Typically, this leads to large errors in $P^{\rm ADM}$ at low resolution, and large errors in $J^{\rm ADM}$ even at our highest resolution.

Higher accuracy can be obtained by assuming that the constraints are satisfied on our computational domain, and utilizing Gauss' law to recast the surface integrals on S_∞ as the sum of a surface integral on a sphere S_0 located at a smaller radius and a volume integral. Utilizing $\Psi(S_\infty) = 1$, we write

$$P^i_{\rm ADM} = \frac{1}{8\pi} \oint_{S_0} \Psi^{10} (K^{ij} - K\gamma^{ij})\, dS_j + \frac{1}{8\pi} \int_{V_0} \frac{\partial}{\partial x^j} \left[\Psi^{10} (K^{ij} - K\gamma^{ij}) \right] dV. \tag{2.17}$$

Here the normal dS_j to S_0 points into the interior of V_0 (e.g. along $+\hat{r}$ if it is a coordinate sphere) and the factor Ψ^{10} was inserted to eliminate terms with spatial derivatives of Ψ from Eq. (2.21). Using the momentum constraint in the absence of sources,

$$\nabla_j (K^{ij} - \gamma^{ij} K) = \frac{\partial (K^{ij} - K\gamma^{ij})}{\partial x^j} + \Gamma^i_{jk} (K^{jk} - \gamma^{jk} K) + \Gamma^j_{jk} (K^{ik} - \gamma^{ik} K) = 0, \tag{2.18}$$

the volume integral can be simplified to

$$P^i_{\rm ADM} = \frac{1}{8\pi} \oint_{S_0} P^{ij}\, dS_j - \frac{1}{8\pi} \int_{V_0} G^i\, dV. \tag{2.19}$$

Here,

$$P^{ij} = \Psi^{10}(K^{ij} - K\gamma^{ij}), \tag{2.20}$$

$$G^i = \tilde{\Gamma}^i_{jk} P^{jk} + \tilde{\Gamma}^j_{jk} P^{ik} - 2\tilde{\gamma}_{jk} P^{jk} \tilde{\gamma}^{il} \partial_l (\ln \Psi), \tag{2.21}$$

where $\tilde{\Gamma}^i_{jk}$ are the connections derived from the conformal metric $\tilde{\gamma}_{ij}$. Note that for conformal flatness and maximal slicing, $G^i = 0$ and the volume integral disappears (see [76]).

In practice, for conformally curved initial data, The outer spherical shell extends to outer radius $\sim 10^{10} M$. Therefore, in the numerical evaluation of the volume integral in Eq. (2.19), the volume element associated with the outermost grid-point becomes very large and introduces numerical noise. To avoid this, we roll off the integrand G^i beyond a certain radius R_c, i.e. we replace G^i by $\tilde{G}^i$ given by

$$\tilde{G}^i = \begin{cases} G^i, & r \le R_c, \\ \frac{R_c^2}{r^2} G^i, & r > R_c. \end{cases} \tag{2.22}$$

We choose $R_c = 1000 \max(w_A, w_B)$, where $w_{A,B}$ are the widths of the Gaussians that enforce exponential falloff to conformal flatness (cf. Eqs. 45 and 46 of Lovelace et al [118]).

The ADM angular momentum is also rewritten using Gauss' law as

$$J^z_{\rm ADM} = \frac{1}{8\pi} \oint_{S_0} (x P^{yj} - y P^{xj})\, dS_j - \frac{1}{8\pi} \int_{V_0} (x G^y - y G^x)\, dV, \tag{2.23}$$

with cyclical permutations of (x, y, z) yielding the other components. For maximal slicing and conformal flatness in V_0, Eq. (2.23) simplifies to

$$J^z_{\rm ADM} = \frac{1}{8\pi} \oint_{S_0} \Psi^{10} (x K^{yj} - y K^{xj})\, dS_j. \tag{2.24}$$

Because Eq. (2.23) relies on the cancellation of large volume terms, it can be sensitive to errors in K^{ij} . Accordingly, we use Eq. (2.24) using a surface S_0 at sufficiently large radius such that in V_0 the metric is conformally flat and $K = 0$.

To illustrate the importance of the transformations applied to the ADM integrals, we consider the convergence test for configuration q50. We evaluate $P_{\rm ADM}$ using Eq. (2.15) and Eq. (2.19), and we evaluate J_{ADM} using Eq. (2.16) and Eq. (2.23). Figure 2.2 shows the results.

The calculation of $P_{\rm ADM}$ is improved by about one order of magnitude when utilizing Gauss' law, whereas $J_{\rm ADM}$ improves by several orders of magnitude. We point out that,

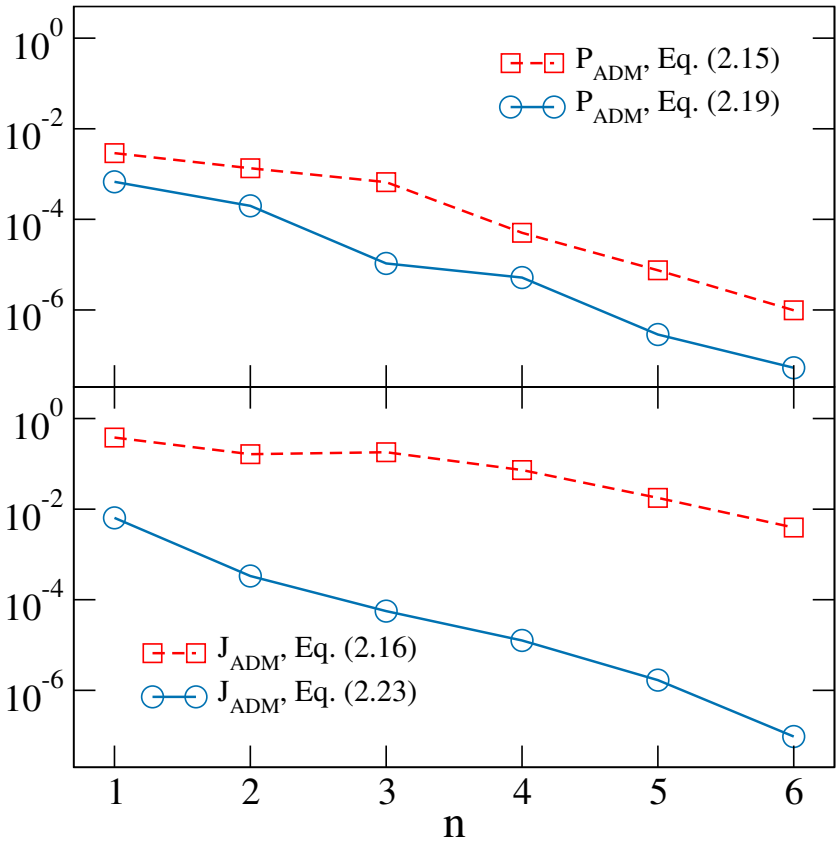

Figure 2.2: Accuracy of the calculation of $P_{\rm ADM}$ and $J_{\rm ADM}$ for two different methods of evaluation. We evaluate $P_{\rm ADM}$ and $J_{\rm ADM}$ when truncation error $E_{DT} = 10^{-n-3}$ is reached, and plot differences to the next lower resolution $n-1$. Data shown for case q50 in Table 2.1.

in order to achieve *any* convergence for the old $J_{\rm ADM}$ calculation, we had to manually increase the radial resolution in the outer sphere by 1 whenever the domain decomposition is adjusted.

We also compute a new diagnostic, the centre-of-mass $\mathbf{C}_{\rm CoM}$ of the initial data sets using the formalism developed in Ref. [20]. In conformal flatness, the expressions from [20] reduce to

$$\mathbf{C}_{\rm CoM} = \frac{3}{8\pi\, E_{\rm ADM}} \lim_{R\to\infty} \oint \Psi^4\, \mathbf{n}\, dA, \tag{2.25}$$

where $\mathbf{n}$ is the outward-pointing unit normal, $\mathbf{n} = \mathbf{r}/r$. Equation (2.25) is numerically evaluated by expanding the conformal factor Ψ in a power-series in $1/r$. We read off the (angle-dependent) coefficient of the $1/r^2$ term, and expand this coefficient in spherical harmonics. Each individual spherical harmonic term can be integrated against $\mathbf{n}$ analytically, so that the integral (2.25) collapses to a linear combination of spherical-harmonic coefficients.

2.3.5 Control of linear momentum and centre of mass

The quasi-equilibrium conformal thin-sandwich formalism to construct binary black hole initial data was developed in a series of papers [57, 49, 148, 118, 38]. In this formalism, one chooses two excised regions (usually taken to be coordinate spheres) with centres $\mathbf{c}_{A,B}$, and solves the extended conformal thin sandwich equations [188, 150] in the exterior. Boundary conditions on the excised regions ensure that they are apparent horizons, and control the spin of each black hole. The locations and the sizes of the excised regions correlate with the position and masses of the two black holes. Orbital rotation is induced by the requirement that certain time-derivatives vanish in a frame rotating with orbital velocity $\mathbf{\Omega}_0$ about the origin. One finally incorporates a radial expansion factor $\dot{a}_0$, which allows fine control of the orbital eccentricity [148, 33, 43, 38]. By a suitable choice of the conformal quantities, the quasi-equilibrium approach can generate initial data with black hole spins of order 0.9998 [118].

One shortcoming of the formalism presented in [38] lies in a lack of control of the center of mass of the binary, and only incomplete control of the ADM linear momentum $\mathbf{P}_{\rm ADM}$. The past implementations use the location of the black holes to partially control $\mathbf{P}_{\rm ADM}$. Consider a small displacement $\delta\mathbf{c}$ applied to the centres of both excision regions. Through the orbital rotation $\mathbf{\Omega}_0$ about the origin, the displacement $\delta\mathbf{c}$ induces a change in velocity of the black holes of $\mathbf{\Omega}_0 \times \delta\mathbf{c}$, with a corresponding change in $\mathbf{P}_{\rm ADM}$. Therefore, $\delta\mathbf{c}$ could be used to cancel the components of $\mathbf{P}_{\rm ADM}$ orthogonal to $\mathbf{\Omega}_0$; however, the cross-product in $\mathbf{\Omega}_0 \times \delta\mathbf{c}$ prevented any correction parallel to $\mathbf{\Omega}_0$. For head-on collisions with $\mathbf{\Omega}_0 = 0$, no control of $\mathbf{P}_{\rm ADM}$ is possible at all. For the non-precessing simulations presented in [38], the component of $\mathbf{P}_{\rm ADM}$ parallel to $\mathbf{\Omega}_0$ vanishes by symmetry, and no problems arose. However, for generic precessing binaries, there will be a non-zero linear

momentum orthogonal to the orbital plane, which results in a drift of the center of mass for very long simulations (see [138] for an extreme example).

Here, we propose a different means to control the full $\mathbf{P}_{\rm ADM}$, while simultaneously allowing us to control the center of mass as well. We fix the relative separation of the centres of the excision spheres,

$$\mathbf{c}_A - \mathbf{c}_B = \mathbf{D}, \tag{2.26}$$

where the separation vector $\mathbf{D}$ is user-specified. We use the choice of $\mathbf{c}_A$ to control the center-of-mass $\mathbf{C}_{\rm CoM}$ of the binary. Once a first initial data set is computed (with, in general, $\mathbf{C}_{\rm CoM} \neq \mathbf{0}$), we can update

$$\mathbf{c}_{{\rm A},k+1} = \mathbf{c}_{{\rm A},k} - \mathbf{C}_{{\rm CoM},k} - \frac{M_{{\rm A},k}\Delta M_{{\rm B},k} - M_{{\rm B},k}\Delta M_{{\rm A},k}}{(M_{{\rm A},k}+M_{{\rm B},k})^2}\,\mathbf{D}. \tag{2.27}$$

With the black-hole centres now used to control the centre of mass, we need a different means to control $\mathbf{P}_{\rm ADM}$. We add in the outer boundary condition on the shift (Eq. (38c) of [118]) a constant velocity $\mathbf{v}_0$:

$$\beta^i = (\mathbf{\Omega}_0 \times \mathbf{r})^i + \dot{a}_0 r^i + v_0^i \qquad \text{on } \mathcal{B}. \tag{2.28}$$

Here $\mathcal{B}$ represents the outer boundary, a sphere with radius $R = 10^{10}M$. The velocity $\mathbf{v}_0$ will effect the overall motion of the binary, and will be reflected in a corresponding change in $\mathbf{P}_{\rm ADM}$ by $E_{\rm ADM}\mathbf{v}_0$, where $E_{\rm ADM}$ is the ADM-energy of the binary. During iterative root-finding of the free parameters, we adjust $\mathbf{v}_0$ to achieve $\mathbf{P}_{\rm ADM} = \mathbf{0}$[3].

To motivate the updating formula for $\mathbf{v}_0$, consider a perturbation of $\mathbf{v}_0$ by $\delta\mathbf{v}_0$, and a perturbation of $\mathbf{c}_A$ by $\delta\mathbf{c}$. If we allow the masses to vary, then a Newtonian-inspired formula is

$$\mathbf{v}_{0,k+1} = \mathbf{v}_{0,k} - \frac{\mathbf{P}_{{\rm ADM},k}}{M_k} + (\Delta M_{{\rm A},k} + \Delta M_{{\rm B},k})(\mathbf{v}_k + \mathbf{\Omega}\times\mathbf{c}_{{\rm A},k}) - \mathbf{\Omega}\times\delta\mathbf{c}_{{\rm A},k} - \frac{\Delta M_{{\rm B},k}}{M_k}\mathbf{\Omega}\times\mathbf{D}. \tag{2.29}$$

To summarize, relative to earlier initial-data sets, we modify the outer boundary condition for the shift by the term $\mathbf{v}_0$, cf. Eq. (2.28), and use updating formulae (2.27) and (2.29) to adjust $\mathbf{c}_A$ and $\mathbf{v}_0$. Section 2.3.4 describes how we compute $\mathbf{P}_{\rm ADM}$ and $\mathbf{C}_{\rm CoM}$.

We demonstrate the efficiency of the updating formulas Eqs. (2.27,2.29) in Fig. 2.3 that shows the magnitude of $\mathbf{C}_{\rm CoM}$ and $\mathbf{P}_{\rm ADM}$ as a function of root-finding iteration for a $q = 10$ precessing binary (case q10 in Table 2.1). The convergence is evidently very fast,

[3]Using the obtained vector β^i as the shift-vector in an *evolution* results in a translating outer boundary; this effect is eliminated by evolving with a shift vector of $\beta^i - v_0^i$.

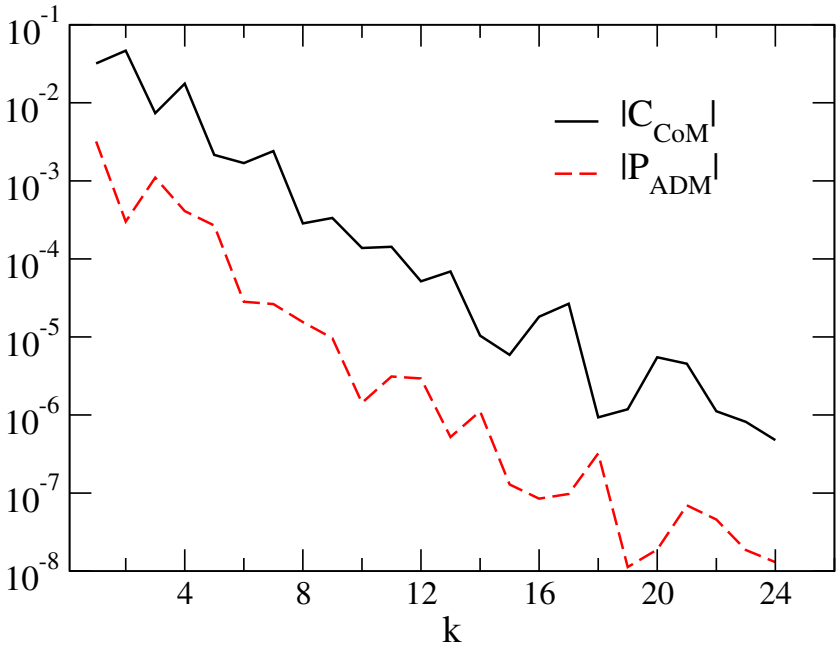

Figure 2.3: Control of the centre of mass and linear momentum for a $q = 10$ generically precessing binary (see case q10 in Table 2.1) . Shown are the magnitude of $\boldsymbol{C}_{\rm CoM}$ (black solid lines) and $\mathbf{P}_{\rm ADM}$ (red dashed lines) as a function of root-finding iteration k.

Table 2.1: Physical parameters of the initial data sets used for testing the new initial data code.

Name	q	$\boldsymbol{\chi}_1$	$\boldsymbol{\chi}_2$	D_0/M	$M\Omega_0$
Spin0.9999	1	(0, 0, 0.9999)	(0, 0, 0.9999)	14.17	0.01682
q3	3	(0, 0.49, -0.755)	(0, 0, 0)	15.48	0.01515
q10	10	(0.815, -0.203, 0.525)	(-0.087, 0.619, 0.647)	15.09	0.01547
q50	50	(-0.045, 0.646, -0.695)	(0, 0, 0)	16	0.01428

with the final values of $\sim 10^{-6}$ and $\sim 10^{-8}$ respectively. This means that even for an inspiral lasting 10^6 M, the drift of the centre of mass due to residual linear momentum in initial data will be only $\sim 0.01M$.

2.4 Numerical results

2.4.1 Initial data construction

We test the improvements described in the previous sections on several cases of interest, whose parameters are summarized in Table 2.1. The parameters were chosen to demonstrate the range of initial data sets that can be constructed with the new code and to provide some overlap with regions of parameter space which could be achieved previously.

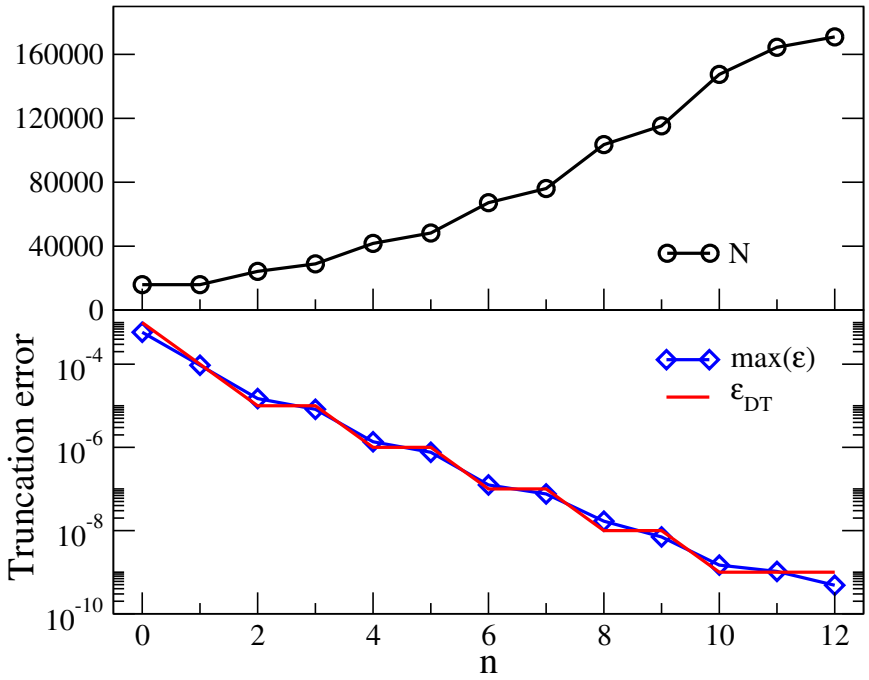

Figure 2.4: Behaviour of the AMR algorithm for case q3 as function of AMR iteration n. **Top**: total number of collocation points. **Bottom**: Highest truncation error in all subdomains, and target truncation error. The free parameters are fixed to their values at the end of root-finding.

We first illustrate the performance of the AMR outlined in Sec. 2.3.2 with the case q3, a configuration we will compare with the old BBH solver below. To demonstrate AMR in isolation, we fix initial data parameters, and start with target truncation error $E_{DT} = 10^{-3}$. We solve the constraint equations, estimate spectral truncation errors and update numerical resolution via Eq. (2.4). Whenever we reach the desired truncation error, we tighten the AMR error tolerances by dividing E_{DT} by 10, until a truncation error of 10^{-9} is reached. Figure 2.4 illustrates the behaviour of the AMR algorithm during this test. The top panel shows the total number of collocation points in the domain, which grows with each AMR iteration. The bottom panel demonstrates that the largest truncation error across all subdomains, $\max \epsilon$, closely tracks the truncation error target E_{DT}.

Figure 2.5 shows a convergence test of the AMR sequence shown in Fig. 2.4. Plotted are various quantities as a function of the effective number of grid-points $N^{1/3}$. The top panel demonstrates the exponential decrease in the L^2 norms of the Hamiltonian and momentum constraints, which implies that this data set is constraint-satisfying. The

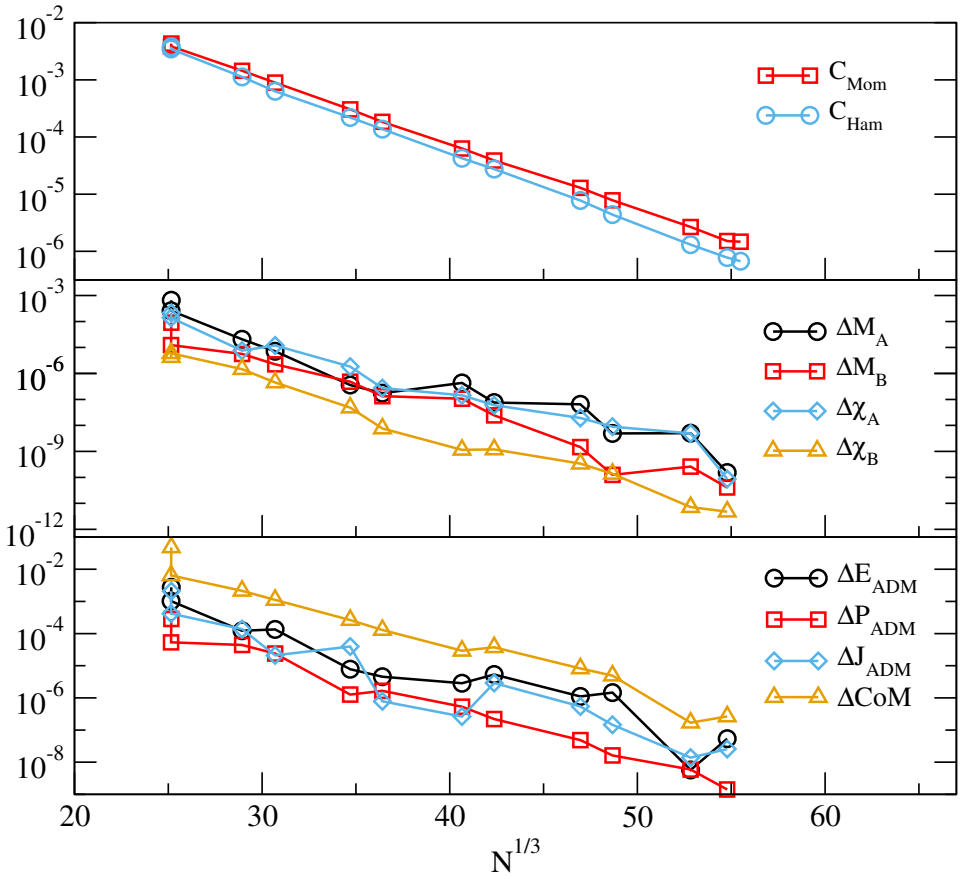

Figure 2.5: Convergence of physical quantities with increasing resolution for case q3. **Top**: the norm of Hamiltonian and momentum constraints, **middle**: masses and spins, **bottom**: ADM quantities and center of mass. "Δ" indicates the difference between the value of the respective quantity at the current resolution and the highest resolutions. The free parameters are fixed to their values at the end of root finding.

constraints are given explicitly by:

$$C_{\rm Ham} = \frac{1}{2}\left(R + K^2 - K_{ab}K^{ab}\right), \tag{2.30}$$

$$C_{\rm Mom} = D_b K^b_a - D_a K, \tag{2.31}$$

where D is the covariant derivative associated with the spatial metric. The L^2 norm is simply the normalized pointwise norm over all collocation points:

$$\|s\|_{L^2} = \sqrt{\frac{1}{N}\sum_i^N s_i^2}. \tag{2.32}$$

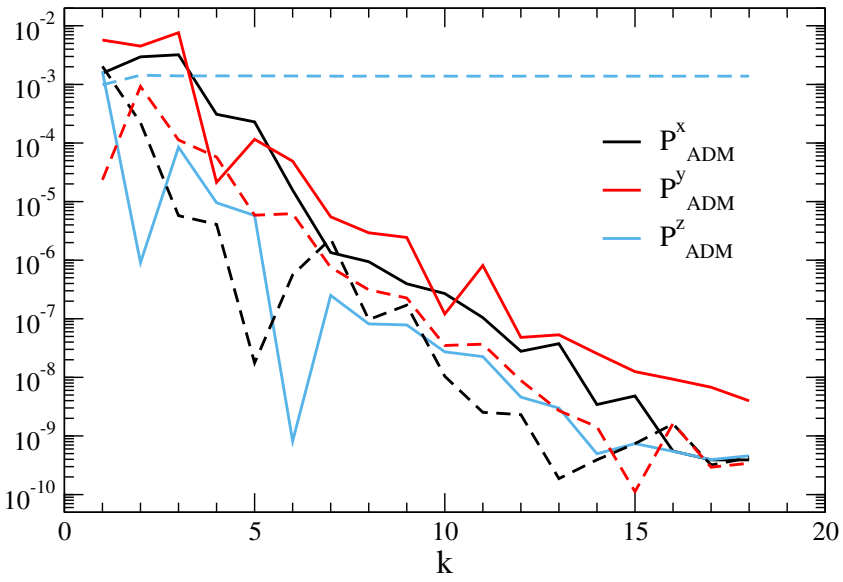

Figure 2.6: Comparison of $\mathbf{P}_{\rm ADM}$ control between the new code (solid lines) and the old code (dashed lines) as a function of root-finding iteration k. Both versions successfully control the x and y components of the linear momentum, but only the new code controls the z-component as well.

The convergence of the masses and spins is shown in the middle panel. Here we plot the norms of the differences between the quantity at a given iteration and its value at the highest resolution:

$$\Delta Q = |Q_i - Q_{\rm max}|. \tag{2.33}$$

Once again, the convergence is essentially exponential. The bottom panel of Fig. 2.5, finally examines the convergence of the ADM quantities and the center-of-mass computation. Though convergence is not as clean as for the constraints, the bottom panel of Figure 2.5 shows that all the asymptotic quantities can be determined to better than 10^{-6}.

To conclude our detailed examination of the initial data set `q3`, we contrast the new code described here with the old code [145, 38]. One of the most important upgrades lies in the control of $\boldsymbol{P}_{\rm ADM}$. Figure 2.6 shows the components of $\boldsymbol{P}_{\rm ADM}$ as a function of root-finding iteration k for both the new and the old code.[4] Both codes successfully drive $P^x_{\rm ADM}$ and $P^y_{\rm ADM}$ to zero as expected. But only the new code also drives $P^z_{\rm ADM}$ to zero, whereas the old code yields $P^z_{ADM} \simeq 0.00138$. As we shall see in the next section, this produces non-trivial differences in the evolution.

[4]Both codes *compute* $\boldsymbol{P}_{\rm ADM}$ in the same way (via Eq. (2.19)), but differ in the way it is *controlled*.

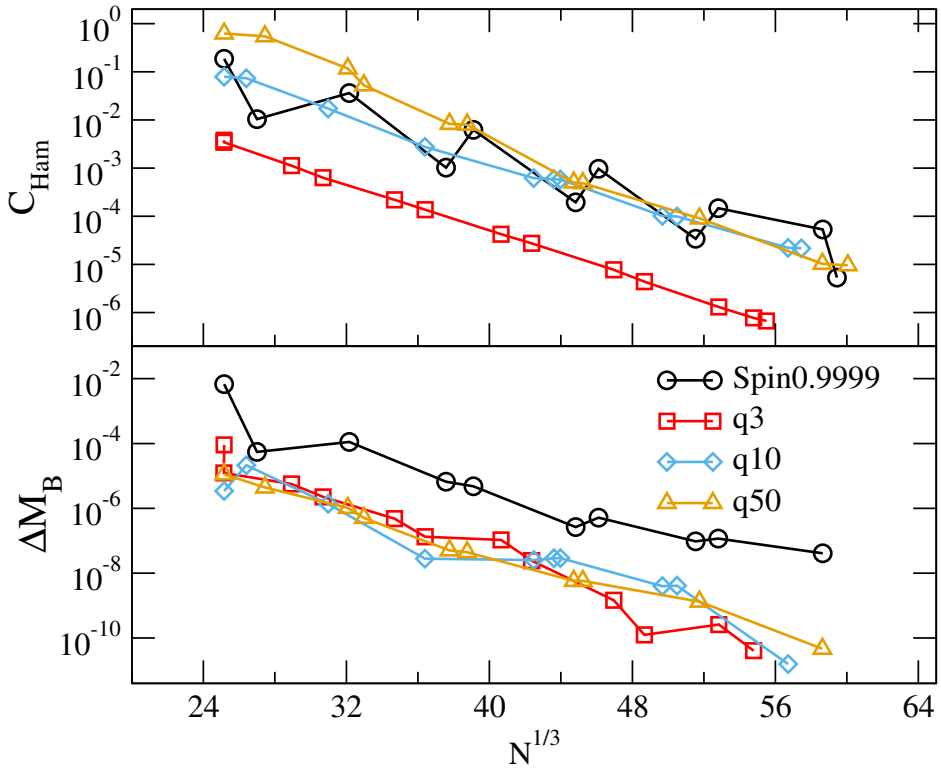

Figure 2.7: Overview of initial data results for cases in Table 2.1. **Top**: convergence of the L^2 norm of the Hamiltonian constraint. **Bottom**: convergence of the mass of the *smaller* black hole.The free parameters are fixed to their values at the end of root-finding.

Turning to the more challenging cases listed in Table 2.1, we have performed similar tests to case `q3`, with the free parameters fixed to their values at the end of root finding and only the resolution changing from iteration to iteration. As an example, Figure 2.7 shows a subset of the convergence data. This figure demonstrates that the exponential convergence shown previously for case `q3` extends to all cases. In particular, the constraints are exponentially convergent. All four cases complete with a maximal resolution of less than 2.5×10^5 points, an improvement of a factor of $2-3$ over the old code.[5] Owing to the more challenging configurations, however, the constraints are 1-2 orders of magnitude larger. The physical parameters are also exponentially convergent with resolution, as illustrated in the lower panel of Fig. 2.7. We use ΔM_B since it is frequently harder in a high mass ratio to resolve the smaller black hole, so this provides a conservative convergence test.

[5]We note that the case q50 could not be constructed with the old code.

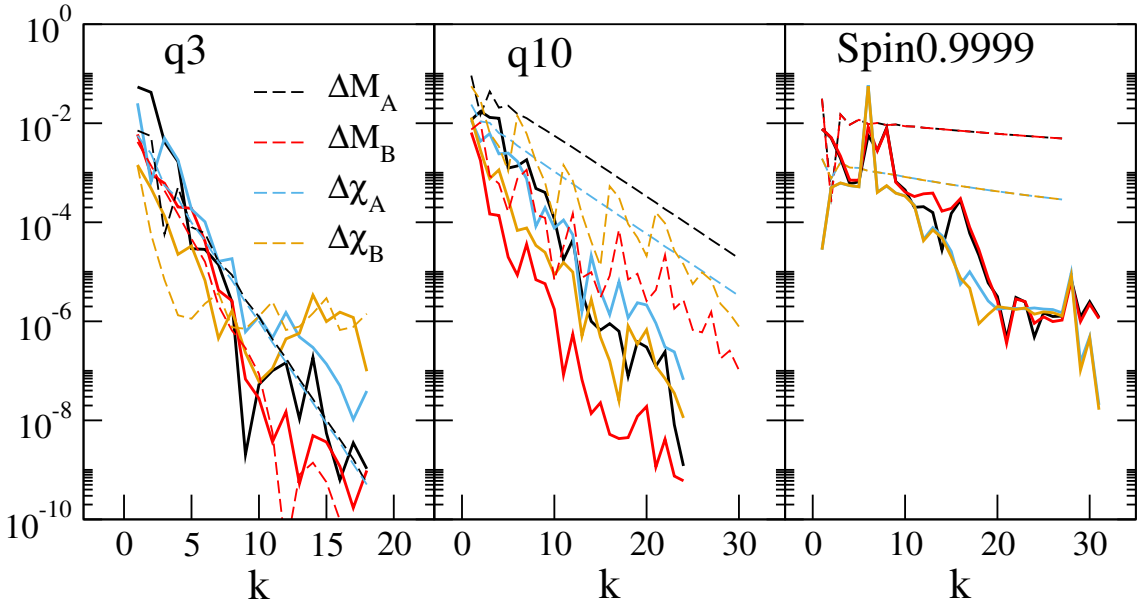

Figure 2.8: Convergence of the root-finding procedure for masses and spins when the old updating formulae are used (dashed lines), and with the new updating formulae developed here (solid lines). For q3 both algorithms perform well, whereas for q10 the new code converges about twice as fast as the old code. Finally for Spin0.9999 the old code fails to achieve desired masses and spins, while the new code gives errors of order 10^{-6}.

2.4.2 Root-finding

It is also important to examine the performance of the updated root-finding procedure based on Broyden's method. Figure 2.8 shows the root-finding results for cases q3, q10 and Spin0.9999 done with the old and new versions of the code. Note that during root-finding the resolution of the subdomains is also allowed to change to achieve the desired truncation error. For low mass ratio both codes show similar rates of convergence and final errors. The situation changes for case q10, where the old code has trouble achieving low errors in masses and spins, while the new root-finding procedure described in Sec. 2.3.3 results in errors of order 10^{-6}. Finally, for case Spin0.9999, the results are drastically different: the old code has errors in the masses of order several $\times 10^{-3}$ and spins of order 10^{-4}. Since we are attempting to construct a binary with dimensionless spins of 0.9999 it becomes clear that the old code is inadequate for this purpose. On the other hand, the new root-finding procedure successfully reduces the errors in physical quantities to the level of 10^{-6}. Thus, the new algorithm allows us to achieve the desired values of the physical quantities which is especially important as we push to higher spin magnitudes.

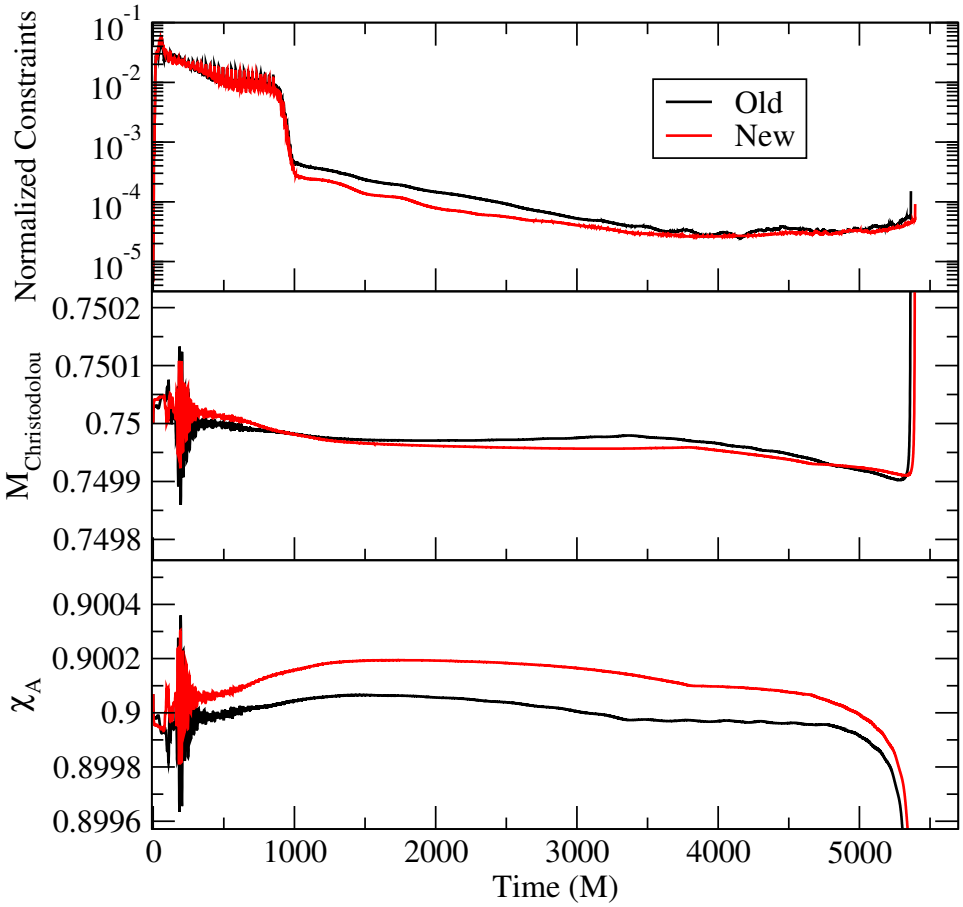

Figure 2.9: **Top**: Evolution of the normalized constraints. **Middle**: Evolution of the Christodolou mass of the large black hole. **Bottom**: Evolution of the spin $|\boldsymbol{\chi}_A|$.

On average, the new code is about 25-50% as fast as the old one. For example, for the case q10, the old code took 12.4 hours to complete, whereas the new took 6 hours on 12 cores of a Westmere node of the Briarée compute cluster. Therefore, the new code is indeed more efficient than the old while achieving the same or better accuracy.

2.4.3 Exploratory evolution

We have emphasized above the importance of controlling $\boldsymbol{P}_{\rm ADM}$. We now evolve initial data for case `q3` constructed with the old and the new initial-data code, and compare the two evolutions in detail.

We being by considering the convergence of constraints and quasi-local quantities during the evolution. The top panel of Figure 2.9 shows the L^2 norm of the normalized constraint violations during the evolution (see Eq.(71) of [108]). It is obvious that both

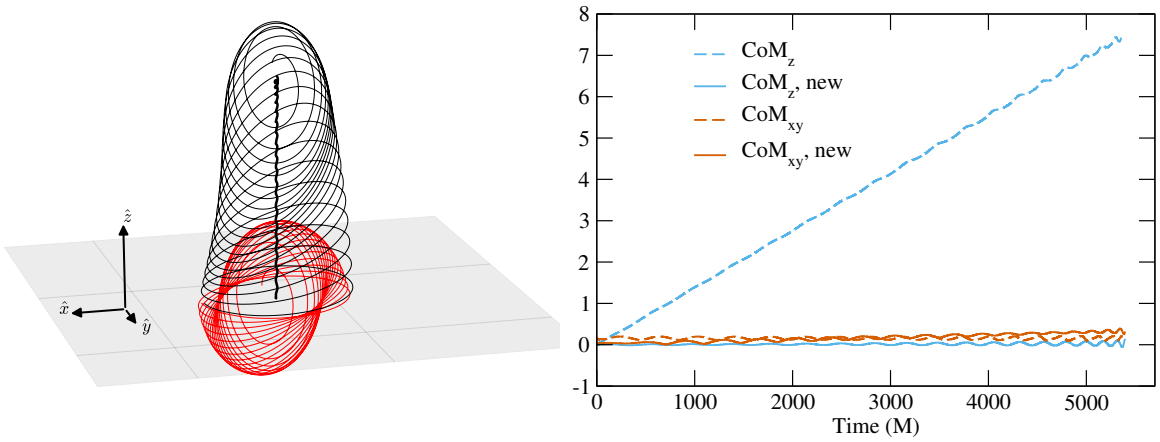

Figure 2.10: **Left**: The trajectories of the centres of the apparent horizons of the big black holes in the inertial frame. The thick black line represents the motion of the coordinate centre of mass for the drifting binary. The thin black curve correspond to initial data with large drift, the thick red, without. **Right**: The components of the coordinate centre of mass for both runs. The dashed curves refer to initial data with large drift, the solid curves without.

codes show similar convergence properties, as expected. Further, the initial spike of constraint violations due to junk radiation is virtually indistinguishable, which indicates that the new method of constructing initial data does not introduce additional constraint-violating modes. The middle and bottom panels of Fig. 2.9 show the evolution of the Christodoulou mass and the spin magnitude of the large black hole. The differences between the evolutions of the old and new initial data sets are consistent with truncation error. Thus we conclude that the quasi-local quantities are the same in both data sets.

Turning attention to the trajectories of the black holes, we find a stark difference in the evolutions. Figure 2.10 shows the motion of the large black hole in inertial coordinates for both runs. The uncontrolled residual linear momentum $P^z_{\rm ADM}$ in the old initial data causes the centre of mass of the binary to drift linearly during the evolution, as shown in the right panel of Figure 2.10. Such a drift may have multiple undesirable consequences. Most immediately, it causes the gravitational wave extraction spheres to be off-center from the center-of-mass of the binary, which will cause mixing of the spherical harmonic modes of the gravitational radiation, an effect discussed in more detail below. Moreover, `SpEC`'s constraint preserving outer boundary conditions [156, 155, 37] are designed to work best for low-order spherical harmonic modes of the outgoing radiation. If the binary is offset relative to the outer boundary (for instance due to a drift of the center of mass), higher order spherical harmonic components will become more important, possibly

leading to an additional runaway acceleration of the center of mass [174].

To examine the dynamics of the binary, we study the orbital frequency vector $\boldsymbol{\Omega} \equiv \boldsymbol{r} \times \dot{\boldsymbol{r}}/|\boldsymbol{r}|^2$. The left panel of Figure 2.11 shows the projection of $\boldsymbol{\Omega}$ onto the unit sphere, making it apparent that the precession and nutation dynamics are very similar until very close to merger. The right panel shows a plot of $\Omega \equiv |\boldsymbol{\Omega}|$ from which several features are apparent. The evolution of Ω is qualitatively the same in both cases, consistent with expectation that removing a coordinate motion of the centre of mass does not change the binary dynamics. Likewise the initial pulse of junk radiation (inset A) appears quite similar. However, small oscillations in Ω are more pronounced in the new code (inset C). This is reflected in the measured values of the eccentricities: $e = 10^{-4}$ for the old, $e = 2.5 \times 10^{-4}$ for the new code. The difference in eccentricity arises because the new term v_o^i in the outer boundary condition Eq. (2.28) *does* slightly modify the content of the initial data. In this particular case, $|v_0| \sim 10^{-3}$, so that it is not unreasonable to expect the orbital eccentricity to change by a comparable magnitude. The initial orbital frequency Ω_0, initial radial velocity $\dot{a}_0$, and initial separation D_0 listed in Table 2.1 were tuned to result in essentially vanishing eccentricity in the *old* initial data [43]. The new initial data constructed from the identical initial data parameters must therefore have a slightly larger eccentricity. If we had tuned to vanishing eccentricity with the *new* initial data, then the old initial data would exhibit the larger eccentricity.

The evolutions of the old and new initial data also result in a different time to merger, cf. panel B of Fig. 2.11. This difference could be caused either by the slightly different inspiral dynamics like eccentricity, or could simply be due to truncation error of our low resolution evolution.

Finally, we examine the waveforms for the two runs. Most strikingly, the movement of the coordinate centre of mass shown in Figure 2.10 is also reflected in the spherical-harmonic decomposition of the waveform. This is most easily seen in the sub-dominant modes. Figure 2.12 shows the $(\ell, m) = (3, 1)$ modes of the spin-weighted spherical-harmonic (SWSH) decompositions of the waveforms $h^{\rm old}$ measured from the old initial data and $h^{\rm new}$ measured from the new initial data. Since gravitational waves in `SpEC` are extracted on a coordinate sphere centered on the origin, a drifting source mixes the modes of the SWSH decomposition. As seen in the lower panel of the figure, this mixing introduces very large effects. To verify that these effects are primarily due to the motion of the center of mass, we have also transformed $h^{\rm new}$ to a frame in which the center of mass is moving as in the original initial data. The initial position of $h^{\rm new}$ is transformed to agree with the center of mass of the old initial data as measured by Eq. (2.25), and its velocity is transformed to agree with $\boldsymbol{P}_{\rm ADM}/M_{\rm ADM}$ of the old initial data as measured by

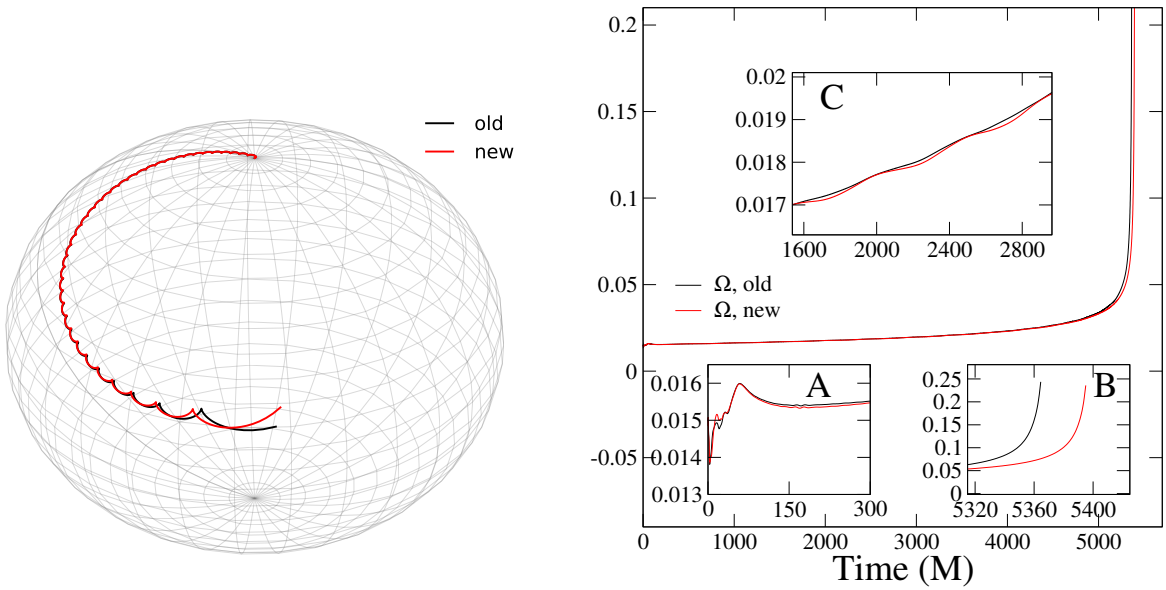

Figure 2.11: **Left**: The direction $\hat{\mathbf{\Omega}}(t)$ of the angular velocity vector on the unit sphere. Note the excellent agreement in precession dynamics. **Right**: The magnitude $\Omega(t)$ of the angular velocity vector. The overall agreement is very good. Insets A and B highlight the different times to merger due to junk radiation dynamics, while inset C demonstrates the different eccentricities.

Eq. (2.19). This transformation is applied entirely at future null infinity by the method described in [32], and is a special case of a BMS transformation [158, 132]. It will thus be seen in any waveforms, whether extrapolated [34] (as seen here) or extracted by Cauchy characteristic methods [23, 16, 179, 81]. As shown in the lower panel of Fig. 2.12, the transformation reproduces the features seen in $h^{\rm old}$ very well.

Mode decompositions like this one are used very frequently for analyzing numerical models, and for constructing analytical models. If they are unmodeled and uncontrolled, effects like those seen in the lower panel will simply appear to be errors in the waveform. This could negatively impact uncertainty estimates of numerical simulations, error estimates for analytical waveforms, or calibration of waveform models to numerical results. These effects will also be present in any calculation that uses the waveforms to compute physical quantities such as the flux of linear and angular momentum. By removing extraneous displacements and boosts, this new initial data code simplifies such analyses.[6]

[6]The drift described here is a linear motion due to residual linear momentum in initial data. Controlling this drift will not help for other types of motion present in very long simulations; see [174].

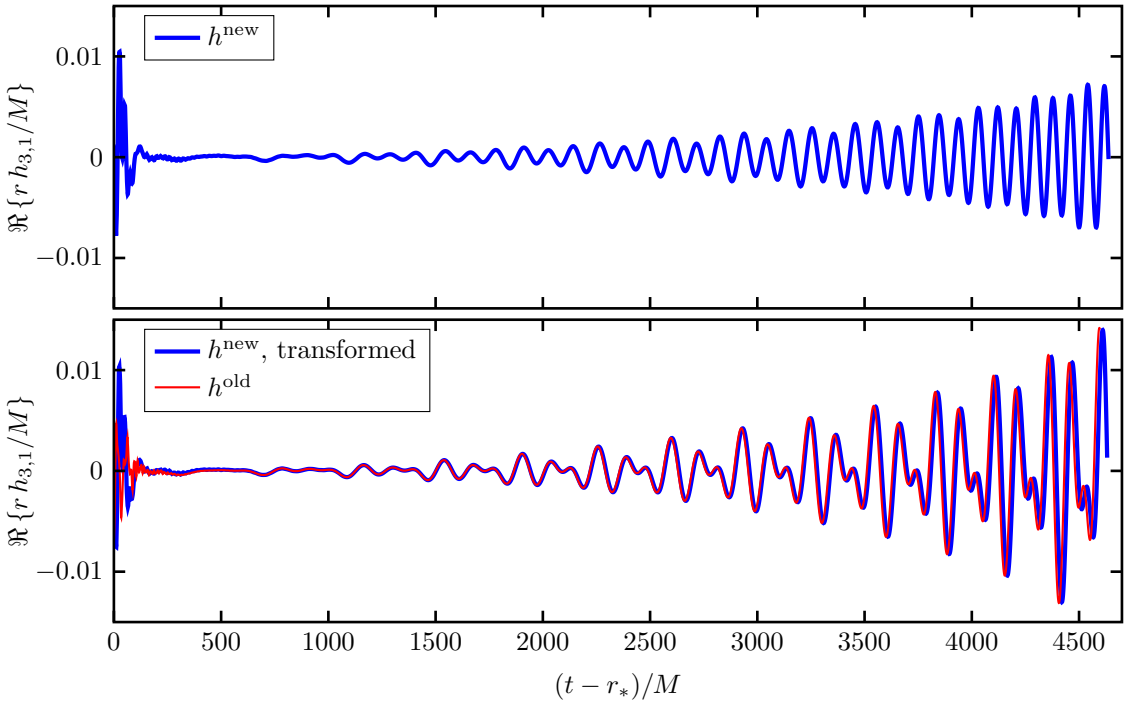

Figure 2.12: The $h_{3,1}$ waveform modes, as measured in evolutions of the original and the new initial data, and extrapolated to future null infinity, $\mathscr{I}^+$. The upper panel shows the waveform $h^{\rm new}$ from the new initial data, measured in a frame that is centered at the origin of the simulation coordinates. The lower panel shows the same data with a transformation applied on $\mathscr{I}^+$ as described in the text, as well as the waveform $h^{\rm old}$ from the original initial data measured in its simulation coordinates—in which the black holes are moving as shown in Fig. 2.10. Essentially, the center of mass is stationary at the origin in the upper panel, and is moving in the lower panel.

2.5 Discussion

Numerical evolution of binary black hole spacetimes requires accurate initial data. In this work we have improved the initial data techniques in `SpEC` to allow access to a much wider parameter space of generically precessing high mass ratio, high-spin binaries. A more flexible domain decomposition allows for stable solution for high-mass ratio and high spin binaries. An enhanced root-finding algorithm is used to achieve desired physical parameters for the binary. This becomes important when a naive analytic Jacobian is not appropriate, which is precisely the case for high mass ratios and spins, see Figure 2.8. Adaptive mesh refinement drastically improves efficiency and robustness of the code, displaying exponential convergence of constraints, c.f. Figure 2.7. Finally, a new method to control the linear momentum is used to eliminate a linear drift of the centre of mass during evolution. This in turn nullifies spurious gravitational mode mixing, which is of paramount importance for construction of hybrid waveforms or calibration of phenomenological models as demonstrated by Figure 2.12.

An interesting application of the improved initial data code is the construction of initial data for hyperbolic encounters. Such systems have been studied in the past (e.g. [63, 169, 90]) and provide a laboratory for exploring strong field physics in a different regime than the binary inspiral. Using the new code, we have successfully constructed initial data for hyperbolic encounters for a selection of mass ratios and spins, which was not possible before in `SpEC`. As a simple example, we evolve two systems of two equal mass black holes that are initially separated by 60M and have a velocity of $\approx 0.14c$. Both systems have the same impact parameter $b_{NR} = 15M$, and differ only in the black hole spins: In one case the black holes are non-spinning, in the other both holes have dimensionless spins $\chi = 0.5$ initially in the x direction. Figure 2.13 shows the trajectories of the two black holes. In the presence of spin, the spin-orbit interactions cause the plane of scattering to change and also change the deflection angle of the hyperbolic encounter. Exploration of other parameters is left to future investigations.

Another application is the construction of initial data for binaries with very small initial separation, corresponding to only a few orbits before merger. This is useful if one is interested in the properties of the merger remnant, e.g. for calibrating analytical waveform models but evolving a long inspiral is too computationally expensive. As an example, we construct initial data for a system with $q = 21$, $\chi_1 = 0.66$, $\chi_2 = 0.41$ (oriented in random directions) and initial orbital frequency of $M\Omega = 0.032$, and initial coordinate separation $D_0 = 8.82$ M.

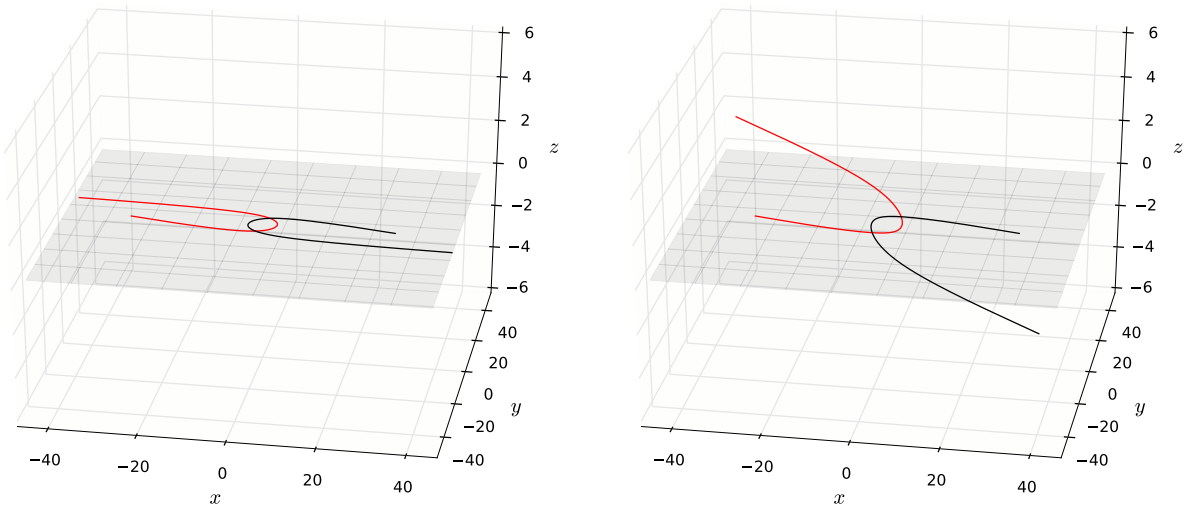

Figure 2.13: Hyperbolic encounter of two equal mass black holes shown through the coordinate trajectories of the black holes. **Left**: non-spinning black holes. **Right**: black holes with spin $\boldsymbol{\chi}_1 = \boldsymbol{\chi_2} = (0.5, 0.0, 0.0)$. The black holes start on the x-axis in the $x-y$ plane (shown in grey). In the spinning case the motion is not confined to this plane.

We note that initial data for binaries near ISCO at high mass-ratio is challenging and further work remains to be done to make it robust for $q > 10$ regime.

Acknowledgements

We thank Geoffrey Lovelace, Larry Kidder and Mark Scheel for helpful discussions. Calculations were performed with the `SpEC`-code [1]. We gratefully acknowledge support from NSERC of Canada, from the Canada Research Chairs Program, and from the Canadian Institute for Advanced Research. FF gratefully acknowledges support from the Vincent and Beatrice Tremaine Postdoctoral fellowship. Support for this work was provided by NASA through Einstein Postdoctoral Fellowship grant numbered PF4-150122. We further gratefully acknowledge support from the Sherman Fairchild Foundation; from NSF Grants PHY-1306125 and AST-1333129 at Cornell; and from NSF Grants No. PHY-1440083 and AST-1333520 at Caltech. Calculations were performed at the Gravity cluster and the GPC supercomputer at the SciNet HPC Consortium [110]; SciNet is funded by: the Canada Foundation for Innovation (CFI) under the auspices of Compute Canada; the Government of Ontario; Ontario Research Fund (ORF) – Research Excellence; and the University of Toronto. Further calculations were performed on the Briarée cluster from Sherbrooke University, managed by Calcul Québec and Compute Canada. The op-

eration of this supercomputer is funded by the Canada Foundation for Innovation (CFI), Ministère de l'Économie, de l'Innovation et des Exportations du Québec (MEIE), RMGA and the Fonds de recherche du Québec - Nature et technologies (FRQ-NT).

Chapter 3

Simulating precessing binaries in SpEC

3.1 Chapter overview[1]

Binary black hole simulations with black hole excision using spectral methods require a coordinate transformation into a co-rotating coordinate system where the black holes are essentially at rest. In this chapter we present and discuss two coordinate transformations that are applicable to *precessing* binary systems, one based on Euler angles, the other on quaternions. Both approaches are found to work well for binaries with moderate precession, i.e. for cases where the orientation of the orbital plane changes by $\ll 90^\circ$. For strong precession, performance of the Euler-angle parameterization deteriorates, eventually failing for a 90° change in orientation because of singularities in the parameterization ("gimbal lock"). In contrast, the quaternion representation is invariant under an overall rotation, and handles any orientation of the orbital plane as well as the Euler-angle technique handles non-precessing binaries.

3.2 Introduction

Gravitational waves offer an exciting new observational window into the universe. With the second generation of gravitational wave detectors such as Advanced LIGO and Advanced Virgo commencing observations in 2015 [2], it is extremely important to develop a detailed picture of the gravitational physics of the most likely sources. A very promising

[1]The material herein is based on Serguei Ossokine, Lawrence E. Kidder, and Harald P. Pfeiffer. *Precession-tracking coordinates for simulations of compact-object-binaries.* Phys. Rev. D, 88:084031, 2013.

source of gravitational waves are inspiraling and merging binary black holes [4]. Because of the weakness of the gravitational wave signal, matched filtering is necessary to pick out the waveform from the noise [71, 72]. Constructing such templates, in turn, requires direct numerical integration of Einstein's equations for the late inspiral, merger and ringdown phase of the coalescing compact object binary; see, e.g. [134]. Since 2005, starting with the seminal works of Pretorius [153], Campanelli et al [48] and Baker et al [17], many groups have successfully simulated binary black hole systems using a variety of different techniques. For recent overviews of the state of the field, see [94, 147].

Compact object inspirals fall into two categories: non-precessing and precessing. While the non-precessing aligned-spin systems arguably represent an important subspace of all binary black hole systems, the more general case features arbitrary spin orientations. In this non-symmetric situation, the interaction of the orbital angular momentum and the black holes' spins leads to precession of the orbital plane, changing its orientation by as much as 180 degrees.

Precession modulates the gravitational waveform. Therefore, it is crucial to explore these strongly precessing systems. Furthermore, precessing systems allow the study of gravitational dynamics in an underexplored regime, providing a new opportunity for comparing numerical relativity to various analytic approximations like Post-Newtonian (see e.g. [25, 24]) and effective-one-body theory (see e.g. [39, 61, 64, 62]). The numerical simulations can be used both to test the accuracy of the analytic treatments and to calibrate them, in some cases, thus improving their accuracy [67, 44, 176]. Furthermore, one can attempt to reproduce numerically predictions from analytic computations such as transitional precession [11], which is known from PN theory but has not yet been observed in numerical simulations.

Numerical simulations of precessing binary black holes have already been undertaken; for example [47, 46, 172, 171, 164, 189, 112, 114]. Given the vastness of parameter space and the need for simulations lasting at least 10 orbits - possibly 100's of orbits - to optimally exploit gravitational wave detectors [134, 60, 159, 31, 135, 122], a lot of extra work remains to be done.

The Spectral Einstein Code `SpEC` [1] allows efficient and accurate simulations of binary black holes; see e.g. [33, 121, 52, 38, 117, 119, 122, 129]. This code applies black hole excision and uses time-dependent coordinate mappings to rotate and deform the computational grid such that the excision regions remain inside the black hole horizons at all times. For non-precessing inspiralling binaries, these coordinate mappings are described in detail in previous work [33, 38, 92].

The purpose of the present chapter is to develop coordinate mappings that are able

to follow a precessing compact object binary through the inspiral, even for strongly precessing systems. We present two different approaches. The first one is based on Euler angles; it works well for moderate precession, but fails when the orientation of the orbital plane changes by 90 degrees or more. The second approach is designed to avoid the deficiencies of the Euler angle parameterization. By using quaternions, we devise coordinate mappings that work for any change of orientation of the orbital plane with a performance comparable to the earlier non-precessing techniques. The techniques developed here have already been used in [74, 130]

This chapter is organized as follows. Section 3.3 describes the computational setup of `SpEC` in more detail (Sec. 3.3.1), and develops the coordinate mappings based on Euler angles (Sec. 3.3.2) and quaternions (Sec. 3.3.3). Section 3.4 presents a sequence of numerical results obtained with both approaches, starting from Newtonian and Post-Newtonian test-cases to simulations of binary black holes with numerical relativity (NR). We summarize our results in Sec. 3.5.

3.3 Methods and Techniques

3.3.1 Dual frames and control systems

As described in Scheel et al. [163], `SpEC` utilizes a dual-frame approach to simulate compact object binaries. Einstein's equations are written down in an asymptotically non-rotating coordinate-system $x^{\bar{a}} = (\bar{t}, x^{\bar{i}})$, referred to as the "inertial frame", and all tensors are represented in the coordinate basis of this frame. In the inertial frame, tensor components remain finite even at large separation. The computational grid is specified in "grid coordinates" $x^a = (t, x^i)$. The collocation points of the spectral expansion are at constant grid coordinates, and numerical derivatives are computed with respect to these coordinates. The two coordinate frames share the same time-coordinate

$$\bar{t} = t. \tag{3.1}$$

The spatial coordinates of the two frames are related by a coordinate transformation

$$x^{\bar{i}} = x^{\bar{i}}\left(x^i; \lambda^\mu(t)\right), \tag{3.2}$$

which depends on a set of parameters $\lambda^\mu(t)$ to be discussed in detail later. The coordinate transformation Eq. (3.2) maps the grid-coordinates into the inertial frame such that the excision surfaces (coordinate spheres in the grid-frame) are mapped to locations

somewhat inside the apparent horizons of the black holes in the inertial frame.

In the original work [163], this coordinate transformation was taken as the composition of a rotation about the z-axis and an overall scaling of the coordinates[2],

$$x^{\bar{i}} = \begin{pmatrix} \bar{x} \\ \bar{y} \\ \bar{z} \end{pmatrix} = a(t) \begin{pmatrix} \cos\psi(t) & -\sin\psi(t) & 0 \\ \sin\psi(t) & \cos\psi(t) & 0 \\ 0 & 0 & 1 \end{pmatrix} \begin{pmatrix} x \\ y \\ z \end{pmatrix}. \tag{3.3}$$

In this simple case, the map $\lambda^\mu(t) = \{a(t), \psi(t)\}$ depends on two parameters: the scale factor $a(t)$ and the rotation angle $\psi(t)$. The map parameters $\lambda^\mu(t)$ are chosen dynamically during the simulation, such that the map tracks the actual motion of the black holes. This can be accomplished by introducing a set of control-parameters Q^μ, such that

1. $Q^\mu = 0$ if the mapped excision spheres are at the desired location in inertial coordinates.

2. Under small variations of the mapping parameters around their current values, the control-errors satisfy
$$\left.\frac{\partial Q^\mu}{\partial \lambda^\nu}\right|_{\lambda^\mu = \lambda^\mu(t)} = -\delta^\mu_\nu \tag{3.4}$$

While not strictly required, Eq. (3.4) allows one to write down uncoupled feedback control equations for the $\lambda^\mu(t)$. In the special case of a linear, uncoupled system, this reduces to $Q^\mu = \lambda^\mu_{target} - \lambda^\mu$.

For black holes orbiting in the xy-plane, Eq. (3.3) suffices to keep the excision boundaries inside the inspiraling black holes, resulting in successful simulations of inspiraling BH–BH binaries in Ref. [148]. Subsequently, the map was refined to avoid a rapid inward motion of the outer boundary [121], to adjust the shapes of the mapped excision boundaries to more closely conform to the distorted apparent horizons [175, 117, 119], and was generalized to unequal mass binaries [38]. Hemberger et al [92] summarizes these maps, and introduces further mappings that are needed during the merger phase of the black hole binary.

The purpose of the present chapter is the development of coordinate mappings that can handle precessing binaries. Because in general the center of mass will move (e.g due to asymmetric GW emission), these coordinate mappings must also allow for a translation

[2]Note that in Ref. [163], the equations give the transformation from the inertial coordinates to the grid coordinates, the rotation angle is ϕ instead of ψ, and the scale factor a is the inverse of the scale factor in this chapter.

of the binary. Rotation and translation couple to each other and must therefore be dealt with simultaneously. The questions addressed in this work are therefore (1) determination of a suitable coordinate mapping for precessing, translating binaries, (2) suitable choice of mapping parameters λ^μ, and (3) derivation of control-parameters Q^μ. Specifically, we will discuss below two generalizations of Eq. (3.3), one based on Euler-angles and one based on quaternions. We will show that the Euler-angle representation suffers from singularities when the inclination of the orbital plane passes through $\pi/2$, and we will demonstrate that the quaternion representation fixes these problems.

3.3.2 Euler angle representation

In the general case where the orbital plane precesses, we use a mapping that composes a scaling $a(t)$, a rotation $R(t)$ and a translation $\vec{T}(t)$. The mapping is given by

$$\vec{\bar{x}} = a(t)\, R(t)\, \vec{x} + \vec{T}. \tag{3.5}$$

A rotation matrix can be specified by Euler angles,

$$R = \begin{pmatrix} \cos\theta\cos\psi & -\cos\phi\sin\psi + \sin\phi\sin\theta\cos\psi & \sin\phi\sin\psi + \cos\phi\sin\theta\cos\psi \\ \cos\theta\sin\psi & \cos\phi\cos\psi + \sin\phi\sin\theta\sin\psi & -\sin\phi\cos\psi + \cos\phi\sin\theta\sin\psi \\ -\sin\theta & \sin\phi\cos\theta & \cos\phi\cos\theta \end{pmatrix}. \tag{3.6}$$

where ϕ is the roll angle around the x-axis, θ is the pitch angle around the y-axis, and ψ is the yaw angle around the z axis and we have suppressed the explicit time-dependence.

For our application, the desired locations of the black holes lie parallel to the x-axis, i.e. the black holes are at grid coordinates (c_A^x, c^y, c^z) and (c_B^x, c^y, c^z). It is straightforward to show that for these two points a rotation about the x-axis is degenerate with a particular translation *because only the location of the black holes is important.* Therefore, we can set $\phi(t) = 0$ so that[3]

$$R = \begin{pmatrix} \cos\theta\cos\psi & -\sin\psi & \sin\theta\cos\psi \\ \cos\theta\sin\psi & \cos\psi & \sin\theta\sin\psi \\ -\sin\theta & 0 & \cos\theta \end{pmatrix}. \tag{3.7}$$

Thus the mapping in Eq. (3.5) will have six parameters in this case, a scaling $a(t)$, a

[3]Note that if the motion is confined to the $x-y$ plane, the pitch will remain fixed at $\theta = 0$ and we recover the rotation matrix in Eq. (3.3).

pitch angle (rotation about y-axis) $\theta(t)$, a yaw angle (rotation about z-axis) $\psi(t)$, and a translation $(T^X(t), T^Y(t), T^Z(t))$.

The goal of the scaling-rotation-translation map is to keep the horizons of the two black holes centered on the excision surfaces. As the binary evolves, the map parameters need to be adjusted by the control system. To derive the control parameters Q^μ, c.f. Eq(3.4), one can consider perturbations of the mapping parameters around their current values. Let $\lambda^\mu = \{a, \theta, \psi, \vec{T} = (T^X, T^Y, T^Z)\}$ be the current imperfect mapping parameters at some time during the evolution. Furthermore, denote the desired parameters $\lambda_0^\mu = \lambda^\mu + \delta\lambda^\mu = \{a_0, \theta_0, \psi_0, T_0^X, T_0^Y, T_0^Z\}$. Finally, let $\vec{x}_A$ and $\vec{x}_B$ denote the current location of the center of black hole A and B, respectively[4], and let $\vec{c}_A$ and $\vec{c}_B$ denote the desired location of the black hole centers; i.e., the centers of the excision spheres. For convenience we also define the vectors $\vec{X} = \vec{x}_A - \vec{x}_B$ and $\vec{C} = \vec{c}_A - \vec{c}_B$. The target mapping λ_0^μ is such that the points $\vec{c}_A,\ \vec{c}_B$ are mapped onto the inertial frame position of the black holes, $\vec{\bar{c}}_A = \vec{\bar{x}}_A,\ \vec{\bar{c}}_B = \vec{\bar{x}}_B$:

$$\vec{\bar{x}}_{\mathrm{A},B} = a_0 R(\theta_0, \psi_0)\vec{c}_{\mathrm{A},B} + \vec{T}_0. \tag{3.8}$$

Rewriting this equation in terms of the current mapping and the grid location of each black hole (i.e $\vec{x}_{A,B}$) yields

$$aR(\theta, \psi)\vec{x}_i + \vec{T} = (a + \delta a)R(\theta + \delta\theta, \psi + \delta\psi)\vec{c}_i + \vec{T} + \delta\vec{T}. \tag{3.9}$$

where $i = A,\ B$.

Equation (3.9) represents six equations for the six unknowns $\delta\lambda^\mu$. Solving this system

[4]The precise definition of "center" is not important; we shall use the coordinate point around which the coordinate radius of the apparent horizon has vanishing $l = 1$ multipoles.

of equations to leading order in the perturbations yields

$$\begin{aligned}
\delta a &= a\left(\frac{X^x}{C^x} - 1\right), && (3.10a)\\
\delta\theta &= \frac{-X^z}{C^x}, && (3.10b)\\
\delta\psi &= \frac{1}{\cos\theta}\frac{X^y}{X^x}, && (3.10c)\\
\delta T^X &= \frac{a}{C^x}\left(\delta t^X \cos\theta\cos\psi - \delta t^Y \sin\psi \right.\\
&\quad \left. + \delta t^Z \sin\theta\cos\psi\right), && (3.10d)\\
\delta T^Y &= \frac{a}{C^x}\left(\delta t^X \cos\theta\sin\psi + \delta t^Y \cos\psi \right.\\
&\quad \left. + \delta t^Z \sin\theta\sin\psi\right), && (3.10e)\\
\delta T^Z &= \frac{a}{C^x}\left(-\delta t^X \sin\theta + \delta t^Z \cos\theta\right), && (3.10f)
\end{aligned}$$

where

$$\begin{aligned}
\delta t^X &= c_A^x x_B - c_B^x x_A + c^y X^y + c^z X^z, && (3.11a)\\
\delta t^Y &= c_A^x y_B - c_B^x y_A - c^y X^x \\
&\quad - c^z X^y \tan\theta, && (3.11b)\\
\delta t^Z &= c_A^x z_B - c_B^x z_A + c^y X^y \tan\theta \\
&\quad + c^z X^x, && (3.11c)
\end{aligned}$$

Furthermore, we have assumed that the centers of the excision surfaces are aligned parallel to the x-axis so that $c_A^y = c_B^y = c^y$ and $c_A^z = c_B^z = c^z$.

Perhaps surprisingly, the $\delta\lambda^\mu$ given by Eq. (3.10a –3.10f) are the desired control parameters Q^μ. This can be seen as follows. For a perfect map, $\lambda^\mu = \lambda_0^\mu$, i.e. $\delta\lambda^\mu = Q^\mu = 0$. Moreover, by definition

$$\frac{\partial Q^\mu}{\partial\lambda^\nu} = \frac{\partial}{\partial\lambda^\nu}\left(\lambda_0^\mu - \lambda^\mu\right) = \frac{\partial\lambda_0^\mu}{\partial\lambda^\mu} - \frac{\partial\lambda^\mu}{\partial\lambda^\nu} = -\delta_\nu^\mu. \tag{3.12}$$

Thus $\delta\lambda^\mu$ defined by Eq. (3.10a –3.10f) satisfy the conditions for Q^μ outlined in section 3.3.1.

The Euler angle prescription as described above is adequate for describing rotations that are close to the $x-y$ plane, and has been used for the `SpEC` simulations presented in [175]. However, the Euler angle prescription carries with it an inherent coordinate singularity that causes a breakdown of the control system for high inclination angles.

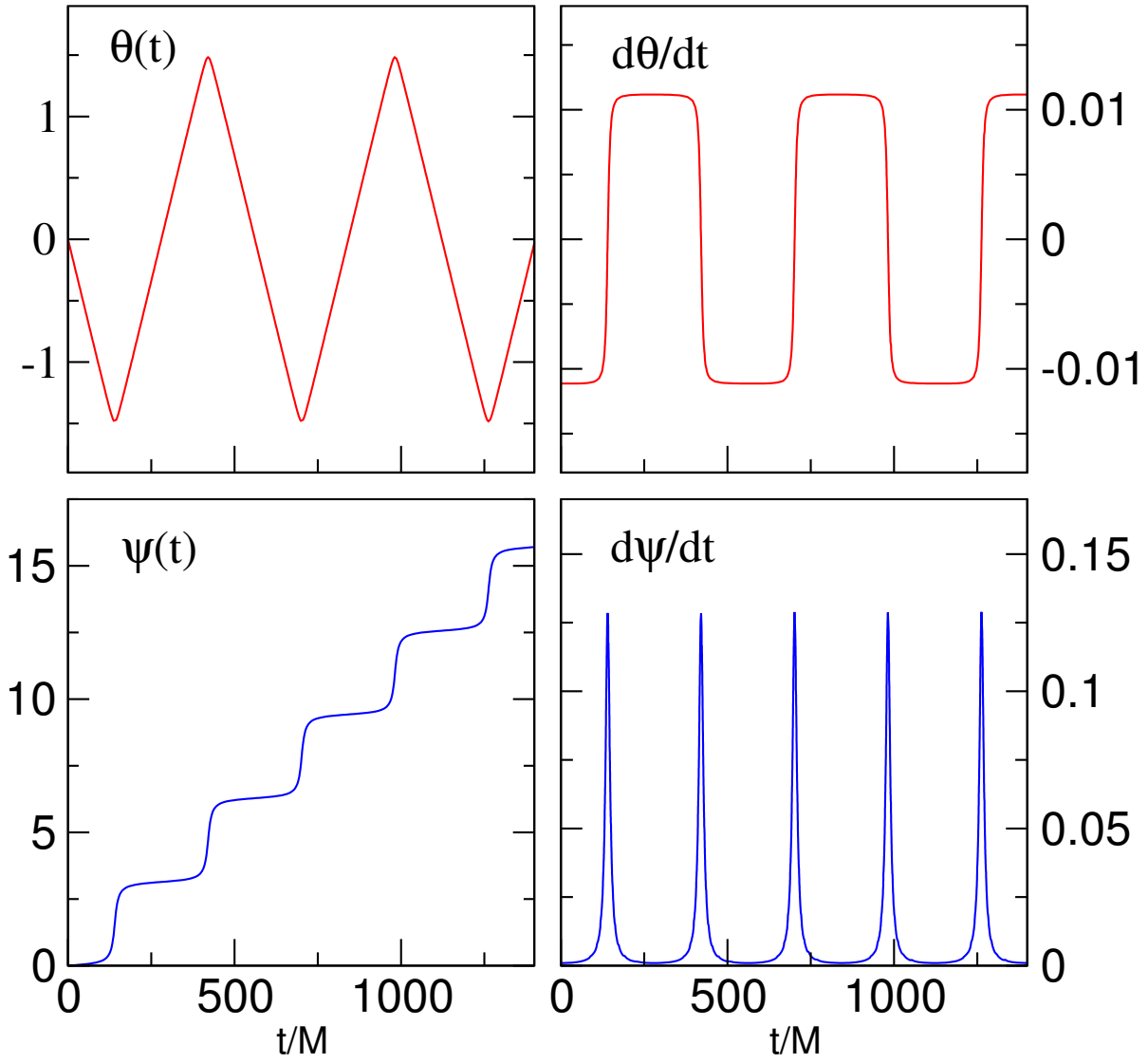

Figure 3.1: Typical behaviour of the Euler angles and their derivatives for a nearly polar orbit inclined at 85 degrees with respect to the $x-y$ plane.

Firstly, note that Eq. (3.10c) shows that $\delta\psi$ will diverge when $\theta = \frac{\pi}{2}$, which would lead to the breakdown of a feedback control system. Further, since `SpEC` uses proportional-derivative-control or proportional-integral-derivative-control [92], we must examine the behaviour of the derivatives of the Euler angles, $\dot{\theta},\ \dot{\psi}$. Notice that we can relate the angular velocity to the derivatives of the Euler angles simply by the relationship

$$(\omega_1, \omega_2, \omega_3)^T = A\ (\dot{\phi}, \dot{\theta}, \dot{\psi})^T, \tag{3.13}$$

the superscript T denotes the transpose and A is the Euler angle rates matrix:

$$A = \begin{pmatrix} \cos\psi\cos\theta & -\sin\psi & 0 \\ \sin\psi\cos\theta & \cos\psi & 0 \\ -\sin\theta & 0 & 1 \end{pmatrix}. \tag{3.14}$$

The black holes move on regular trajectories with a slowly varying orbital frequency $\vec{\omega}$ in inertial coordinates; therefore, the left-hand side of Eq. (3.13) is continuous. However, $|\det A| = |\cos(\theta)|$, so that for $\theta = \frac{\pi}{2}$ the time-derivatives of the Euler angles will diverge since, by Cramer's rule, the inverse of A scales as $1/\det A$.

There is another way to envision the divergence of the derivatives of the Euler angles. Consider the unit vector in the direction connecting the centers of the two compact objects in inertial coordinates, $\hat{u} = \frac{\vec{x}_B - \vec{x}_A}{|\vec{x}_B - \vec{x}_A|}$. Before, we considered $\psi,\ \theta$ as parameters in a mapping. Let us now consider them as spherical polar coordinates that describe this vector[5]

$$\begin{pmatrix} u_x \\ u_y \\ u_z \end{pmatrix} = \begin{pmatrix} \cos\psi\cos\theta \\ \sin\psi\cos\theta \\ \sin\theta \end{pmatrix}. \tag{3.15}$$

We can immediately derive the expressions for $\dot{\theta},\ \dot{\psi}$ as functions of $\dot{u}_x,\ \dot{u}_y,\ \dot{u}_z$:

$$\dot{\theta} = \frac{\dot{u}_z}{\cos\theta}, \tag{3.16}$$

$$\dot{\psi} = \frac{1}{\cos\theta}\sqrt{\dot{u}_x^2 + \dot{u}_y^2 - \dot{u}_z^2\tan^2\theta}. \tag{3.17}$$

From these equations it is obvious that the derivatives of θ and ϕ behave abnormally when $\hat{u}$ moves across one of the poles at uniform velocity. In fact, $\dot{\theta}$ does not exist, and

[5] θ here means the angle to the xy plane rather then the angle to the z-axis. Therefore the following equations differ slightly from standard spherical polar coordinates.

its second derivative diverges (see the top panels of Fig. 3.1). Meanwhile, $\dot{\psi}$ diverges: letting $\delta\theta = \frac{\pi}{2} - \theta$ we can write, for $\delta\theta \ll 1$:

$$\dot{\psi} \propto \frac{\omega}{\delta\theta}. \tag{3.18}$$

This behaviour is demonstrated clearly in Figure 3.1, where the derivatives of both Euler angles angles demonstrate sharp and nearly discontinuous features.

This is the fundamental reason why Euler angles are not a suitable parametrization of rotations: there exist situations, which we would like to study, when their derivatives grow extremely fast numerically.

3.3.3 Rotation–invariant Quaternion representation

The origin of the break-down of the Euler angle representation lies in its reliance of a preferred coordinate system, which is implicit in the adoption of Euler angles. The physics of compact object inspirals is invariant under rotations of the spatial coordinates. Ideally, the numerical methods used to describe such a system should also be invariant, and should work equally well independent of the orbital plane of the black holes.

The singularities in the Euler angle representation arise from a poor choice of representation of the rotation group, which relied on preferred directions in space (namely the coordinate axes). Therefore, a suitable representation must be independent of any special directions. We employ quaternions to represent rotations and build up the overall rotation from a sequence of infinitesimal rotations.

It should be noted that a similar construction can be done with a different paramtetrization of rotations. See the Appendix for an example using orthogonal infinitesimal rotation matrices.

Quaternion algebra

Quaternions are an extension of the complex numbers, with three imaginary units i, j, and k, obeying

$$i^2 = j^2 = k^2 = ijk = -1, \tag{3.19}$$

as well as certain further multiplication rules. A quaternion $\boldsymbol{q}$ has the form

$$\boldsymbol{q} = q_0 + q_1 i + q_2 j + q_3 k, \qquad q_0, \ldots, q_3 \in \mathbb{R}. \tag{3.20}$$

This is conveniently written as $\boldsymbol{q} = (q_0, \vec{q})$, where $\vec{q} = (q_1, q_2, q_3)$. Addition and

scalar multiplication are defined in analogy with complex numbers. With the structure introduced so far, the set of quaternions

$$\mathbb{H} = \{q_0 + q_1 i + q_2 j + q_3 k | q_i \in \mathbb{R}\} \tag{3.21}$$

is a 4-dimensional vector space over the real numbers. Multiplication is defined by

$$\boldsymbol{q}\,\boldsymbol{p} = (p_0 q_0 - \vec{p}\cdot\vec{q}, p_0\vec{q} + q_0\vec{p} + \vec{p}\times\vec{q}), \tag{3.22}$$

where $\vec{q}\cdot\vec{q}$ and $\vec{q}\times\vec{p}$ are the standard Euclidean dot and cross products respectively. Complex conjugation is given by

$$\boldsymbol{q}^* = (q_0, -\vec{q}). \tag{3.23}$$

It follows that the multiplicative inverse is given by

$$\boldsymbol{q}^{-1} = \frac{\boldsymbol{q}^*}{|\boldsymbol{q}|}, \tag{3.24}$$

where the norm $|\boldsymbol{q}|$ satisfies

$$|\boldsymbol{q}|^2 = \boldsymbol{q}\,\boldsymbol{q}^* = q_0^2 + \vec{q}^{\,2}. \tag{3.25}$$

More details can be found for example in [102].

Restricting our attention now to the set of all unit quaternions
$Sp(1) = \{\boldsymbol{q} \in \mathbb{H}, |\boldsymbol{q}| = 1\}$, it is easy to show that $Sp(1)$ is isomorphic to $SU(2)$ where $SU(2)$ is the group of all 2×2 unitary matrices with unit determinant [10]. $SU(2)$ is a double cover of the rotation group $SO(3)$, which means that unit quaternions do represent rotations.

Unit quaternions are related to rotations in the following manner. Let $\hat{n}$ be a unit-vector, and define

$$\boldsymbol{q} = (\cos\frac{\theta}{2}, \hat{n}\sin\frac{\theta}{2}) \tag{3.26}$$

for some angle θ. The quaternion $\boldsymbol{q}$ rotates a vector $\vec{v}$ into the vector $\vec{v}'$, around the axis $\hat{n}$ by angle θ in the right-handed sense via

$$\boldsymbol{v}' = \boldsymbol{q}\,\boldsymbol{v}\,\boldsymbol{q}^*. \tag{3.27}$$

In this equation, 3-vectors are to be promoted to quaternions by the rule $\boldsymbol{v} = (0, \vec{v})$, $\boldsymbol{v}' = (0, \vec{v}')$,and $|\boldsymbol{q}| = 1$ implies that $\boldsymbol{v}'$ has indeed a vanishing real part. Equation (3.27)

is equivalent to $\vec{v}\,' = R_{\boldsymbol{q}}\vec{v}$, with rotation matrix

$$R_{\boldsymbol{q}} = \begin{pmatrix} q_0^2+2q_1^2-\vec{q}^{\,2} & 2(q_1q_2-q_0q_3) & 2(q_0q_2+q_1q_3) \\ 2(q_1q_2+q_0q_3) & q_0^2+2q_2^2-\vec{q}^{\,2} & 2(q_2q_3-q_0q_1) \\ 2(q_1q_3-q_0q_2) & 2(q_0q_1+q_2q_3) & q_0^2+2q_3^2-\vec{q}^{\,2} \end{pmatrix}. \tag{3.28}$$

We can now rewrite Eq. (3.5) in quaternion language,

$$\bar{\boldsymbol{x}} = a\,\boldsymbol{q}\,\boldsymbol{x}\,\boldsymbol{q}^* + \boldsymbol{T}. \tag{3.29}$$

Here, $\vec{x}, \bar{\vec{x}}, \vec{T}$ have been promoted to quaternions; e.g., $\boldsymbol{T} = (0, \vec{T})$.

Our next task is to derive equations that determine the time evolution of $\boldsymbol{q}$ as well as the control parameters Q^μ.

Quaternion kinematics

In this section we derive the differential equation obeyed by the rotation quaternion $\boldsymbol{q}$. Consider a time-dependent unit-quaternion $\boldsymbol{q}(t) : \mathbb{R} \to Sp(1)$. The derivative is defined by

$$\dot{\boldsymbol{q}} = \lim_{h\to 0} \frac{\boldsymbol{q}(t+h) - \boldsymbol{q}(t)}{h}. \tag{3.30}$$

We write the rotation $\boldsymbol{q}(t+h)$ at time $t+h$, as a product of $\boldsymbol{q}(t)$ and a quaternion $\boldsymbol{u}$ representing an infinitesimal rotation,

$$\boldsymbol{q}(t+h) = \boldsymbol{u}\,\boldsymbol{q}(t). \tag{3.31}$$

The quaternion $\boldsymbol{u}$ is easily obtained by expanding the right hand side of Eq. (3.26) to first order in θ using $\cos\frac{\theta}{2} \approx 1,\ \sin\frac{\theta}{2} \approx \frac{\theta}{2}$:

$$\boldsymbol{u} = (1, \hat{n}\frac{\theta}{2}) = 1 + \boldsymbol{\delta q}/2, \tag{3.32}$$

with $\boldsymbol{\delta q} = (0, \hat{n}\theta)$. If the rotational velocity is $\vec{\omega}$ in inertial coordinates, then $\hat{n} = \hat{\omega}$ and $\delta\theta = \omega\,h$, so that $\boldsymbol{\delta q} = \boldsymbol{\omega}\,h$. Thus we can write $\boldsymbol{q}(t+h) = (I + \boldsymbol{\delta q}/2)\boldsymbol{q}(t)$. Substituting,

$$\dot{\boldsymbol{q}} = \lim_{h\to 0} \frac{(I + \boldsymbol{\delta q}/2)\boldsymbol{q}(t) - \boldsymbol{q}(t)}{h} = \frac{1}{2}\boldsymbol{\omega}\,\boldsymbol{q}. \tag{3.33}$$

Noting that in grid coordinates the angular velocity is $\boldsymbol{\Omega} = \boldsymbol{q}^*\boldsymbol{\omega}\boldsymbol{q}$, we finally obtain

[13][6]

$$\dot{\boldsymbol{q}} = \frac{1}{2}\boldsymbol{q}\,\boldsymbol{\Omega}. \tag{3.34}$$

Quaternion control system

The goal of the sector of the control-system for rotations is to keep the vector $\vec{X}$ parallel to the vector $\vec{C}$. The misalignment between them can be measured by the rotation needed to make these vectors parallel:

$$\vec{Q}_R = \frac{\vec{C}\times\vec{X}}{\|\vec{C}\|^2} \simeq \frac{\vec{C}\times\vec{X}}{\vec{C}\cdot\vec{X}}, \tag{3.35}$$

where the subscript 'R' indicates that this quantity is of relevance for rotations.[7] The dot and cross products are defined in the standard Euclidean sense. The control-system needs to adjust the angular velocity $\vec{\Omega}$ such that $\vec{Q}_R \approx 0$. As long as the control-system works, this instantaneous rotation is small, and therefore, non-commutativity of rotations can be neglected. This suggests to control the angular velocity in the moving frame $\vec{\Omega}$ based on the control-parameter $\vec{Q}_R$.

We proceed as follows: We measure $\vec{Q}_R$ regularly during the BBH evolution,and compute its first and second time-derivatives. As in earlier work [163] (and in many papers since [119, 52, 33, 148, 121, 38, 129]), we use this to reset the third time-derivative of the mapping-parameters that determine the rotation. These parameters are the second time-derivative of $\vec{\Omega}(t)$; thus, we choose $\vec{\Omega}(t)$ such that it has constant second time-derivative. We periodically reset this constant using the equation

$$\frac{d^2\vec{\Omega}}{dt^2} = \alpha\vec{Q}_R + \beta\frac{d\vec{Q}_R}{dt} + \gamma\frac{d^2\vec{Q}_R}{dt^2}. \tag{3.36}$$

A constant value of $d^2\vec{\Omega}/dt^2$ implies that $\Omega(t)$ is a piece-wise quadratic polynomial. Whenever the second derivative is reset, we choose integration constants such that $\vec{\Omega}$ and $d\vec{\Omega}/dt$ are continuous. Finally, we use $\vec{\Omega}(t)$ to determine the actual rotation-matrix via Eq. (3.34).

There are alternative control-feedback equations to Eq. (3.36). Some of them are discussed in [92]. The details of the feedback equation do not influence the main focus of this chapter which is how to represent rotations and control parameters.

[6]This reference uses the opposite convention of the one adapted here: Ω is the angular velocity in the fixed frame whereas ω is the angular velocity in the rotating frame.

[7]The normalization chosen corresponds to the fact that only the direction of the two vectors matter in the context of rotations, and due to the scaling control system we should have to first order, $\|\vec{X}\| \simeq \|\vec{C}\|$. The second approximate equality holds when the deviation from the initial position is small.

In SpEC, Eq. (3.34) is integrated with a 5-th order Dormand-Prince time-stepper [152].

While Eq. (3.34) analytically preserves the unit-norm of $\boldsymbol{q}$, numerical integration will not identically preserve $|\boldsymbol{q}| = 1$. Therefore, the $\boldsymbol{q}(t)$ returned by the ODE-integrator is rescaled to unit-length, $\boldsymbol{q} \to \boldsymbol{q}/|\boldsymbol{q}|$ before it is used to construct rotations.

Whenever $d^2\vec{\Omega}/dt^2$ is reset via Eq. (3.36), $\boldsymbol{q}$ of the ODE integrator is also rescaled to unit length.

Equation (3.35) can also be derived with the formal procedure introduced in Section 3.3.2. This derivation will highlight an ambiguity not visible in Eq. (3.35), and will also result in the control parameters for scaling and translation. We start with

$$\bar{\boldsymbol{x}} = a\,\boldsymbol{q}\,\boldsymbol{x}\,\boldsymbol{q}^* + \boldsymbol{T}, \tag{3.37}$$

where $\bar{\boldsymbol{x}}, \boldsymbol{x}, \boldsymbol{q}, \boldsymbol{T}$ are quaternions and $a \in \mathbb{R}$. All vector quantities are now treated as quaternions via the identification map $\boldsymbol{v} = (0, \vec{v})$. We now perturb $a \to a + \delta a$, $\boldsymbol{T} \to \boldsymbol{T} + \boldsymbol{\delta T}$, $\boldsymbol{q} \to \boldsymbol{q}\left(1 + \frac{\boldsymbol{\delta q}}{2}\right)$. The $\boldsymbol{q}$ - perturbation will result in vectors $\vec{v}$ being mapped to

$$\boldsymbol{v}' = \boldsymbol{q}\left(1 + \frac{\boldsymbol{\delta q}}{2}\right)\boldsymbol{v}\left(1 - \frac{\boldsymbol{\delta q}}{2}\right)\boldsymbol{q}^* = \boldsymbol{q}\,\boldsymbol{w}\,\boldsymbol{q}^*, \tag{3.38}$$

where $\boldsymbol{w} \equiv \left(1 + \frac{\boldsymbol{\delta q}}{2}\right)\boldsymbol{v}\left(1 - \frac{\boldsymbol{\delta q}}{2}\right)$. This shows that the imaginary part $\vec{\delta q}$ of $\boldsymbol{\delta q} = (0, \vec{\delta q})$ represents a rotation in *grid* coordinates.

The quaternion version of Eq. (3.9) is:

$$\begin{aligned} &a\boldsymbol{q}\boldsymbol{x_i}\boldsymbol{q}^* + \boldsymbol{T} = \\ &(a + \delta a)\boldsymbol{q}\left(1 + \frac{\boldsymbol{\delta q}}{2}\right)\boldsymbol{c_i}\left(1 - \frac{\boldsymbol{\delta q}}{2}\right)\boldsymbol{q}^* + \boldsymbol{T} + \boldsymbol{\delta T}. \end{aligned} \tag{3.39}$$

with $i = A, B$. Because the real part of Eqs. (3.39) are trivially satisfied, Eqs. (3.39) represent six equations, three each for black hole A and for black hole B. We seek to solve Eqs. (3.39) for the unknowns δa, $\boldsymbol{\delta T} = (0, \vec{\delta T})$, and $\boldsymbol{\delta q} = (0, \vec{\delta q})$. Because $\boldsymbol{\delta T}$ and $\boldsymbol{\delta q}$ have three components each, we have in total seven unknowns. The additional degree of freedom arises because the rotation around $\vec{C}$ is not yet fixed. Recall that in the Euler angle representation, we remove this degree of freedom by setting $\phi = 0$, c.f. Eq. (3.7). Expanding Eq. (3.39) to linear order in the perturbations and subtracting the equation for black hole B from that for black hole A, it is straightforward to show that

$$\delta a = \left(\frac{\vec{X} \cdot \vec{C}}{\|\vec{C}\|^2} - 1\right) a, \tag{3.40}$$

$$\vec{\delta q} = \frac{\vec{C} \times \vec{X}}{\|\vec{C}\|^2} + \alpha \vec{C}, \tag{3.41}$$

and

$$(0, \vec{\delta T}) = a\boldsymbol{q}\left(\boldsymbol{x}_A - \boldsymbol{c}_A - \boldsymbol{\delta q} \wedge \boldsymbol{c}_A - \frac{\delta a}{a}\boldsymbol{c}_A\right)\boldsymbol{q}^*. \tag{3.42}$$

In Eq. (3.42, $\boldsymbol{\delta q} \wedge \boldsymbol{c}_A \equiv (0, \vec{\delta q} \times \vec{c}_A)$ and $\boldsymbol{\delta q},\ \delta a$ are to be substituted from Eq. (3.40, 3.41). The parameter α in Eq. (3.41) is undetermined, reflecting the extra degree of freedom already mentioned after Eq. (3.39). It parameterizes the component of $\vec{\delta} q$ parallel to $\vec{C}$; i.e., a rotation about the axis $\vec{C}$ connecting the two excision spheres. We shall choose it to minimize the overall rotation $\|\vec{\delta q}\|$:

$$\alpha = 0. \tag{3.43}$$

With this choice Eq. (3.41) simplifies to Eq. (3.35). The choice $\alpha = 0$ is equivalent to the minimal rotation frame of Boyle et al. [35]; it minimizes artificial activity of the control system that is not connected to the physics of the binary black hole.

3.4 Numerical Results

To test our new approach to the rotation control system we begin with the simplest possible system that still exhibits the desired behaviour, namely a *Newtonian* circular binary. We consider an equal mass, non-spinning, circular binary at separation of 20 M. The orbital plane is inclined with respect to the xy-plane by angles $\beta = 0, 10, 70$ degrees. The performance of the control system is quantified by the magnitude of the control parameters $\|Q\| \equiv \sqrt{\sum_i Q_i^2}$ where the summation extends over all the components of the control error for rotation, defined by Eqs. (3.10b, 3.10c) for Euler angles and Eq. (3.41) for quaternions. Independent of the inclination β, we always initialize the control system as if the binary is in the xy-plane. This is of course only correct for $\beta = 0$; for $\beta \neq 0$, the control system will also have to demonstrate that it can compensate for an utterly erroneous initialization. All our numerical results are obtained with a PD controller [92]. Because the Quaternion control system removes temporal structure from the mapping parameters, the improvements we demonstrate here with the PD controller will carry over to any other controller, e.g. a PID controller [92].

Figure 3.2 shows $\|Q\|$ for the three cases. For $\beta = 0°$ both control systems perform very well with an extremely small value of $Q \sim 10^{-11}$. For $\beta \neq 0$, there are initial transients due to the intentionally wrong initialization of λ^μ. These transients decay

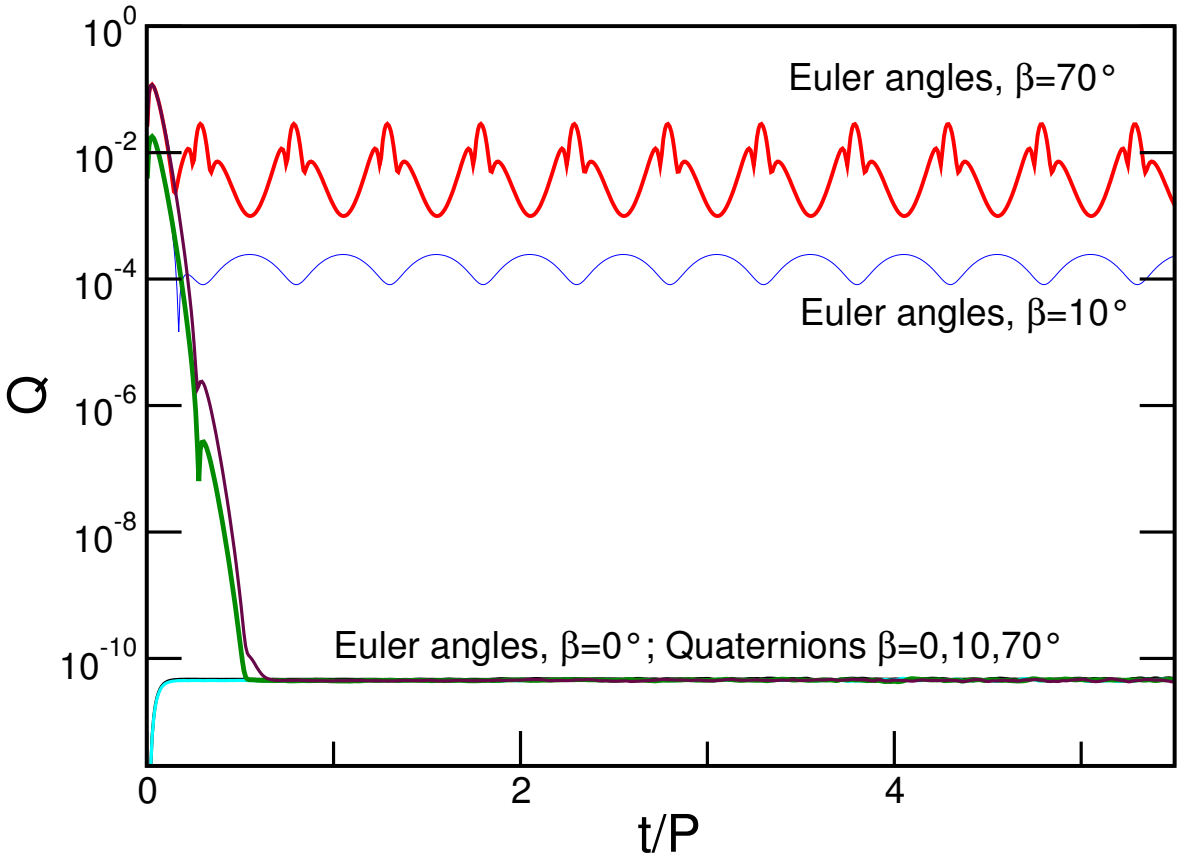

Figure 3.2: Newtonian simulations with inclination of the orbital plane of angle $\beta = 0, 10, 70$ degrees from the xy plane, performed with both control systems. Time is measured in units of orbital period.

exponentially on the damping timescale of the control system; here, $\tau = P/56$ where P is the orbital period. Once the transients have disappeared for $\beta = 10°$, the quaternion results are unchanged while the Euler-angle control error has increased by 6 orders of magnitude. This comparatively large value even for the seemingly small inclination $\beta = 10°$ is not related to the singularity in the Euler angle parameterization at $\beta = 90°$. Rather, it arises, because the control system needs to track the angle $\theta(t)$, which oscillates between $-\beta$ and β in each orbit. Analyzing the control-feedback equation for this motion (see Appendix B), one finds an oscillatory $Q(t)$ which is $\pi/2$ out of phase with $\theta(t)$ and which oscillates with amplitude $\beta(\omega\tau)^3 \sim 2.5\times10^{-4}$. In contrast, the controlled mapping-parameters of the quaternion-representation, the instantaneous orbital frequency $\vec{\Omega}(t)$, is constant for any value of β. The absence of time-dependence in $\vec{\Omega}(t)$ allows the quaternion control-system to achieve $Q \sim 10^{-10}$. This is demonstrated with the $\beta = 70°$ data in Fig. 3.2. In this case, the Euler-angle parameterization shows sharp oscillatory features in $\|Q\|$ when $\theta(t)$ is extremal, caused by the approach to the pole singularity of the Euler angles.

Figure 3.2 foreshadows already the main conclusion of this work: The Euler-angle approach depends on the plane of the orbit, and has increasing difficulty in controlling the coordinate mappings as the orbital plane becomes orthogonal to the xy-plane. While the Euler-angle control system becomes singular only at exactly $\beta = 90°$, the effects of this singularity are already clearly visible for $\beta = 70°$. In contrast, the quaternion control system is rotationally invariant, and hence, it controls the coordinate mapping equally well for any inclination β.

Next, we turn to a more interesting test that also involves the control system for the expansion factor $a(t)$. We consider a Post-Newtonian equal mass, non-spinning black hole binary. The relevant PN equations of motion can be found in [98]. Figure 3.3 displays a set of three runs done with both control systems, again choosing to tilt the orbit relative to the xy-plane by angles $\beta = 0, 10, 70$ degrees.

After the initial transients due to intentionally wrong initialization of the control system, both of the control systems handle the $\beta = 0$ case equally well with $\|Q\| \sim 10^{-5}$ showing regular oscillations due to a small eccentricity of the orbit. When $\beta = 10°$, the Euler-angle system is dominated by tracking the $\theta(t)$ angle, as for the Newtonian case in Fig. 3.2, with $\|Q\| \sim 10^{-3}$. The situation grows worse still for Euler angles when $\beta = 70°$, where the control error increases by another two orders of magnitude and sharp features appear.

Meanwhile, the curves corresponding to the quaternion control system show exactly (to within numerical accuracy) the same value of $\|Q\|$ for all inclinations. This is exactly

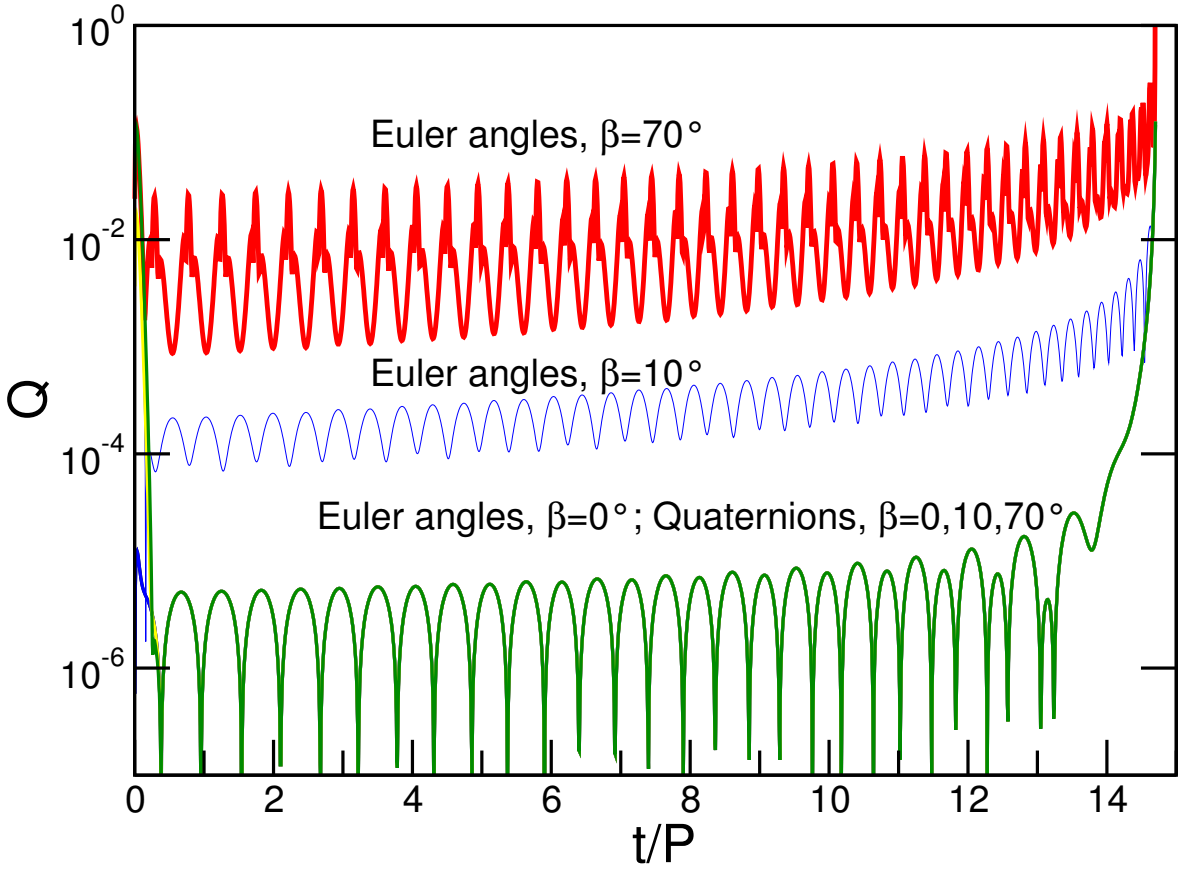

Figure 3.3: Post-Newtonian simulations with inclination of the orbital plane angle $\beta = 0, 10, 70$ degrees from the $x-y$ plane, performed with both control systems. Time is measured in units of initial orbital period. The binary is equal mass and non-spinning, with the initial coordinate separation of 20.

Name	q	$\vec{\chi}_1$	$\vec{\chi}_2$	D_0/M	$\dot{a}_0$	$M\Omega_0$
d11.68q2.5	2.5	(0.000, 0.575, -0.556)	(0.000, 0.360,-0.347)	11.68	-0.000290589649	0.02264246
d12q2.5	2.5	(0.000, 0.410, -0.287)	(0, 0, 0)	12	-0.000108923113	0.02180603
d14.5q1.5	1.5	(0.000,0.285, 0.093)	(0, 0, 0)	14.5	-0.000016947638	0.01664958

Table 3.1: The initial conditions used for the numerical relativity runs. Given are the mass ratio $q = m_1/m_2$, the dimensionless spin-vectors $\vec{\chi}_1$ and $\vec{\chi}_2$, the initial separation D_0, initial radial velocity $\dot{a}_0$, initial orbital frequency Ω_0. The initial orbital angular momentum is in the $\hat{z}$ direction and the line connecting the two black holes is parallel to the x-axis.

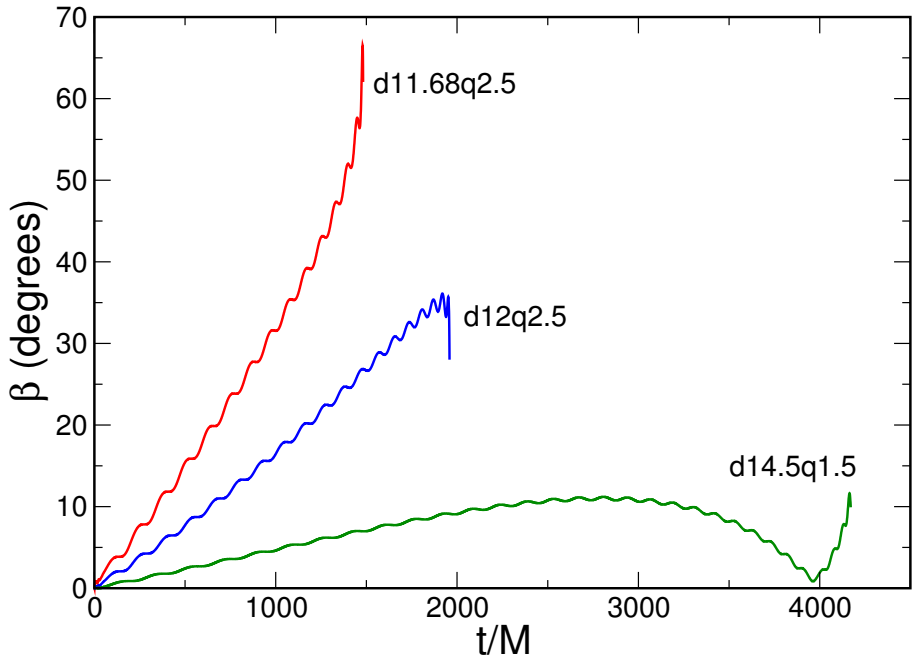

Figure 3.4: The inclination angle, β for the three systems under study. The curves stop just after a common horizon is detected.

what we expect from a rotationally invariant control system - the orientation of the orbital plane is irrelevant.

Finally, we test the quaternion-based control system using its main application: simulations of precessing binary black hole systems in full numerical relativity. Quite generally, this precession may cause the orbital plane to rotate by 90 or more degrees with respect to the initial conditions. The behaviour of the system depends on mass ratio and the two spin vectors. We choose a set of three simulations to be evolved using full numerical relativity that exhibits mild to significant precession. Table 3.1 summarizes the initial conditions. The initial data was constructed from the superposition of two Kerr-Schild metrics for the conformal metric as in [118] (so called SKS initial data). The eccentricity has been removed by an iterative process [43], so that the final eccentricities for all three

cases are a few $\times 10^{-4}$.

Figure 3.4 shows the inclination angle $\beta \equiv \arccos(\Omega_z/|\vec{\Omega}|)$ which measures the angle between the normal to the instantaneous orbital plane and the initial direction of the normal, which is by convention in the z-direction. The high-frequency oscillatory features are due to the nutation of the orbital angular momentum, while the secular evolution is due to precession. Notice that the d14.5q1.5 run completes a full precession cycle at $t = 4000M$. The curves end when the black holes merge. The maximum inclination angles are similar to those used for the Post-Newtonian evolutions above. Figure 3.5 shows the trajectories of the black holes in inertial coordinates.

Figure 3.6 presents $\|Q\|$ for the three runs done with the quaternion control system. In the main panel of Figure 3.6 it is difficult to compare the $\|Q\|$ of different runs because of the difference in orbital frequency. The inset shows the same $\|Q\|$ residuals for the three simulations but timeshifted such that the orbital frequency of $M\Omega = 0.025$ occurs at $t = 0$. As one can see the control error norms lie very close to each other, and exhibit qualitatively similar oscillations with virtually no sharp features.The remaining differences in behaviour are associated mostly with the different eccentricities as well as masses and spins. The growth of the control parameters with time is caused by the more rapid inspiral towards merger. Our numerical experiments demonstrate that the quaternion approach is indeed suitable for simulating arbitrarily precessing configurations.

To close this section, we compare two simulations of the same initial data performed with the new Quaternion control system, and the older Euler-angle parameterization. We choose the simulation d14.5q1.5, which was already discussed, and also evolve it with the Euler angle-parameterization.

Figure 3.7 shows the translation parameters $T^i(t)$ for these two simulations. During the inspiral, $t \lesssim 4100M$, the translation parameters change linearly in time with modulations on the orbital time-scale. The linear change arises because of a non-zero initial ADM linear momentum $P^i_{\rm ADM}$, and the drift is indeed consistent with a velocity of $P^i_{\rm ADM}/M$. The modulations arise because the center of rotation of the rotation map R is not precisely at the center of mass of the binary. `SpEC` simulations generally impose $P^i_{\rm ADM} = 0$ to a much higher precision than the simulation shown here; in the present case, the linear drift is used as an additional test of the translation control systems (the linear drift was removed from the data plotted in Fig. 3.5). The trajectories in Fig. 3.7 exhibit a change in slope around time of merger, $t \sim 4100M$, indicating a mild BH kick imparted on the remnant black hole of approximately $700 km/s$, predominantly along the +z direction.

The lower panel of Fig. 3.7 shows the differences in translation parameters between

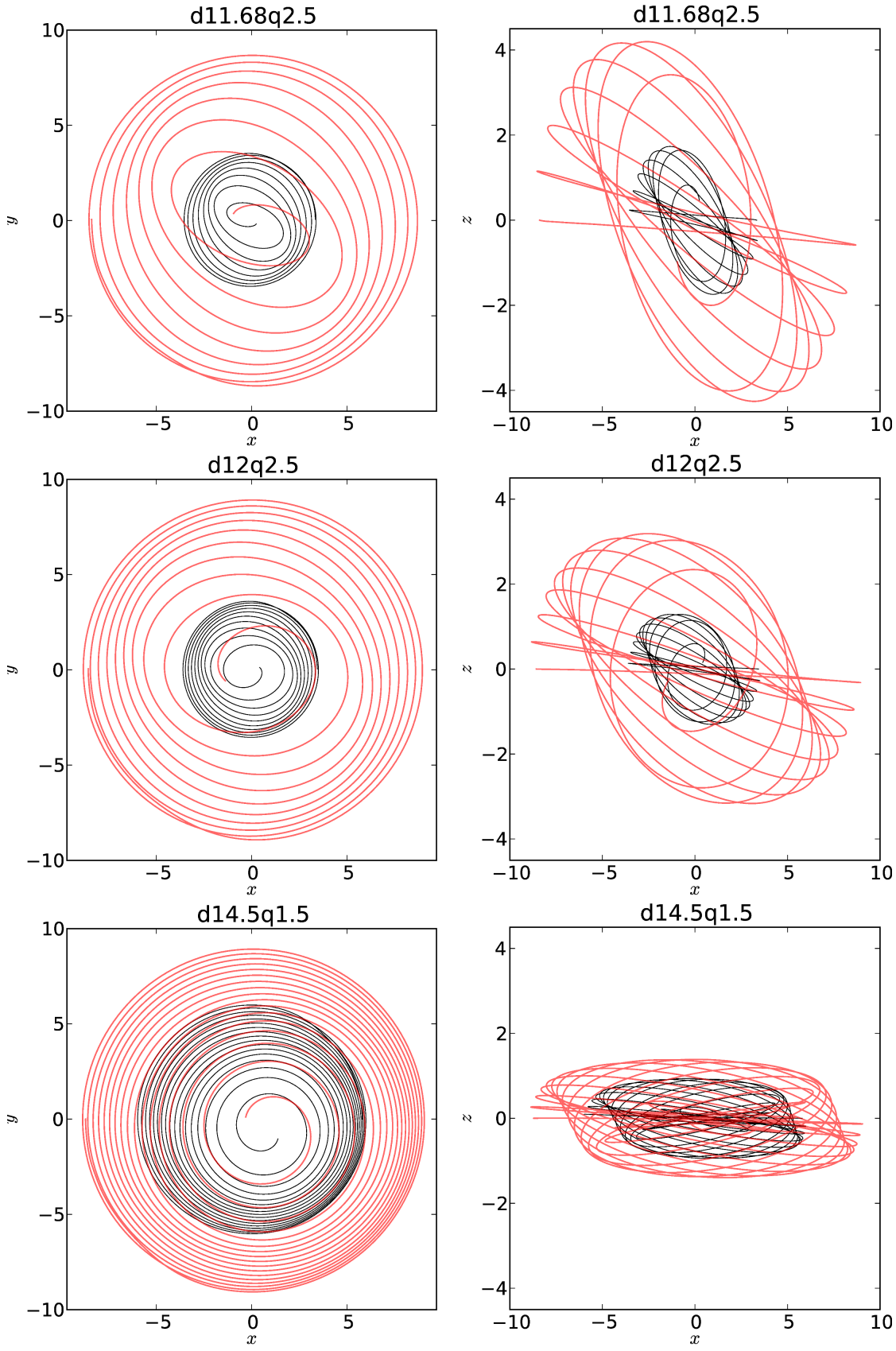

Figure 3.5: The trajectories of the centers of the apparent horizons of the black holes in inertial coordinates for the 3 simulations. Top to bottom: d11.68q2.5, d12q2.5, d14.5q1.5. The left panels show the projection onto the xy plane and the right, the xz plane.

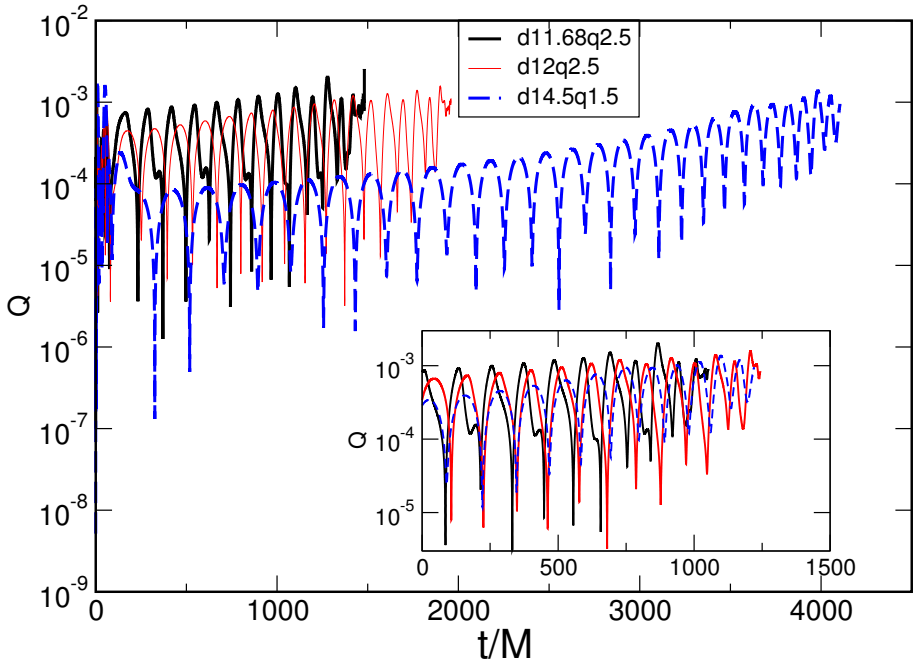

Figure 3.6: Three full NR simulations performed with the quaternion control systems with initial conditions listed in Table 3.1.

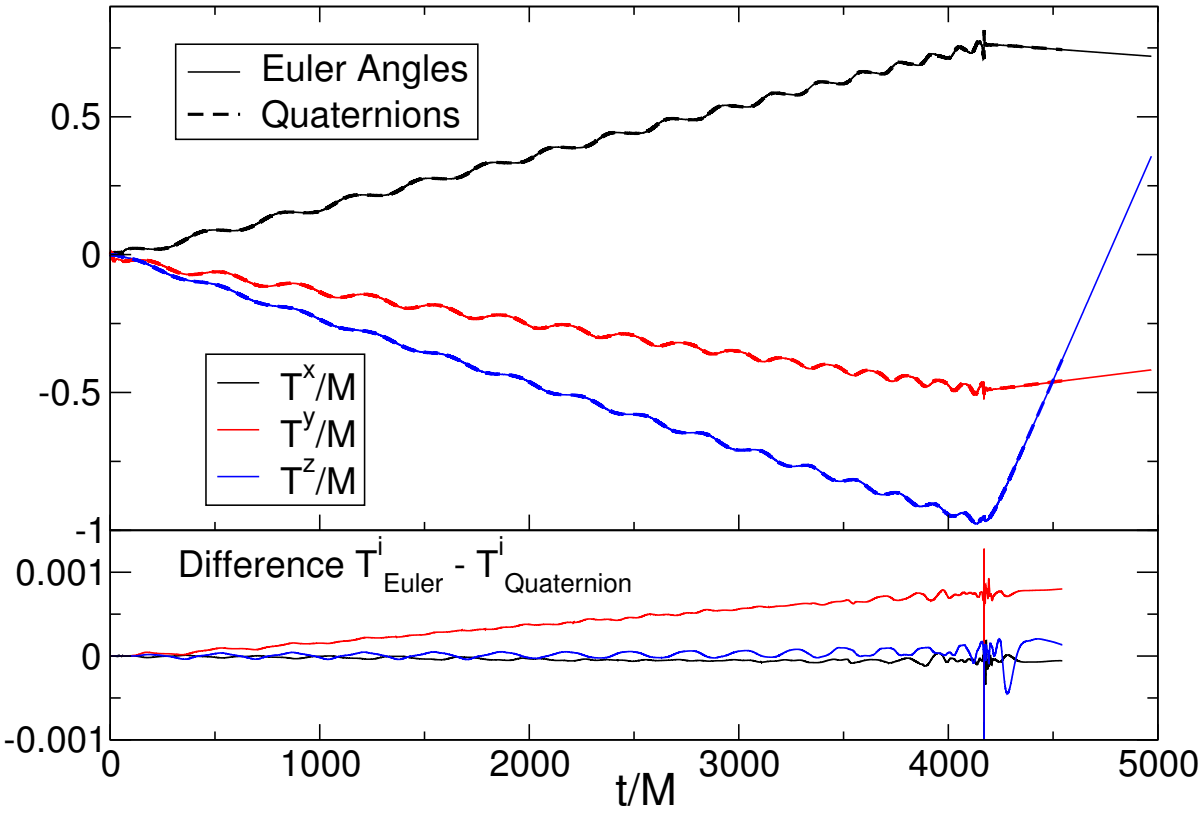

Figure 3.7: Translation control system output for case d14.5q1.5 done with the quaternion and the Euler angle control systems.

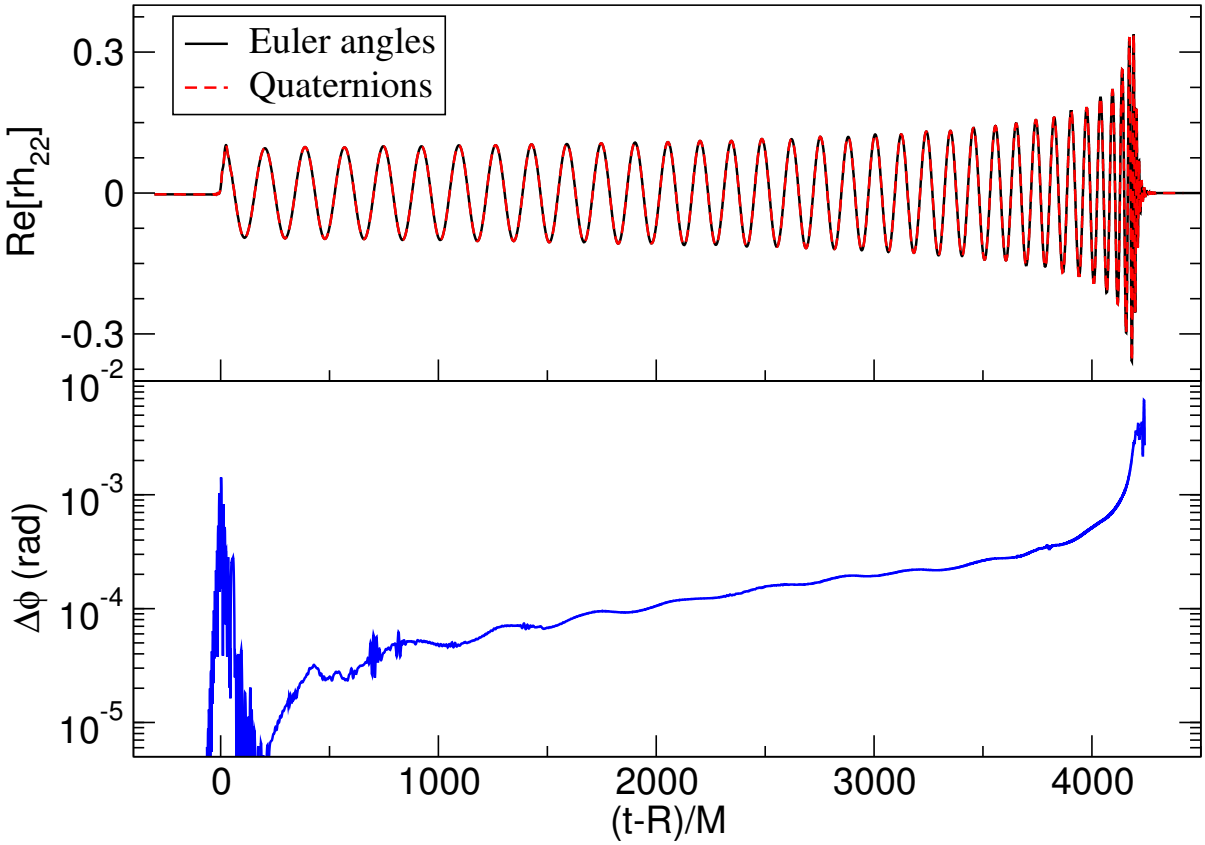

Figure 3.8: Top: the real part of rh_{22} extracted at $R = 304$ for the simulation d14.5q1.5 done with both control systems. Bottom: the phase differences. The data has been time-shifted by the extraction radius.

the Quaternion- and Euler-angle evolutions. The translation parameters agree to about 1 part in 1000. There is a slight difference, corresponding to a change in the center-of-mass velocity of about $2 \times 10^{-7} c$. This difference is smaller than the numerical truncation error of these runs, and so these small differences are consistent with our expectations.

Figure 3.8 compares the (2,2) mode of the gravitational waveforms between the Quaternion and the Euler-angle evolutions of the configuration d14.5q1.5. The waveforms itself in the upper panel cannot be distinguished. The lower panel indicates a phase-difference of less than 0.004 radian, about an order of magnitude smaller than numerical truncation error of high accuracy `SpEC` simulations (e.g. [38, 130]). The runs presented here are not at such high resolution, and so the phase differences shown in Fig. 3.8 are significantly smaller than the numerical truncation error.

3.5 Discussion

Simulating precessing binaries poses a challenge for dual-frame, spectral codes using excision-based numerical techniques. This challenge is resolved here by developing coordinate mappings which make the black holes be at rest in grid coordinates. This transformation is dynamically controlled by a feedback control system since the trajectories of the black holes are not known in advance. In the most general case this map involves a rotation, and while Euler angle parametrization works well for mildly precessing binaries, it exhibits coordinate singularities for polar orbits which leads to the breakdown of the simulation. To rectify the situation, we have created a control system that represents rotations using quaternions. Quaternions do not suffer from coordinate singularities and work for generically precessing systems. The quaternion-based control system is able to successfully perform fully general relativistic simulations of highly-precessing binaries, allowing the investigation strongly precessing binary black holes and broadening the range of parameter space that can be explored. The techniques developed here have already been utilized in the simulations presented in [74, 130]

The quaternion control system, as described and developed above, is related to the minimal rotation frame [35] (see also [41]). For the control-system developed here, as in the minimal rotation frame, a preferred *axis* exists (the line connecting the two black holes vs. the instantaneous preferred emission axis of the gravitational waves). In both cases, the rotation *about* this axis is not a priori determined. And in both cases, this rotation is chosen such that the instantaneous rotation frequency of the rotating frame is minimal. In the present context, this condition is imposed by Eq. (3.43).

As a useful byproduct of the quaternion control system, one obtains an accurate estimate of the orbital frequency and the orbital phase during the numerical run without the need for any post-processing. The $\mathbf{\Omega}$ in Eq. (3.34) is the instantaneous rotation frequency of the grid frame relative to the inertial frame, given in components of the grid frame. Converting to the inertial frame,

$$(0, \vec{\omega}) = \boldsymbol{q}\, \mathbf{\Omega}\, \boldsymbol{q}^*. \tag{3.44}$$

If the control system were perfect —i.e. if $Q \equiv 0$— then $\vec{\omega}$ given by Eq. (3.44) would be the instantaneous orbital frequency. Because $Q \neq 0$, Eq. (3.44) only gives an approximate orbital frequency, albeit a very good one: The upper panel of Fig. 3.9 shows the fractional difference between $|\vec{\omega}|$ from Eq. (3.44) and the exact numerical orbital frequency obtained by post-processing. The difference oscillates around zero with relative amplitude of 1×10^{-3}. It is also straightforward to integrate

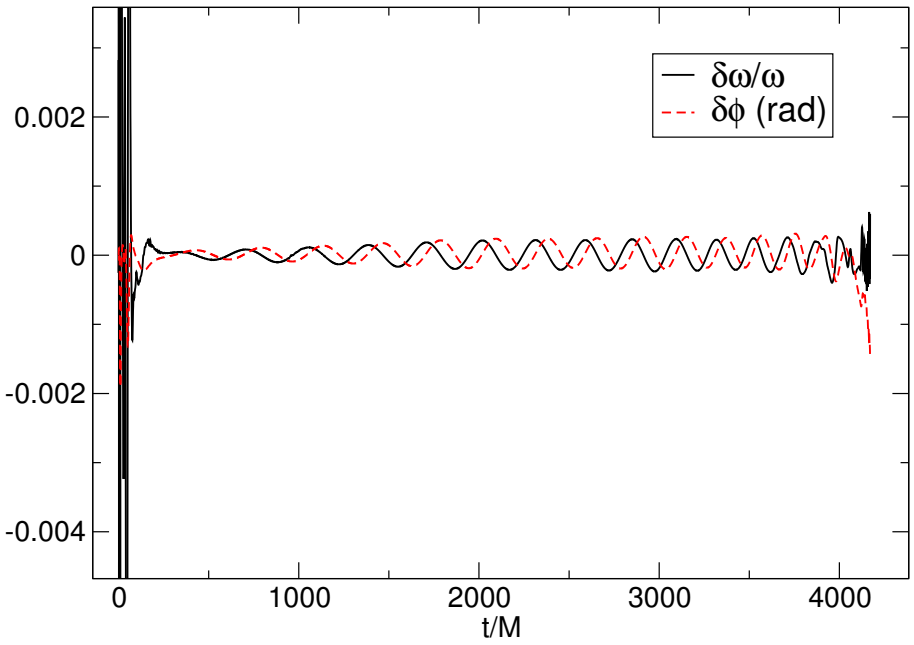

Figure 3.9: The fractional difference in orbital frequency estimated from quaternions and from trajectories (solid) and the orbital phase difference in radians (dashed). The data is from the run d14.5q1.5.

$$\dot{\phi} = |\vec{\Omega}| = |\vec{\omega}| \tag{3.45}$$

to obtain the orbital phase of the precessing binary. In practice, we add Eq. (3.45) to the set of ordinary differential equations Eq. (3.34) that are integrated to obtain the rotation quaternion $\boldsymbol{q}(t)$. The difference between the orbital phase from the control system Eq. (3.45) and the exact orbital phase from the BH trajectories is shown in the lower panel of Fig. 3.9. The difference is $\sim 10^{-4}$ radians until merger, during an inspiral lasting 105 radians. Incidentally, this again demonstrates that our control system works exactly as expected.

Acknowledgements

We thank Mark Scheel for assistance in implementing the quaternion control system in `SpEC`, and Mark Scheel and Béla Szilágyi for assistance with running the mergers of the black hole binaries discussed in Sec. 3.4. We gratefully acknowledge support from NSERC of Canada, from the Canada Research Chairs Program, and from the Canadian Institute for Advanced Research. We further gratefully acknowledge support from the Sherman Fairchild Foundation, NSF Grants No. PHY-0969111 and No. PHY-1005426

and NASA Grant No. NNX09AF96G at Cornell. Calculations were performed at the GPC supercomputer at the SciNet HPC Consortium [110]; SciNet is funded by: the Canada Foundation for Innovation (CFI) under the auspices of Compute Canada; the Government of Ontario; Ontario Research Fund (ORF) – Research Excellence; and the University of Toronto. Further computations were performed on the Caltech compute cluster Zwicky, which was funded by the Sherman Fairchild Foundation and the NSF MRI-R2 grant No. PHY-0960291, and on the Gravity compute cluster funded by CFI, ORF, and the University of Toronto.

3.6 Appendix

3.6.1 Rotation control parameters in matrix notation

The underlying idea for the rotational control system that we have described in section 3.3.3 is independent of the use of quaternions to represent rotations. For example, one could have used infinitesimal rotation matrices to achieve the same goal. Below is the demonstration of the same derivation as in section 3.3.3 but now in terms of a rotation matrix R. We start with the following version of Eq. (3.9):

$$aR\vec{x}_i + \vec{T} = (a + \delta a)R(I + \delta R)\vec{c}_i + \vec{T} + \delta\vec{T} \tag{3.46}$$

where as usual $i = A,\ B,\ \vec{x}_i, \vec{c}_i, \vec{T},\ \delta\vec{T} \in \mathbb{R}^3$, I is the identity matrix, $a,\ \delta a \in \mathbb{R}$ and $R,\ \delta R \in M_{3\times 3}$. Once more we seek to solve this system of six equations for the unknowns δa, $\delta\vec{T}$, and δR. Note that since δR is an infinitesimal rotation matrix, it is skew symmetric and thus has three independent components, for a total of seven unknowns. Expanding Eq. (3.46) to first order in perturbation and subtracting the equation for black hole B from that of black hole A one can show that:

$$\delta a = \left(\frac{\vec{X}\cdot\vec{C}}{\|\vec{C}\|^2} - 1\right) a, \tag{3.47}$$

$$\delta R_{ij} = \epsilon_{ijk}\delta\phi^j,\ \delta\vec{\phi} = \frac{\vec{C}\times\vec{X}}{\|\vec{C}\|^2} + \alpha\vec{C}, \tag{3.48}$$

$$\delta\vec{T} = aR\left(\vec{x}_A - \vec{c}_A - \delta\vec{\phi}\times\vec{c}_A - \frac{\delta a}{a}\vec{c}_A\right). \tag{3.49}$$

These results match exactly Eqs. (3.40)-(3.42). Thus we see that indeed infinitesimal rotation matrices could have been used to represent rotation. We selected quaternions for

our work primarily for numerical reasons, the main being the ease of correcting numerical drift from a rotation, which for quaternions amounts to a simple renormalization.

3.6.2 Euler angle control system for small inclinations

Assume a circular motion with orbital frequency ω around an axis tilted by an angle $\beta \ll 1$ relative to the z-axis. To first order in β, the Euler angles behave as

$$\hat{\theta}(t) = \beta e^{i\omega t}, \quad \hat{\psi}(t) = \omega t. \tag{3.50}$$

Because $\hat{\psi}(t)$ is linear in t, it will be tracked precisely by the control system after initial transients decay. $\hat{\theta}(t)$, however, oscillates and the control system must continuously update $\theta(t)$ to track $\hat{\theta}(t)$. This is accomplished via the differential equation (Eq. (15) of Ref. [163])

$$\frac{d^3\theta}{dt^3} = 3\lambda\frac{d^2Q}{dt^2} + 3\lambda^2\frac{dQ}{dt} + \lambda^3 Q, \tag{3.51}$$

where $Q(t) = \hat{\theta}(t) - \theta(t)$, and $\lambda = 1/\tau$ is the inverse of the damping time-scale of the control system. Substituting $\theta = \hat{\theta} - Q$ into the left-hand-side of Eq. (3.51), we find

$$\frac{d^3Q}{dt^3} + 3\lambda\frac{d^2Q}{dt^2} + 3\lambda^2\frac{dQ}{dt} + \lambda^3 Q = \frac{d^3\hat{\theta}}{dt^3} = -i\beta\omega^3 e^{i\omega t}. \tag{3.52}$$

Equation (3.52) is solved by

$$Q = \frac{-i\beta(\omega\tau)^3}{(1+i\omega\tau)^3}e^{i\omega t}. \tag{3.53}$$

In the limit $\tau \ll \omega$ this reduces to $Q = -i\beta(\omega\tau)^3 e^{i\omega t}$, the result quoted in Sec. 3.4.

Chapter 4

Comparing Post-Newtonian and Numerical-Relativity Dynamics

4.1 Chapter overview[1]

In this chapter we compare the results of numerical relativity simulations of precessing binary black hole systems done to Post-Newtonian theory. In BBH systems if the spins are not colinear with each other or with the orbital angular momentum, these systems exhibit complicated precession dynamics that are imprinted on the gravitational waveform. We develop a new procedure to match the precession dynamics computed by post-Newtonian (PN) theory to those of numerical binary black-hole simulations in full general relativity. For numerical relativity (NR) simulations lasting approximately two precession cycles, we find that the PN and NR predictions for the directions of the orbital angular momentum and the spins agree to better than $\sim 1^\circ$ with NR during the inspiral, increasing to 5° near merger. Nutation of the orbital plane on the orbital time-scale agrees well between NR and PN, whereas nutation of the spin direction shows qualitatively different behavior in PN and NR. We also examine how the PN equations for precession and orbital-phase evolution converge with PN order, and we quantify the impact of various choices for handling partially known PN terms.

[1]The material herein is based on Serguei Ossokine, Michael Boyle, Lawrence E. Kidder, Harald P. Pfeiffer, Mark A. Scheel, and Béla Szilágyi. *Comparing post-Newtonian and numerical-relativity precession dynamics.* arXiv:1502:01747, 2015.

4.2 Introduction

Binary black holes (BBH) are among the most important sources of gravitational waves for upcoming gravitational-wave detectors like Advanced LIGO [180] and Virgo [182]. Accurate predictions of the gravitational waveforms emitted by such systems are important for detection of gravitational waves and for parameter estimation of any detected binary [5]. When either black hole carries spin that is *not* aligned with the orbital angular momentum, there is an exchange of angular momentum between the components of the system, leading to complicated dynamical behavior. Figure 4.1 exhibits the directions of the various angular momenta in several simulations described in this chapter. This behavior is imprinted on the emitted waveforms [11, 143, 30], making them more feature-rich than waveforms from aligned-spin BBH systems or non-spinning BBH systems. In order to model the waveforms accurately, then, we need to understand the dynamics.

The orbital-phase evolution of an inspiraling binary, the precession of the orbital angular momentum and the black-hole spins, and the emitted gravitational waveforms can be modelled with post-Newtonian theory [25], a perturbative solution of Einstein's equations in powers of v/c, the ratio of the velocity of the black holes to the speed of light. Such post-Newtonian waveforms play an important role in the waveform modeling for ground-based interferometric gravitational-wave detectors (see, e.g., [134]).

For non-spinning and aligned-spin BBH, a large number of comparisons between PN and NR have been performed, among them [18, 66, 33, 85, 84, 123, 117, 168, 122, 95, 174]. For these non-precessing systems, gravitational wave phasing reduces to only one degree of freedom, generally taken to be the argument of the complex-valued $(2, 2)$ mode of the emitted gravitational radiation. Because phasing is of high importance for matching filtering, PN-NR comparisons for non-precessing binaries have focused on the accumulated phase differences in the dominant (2,2) mode of the gravitational waveform. It was found that the PN error due to truncation of the PN-series at some finite order (typically 3.5PN) can be quite large, especially at mass-ratios $\gtrsim 5$ and for spinning black holes. The resulting phase error was identified as one of the dominant limitations of waveform modeling for non-precessing BBH [60, 31, 135, 123, 122, 133]. By coincidence, the uncontrolled higher-order terms in PN approximants can sometimes be close to the correct, unknown values. Comparisons that rely on only one PN approximant are therefore prone to underestimate the error of PN. The best known case for this behavior are equal mass, non-spinning BBH, where the TaylorT4 approximant appears significantly more accurate than other Taylor approximants [18, 33].

Precessing waveform models (e.g., [86, 177, 141, 120, 30]) depend on the orbital phase

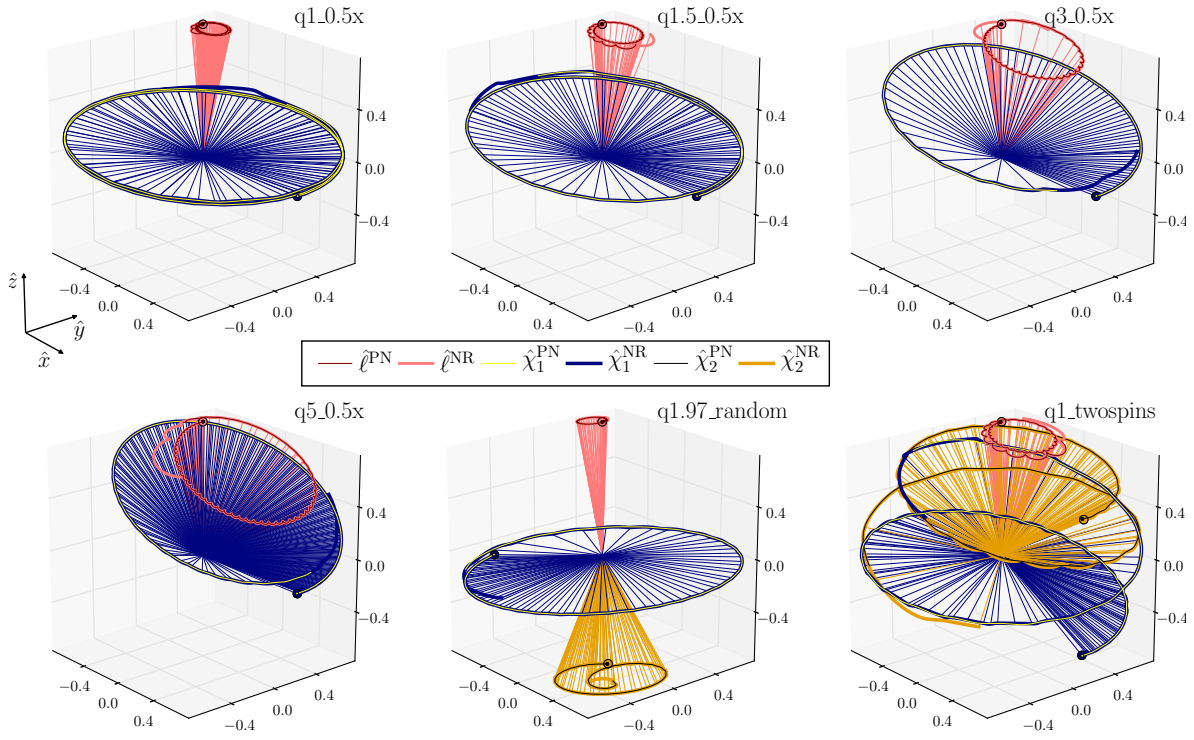

Figure 4.1: Precession cones of the six primary precessing simulations considered here, as computed by NR and PN. Shown are the paths traced on the unit sphere by the normal to the orbital plane $\hat{\ell}$ and the spin-directions $\hat{\chi}_{1,2}$. The thick lines represent the NR data, with the filled circles indicating the start of the NR simulations. The lines connecting the NR data to the origin are drawn to help visualize the precession-cones. The PN data, plotted with thin lines, lie on the scale of this figure almost precisely on top of the NR data. (The PN data was constructed using the Taylor T4 approximant matched at frequency $m\Omega_m = 0.021067$, with a matching interval width $\delta\Omega = 0.1\Omega_m$.)

evolution and the precession dynamics. Therefore, it is important to quantify the accuracy of the post-Newtonian approximation for modeling the precession dynamics itself, and the orbital-phase evolution of precessing binaries. The first such comparison was performed by Campanelli et al [46] finding fairly good agreement between PN and NR, with phase differences of about a cycle close to merger. They also found that 3.5 PN approximant performed significantly better than 2.5 PN. Lousto and Zlochower [111] studied the precession dynamics of a long numerical relativity simulation undergoing a reversal of the black hole spin direction, and found excellent agreement between NR and PN until close to merger.
In 2013, the SXS collaboration published numerical-relativity solutions to the full Einstein equations for precessing BBH systems [130]. These simulations cover $\gtrsim 30$ orbits and up to two precession cycles. Therefore, they offer a novel opportunity to systematically quantify the accuracy of the post-Newtonian precession equations, the topic of this chapter. The first such comparisons based on the SXS catalog were made in [141, 130]. Ref. [141] found that Taylor T4 model disagreed with the the NR data much more than the spinning EOB model. The PN precession equations used in [141], however, were only leading order, and it remained unclear whether the disagreement of Taylor T4 arises because of the low order of precession equations, or more general deficiencies of PN. The preliminary comparison of 2 precessing cases in [130] demonstrated good agreement of spin and angular momentum precession and motivated the current work. That study is expanded and refined here to include higher-order PN terms in the precession equations and the evolution of the orbital frequency.

While this chapter focuses on comparison of the orbital dynamics (angular momenta directions and orbital phase), in order to disentangle different aspects of the precessing BBH inspirals, some authors have performed comparisons of the emitted waveforms [46, 177, 86].Tarrachini et al [177] computed the unfaithfullness of the SEOBNRv3 model for a $q = 5$, $\chi_1 = 0.5$, $\chi_2 = 0$ (see case q5_0.5x in Table 4.1) and found to be less than 3% which would translate to negligible losses in detection rate. Hannam et al [86] computed fitting factors between PN-NR hybrid models and a phenomenological precessing `PhenomP` model and found fitting factors ≥ 0.965 for most sky orientations for cases with $q \leq 3$, in contrast to lower fitting factors obtained when using the non-precessing `PhenomC` [159] model.

In this chapter, we develop a new technique to match the initial conditions of post-Newtonian dynamics to a numerical relativity simulation. We then use this technique to study the level of agreement between the post-Newtonian precession equations and the numerical simulations. The agreement is remarkably good, the directions of orbital

angular momentum and spin axes in post-Newtonian theory reproduces the numerical simulations usually to better than 1 degree. We also investigate nutation effects on the orbital time-scale that are imprinted both in the orbital angular momentum and the spin-directions. For the orbital angular momentum, NR and PN yield very similar nutation features, whereas for the spin direction, nutation is qualitatively different in PN and the investigated NR simulations. Considering the orbital-phase evolution, we find that the disagreement between post-Newtonian orbital phase and numerical relativity simulation is comparable to the aligned-spin case. This implies that the orbital phase evolution will remain an important limitation for post-Newtonian waveforms even in the precessing case. Finally, we study the convergence with post-Newtonian order of the precession equations, and establish very regular and fast convergence, in contrast to post-Newtonian orbital phasing.

This chapter is organized as follows: Section 4.3 describes the post-Newtonian expressions utilized, the numerical simulations, how we compare PN and NR systems with each other, and how we determine suitable "best-fitting" PN parameters for a comparison with a given NR simulation. Section 4.4 presents our results, starting with a comparison of the precession dynamics in Sec. 4.4.1, and continuing with an investigation in the accuracy of the orbital phasing in Sec. 4.4.2. The following two sections study the convergence of the PN precession equations and the impact of ambiguous choices when dealing with incompletely known spin-terms in the PN orbital phasing. Section 4.4.5, finally, is devoted to some technical numerical aspects, including an investigation into the importance of the gauge conditions used for the NR runs. We close with a discussion in Sec. 4.5. The appendices collect the precise post-Newtonian expressions we use and additional useful formulae about quaternions.

4.3 Methodology

4.3.1 Post-Newtonian Theory

Post-Newtonian (PN) theory is an approximation to General Relativity in the weak-field, slow-motion regime, characterized by the small parameter $\epsilon \sim (v/c)^2 \sim \frac{Gm}{rc^2}$, where m, v, and r denote the characteristic mass, velocity, and size of the source, c is the speed of light, and G is Newton's gravitational constant. For the rest of this chapter, the source is always a binary black-hole system with total mass m, relative velocity v and separation r, and we use units where $G = c = 1$.

Restricting attention to quasi-spherical binaries in the adiabatic limit, the local dy-

namics of the source can be split into two parts: the evolution of the orbital frequency, and the precession of the orbital plane and the spins. The leading-order precessional effects [19] and spin contributions to the evolution of the orbital frequency [100, 99] enter post-Newtonian dynamics at the 1.5 PN order (i.e., $\epsilon^{3/2}$) for spin-orbit effects, and 2 PN order for spin-spin effects. We also include non-spin terms to 3.5 PN order [25], the spin-orbit terms to 4 PN order [125], spin-spin terms to 2 PN order [99][2]. For the precession equations, we include the spin-orbit contributions to next-to-next-to-leading order, corresponding to 3.5 PN [27]. The spin-spin terms are included at 2 PN order[3].

Orbital dynamics

Following earlier work (e.g., Ref. [99]) we describe the precessing BH binary by the evolution of the orthonormal triad $(\hat{n}, \hat{\lambda}, \hat{\ell})$, as indicated in Fig. 4.2: $\hat{n}$ denotes the unit separation vector between the two compact objects, $\hat{\ell}$ is the normal to the orbital plane and $\hat{\lambda} = \hat{\ell} \times \hat{n}$ completes the triad. This triad is time-dependent, and is related to the constant inertial triad $(\hat{x}, \hat{y}, \hat{z})$ by a time-dependent rotation R_f, as indicated in Fig. 4.2. The rotation R_f will play an important role in Sec. 4.3.3. The orbital triad obeys the following equations:

$$\frac{d\hat{\ell}}{dt} = \varpi \hat{n} \times \hat{\ell}, \tag{4.1a}$$

$$\frac{d\hat{n}}{dt} = \Omega \hat{\lambda}, \tag{4.1b}$$

$$\frac{d\hat{\lambda}}{dt} = -\Omega \hat{n} + \varpi \hat{\ell}. \tag{4.1c}$$

Here, Ω is the instantaneous orbital frequency and ϖ is the precession frequency of the orbital plane.

The dimensionless spin vectors $\vec{\chi}_i = \vec{S}_i/m_i^2$ also obey precession equations:

$$\frac{d\vec{\chi}_1}{dt} = \vec{\Omega}_1 \times \vec{\chi}_1, \tag{4.2a}$$

$$\frac{d\vec{\chi}_2}{dt} = \vec{\Omega}_2 \times \vec{\chi}_2. \tag{4.2b}$$

[2]During the preparation of this manuscript, the 3 PN spin-spin contributions to the flux and binding energy were completed in [26]. These terms are not used in the analysis presented here.

[3]The investigation of the effects of spin-spin terms at higher PN orders (see e.g. [89, 104, 151, 105, 107] and references therein), and terms which are higher order in spin (e.g cubic spin terms) [124, 106] is left for future work.

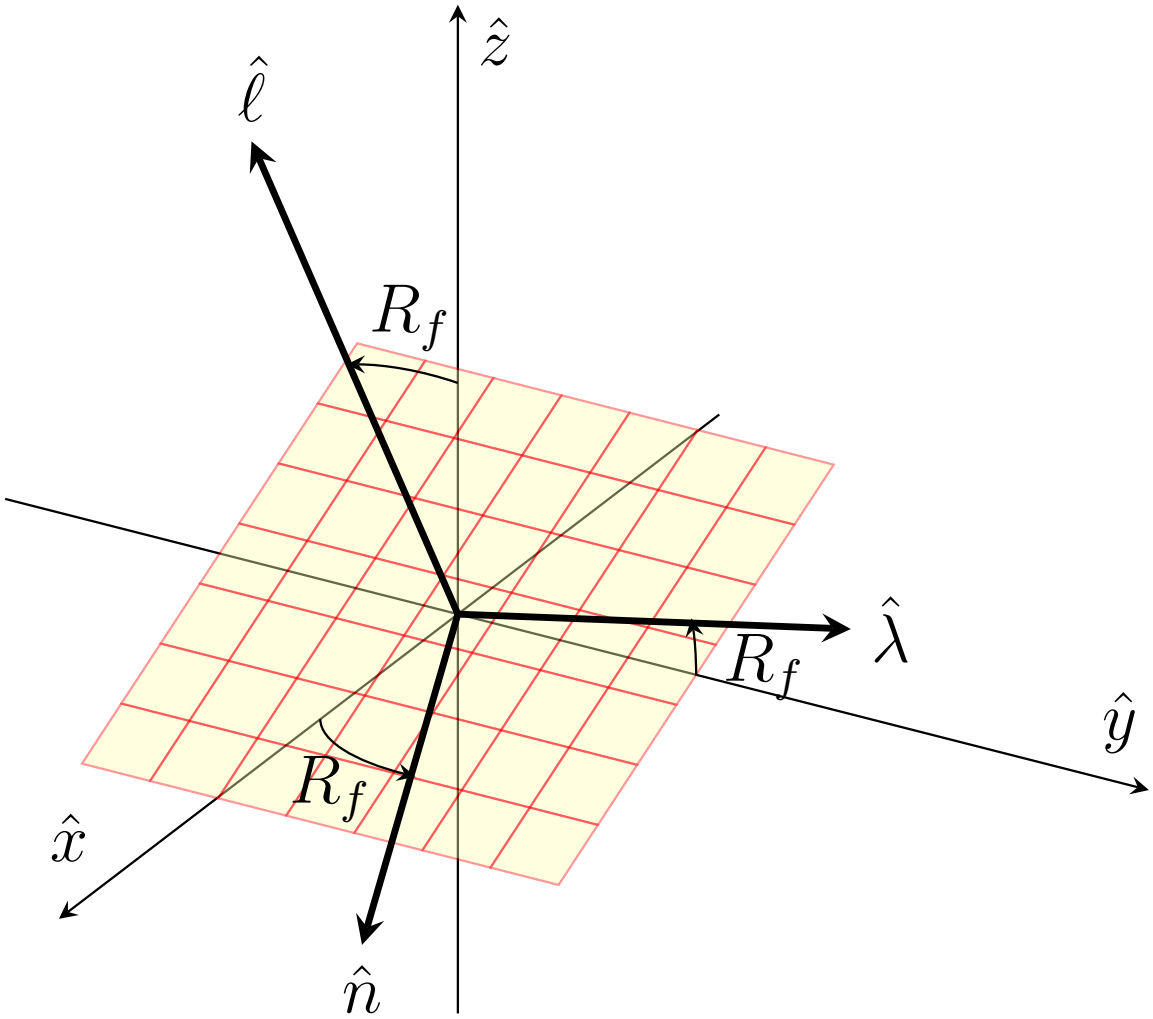

Figure 4.2: Vectors describing the orbital dynamics of the system. The yellow plane denotes the orbital plane. $R_{\rm f}(t)$ is the rotor that rotates the coordinate triad $(\hat{x}, \hat{y}, \hat{z})$ into the orbital triad $(\hat{n}, \hat{\lambda}, \hat{\ell})$.

The precession frequencies $\vec{\Omega}_{1,2}$, ϖ are series in the PN expansion parameter ϵ; their explicit form is given in Appendix 4.6.1.

The evolution of the orbital frequency is derived from energy balance:

$$\frac{dE}{dt} = -\mathcal{F}, \tag{4.3}$$

where E is the energy of the binary and $\mathcal{F}$ is the gravitational-wave flux. E and $\mathcal{F}$ are PN series depending on the orbital frequency Ω, the vector $\hat{\ell}$, and the BH spins $\vec{\chi}_1$, $\vec{\chi}_2$. Their explicit formulas are given in Appendix 4.6.1. In terms of $x \equiv (m\Omega)^{2/3} \sim \epsilon$, Eq. (4.3) becomes:

$$\frac{dx}{dt} = -\frac{\mathcal{F}}{dE/dx}, \tag{4.4}$$

where the right-hand side is a ratio of two PN series.

There are several well known ways of solving Eq. (4.4), which lead to different treatment of uncontrolled higher-order PN terms—referred to as the Taylor T1 through T5 approximants [65, 6]. The most straightforward approach is to evaluate the numerator and denominator of Eq. (4.4) and then solve the resulting ordinary differential equation numerically, which is the Taylor T1 approximant. Another approach is to re-expand the ratio $\mathcal{F}/(dE/dx)$ in a new power series in x, and then truncate at the appropriate order. This gives the Taylor T4 approximant. Finally, one can expand the *inverse of the right-hand-side of Eq.* (4.4) in a new power series in x, truncate it at the appropriate order, and then substitute the inverse of the truncated series into the right-hand side in Eq. (4.4). This last approach, known as the Taylor T5 approximant [6], has been introduced fairly recently.

Handling of spin terms

When constructing Taylor approximants that include the re-expansion of the energy balance equation, the handling of spin terms becomes important. In particular, terms of quadratic and higher order in spins, such as $(\vec{S}_i)^2$, appear in the evolution of the orbital frequency at 3 PN and higher orders. These terms arise from lower-order effects and represent incomplete information, since the corresponding terms are unknown in the original power series for the binding energy E and the flux $\mathcal{F}$,

Table 4.1: Numerical relativity simulations utilized here. SXS ID refers to the simulation number in Ref. [130], $q = m_1/m_2$ is the mass ratio, $\vec{\chi}_{1,2}$ are the dimensionless spins, given in coordinates where $\hat{n}(t=0) = \hat{x}$, $\hat{\ell}(t=0) = \hat{z}$. D_0, Ω_0 and e are the initial coordinate separation, the initial orbital frequency, and the orbital eccentricity, respectively. The first block lists the precessing runs utilized, where $\vec{\chi}_{1,r} = (-0.18, -0.0479, -0.0378)$ and $\vec{\chi}_{2,r} = (-0.0675, 0.0779, -0.357)$. The second block indicates 31 further precessing simulations used in Fig. 4.13, and the last block lists the aligned spin systems for orbital phase comparisons.

Name	SXS ID	q	$\vec{\chi}_1$	$\vec{\chi}_2$	D_0/M	$m\Omega_0$	e
q1_0.5x	0003	1.0	(0.5,0.0,0)	(0,0,0)	19	0.01128	0.003
q1.5_0.5x	0017	1.5	(0.5,0,0)	(0,0,0)	16	0.01443	$< 2 \times 10^{-4}$
q3_0.5x	0034	3.0	(0.5,0,0)	(0,0,0)	14	0.01743	$< 2 \times 10^{-4}$
q5_0.5x		5.0	(0.5,0,0)	(0,0,0)	15	0.01579	0.002
q1_two_spins	0163	1.0	(0.52,0,-0.3)	(0.52,0,0.3)	15.3	0.01510	0.003
q1.97_random	0146	1.97	$\vec{\chi}_{1,r}$	$\vec{\chi}_{2,r}$	15	0.01585	$< 10^{-4}$
31 random runs	115–145	$[1, 2]$	$\chi_1 \leq 0.5$	$\chi_2 \leq 0.5$	15	≈ 0.0159	$[10^{-4}, 10^{-3}]$
q1_0.5z	0005	1.0	(0,0,0.5)	(0,0,0)	19	0.01217	0.0003
q1_-0.5z	0004	1.0	(0,0,0.5)	(0,0,0)	19	0.01131	0.0004
q1.5_0.5z	0013	1.5	(0,0,0.5)	(0,0,0)	16	0.01438	0.00014
q1.5_-0.5z	0012	1.5	(0,0,-0.5)	(0,0,0)	16	0.01449	0.00007
q3_0.5z	0031	3.0	(0,0,0.5)	(0,0,0)	14	0.01734	$< 10^{-4}$
q3_-0.5z	0038	3.0	(0,0,-0.5)	(0,0,0)	14	0.01756	$< 10^{-4}$
q5_0.5z	0061	5.0	(0,0,0.5)	(0,0,0)	15	0.01570	0.004
q5_-0.5z	0060	5.0	(0,0,-0.5)	(0,0,0)	15	0.01591	0.003
q8_0.5z	0065	8.0	(0,0,0.5)	(0,0,0)	13	0.01922	0.004
q8_-0.5z	0064	8.0	(0,0,-0.5)	(0,0,0)	13	0.01954	0.0005

$$E(x) = -\frac{1}{2}\, m\nu x \left(1 + \sum_{k=2} a_k x^{k/2}\right), \tag{4.5}$$

$$\mathcal{F}(x) = \frac{32}{5}\nu^2 x^5 \left(1 + \sum_{k=2} b_k x^{k/2}\right), \tag{4.6}$$

where $m = m_1 + m_2$ and $\nu = m_1 m_2/m^2$, and $m_{1,2}$ are the individual masses.

In these expansions, the spin-squared terms come in at 2 PN order and thus appear in a_4 and b_4, cf. Eqs. (4.38) and (4.44). Then, in the re-expansion series of Taylor T4,

$$S \equiv -\frac{\mathcal{F}}{dE/dx} = \frac{64\nu}{5m} x^5 (1 + \sum_{k=2} s_k x^{k/2}), \tag{4.7}$$

the coefficients s_k can be recursively determined, e.g.

$$s_4 = b_4 - 3a_4 - 2s_2 a_2, \tag{4.8}$$

$$s_6 = b_6 - (4a_6 + 3s_2 a_4 + \frac{5}{2} s_3 a_3 + 2s_4 a_2). \tag{4.9}$$

Thus, the spin-squared terms in a_4 and b_4 will induce spin-squared terms at 3PN order in s_6. The analogous conclusion holds for Taylor T5. These spin-squared terms are incomplete as the corresponding terms in the binding energy and flux (i.e. in a_6 and b_6) are not known.

This re-expansion has been handled in several ways in the literature. For example, Nitz et al. [133] include only terms which are linear in spin beyond 2 PN order. On the other hand, Santamaría et al. [159] keep *all* terms in spin arising from known terms in E and $\mathcal{F}$. In the present work, we also keep all terms up to 3.5 PN order, which is the highest order to which non-spin terms are completely known. Similarly, we include all terms when computing the precession frequency (see 4.6.1). We investigate the impact of different spin-truncation choices in Sec. 4.4.4, along with the impact of partially known 4 PN spin terms.

4.3.2 Numerical Relativity Simulations

To characterize the effectiveness of PN theory in reproducing NR results, we have selected a subset of 16 simulations from the SXS waveform catalog described in Ref. [**?**].[4] Our

[4]The waveform and orbital data are publicly available at `https://www.black-holes.org/waveforms/`.

primary results are based on six precessing simulations and a further ten non-precessing ones for cross-comparisons. To check for systematic effects, we use a further 31 precessing simulations with random mass-ratios and spins. The parameters of these runs are given in Table 4.1. They were chosen to represent various degrees of complexity in the dynamics: (i) precessing versus non-precessing simulations, the latter with spins parallel or anti-parallel to $\hat{\ell}$; (ii) one versus two spinning black holes; (iii) coverage of mass ratio from $q = 1$ to $q = 8$; (iv) long simulations that cover more than a precession cycle; and (v) a variety of orientations of $\hat{\chi}_1, \hat{\chi}_2, \hat{\ell}$. Figure 4.1 shows the precession cones of the normal to the orbital plane and the spins for for the six primary precessing cases in Table 4.1. The PN data were computed using the Taylor T4 3.5 PN approximant.

The simulations from the catalog listed in Table 4.1 were run with numerical methods similar to [38]. A generalized harmonic evolution system [77, 79, 154, 108] is employed, and the gauge is determined by gauge source functions H_a. During the inspiral phase of the simulations considered here, H_a is kept constant in the co-moving frame, cf. [121, 52, 33]. About 1.5 orbits before merger, the gauge is changed to damped harmonic gauge [109, 175, 51]. This gauge change happens outside the focus of the comparisons presented here.

The simulation q5_0.5x analyzed here is a re-run of the SXS simulation SXS:BBH:0058 from Ref. [**?**]. We performed this re-run for two reasons: First, SXS:BBH:0058 changes to damped harmonic gauge in the middle of the inspiral, rather than close to merger as all other cases considered in this work. Second, SXS:BBH:0058 uses an unsatisfactorily low numerical resolution during the calculation of the black hole spins. Both these choices leave noticeable imprints on the data from SXS:BBH:0058, and the re-run q5_0.5x allows us to quantify the impact of these deficiencies. We discuss these effects in detail in Secs. 4.4.5 and 4.4.5. The re-run q5_0.5x analyzed here is performed with improved numerical techniques. Most importantly, damped harmonic gauge is used essentially from the start of the simulation, $t \gtrsim 100M$. The simulation q5_0.5x also benefits from improved adaptive mesh refinement [**?**] and improved methods for controlling the shape and size of the excision boundaries; the latter methods are described in Sec.II.B. of Ref. [**?**].

We have performed convergence tests for some of the simulations; Sec. 4.4.5 will demonstrate with Fig. 4.19 that numerical truncation error is unimportant for the comparisons presented here.

4.3.3 Characterizing Precession

The symmetries of non-precessing systems greatly simplify the problem of understanding the motion of the binary. In a non-precessing system, the spin vectors are essentially constant, and two of the rotational degrees of freedom are eliminated in the binary's orbital elements. Assuming quasi-circular orbits, the entire system can be described by the orbital phase Φ, which can be defined as the angle between $\hat{n}$ and $\hat{x}$. In post-Newtonian theory the separation between the black holes can be derived from $d\Phi/dt$. Thus comparison between post-Newtonian and numerical orbits, for example, reduces entirely to the comparison between $\Phi_{\rm PN}$ and $\Phi_{\rm NR}$ [42, 33]. For precessing systems, on the other hand, the concept of an orbital phase is insufficient; Φ could be thought of as just one of the three Euler angles. We saw in Sec. 4.3.1 that the orbital dynamics of a precessing system can be fairly complex, involving the triad $(\hat{n}, \hat{\lambda}, \hat{\ell})$ (or equivalently the frame rotor $R_{\rm f}$) as well as the two spin vectors $\vec{\chi}_1$ and $\vec{\chi}_2$—each of which is, of course, time dependent. When comparing post-Newtonian and numerical results, we need to measure differences between each of these quantities in their respective systems.

To compare the positions and velocities of the black holes themselves, we can condense the information about the triads into the quaternion quantity [**?**]

$$R_\Delta \coloneqq R_{\rm f}^{\rm PN}\, \bar{R}_{\rm f}^{\rm NR} \ , \tag{4.10}$$

which represents the rotation needed to align the PN frame with the NR frame. This is a geometrically meaningful measure of the relative difference between two frames. We can reduce this to a single real number by taking the magnitude of the logarithm of this quantity, defining the angle[5]

$$\Phi_\Delta \coloneqq 2\,|\log R_\Delta| \ . \tag{4.11}$$

This measure has various useful qualities. It is invariant, in the sense that any basis frame used to define $R_{\rm f}^{\rm PN}$ and $R_{\rm f}^{\rm NR}$ will result in the same value of Φ_Δ. It conveniently distills the information about the difference between the frames into a single value, but is also non-degenerate in the sense that $\Phi_\Delta = 0$ if and only if the frames are identical. It also reduces precisely to $\Phi_{\rm PN} - \Phi_{\rm NR}$ for non-precessing systems; for precessing systems it also incorporates contributions from the relative orientations of the orbital planes.[6]

[5] More explanation of these expressions, along with relevant formulas for calculating their values, can be found in Appendix 4.6.2.

[6] It is interesting to note that any attempt to define the orbital phases of precessing systems separately, and then compare them as some $\Phi_B - \Phi_A$, is either ill defined or degenerate—as shown in Appendix 4.6.2. This does not mean that it is impossible to define such phases, but at best they will be degenerate; multiple angles would be needed to represent the full dynamics.

Despite these useful features of Φ_Δ, it may sometimes be interesting to use different measures, to extract individual components of the binary evolution. For example, Eq. (4.1a) describes the precession of the orbital plane. When comparing this precession for two approaches, a more informative quantity than Φ_Δ is simply the angle between the $\hat{\ell}$ vectors in the two systems:

$$\angle L = \cos^{-1}\left(\hat{\ell}^{\rm PN}\cdot\hat{\ell}^{\rm NR}\right). \tag{4.12}$$

Similarly, we will be interested in understanding the evolution of the spin vectors, as given in Eqs. (4.2). For this purpose, we define the angles between the spin vectors:

$$\angle\chi_1 = \cos^{-1}\left(\hat{\chi}_1^{\rm PN}\cdot\hat{\chi}_1^{\rm NR}\right), \tag{4.13a}$$
$$\angle\chi_2 = \cos^{-1}\left(\hat{\chi}_2^{\rm PN}\cdot\hat{\chi}_2^{\rm NR}\right). \tag{4.13b}$$

We will use all four of these angles below to compare the post-Newtonian and numerical orbital elements.

4.3.4 Matching Post-Newtonian to Numerical Relativity

When comparing PN theory to NR results, it is important to ensure that the initial conditions used in both cases represent the same physical situation. We choose a particular orbital frequency Ω_m and use the NR data to convert it to a time t_m. To initialize a PN evolution at t_m, we need to specify

$$q, \chi_1, \chi_2, \tag{4.14}$$
$$\hat{\ell}, \hat{n}, \hat{\chi}_1, \hat{\chi}_2, \tag{4.15}$$
$$\Omega. \tag{4.16}$$

The quantities (4.14) are conserved during the PN evolution. The quantities (4.15) determine the orientation of the the binary and its spins relative to the inertial triad $(\hat{x}, \hat{y}, \hat{z})$. The orbital frequency Ω in Eq. (4.16), finally, parametrizes the separation of the binary at t_m. The simplest approach is to initialize the PN evolution from the respective quantities in the initial data of the NR evolution. This would neglect initial transients in NR data as in, e.g., Fig. 1 of Ref. [52]. These transients affect the masses and spins of the black holes, so any further PN-NR comparisons would be comparing slightly different physical configurations. The NR transients decay away within the first orbit of the NR simulation, so one can consider initializing the PN evolution from NR

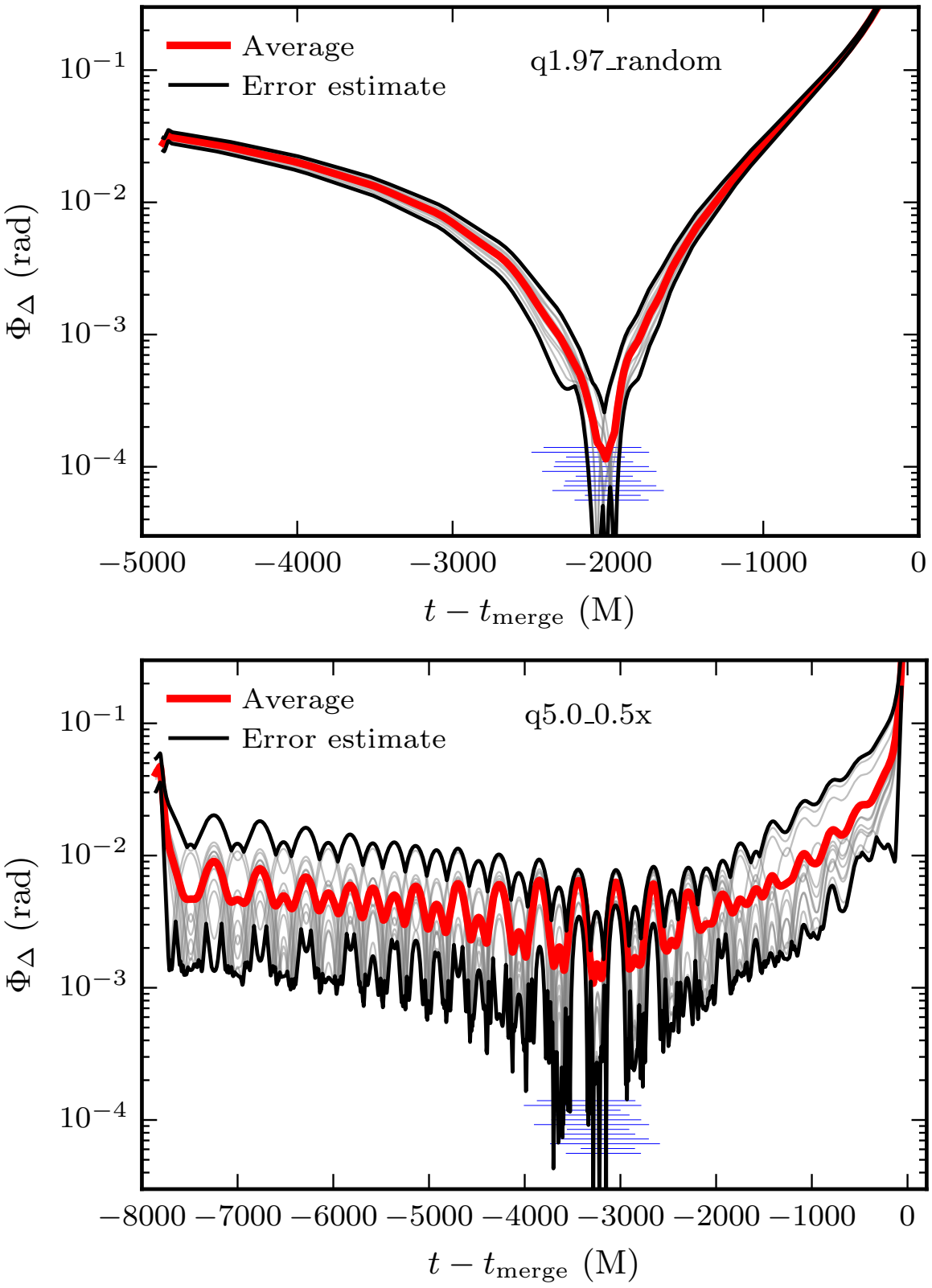

Figure 4.3: Examples of the averaging procedure and error estimates employed for all comparisons. Shown here are q1.97_random and q5.0_0.5x. PN evolutions were performed with the Taylor T1 approximant. The thin blue lines show all the PN-NR matching intervals.

at a time after the NR run has settled down. However, the generally non-zero (albeit very small) orbital eccentricity in the NR simulation can lead to systematic errors in the subsequent comparison as pointed out in Ref. [33].

Therefore, we use time-averaged quantities evaluated after the initial transients have vanished. In particular, given a numerical relativity simulation, we set the PN variables listed in Eq. (4.14) to their numerical relativity values after junk radiation has propagated away.

The remaining nine quantities Eqs. (4.15) and (4.16) must satisfy the constraint $\hat{\ell} \cdot \hat{n} \equiv 0$. We determine them with constrained minimization by first choosing an orbital frequency interval $[\Omega_m - \delta\Omega/2, \Omega_m + \delta\Omega/2]$ of width $\delta\Omega$. Computing the corresponding time interval $[t_i, t_f]$ in the NR simulation, we define the time average of any quantity Q by

$$\langle Q \rangle = \frac{1}{t_f - t_i} \int_{t_i}^{t_f} Q \, dt. \tag{4.17}$$

Using these averages, we construct the objective functional $\mathcal{S}$ as

$$\mathcal{S} = \langle (\angle L)^2 \rangle + \langle (\angle \chi_1)^2 \rangle + \langle (\angle \chi_2)^2 \rangle + \langle (\angle n)^2 \rangle + \langle (\Delta\Omega)^2 \rangle \tag{4.18}$$

where $\Delta\Omega = (\Omega_{\rm PN} - \Omega_{\rm NR})/\Omega_{\rm NR}$, and $\angle n$ is defined analogously to Eq. (4.12). When a spin on the black holes is below 10^{-5} the corresponding term is dropped from Eq. (4.18). The objective functional is then minimized using the SLSQP algorithm [101, 144] to allow for constrained minimization. In Eq. (4.18) we use equal weights for each term; other choices of the weights do not change the qualitative picture that we present.

The frequency interval $[\Omega_m \pm \delta\Omega/2]$ is chosen based on several considerations. First it is selected after junk radiation has propagated away. Secondly, it is made wide enough so that any residual eccentricity effects average out. Finally, we would like to match PN and NR as early as possible. But since we want to compare various cases to each other, the lowest possible matching frequency will be limited by the shortest NR run (case q8_-0.5z). Within these constraints, we choose several matching intervals, in order to estimate the impact of the choice of matching interval on our eventual results. Specifically, we use three matching frequencies

$$m\Omega_m \in \{0.021067, 0.021264, 0.021461\}, \tag{4.19}$$

and employ four different matching windows for each, namely

$$\delta\Omega/\Omega_m \in \{0.06, 0.08, 0.1, 0.12\}. \tag{4.20}$$

These frequencies correspond approximately to the range between 10-27 orbits to merger depending on the parameters of the binary, with the lower limit for the case q1.0_-0.5x and the upper for q8.0_0.5x.

Matching at multiple frequencies and frequency windows allows an estimate on the error in the matching and also ensures that the results are not sensitive to the matching interval being used. In this article, we generally report results that are averaged over the 12 PN-NR comparisons performed with the different matching intervals. We report error bars ranging from the smallest to the largest result among the 12 matching intervals. As examples, Fig. 4.3 shows Φ_Δ as a function of time to merger $t_{\rm merge}$ for the cases q1.97_random and q5_0.5x for all the matching frequencies and intervals, as well as the average result and an estimate of the error. Here $t_{\rm merge}$ is the time in the NR simulation when the common horizon is detected.

4.4 Results

4.4.1 Precession Comparisons

We apply the matching procedure of Sec. 4.3.4 to the precessing NR simulations in Table 4.1. PN–NR matching is always performed at the frequencies given by Eq. (4.19) which are the lowest feasible orbital frequencies across all cases in Table 4.1. Figure 4.1 shows the precession cones for the normal to the orbital plane $\hat{\ell}$ and the spins $\hat{\chi}_{1,2}$. As time progresses, $\hat{\ell}$ and $\hat{\chi}_{1,2}$ undergo precession and nutation, and the precession cone widens due to the emission of gravitational radiation. Qualitatively, the PN results seem to follow the NR results well, until close to merger.

We now turn to a quantitative analysis of the precession dynamics, establishing first that the choice of Taylor approximant is of minor importance for the precession dynamics. We match PN dynamics to the NR simulations q5_0.5x and q1_0.5x for the Taylor approximants T1, T4 and T5. We then compute the angles $\angle L$ and $\angle\chi_1$. Figure 4.4 shows the resulting $\angle L$. During most of the inspiral, we find $\angle L$ of order a few 10^{-3} radians increasing to ~ 0.1 radians during the last $1000M$ before merger. Thus the direction of the normal to the orbital plane is reproduced well by PN theory. This result is virtually independent of the Taylor approximant suggesting that the choice of approximant only weakly influences how well PN precession equations track the motion of the orbital plane. In other words, precession dynamics does not depend on details of orbital phasing like the unmodeled higher-order terms in which the Taylor approximants differ from each other.

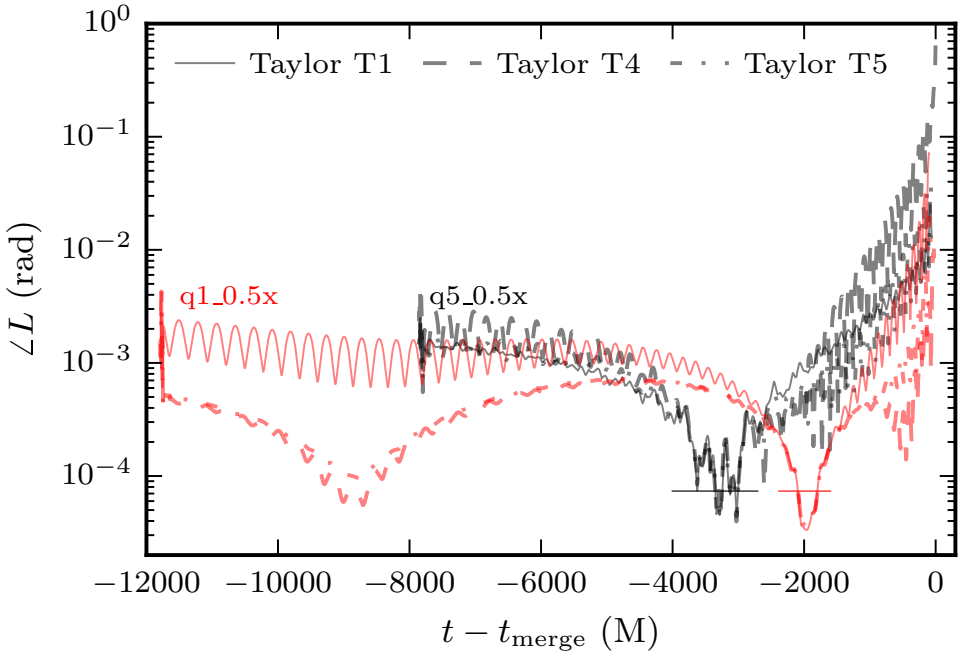

Figure 4.4: Angle $\angle L$ by which $\hat{\ell}^{\rm PN}(t)$ differs from $\hat{\ell}^{\rm NR}(t)$ for the configuration q1_0.5x (red lines) and q5_0.5x (black lines). $\angle L \leq 0.2^\circ$ except very close to merger. In each case, the PN predictions based on different PN approximants are shown in different line styles. Shown is the point-wise average of 12 $\angle L(t)$ curves, i.e. the thick red line of Fig. 4.3. The thin horizontal lines show the widest edges of the PN matching intervals.

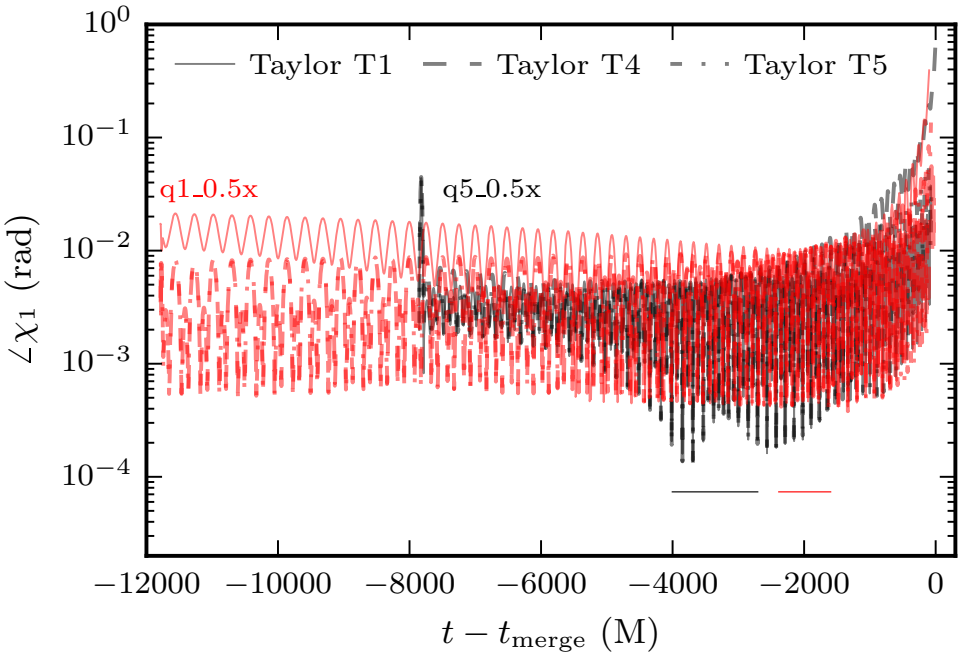

Figure 4.5: Angle $\angle\chi_1$ by which $\vec{\chi}_1^{\rm PN}(t)$ differs from $\vec{\chi}_1^{\rm NR}(t)$ for the configuration q1_0.5x (red lines) and q5_0.5x (black lines). In each case, the PN predictions based on different PN approximants are shown in different line styles. The thin horizontal lines show the widest edges of the PN matching intervals.

Turning to the spin direction $\hat{\chi}_1$ we compute the angle $\angle\chi_1$ between $\hat{\chi}_1^{\rm NR}(t)$ and $\hat{\chi}_1^{\rm PN}(t)$ and plot the result in Fig. 4.5. While Fig. 4.5 looks busy, the first conclusion is that $\angle\chi_1$ is quite small $\lesssim 0.01$ rad through most of the inspiral, and rises somewhat close to merger.

The pronounced short-period oscillations of $\angle\chi_1$ in Fig. 4.5 are caused by differences between PN-nutation features and NR-nutation features. To better understand the nutation features and their impact on the angle $\angle\chi_1$, we remove nutation features by filtering out all frequencies comparable to the orbital frequency. This is possible because the precession frequency is much smaller than the nutation frequency. The filtering is performed with a 3rd order, bi-directional low pass Butterworth filter [140] with a fixed cutoff frequency chosen to be lower than the nutation frequency at the start of the inspiral. Due to the nature of the filtering, the resulting averaged spin will suffer from edge effects which affect approximately the first and last 1000 M of the inspiral. Furthermore, the precession frequency close to merger becomes comparable to the nutation frequency at the start of the simulation and thus filtering is no longer truthful in this region. Therefore, we only use the "averaged" spins where such features are absent.

Applying this smoothing procedure to both $\hat{\chi}_1^{\rm PN}$ and $\hat{\chi}_1^{\rm NR}$ for the run q5_0.5x, we

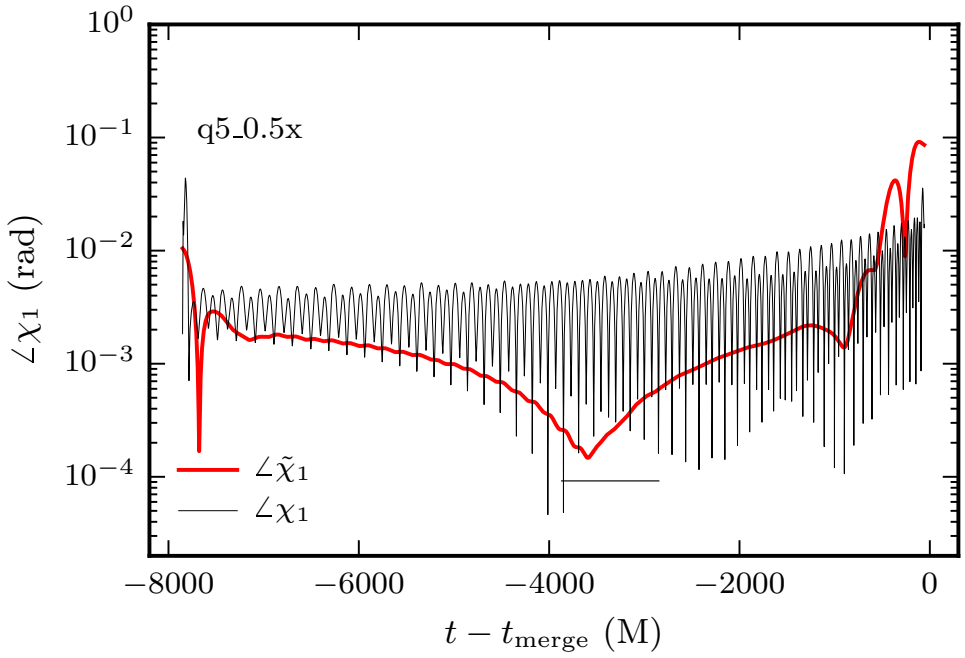

Figure 4.6: Angle $\angle\tilde{\chi}_1$ between the "orbit-averaged" spins for the configuration q5_0.5x. The non orbit-averaged difference $\angle\chi_1$ (cf. Fig. 4.5) is shown for comparison. Shown is one matching interval as indicated by the thin horizontal line.

compute the angle $\angle\tilde{\chi}_1$ between the averaged spin vectors, $\tilde{\chi}_1^{\rm PN}$ and $\tilde{\chi}_1^{\rm NR}$. This angle is plotted in Fig. 4.6[7], where results only for the Taylor T1 approximant are shown, and for only one matching interval specified by $m\Omega_m = 0.0210597$ and $\delta\Omega/\Omega_m = 0.1$. The orbit-averaged spin directions $\tilde{\chi}_1^{\rm NR/PN}$ agree significantly better with each other than the non-averaged ones (cf. the black line in Fig. 4.6, which is duplicated from Fig. 4.5). In fact, the orbit-averaged spin precessing between NR and PN agrees as well as the orbital angular momentum precession, cf. Fig. 4.4. Thus, the difference in the spin dynamics is dominated by the nutation features, with the orbit-averaged spin dynamics agreeing well between PN and NR.

Motivated by the separation of timescales, orbit-averaged PN precession equations were developed and widely used in literature (see e.g. [11, 99, **?**]). Because these equations eliminate the orbital time-scale, they are much easier to integrate. For example, the SpinTaylorT4 model of the LIGO Algorithm Library [54] utilizes the leading order orbit-averaged precession equations [40]. As an example, we construct and match orbit-averaged and full PN precession equations at leading order in spin-orbit and spin-spin couplings (i.e, the precession equations are at 2 PN order). Figure 4.7 presents χ and $\hat{\ell}$

[7] To illustrate edge effects of the Butterworth filter, Fig. 4.6 includes the early and late time periods where the filter affects $\angle\tilde{\chi}_1$.

for the case q5_0.5x for averaged and unaveraged 2 PN precession equations, as well as the full 3.5PN precession equations and NR data. It is evident that the orbit-averaged equations do indeed reproduce the non-averaged behaviour. Further, we note that the 2PN results diverge from the NR data quickly outside of the matching region. Meanwhile the 3.5PN precession equations match the NR results much better throughout the inspiral. Therefore, to improve on the leading-order orbit-averaged precession equations, it is more important to increase the PN order than to avoid orbit-averaging.

We also test that our a posteori orbit-averaging reproduces the analytically orbit-averaged precession equations. This is indeed the case as can be seen in Fig. 4.8. Shown are the angles $\angle\chi_1$ and $\angle L$ for the various choices of PN approximants. As one can see, the angle between the aposteori-averaged PN equations and smoothed NR data (e.g. $\tilde{\chi}_1$) lies on top of the angle between the orbit-averaged PN precession equations and the smoothed NR data. Further, all of the curves lie essentially on top of one another, reflecting that a priory and aposteori matching do not significantly bias the comparison. Finally, the angle between the aposteori-averaged PN and the averaged precession equations is approximately $10-20$ times smaller than the angle between PN and NR. We thus have further confidence that the ad-hoc filtering procedure is a useful tool for smoothing the NR data.

To characterize the nutation features in the spin vectors, we introduce a coordinate system which is specially adapted to highlighting nutation effects. The idea is to visualize nutation with respect to the averaged spin vector $\tilde{\chi}$. We compute the time-derivative $\dot{\tilde{\chi}}$ numerically. Assuming that the "averaged" spin is undergoing pure precession, so that $\tilde{\chi}\cdot\dot{\tilde{\chi}}=0$, we define a new coordinate system $(\hat{e}_1,\hat{e}_2,\hat{e}_3)$ by $\hat{e}_1=\tilde{\chi}, \hat{e}_2=\dot{\tilde{\chi}}/|\dot{\tilde{\chi}}|, \hat{e}_3=\hat{e}_1\times\hat{e}_2$. The spin is now projected onto the $\hat{e}_2-\hat{e}_3$ plane, thus showing the motion of the spin in a frame "coprecessing" with the averaged spin. This allows us to approximately decouple precession and nutation and compare them separately between PN and NR.

Figure 4.9 plots the projection of the spins $\chi_1^{\rm NR}$ and $\chi_1^{\rm PN}$ onto their respective "orbit averaged" $\hat{e}_2-\hat{e}_3$ planes. We see that the behavior of the NR spin and the PN spins are qualitatively different: For this single-spin system, the PN spin essentially changes only in the $\hat{e}_3$ direction (i.e., orthogonal to its average motion $\dot{\tilde{\chi}}^{\rm PN}$). In contrast, the NR spin undergoes elliptical motion with the excursion along its $\hat{e}_2$ axis (i.e., along the direction of the average motion) about several times larger than the oscillations along $\hat{e}_3$. The symbols plotted in Fig. 4.9 reveal that each of the elliptic "orbits" corresponds approximately to half an orbit of the binary, consistent with the interpretation of this motion as nutation. The features exhibited in Fig. 4.10 are similar across all the single-spinning precessing cases considered in this work. The small variations in spin direction exhibited

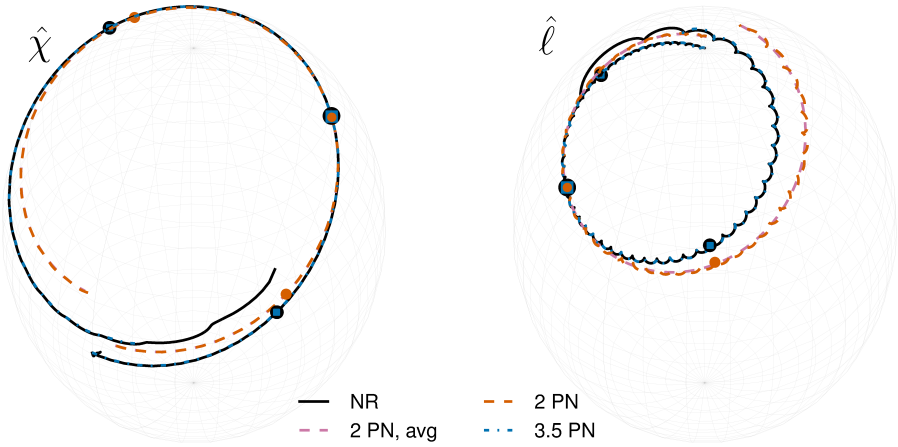

Figure 4.7: Comparison of orbit averaged PN precession equations with the non-orbit averaged equations. Plotted are $\hat{\chi}$ (left) and $\hat{\ell}$ (right) on the unit sphere for 2 PN averaged and non-averaged precession equations, 3.5 PN unaveraged precession equations and NR data. The large black dot represents the centre (in time) of the matching interval (several symbols overlap here). The other black dots represent the interval $\pm$2000 M from the matching point. The same is done for 2PN (orange dots) and 3.5PN (blue squares). Both 2PN curves lie on top of each other and match the NR data well close to the matching region but then quickly diverge away. The 3.5 PN curve matches the NR result much better throughout the inspiral.

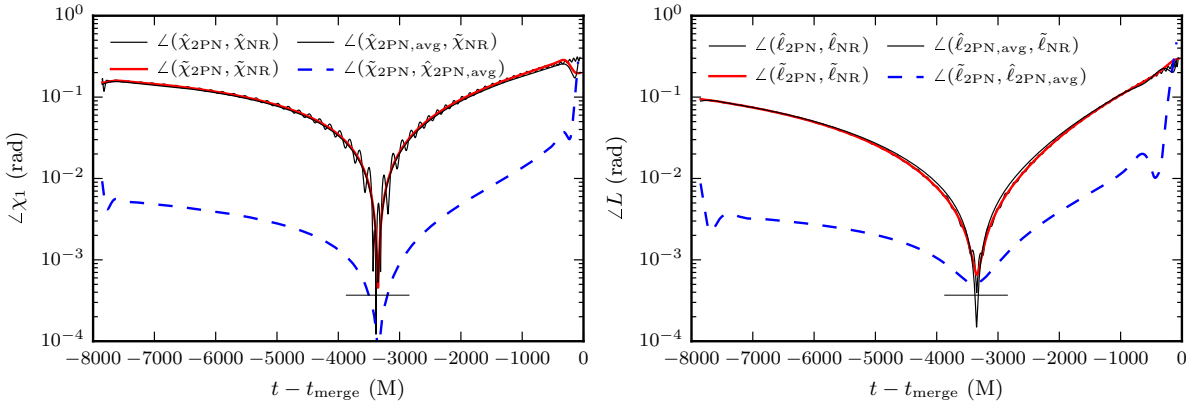

Figure 4.8: Comparison of aposteori averaging procedure described above to using orbit-averaged PN precession equations for PN evolution for configuration q5_0.5x. The curves labelled with *2PN avg* use orbit-averaged precession equations. A $\tilde{v}$ means aposteori smoothing of $\hat{v}$. There is virtually no difference between using the full precession equations and filtering aposteori and using the orbit-averaged precession equations. The angle between the orbit-averaged PN results and the aposteori-averaged PN results is 10-20 times smaller than the angles between PN and NR data showing that aposteori-averaging does not bias the comparison. Shown is one matching interval as indicated by the thin horizontal line.

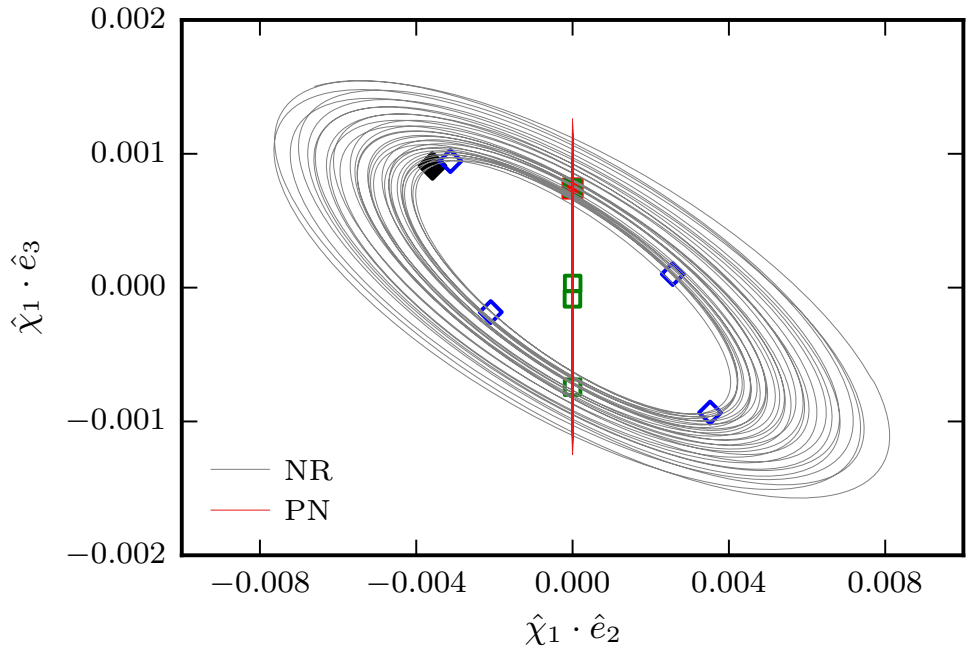

Figure 4.9: The projection of $\hat{\chi}_1^{\rm NR}$ and $\hat{\chi}_1^{\rm PN}$ onto the $\hat{e}_2 - \hat{e}_3$ plane described in the text for case q5_0.5x. The system is shown in the interval $t - t_{\rm merge} \in [-6662, -1556]$. along the $\hat{e}_3$ axis. Meanwhile, the NR data show variations in $\hat{e}_2$ and $\hat{e}_3$ directions of comparable magnitude. The solid symbols (black diamond for NR, red square for PN) indicate the data at the start of the plotted interval, chosen such that $\hat{\chi}_{\rm r}\hat{n}$ is maximal—i.e., where the spin projection into the orbital plane is parallel to $\hat{n}$. The subsequent four open symbols (blue diamonds for NR, green squares for PN) indicating the position 1/8-th, 1/4-th, 3/8-th and 1/2 of an orbit later.

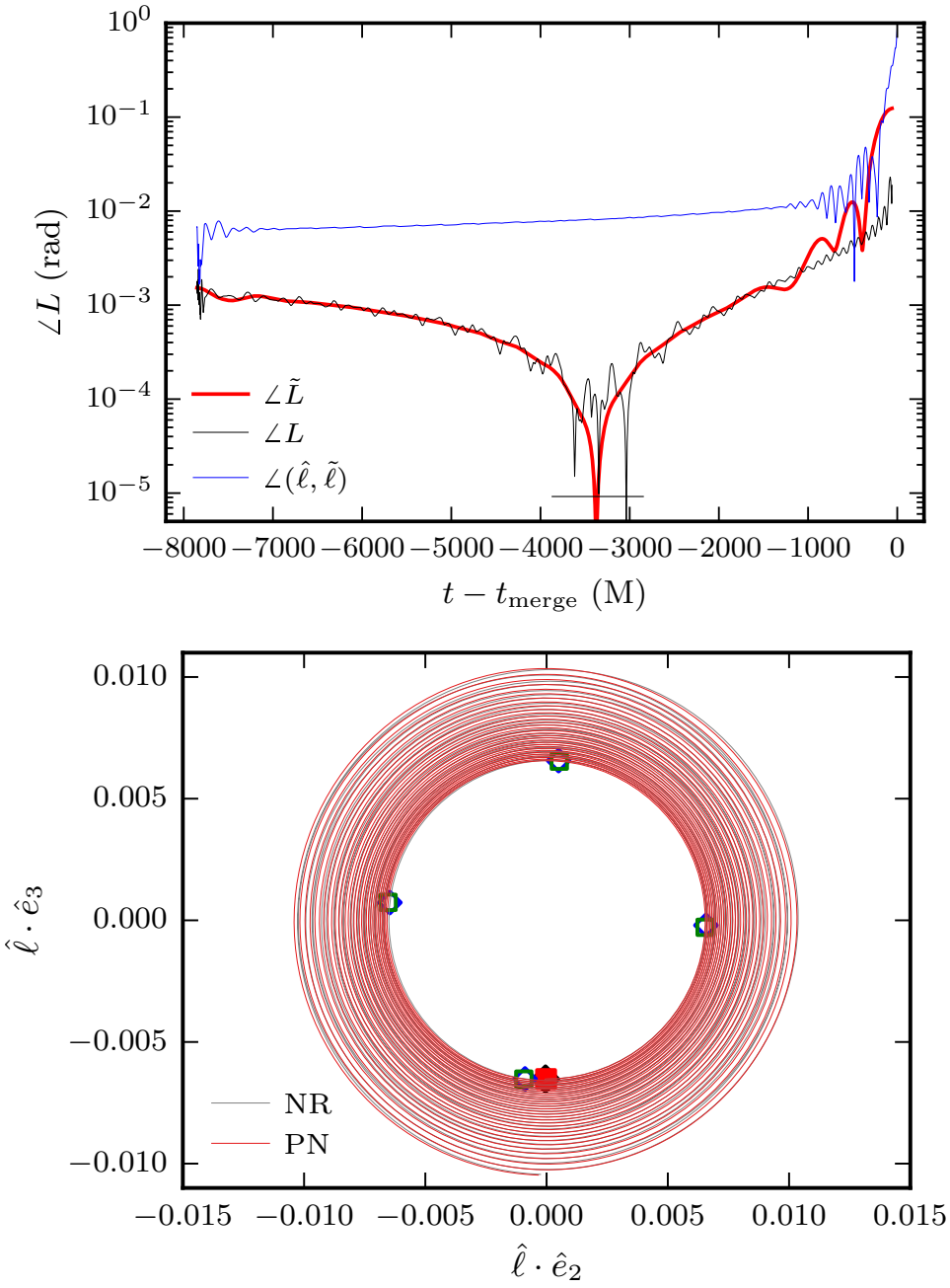

Figure 4.10: Characterization of nutation effects of the orbital angular momentum. **Top**: angle $\angle\tilde{L}$ between the "averaged" $\hat{\ell}$ in PN and NR for the configuration q5_0.5x (thick red line). $\angle L$ is shown in thin black line for comparison (cf. Fig. 4.6). The thin blue line shows $\angle(\hat{\ell},\tilde{\ell})$ between the averaged and the filtered signal. Note that it is larger than both $\angle L$ and $\angle\tilde{L}$. **Bottom**: the projection of $\hat{\ell}^{\rm NR}$ (gray) and $\hat{\ell}^{\rm PN}$ (red) onto the $\hat{e}_2 - \hat{e}_3$ plane described in the text for case q5_0.5x (cf. Fig. 4.10). The system is shown in the interval $[-6662, -1556]$. Both PN and NR show the same behavior, in contrast to the behavior of the spin in Fig. 4.9. The PN-NR matching interval is indicated by the horizontal line in the top panel.

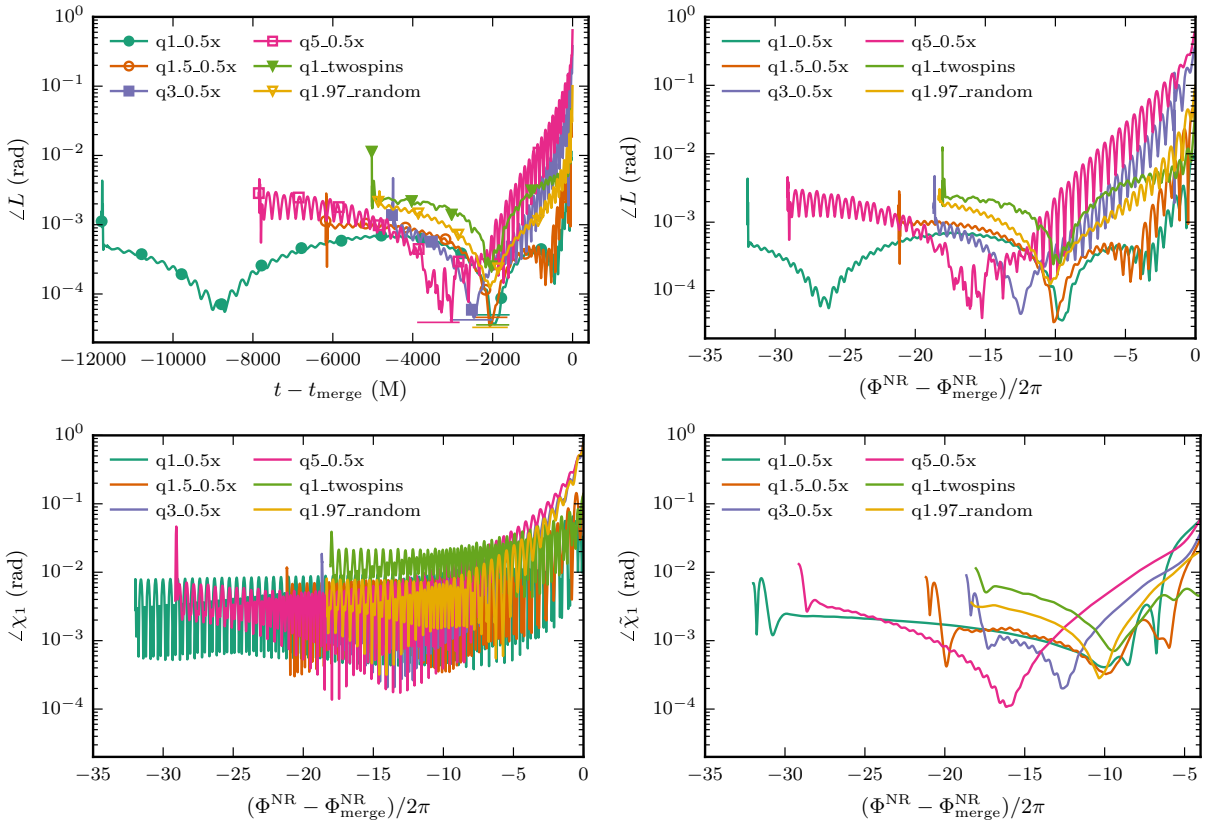

Figure 4.11: Comparison of orbital plane and spin precession for the primary six precessing NR simulations. **Top Left**: $\angle L$ as a function of time to merger. **Top right**: $\angle L$ as a function of *orbital phase in NR*. **Bottom left**: $\angle \chi_1$ as a function of orbital phase. **Bottom right**: $\angle \tilde{\chi}_1$ between the averaged spins. All data plotted are averages over 12 matching intervals, cf. Fig. 4.3, utilizing the Taylor T4 PN approximant. The thin horizontal lines in the top left panel show the widest edges of the PN matching intervals.

in Fig. 4.9 are orders of magnitude smaller than parameter estimation capabilities of LIGO, e.g. [**?**], and so we do not expect that these nutation features will have a negative impact on GW detectors. To understand the features of Fig. 4.9 in more detail, it would be beneficial to carefully compare gauge conditions between NR and PN, and to consider spin supplementary conditions.

Let us now apply our nutation analysis to the orbital angular momentum directions $\hat{\ell}$. Analogous to the spin, we compute averages $\tilde{\ell}^{\rm NR}$ and $\tilde{\ell}^{\rm PN}$, and compute the angle between the directions of the averages, $\angle \tilde{L} = \angle \left(\tilde{\ell}^{\rm PN}, \tilde{\ell}^{\rm NR} \right)$. This angle—plotted in the top panel of Fig. 4.10—agrees very well with the difference $\angle L$ that was computed without orbit-averaging. This indicates that the nutation features of $\hat{\ell}$ agree between NR and PN. The top panel of Fig. 4.11 also plots the angle between the raw $\hat{\ell}^{\rm NR}$ and the averaged $\tilde{\ell}^{\rm NR}$, i.e. the opening angle of the nutation oscillations. As is apparent in Fig. 4.10, the angle

between $\hat{\ell}^{\rm NR}$ and $\tilde{\ell}^{\rm NR}$ is about 10 times larger than the difference between NR and PN ($\angle L$ or $\angle \tilde{L}$), confirming that nutation features are captured. The lower panel of Fig. 4.10 shows the projection of $\hat{\ell}$ orthogonal to the direction of the average $\tilde{\ell}$. In contrast to the spins shown in Fig. 4.9, the nutation behavior of $\hat{\ell}$ is in close agreement between NR and PN: For both, $\hat{\ell}$ precesses in a circle around $\tilde{\ell}$, with identical period, phasing, and with almost identical amplitude. We also point out that the shape of the nutation features differs between $\hat{\ell}$ and $\hat{\chi}_1$: $\hat{\ell}$ circles twice per orbit around its average $\tilde{\ell}$, on an almost perfect circle with equal amplitude in the $\hat{e}_2$ and $\hat{e}_3$ direction.

We now extend our precession dynamics analysis to the remaining five primary precessing NR simulations listed in Table 4.1. The top left panel of Figure 4.11 shows $\angle L$. The difference in the direction of the normal to the orbital plane is small; generally $\angle L \lesssim 10^{-2}$ radians, except close to merger. Thus it is evident that the trends seen in Fig. 4.4 for $\angle L$ hold across all the precessing cases. To make this behavior clearer, we parameterize the inspiral using the orbital phase instead of time, by plotting the angles versus the orbital phase in the NR simulation, as shown in the top right panel of Fig. 4.11. Thus, until a few orbits to merger PN represents the precession and nutation of the orbital plane well.

The bottom left panel of Fig. 4.11 establishes qualitatively good agreement for $\angle \chi_1$, with slightly higher values than $\angle L$. As already illustrated in Fig. 4.6, nutation features dominate the difference. Averaging away the nutation features, we plot the angle $\angle \tilde{\chi}_1$ between the smoothed spins in the bottom left panel of Fig. 4.11, where the behavior of $\angle \chi_1$ is very similar to that of $\angle L$. This confirms that the main disagreement between PN and NR spin dynamics comes from nutation features, and suggests that the secular precession of the spins is well captured across all cases, whereas the nutation of the spins is not. For completeness, we also show a parametric plot of $\angle L$ and $\angle S$ versus orbital frequency in the NR simulation in Fig. 4.12.

All configurations considered so far except q1.97_random have $\vec{S} \cdot \hat{\ell} = 0$ at the start of the simulations, where $\vec{S} = \vec{S}_1 + \vec{S}_2$ is the total spin angular momentum of the system. When $\vec{S} \cdot \hat{\ell} = 0$, several terms in PN equations vanish, in particular the spin orbit terms in the expansions of the binding energy, the flux and the orbital precession frequency, see Eqs. (4.34), (4.35), and (4.51) in Appendix A.

To verify whether $\vec{S} \cdot \hat{\ell} = 0$ introduces a bias to our analysis, we perform our comparison on an additional set of 31 binaries with randomly oriented spins. These binaries have mass ratio $1 \leq q \leq 2$, spin magnitudes $0 \leq \chi_{1,2} \leq 0.5$, and correspond to cases SXS:BBH:0115 - SXS:BBH:0146 in the SXS catalog. Fig. 4.13 plots $\angle L$ for these additional 31 PN-NR comparisons in gray, with q1.97_random highlighted in orange. The

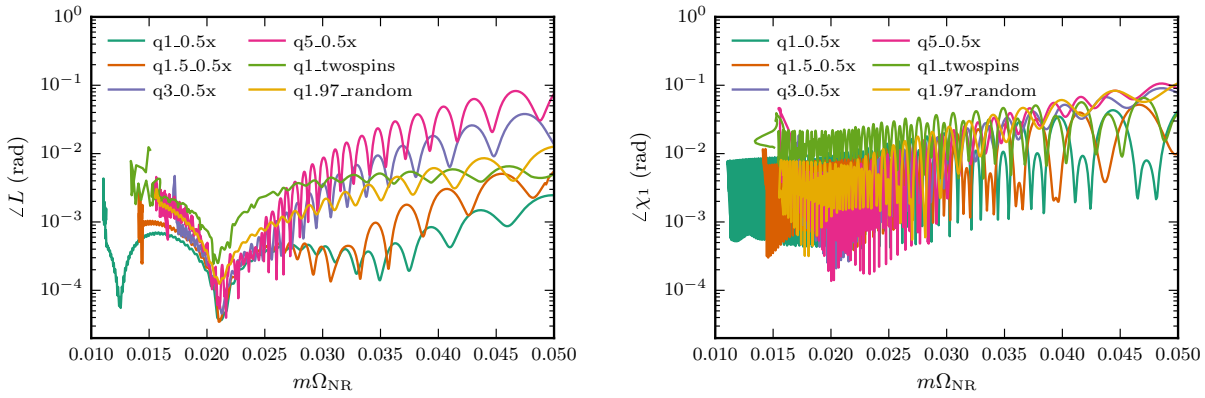

Figure 4.12: Comparison of orbital plane and spin precession for the primary six precessing NR simulations as functions of *orbital frequency in NR*. **Right**: $\angle L$;**Left**: $\angle \chi_1$. All data plotted are averages over 12 matching intervals, cf. Fig. 4.3, utilizing the Taylor T4 PN approximant.

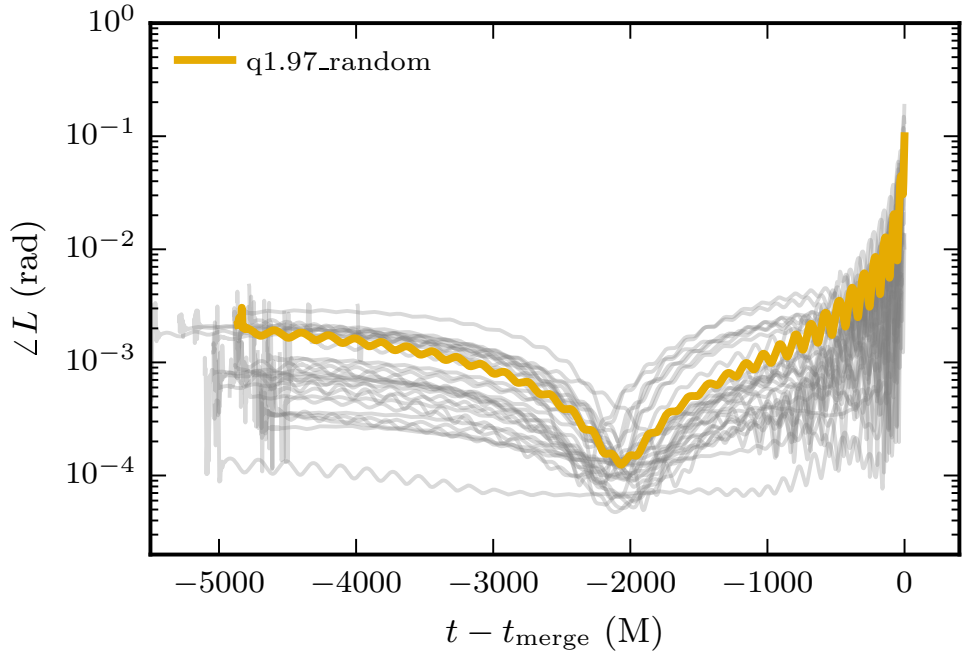

Figure 4.13: $\angle L$ for additional 31 precessing configurations with arbitrary oriented spins as well as the case q1.97_random. Here $q \in (1, 2)$, $\chi_{1,2} \leq 0.5$. For all cases, $\angle L < 0.5°$ throughout most of the inspiral. All data plotted are averages over 12 matching intervals, cf. Fig. 4.3.

disagreement between PN and NR is similarly small in all of these cases, leading us to conclude that our results are robust in this region of the parameter space.

4.4.2 Orbital Phase Comparisons

Along with the precession quantities described above, the orbital phase plays a key role in constructing PN waveforms. We use Φ_Δ, a geometrically invariant angle that reduces to the orbital phase difference for non-precessing binaries (cf. Sec. 4.3.3) to characterize phasing effects. We focus on single spin systems with mass-ratios from 1 to 8, where the more massive black hole carries a spin of $\chi_1 = 0.5$, and where the spin is aligned or anti-aligned with the orbital angular momentum, or where the spin is initially tangent to the orbital plane. We match all NR simulations to post-Newtonian inspiral dynamics as described in Sec. 4.3.4, using the 12 matching intervals specified in Eqs. (4.19) and (4.20). We then compute the phase difference Φ_Δ at the time at which the NR simulation reaches orbital frequency $m\Omega_{NR} = 0.03$.

The results are presented in Fig. 4.14, grouped based on the initial orientation of the spins: aligned, anti-aligned, and in the initial orbital plane. For aligned runs, there are clear trends for Taylor T1 and T5 approximants: for T1, differences decrease with increasing mass ratio (at least up to $q = 8$); for T5, differences increase. For Taylor T4, the phase difference Φ_Δ has a minimum and there is an overall increase for higher mass ratios. For anti-aligned runs, Taylor T5 shows the same trends as for the aligned spins. Taylor T4 and T1 behaviors, however, have reversed: T4 demonstrates a clear increasing trend with mass ratio, whereas T1 passes through a minimum with overall increases for higher mass ratios. Our results are also qualitatively consistent with the results described in [84] as we find that for equal mass binaries, the Taylor T4 approximant performs better than the Taylor T1 approximant (both for aligned and anti-aligned spins).

For the in-plane precessing runs, we see clear trends for all 3 approximants: Taylor T4 and T5 both show increasing differences with increasing mass ratio, and T1 shows decreasing differences. These trends for precessing binaries are consistent with previous work on non-spinning binaries [122], which is expected since for $\vec{S} \cdot \hat{\ell}$ many of the same terms in the binding energy and flux vanish as for non-spinning binaries. Overall, we find that for different orientations and mass ratios, no one Taylor approximant performs better than the rest, as expected if the differences between the approximants arise from different treatment of higher-order terms.

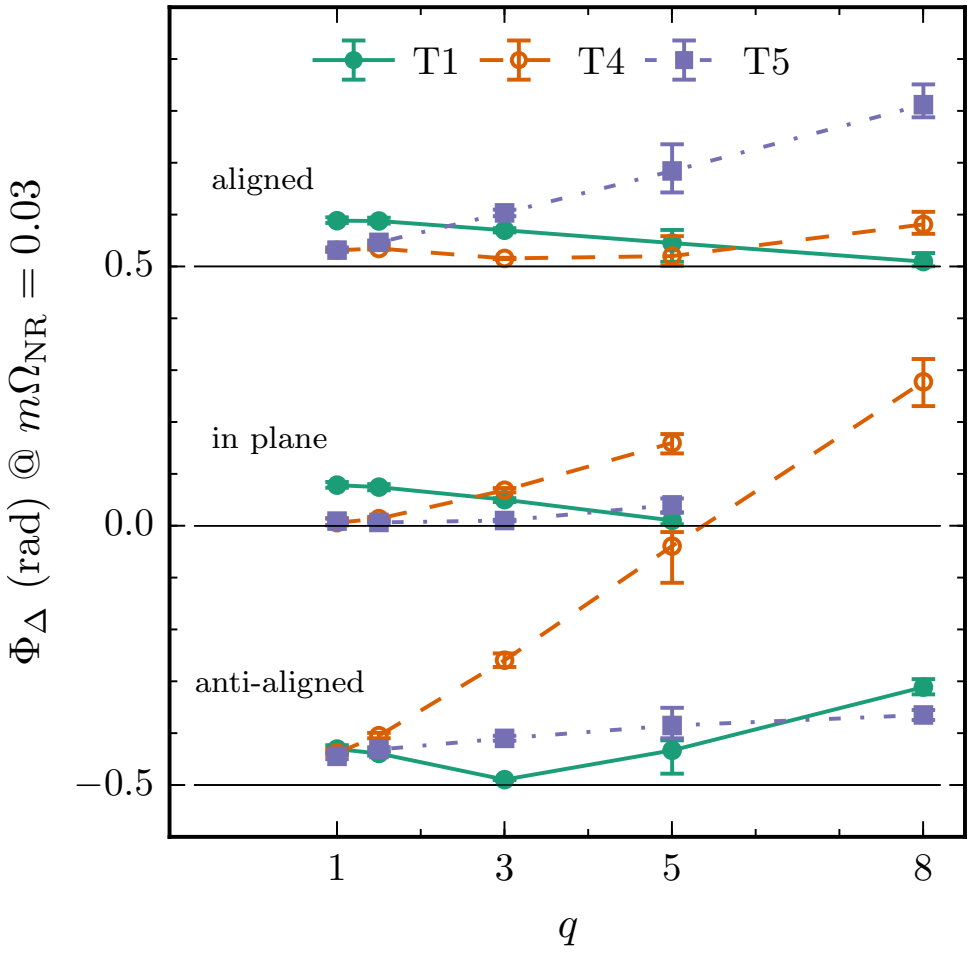

Figure 4.14: Φ_Δ as a function of mass ratio for BBH systems with $\chi_1 = 0.5$, and spin direction aligned (top), orthogonal (middle), and anti-aligned (bottom) with the orbital angular momentum. For clarity, the aligned/anti-aligned data are offset by $+0.5$ and -0.5, respectively, with the thin horizontal black lines indicating zero for each set of curves. Plotted is Φ_Δ averaged over the 12 matching intervals, cf. Fig. 4.3, and for three different Taylor approximants.

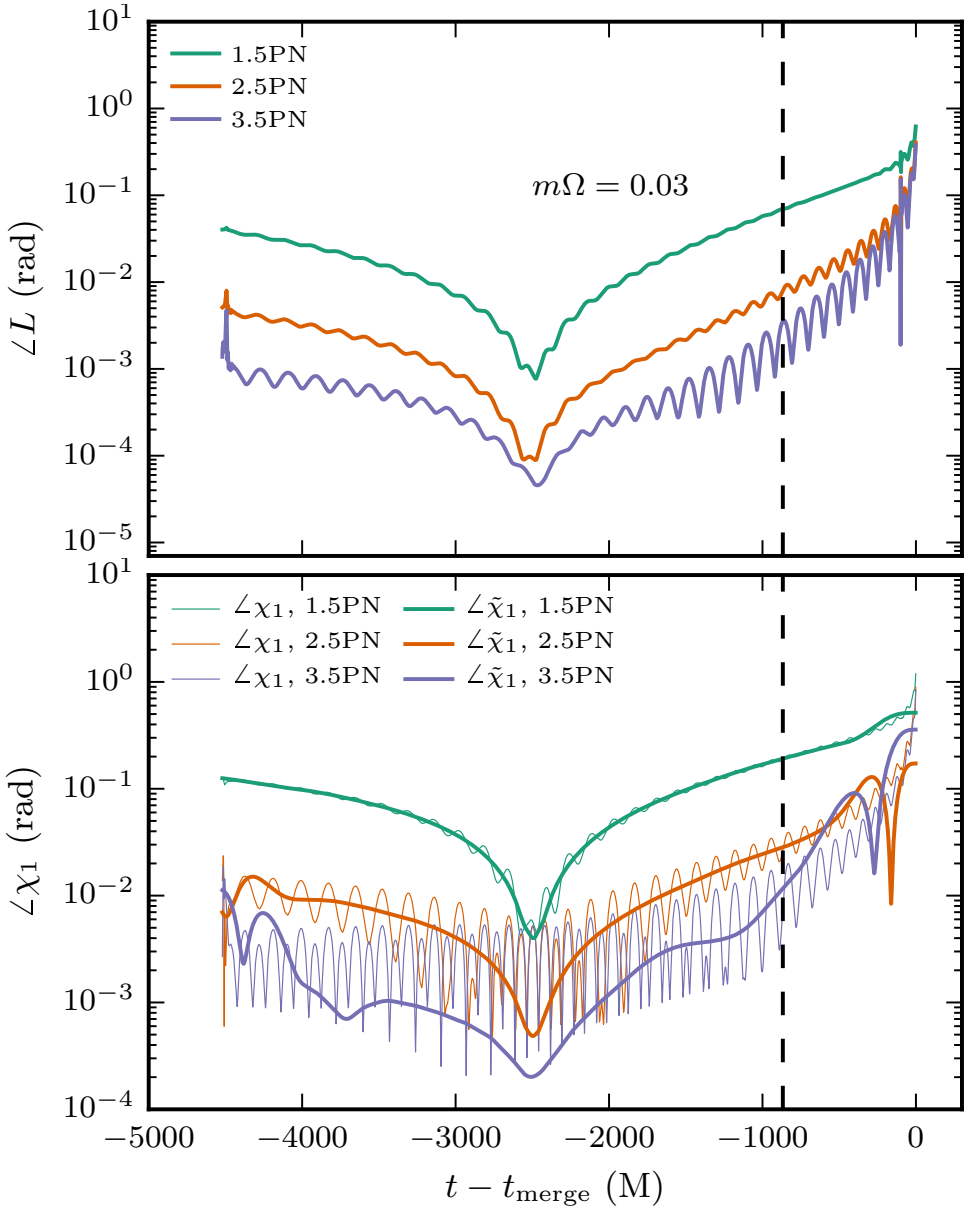

Figure 4.15: Comparison of PN-NR precession dynamics when the expansion order of the PN precession equations is varied. Shown is the case q3_0.5x. The top panel shows the precession of the orbital plane, and the bottom panel of the spin $\hat{\chi}_1$ (without and with averaging). All data shown are averages over 12 matching intervals, cf. Fig. 4.3.

4.4.3 Convergence with PN order

So far all comparisons were performed using all available post-Newtonian information. It is also instructive to consider behavior at different PN order, as this reveals the convergence properties of the PN series, and allows estimates of how accurate higher order PN expressions might be.

The precession frequency ϖ, given in Eq. (4.51), is a product of series in the frequency parameter x. We multiply out this product, and truncate it at various PN orders from leading order (corresponding to 1.5PN) through next-to-next-to-leading order (corresponding to 3.5PN). Similarly, the spin precession frequencies $\vec{\Omega}_{1,2}$ in Eqs. (4.2) and (4.52) are power series in x. We truncate the power series for $\vec{\Omega}_{1,2}$ in the same fashion as the power series for ϖ, but keep the orbital phase evolution at 3.5PN order, where we use the TaylorT4 prescription to implement the energy flux balance. For different precession-truncation orders, we match the PN dynamics to the NR simulations with the same techniques and at the same matching frequencies as in the preceding sections.

When applied to the NR simulation q3_0.5x, we obtain the results shown in Fig. 4.15. This figure shows clearly that with increasing PN order in the precession equations, PN precession dynamics tracks the NR simulation more and more accurately. When only the leading order terms of the precession equations are included (1.5PN order), $\angle L$ and $\angle\chi_1$ are ≈ 0.1rad; at 3.5PN order this difference drops by nearly two orders of magnitude.

We repeat this comparison for our six main precessing cases from Table 4.1. The results are shown in Fig. 4.16 and once again the angles are evaluated at the time the NR simulation reaches orbital frequency of $m\Omega_{NR} = 0.03$. It is evident that for *all cases* $\angle L$ decreases with increasing order in the precession equations with almost 2 orders of magnitude improvement between leading order and next-to-next leading order truncations. A similar trend is seen in the convergence of the spin angle $\angle\chi_1$ shown in bottom panel of Fig. 4.16. The angle decreases with PN order almost monotonically for all cases except q1.0_twospins. However, this is an artificial consequence of picking a particular matching point at $m\Omega = 0.03$: as can be seen from the bottom panel of Fig. 4.15 $\angle\chi_1$ shows large oscillations and it is a coincidence that the matching point happens to be in a "trough" of χ_1.

So far we have varied the PN order of the precession equations, while keeping the orbital frequency evolution at 3.5PN order. Let us now investigate the opposite case: varying the PN order of the orbital frequency and monitoring its impact on the orbital phase evolution. We keep the PN order of the precession equations at 3.5PN, and match PN with different orders of the orbital frequency evolution (and TaylorT4 energy-balance prescription) to the NR simulations. We then evaluate Φ_Δ (a quantity that reduces to the

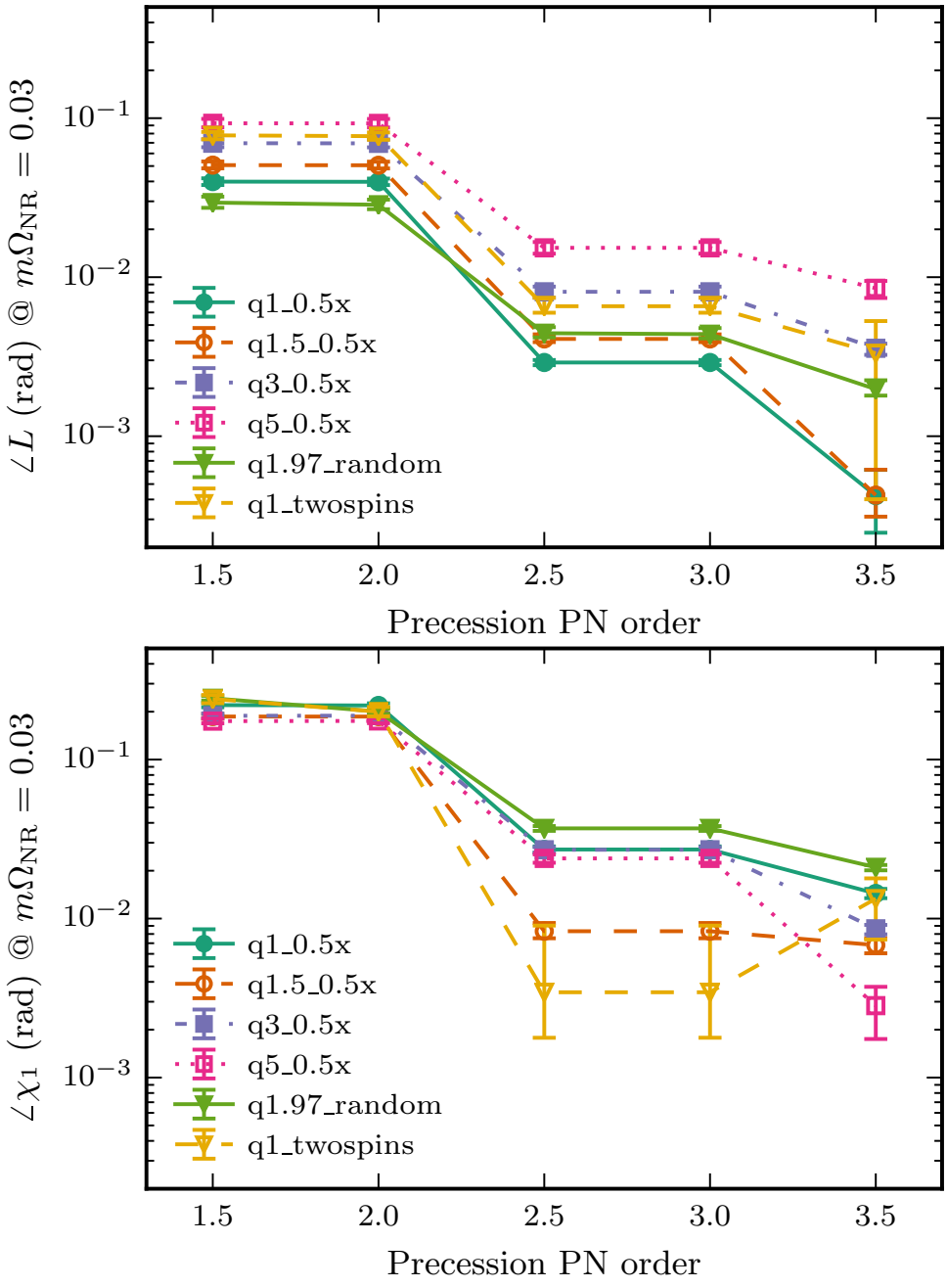

Figure 4.16: Convergence of the PN precession equations for all cases in Table 4.1. The evolution was done with the Taylor T4 approximant at 3.5 PN order. The leading order spin-orbit correction is at 1.5 PN order and the spin-squared corrections appear at 2 PN order. Each data point is the average $\angle L$ over PN-NR comparisons performed using 12 matching intervals, cf. Fig. 4.3, with error bars showing the maximal and minimal $\angle L$ and $\angle \chi_1$ of the 12 fits.

orbital phase difference in cases where the latter is unambiguously defined) at the time at which the NR simulation reaches the frequency $m\Omega_{NR} = 0.03$. We examine our six primary precessing runs, and also the aligned-spin and anti-aligned spin binaries listed in Table 4.1.

When the spin is initially in the orbital plane, as seen in the top panel of Fig. 4.17, the overall trend is a non-monotonic error decrease with PN order, with spikes at 1 and 2.5 PN orders as has been seen previously with non-spinning binaries [33]. All of the aligned cases show a large improvement at 1.5 PN order, associated with the leading order spin-orbit contribution. The phase differences then spike at 2 and 2.5 PN orders and then decrease at 3 PN order. Finally, different cases show different results at 3.5 PN with some showing decreases differences while for others the differences increase.

For the anti-aligned cases the picture is similar to precessing cases with a spike at 1 and 2.5 PN orders and monotonic improvement thereafter. The main difference from precessing cases is the magnitude of the phase differences, which is larger by a factor of ~ 5 at 3.5 PN order for the anti-aligned cases (see for example q1.5_s0.5x_0).

These results suggest that convergence of the orbital phase evolution depends sensitively on the exact parameters of the system under study. Further investigation of the parameter space is warranted.

4.4.4 Impact of PN spin truncation

As mentioned in Sec. 4.3.1, post-Newtonian expansions are not fully known to the same orders for spin and non-spin terms. Thus, for example, the expression for flux $\mathcal{F}$ is complete to 3.5 PN order for non-spinning systems, but spinning systems may involve unknown terms at 2.5 PN order; a similar statement holds for dE/dx. This means that when the ratio in Eq. (4.4), $\mathcal{F}/(dE/dx)$, is re-expanded as in the T4 approximant, known terms will mix with unknown terms. It is not clear, *a priori*, how such terms should be handled when truncating that re-expanded series.

Here we examine the effects of different truncation strategies. We focus on the Taylor T4 approximant while considering various possible truncations of the re-expanded form of $\mathcal{F}/(dE/dx)$. We denote these possibilities by the orders of (1) the truncation of non-spin terms, (2) the truncation of spin-linear terms, and (3) the truncation of spin-quadratic terms. Thus, for example, in the case where we keep non-spin terms to 3.5 PN order, keep spin-linear terms to 2.5 PN order, and keep spin-quadratic terms only to 2.0 PN order, we write (3.5, 2.5, 2.0). We consider the following five possibilities:

(i) (3.5, 3.5, 3.5)

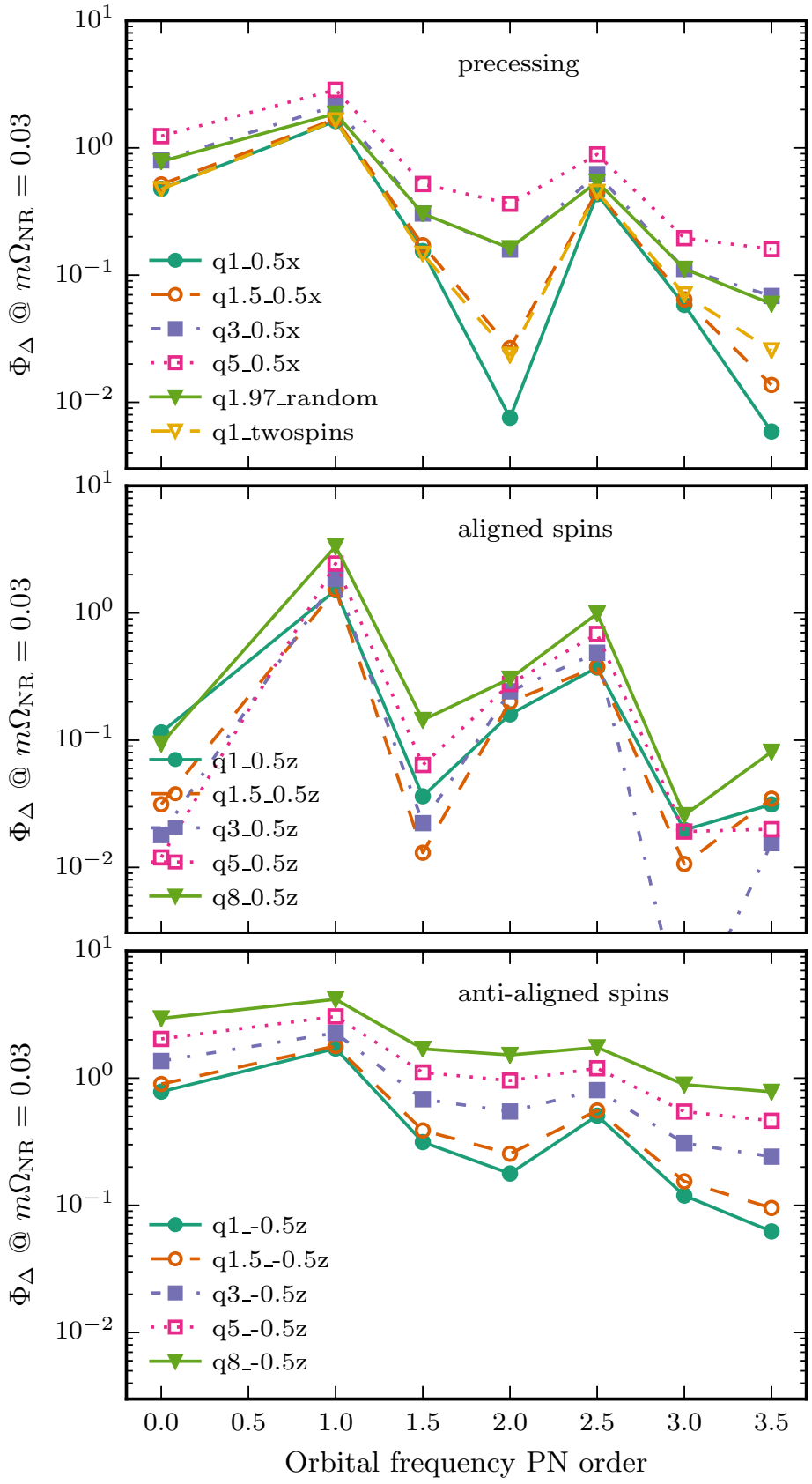

Figure 4.17: Convergence of the Taylor T4 approximant with PN order. Shown are all cases from Table 4.1. **Top**: all precessing cases. **Middle**: aligned spin cases. **Bottom**: anti-aligned spin cases. Each data point shown is averaged over PN-NR comparison with 12 matching intervals, cf. Fig. 4.3. Error bars are omitted for clarity, but would be of similar size to those in Fig. 4.18.

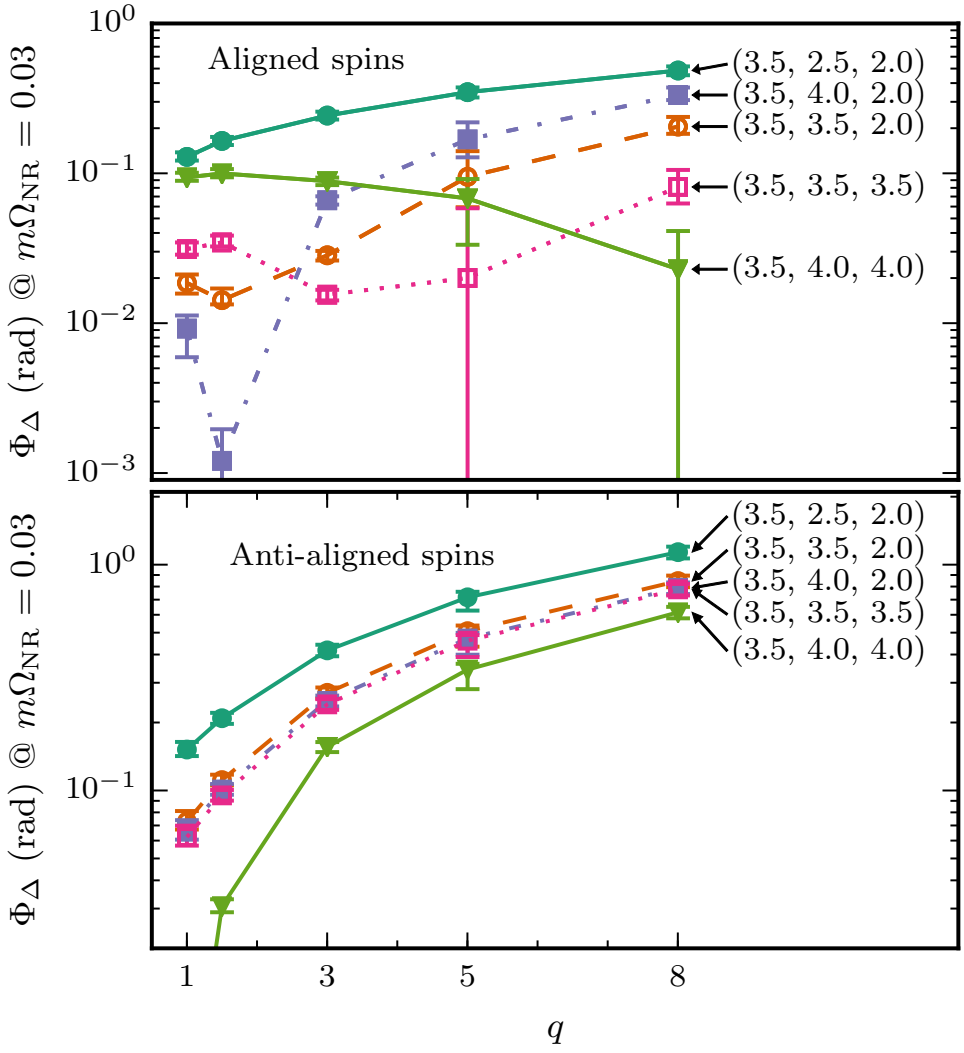

Figure 4.18: Impact of different choices for spin truncation on orbital phase difference Φ_Δ, as a function of mass ratio. The lines are labelled by the truncation types, as explained in the text. The upper panel shows all cases for which the spins are aligned with the orbital angular momentum; the lower panel shows the anti-aligned cases.

(ii) (3.5, 4.0, 4.0)
(iii) (3.5, 2.5, 2.0)
(iv) (3.5, 3.5, 2.0)
(v) (3.5, 4.0, 2.0).

To increase the impact of the spin-orbit terms, we examine aligned and anti-aligned cases from Table 4.1, with results presented in Fig. 4.18,where once more Φ_Δ is evaluated at the time at which the NR simulation reaches the frequency $m\Omega_{NR} = 0.03$. For aligned cases, no one choice of spin truncation results in small differences across all mass ratios. All choices of spin truncation excepting (3.5, 4.0, 4.0) have increasing errors with increasing mass ratio. Truncating spin corrections at 2.5 PN order (3.5, 2.5, 2) consistently results in the worst matches. On the other hand, we find that, for anti-aligned runs, adding higher order terms always improves the match, keeping all terms yields the best result, and all choices of truncation give errors which are monotonically increasing with mass ratio. Overall, anti-aligned cases have larger values of Φ_Δ when compared to cases with same mass ratios. This result is consistent with findings by Nitz et al. [133] for comparisons between TaylorT4 and EOBNRv1 approximants.

4.4.5 Further numerical considerations

Numerical truncation error

Still to be addressed is the effect of the resolution of NR simulations in the present work. The simulation q1_twospins is available at four different resolutions labeled N1, N2, N3 and N4. We match each of these four numerical resolutions with the Taylor T4 approximant, and plot the resulting phase differences Φ_Δ in Fig. 4.19 as the data with symbols and error bars (recall that the error bars are obtained from the 12 different matching regions we use, cf. Fig. 4.3). All four numerical resolutions yield essentially the same Φ_Δ. We furthermore match the three lowest numerical resolutions against the highest numerical resolution N4 and compute the phase difference Φ_Δ. The top panel of Figure 4.19 shows Φ_Δ computed with these 4 different numerical resolutions. All the curves lie on top of each other and the differences between them are well within the uncertainties due to the matching procedure. The bottom panel shows the differences in Φ_Δ between the highest resolution and all others. Throughout most of the inspiral, the difference is $\sim 10\%$. Similar behavior is observed in other cases where multiple resolutions of NR simulations are available. We therefore conclude that the effects of varying numerical resolution do not impact our analysis.

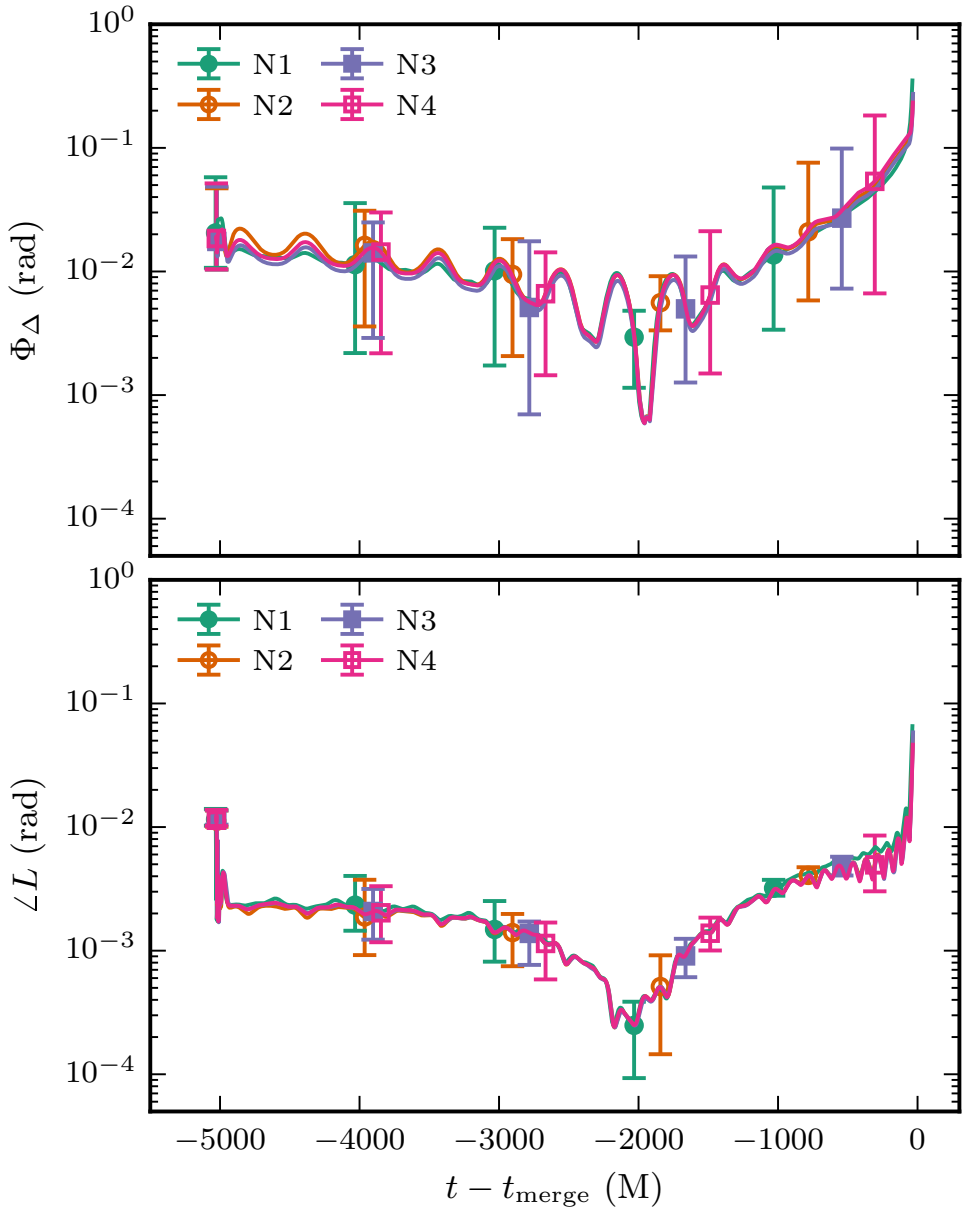

Figure 4.19: Convergence test with the numerical resolution of the NR simulation q1_twospins. **Top panel**: Φ_Δ with comparisons done at different resolutions. All the curves lie within uncertainties due to the matching procedure, indicating that numerical truncation error does is not important in this comparison. The difference between each curve and the highest resolution are of order 15% and are within the matching uncertainties. **Bottom panel**: $\angle L$ with comparisons done at all the resolutions. The curves lie within the matching uncertainties.

Numerical gauge change

The simulation SXS:BBH:0058 in the SXS catalog uses identical BBH parameters than q5_0.5x, but suffers from two deficiencies, exploration of which will provide some additional insights. First, the switch from generalized harmonic gauge with *fixed* gauge-source functions [33] to *dynamical* gauge-source functions [109, 175] happens near the middle of the inspiral, rather than close to merger as for the other simulations considered. This will give us an opportunity to investigate the impact of such a gauge change, the topic of this subsection. Second, this simulation also used too low resolution in the computation of the black hole spin during the inspiral, which we will discuss in the next subsection. We emphasize that the comparisons presented above did not utilize SXS:BBH:0058, but rather a re-run with improved technology. We use SXS:BBH:0058 in this section to explore the effects of its deficiencies.

While the difference between PN and NR gauges does not strongly impact the nature of the matching results, a gauge change performed during some of the runs *does* result in unphysical behavior of physical quantities such as the orbital frequency. Figure 4.20 demonstrates this for case q5_s0.5x. The old run SXS:BBH:0058 with the gauge change exhibits a bump in the orbital frequency (top panel), which is not present in the re-run (solid curve). When matching both the old and the new run to PN, and computing the phase difference Φ_Δ, the old run exhibits a nearly discontinuous change in Φ_Δ (bottom panel, dashed curves) while no such discontinuity is apparent in the re-run.

Problems in quasi-local quantities

Computation of the quasi-local spin involves the solution of an eigenvalue problem on the apparent horizon followed by an integration over the apparent horizon, cf. [118, 139, 58]. In the simulations q1.0_0.5x, q1.5_0.5x and q3.0_0.5x and in SXS:BBH:0058 (corresponding to q5_0.5x), too low numerical resolution was used for these two steps. While the evolution itself is acceptable, the extracted spin shows unphysical features. Most importantly, the reported spin magnitude is not constant, but varies by several per cent. Figure 4.21 shows as example χ_1 from SXS:BBH:0058. For $t - t_{\rm merge} \leq 3200M$ oscillations are clearly visible. These oscillations vanish at $t - t_{\rm merge} \approx 3200M$, coincident with a switch to damped harmonic gauge (cf. Sec. 4.4.5). Similar oscillations in q3_0.5 disappear when the resolution of the spin computation is manually increased about 1/3 through the inspiral, without changing the evolution gauge. Our new re-run q5_0.5x (using damped harmonic gauge throughout), also reports a clean χ_1, cf. Fig. 4.21. Thus, we conclude that the unphysical variations in the spin magnitude are only present if *both*

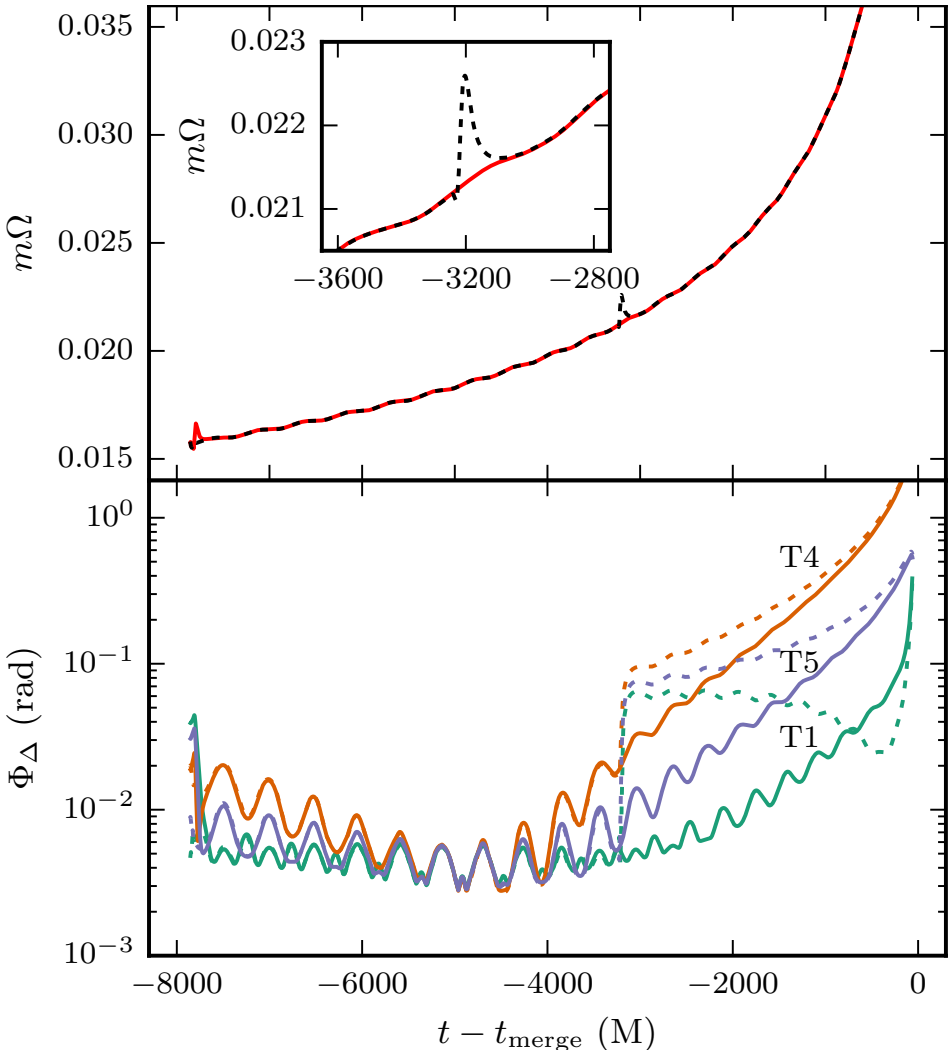

Figure 4.20: Gauge change during numerical simulation q5_s0.5x. The solid curves represent the recent re-run of q5_0.5x that is analyzed in the rest of this chapter. The dashed curves represent an earlier run SXS:BBH:0058 which changes the gauge at $t - t_{\rm merge} \approx -3200M$. **Top**: behavior of the orbital frequency $m\Omega$ in evolution with (dashed curve) and without gauge change (solid curve). **Bottom:** Φ_Δ for all Taylor approximants. To avoid matching during the gauge change, the matching was done with $m\Omega_c = 0.017$.

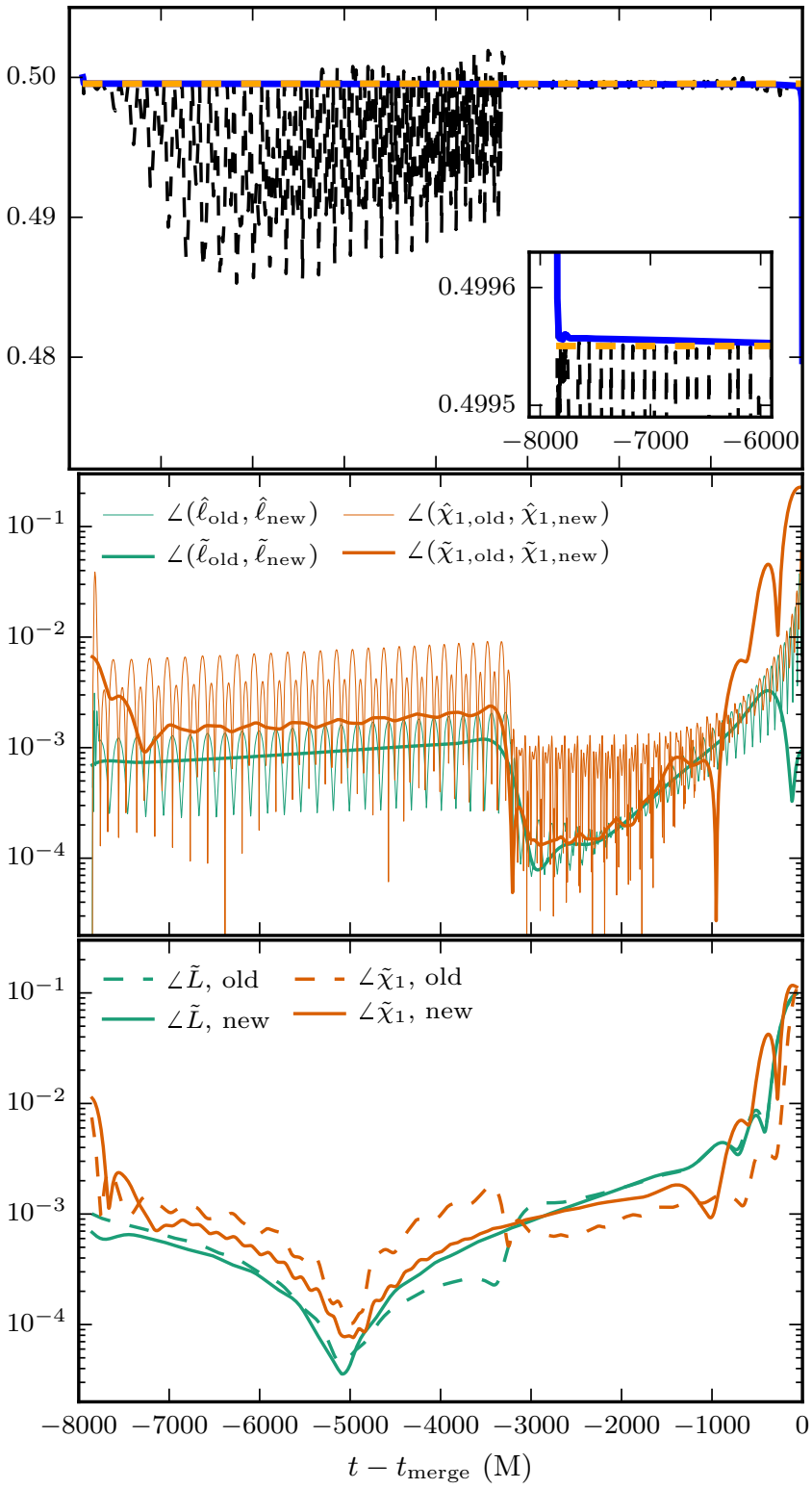

Figure 4.21: **Top**: The magnitude of the spin as a function of time in the original run (black) and the new run (blue) as well as the value computed with the procedure described in the text (orange). **Middle panel**: angles between the spins and normals to the orbital plane (thin curves) and their averaged values (bold curves) for the original run and the re-run. **Lower panel**: $\angle\tilde{\chi}_1$ and $\angle\tilde{\ell}$ for both the old run and the re-run (the data of this panel are averaged over 12 matching intervals, cf. Fig. 4.3). To avoid matching during the gauge change, the matching was done with $m\Omega_c = 0.017$.

the resolution of the spin computation is low, and the old gauge conditions of constant H_a are employed.

The NR spin magnitude is used to initialize the PN spin magnitude, cf. Eq. (4.14). Therefore, an error in the calculation of the NR spin would compromise our comparison with PN. For the affected runs, we correct the spin reported by the quasi-local spin computation by first finding all maxima of the spin-magnitude χ between $500M$ and $2000M$ after the start of the numerical simulation. We then take the average value of χ at those maxima as the corrected spin-magnitude of the NR simulation. Figure 4.21 shows the case q5_0.5x as well as the rerun described in Sec. 4.4.5. It is evident that this procedure produces a spin value which is very close to the spin in the rerun where the problematic behavior is no longer present. Thus, we adopt it for the three cases where an oscillation in the spin magnitude is present.

The nutation features shown in Fig. 4.9 are qualitatively similar for all our simulations, independent of resolution of the spin computation and evolution gauge. When the spin is inaccurately measured, the nutation trajectory picks up extra modulations, which are small on the scale of Fig. 4.9 and do not alter the qualitative behavior.

The lower two panels of Fig. 4.21 quantify the impact of inaccurate spin measurement on the precession-dynamics comparisons performed in this chapter: The middle panel shows the differences between the spin directions in the original 0058 run and our re-run q5_0.5x. The spin directions differ by as much as 0.01 radians. However, as the lower panel shows, this difference can mostly be absorbed by the PN matching, so that $\angle\chi_1$ and $\angle L$ are of similar magnitude of about 10^{-3} radians.

4.5 Discussion

We have presented an algorithm for matching PN precession dynamics to NR simulations which uses constrained minimization. Using this algorithm, we perform a systematic comparison between PN and NR for precessing binary black hole systems. The focus of the comparison is black hole dynamics only, and we defer discussion of waveforms to future work. By employing our matching procedure, we find excellent agreement between PN and NR for the precession and nutation of the orbital plane. The normals to the orbital plane generally lie within 10^{-2} radians, cf. Fig. 4.11. Moreover, nutation features on the orbital time-scale also agree well between NR and PN, cf. Fig. 4.10.

For the black hole spin direction, the results are less uniform. The NR spin direction $\hat{\chi}_1^{\rm NR}$ shows nutation features that are qualitatively different than the PN nutation features, cf. Fig. 4.9. The disagreement in nutation dominates the agreement of $\hat{\chi}_1^{\rm NR}$ with

$\hat{\chi}_1^{\rm PN}$; averaging away the nutation features substantially improves agreement, cf. Fig. 4.6. The orbit-averaged spin directions agree with PN to the same extent that the $\hat{\ell}$ direction does (with and without orbit averaging), cf. Fig. 4.11.

Turning to the convergence properties of PN, we have performed PN-NR comparisons at different PN order of the precession equations. For both orbital angular momentum $\hat{\ell}$ and the spin direction $\hat{\chi}_1$, we observe that the convergence of the PN results toward NR is fast and nearly universally monotonic, cf. Fig. 4.16. At the highest PN orders, the spin results might be dominated by the difference in nutation features between PN and NR.

The good agreement between PN and NR precession dynamics are promising news for gravitational wave modeling. Precessing waveform models often rely on the post-Newtonian precession equations, e.g. [14, 86]. Our results indicate that the PN precession equations are well suited to model the precessing frame, thus reducing the problem of modeling precessing waveforms to the modeling of orbital phasing only.

The accuracy of the PN orbital phase evolution, unfortunately, does not improve for precessing systems. Rather, orbital phasing errors are comparable between non-precessing and precessing configurations, cf. Fig. 4.17. Moreover, depending on mass-ratio and spins, some Taylor approximants match the NR data particularly well, whereas others give substantially larger phase differences, cf. Fig. 4.14. This confirms previous work [60, 82, 82, 159, 122, 123] that the PN truncation error of the phase evolution is important for waveform modeling.

We have also examined the effects of including partially known spin contributions to the evolution of the orbital frequency for the Taylor T4 approximant. For aligned runs, including such incomplete information usually improves the match, but the results are still sensitive to the mass ratio of the binary (top panel of Fig 4.18). For anti-aligned runs, it appears that incomplete information always improves the agreement of the phasing between PN and NR (bottom panel of Fig 4.18).

In this work we compare gauge-dependent quantities, and thus must examine the impact of gauge choices on the conclusions listed above. We consider it likely that the different nutation features of $\hat{\chi}_1$ are determined by different gauge choices. We have also seen that different NR gauges lead to measurably different evolutions of $\hat{\chi}$, $\hat{\ell}$, and the phasing, cf. Fig. 4.20 and 4.21. We expect, however, that our conclusions are fairly robust to the gauge ambiguities for two reasons. First, in the matched PN-NR comparison, the impact of gauge differences is quite small, cf. lowest panel of Fig. 4.21. Second, the near universal, monotonic, and quick convergence of the precession dynamics with precession PN order visible in Fig. 4.16 would not be realized if the comparison were dominated by

gauge effects. Instead, we would expect PN to converge to a solution *different* from the NR data.

Acknowledgments

We thank Kipp Cannon, Francois Foucart, Prayush Kumar, Abdul Mroué and Aaron Zimmerman for useful discussions. Calculations were performed with the `SpEC`-code [1]. We gratefully acknowledge support from NSERC of Canada, from the Canada Research Chairs Program, and from the Canadian Institute for Advanced Research. We further gratefully acknowledge support from the Sherman Fairchild Foundation; from NSF Grants PHY-1306125 and AST-1333129 at Cornell; and from NSF Grants No. PHY-1440083 and AST-1333520 at Caltech. Calculations were performed at the GPC supercomputer at the SciNet HPC Consortium [110]; SciNet is funded by: the Canada Foundation for Innovation (CFI) under the auspices of Compute Canada; the Government of Ontario; Ontario Research Fund (ORF) – Research Excellence; and the University of Toronto. Further computations were performed on the Zwicky cluster at Caltech, which is supported by the Sherman Fairchild Foundation and by NSF award PHY-0960291; and on the NSF XSEDE network under grant TG-PHY990007N.

4.6 Appendix

4.6.1 Post-Newtonian dynamics

We consider compact object binary with masses $m_{1,2}$ and carrying angular momentum $\vec{S}_{1,2}$. The post-Newtonian expressions are most conveniently written using the following symbols:

$$m = m_1 + m_2, \tag{4.21}$$

$$\nu = \frac{m_1 m_2}{m^2}, \tag{4.22}$$

$$\delta = \frac{m_1 - m_2}{m}, \tag{4.23}$$

$$\vec{S} = \vec{S}_1 + \vec{S}_2, \tag{4.24}$$

$$s_l = \frac{\vec{S}\cdot\hat{\ell}}{m^2}, \tag{4.25}$$

$$s_n = \frac{\vec{S}\cdot\hat{n}}{m^2}, \tag{4.26}$$

$$\vec{\Sigma} = \frac{m}{m_2}\vec{S}_2 - \frac{m}{m_1}\vec{S}_1, \tag{4.27}$$

$$\sigma_l = \frac{\vec{\Sigma}\cdot\hat{\ell}}{m^2}, \tag{4.28}$$

$$\sigma_n = \frac{\vec{\Sigma}\cdot\hat{n}}{m^2}, \tag{4.29}$$

$$\vec{\chi}_s = \frac{1}{2}\left(\vec{\chi}_1 + \vec{\chi}_2\right), \tag{4.30}$$

$$\vec{\chi}_a = \frac{1}{2}\left(\vec{\chi}_1 - \vec{\chi}_2\right), \tag{4.31}$$

$$\vec{S}_0 = \frac{m}{m_1}\vec{S}_1 + \frac{m}{m_2}\vec{S}_2, \tag{4.32}$$

$$\vec{s}_0 = \frac{\vec{S}_0}{m^2}. \tag{4.33}$$

Energy and Flux

The energy and flux are written as power series in the expansion parameter $x \equiv (m\Omega)^{2/3}$:

$$E(x) = -\tfrac{1}{2}\,m\nu x\,\left(1 + \textstyle\sum_{k=2} a_k x^{k/2}\right), \tag{4.34}$$

$$\mathcal{F}(x) = \tfrac{32}{5}\nu^2 x^5\left(1 + \textstyle\sum_{k=2} b_k x^{k/2}\right). \tag{4.35}$$

For the energy, coefficients are given explicitly by:

$$a_2 = -\frac{3}{4} - \frac{\nu}{12}, \tag{4.36}$$

$$a_3 = 2\delta\sigma_l + \frac{14}{3}s_l, \tag{4.37}$$

$$\begin{aligned} a_4 = {} & -\frac{27}{8} + \frac{19}{8}\nu - \frac{1}{24}\nu^2 + \nu(\vec{\chi}_s^2 - \vec{\chi}_a^2 - 3[(\vec{\chi}_s\cdot\hat{\ell})^2 - (\vec{\chi}_a\cdot\hat{\ell})^2] \\ & +(\frac{1}{2} - \nu)\{\vec{\chi}_s^2 + \vec{\chi}_a^2 - 3[(\vec{\chi}_s\cdot\hat{\ell})^2 + (\vec{\chi}_a\cdot\hat{\ell})^2]\} \\ & +\delta\{\vec{\chi}_s\cdot\vec{\chi}_a - 3[(\vec{\chi}_s\cdot\hat{\ell})(\vec{\chi}_a\cdot\hat{\ell})]\}, \end{aligned} \tag{4.38}$$

$$a_5 = 11 s_l + 3\delta\sigma_l + \nu\left[-\frac{61}{9}s_l - \frac{10}{3}\delta\sigma_l\right], \tag{4.39}$$

$$a_6 = -\frac{675}{64} + \left[\frac{34445}{576} - \frac{205}{96}\pi^2\right]\nu - \frac{155}{96}\nu^2 - \frac{35}{5184}\nu^3, \tag{4.40}$$

$$a_7 = \left(\frac{135}{4} - \frac{367}{4}\nu + \frac{29}{12}\nu^2\right)s_l + \delta\left(\frac{27}{4} - 39\nu + \frac{5}{4}\nu^2\right)\sigma_l. \tag{4.41}$$

Meanwhile for the flux $\mathcal{F}$:

$$b_2 = -\frac{1247}{336} - \frac{35}{12}\nu, \tag{4.42}$$

$$
\begin{aligned}
b_3 &= 4\pi - 4s_l - \frac{5}{4}\delta\sigma_l, && (4.43)\\
b_4 &= -\frac{44711}{9072} + \frac{9271}{504}\nu + \frac{65}{18}\nu^2 + \left(\frac{287}{96} + \frac{\nu}{24}\right)(\vec{\chi}_s\cdot\hat{\ell})^2 \\
&\quad - \left(\frac{89}{96} + \frac{7\nu}{24}\right)\vec{\chi}_s^2 + \left(\frac{287}{96} - 12\nu\right)(\vec{\chi}_a\cdot\hat{\ell})^2 + \left(-\frac{89}{96} + 4\nu\right)\vec{\chi}_a^2 \\
&\quad + \frac{287}{48}\delta(\vec{\chi}_s\cdot\hat{\ell})(\vec{\chi}_a\cdot\hat{\ell}) - \frac{89}{48}\delta(\vec{\chi}_s\cdot\vec{\chi}_a), && (4.44)\\
b_5 &= -\frac{8191}{672}\pi - \frac{9}{2}s_l - \frac{13}{16}\delta\sigma_l + \nu\left[-\frac{583}{24}\pi + \frac{272}{9}s_l + \frac{43}{4}\delta\sigma_l\right], && (4.45)\\
b_6 &= \frac{6643739519}{69854400} + \frac{16}{3}\pi^2 - \frac{1712}{105}\gamma_E - \frac{856}{105}\log(16x) + \left(\frac{-134543}{7776} + \frac{41}{48}\pi^2\right)\nu \\
&\quad - \frac{94403}{3024}\nu^2 - \frac{775}{324}\nu^3 - 16\pi s_l - \frac{31\pi}{6}\delta\sigma_l, && (4.46)\\
b_7 &= \left(\frac{476645}{6804} + \frac{6172}{189}\nu - \frac{2810}{27}\nu^2\right)s_l + \left(\frac{9535}{336} + \frac{1849}{126}\nu - \frac{1501}{36}\nu^2\right)\delta\sigma_l \\
&\quad + \left(-\frac{16285}{504}\frac{214745}{1728}\nu + \frac{193385}{3024}\nu^2\right)\pi, && (4.47)\\
b_8 &= \left(-\frac{3485\pi}{96} + \frac{13879\pi}{72}\nu\right)s_l + \left(-\frac{7163\pi}{672} + \frac{130583\pi}{2016}\nu\right)\delta\sigma_l, && (4.48)
\end{aligned}
$$

where γ_E denotes Euler's constant.

Precession dynamics

The evolution of the orbital plane is governed by the frequency ϖ in Eq. (4.1a), which is defined in terms of two auxiliary quantities, $\gamma = m/r$ and $a_l = \vec{a}\cdot\hat{\ell}$:

$$
\begin{aligned}
\gamma &= x\Bigg\{1 + \frac{3-\nu}{3}x + \frac{3\sigma_l + 5s_l}{3}x^{3/2} + \frac{12 - 65\nu}{12}x^2 + \left(\frac{30+8\nu}{9}s_l + 2\sigma_l\delta\right)x^{5/2} \\
&\quad + \left[1 + \nu\left(-\frac{2203}{2520} - \frac{41\pi^2}{192}\right) + \frac{229\nu^2}{36} + \frac{\nu^3}{81}\right]x^3 \\
&\quad + \left(\frac{60 - 127\nu - 72\nu^2}{12}s_l + \frac{16 - 61\nu - 16}{6}\sigma_l\delta\right)x^{7/2} \\
&\quad + x^2\left(\vec{s}_0^2 - 3(\vec{s}_0\cdot\vec{\ell})^2\right)\Bigg\}, && (4.49)\\
a_l &= \frac{x^{\frac{7}{2}}}{m}\left\{7s_n + 3\sigma_n\delta + x\left[s_n\left(-\frac{29\nu}{3} - 10\right) + \sigma_n\delta\left(-\frac{9\nu}{2} - 6\right)\right]\right. \\
&\quad \left. + x^2\left[s_n\left(\frac{52\nu^2}{9} + \frac{59\nu}{4} + \frac{3}{2}\right) + \sigma_n\delta\left(\frac{17\nu^2}{6} + \frac{73\nu}{8} + \frac{3}{2}\right)\right]\right\}
\end{aligned}
$$

$$-\frac{3x^4}{m}(\vec{s}_0\cdot\hat{\ell})(\vec{s}_0\cdot\hat{n}). \tag{4.50}$$

Note that we have dropped the pure gauge term $-\frac{22}{3}\ln(r/r'_0)$ from γ. We now have

$$\varpi = \frac{a_l\,\gamma}{x^{3/2}}. \tag{4.51}$$

The spins obey Eqs. (4.2) with

$$\begin{aligned}\vec{\Omega}_1 &= \hat{\ell}\frac{x^{\frac{5}{2}}}{m}\left\{\frac{-3\delta+2\nu+3}{4}+x\left[\frac{10\nu-9}{16}\delta-\frac{\nu^2}{24}+\frac{5\nu}{4}+\frac{9}{16}\right]\right.\\ &\quad\left.+x^2\left[\frac{-5\nu^2+156\nu-27}{32}\delta-\frac{\nu^3}{48}-\frac{105\nu^2}{32}+\frac{3\nu}{16}+\frac{27}{32}\right]\right\}\\ &\quad+\frac{x^3}{m^3}\left[\frac{3m_1^2}{q}(\vec{\chi}_1\cdot\hat{n})\hat{n}-m_2^2\vec{\chi}_2+3m_2^2(\vec{\chi}_2\cdot\hat{n})\hat{n}\right].\end{aligned} \tag{4.52}$$

The expression for $\vec{\Omega}_2$ is obtained by $\vec{\chi}_1\leftrightarrow\vec{\chi}_2$, $m_1\leftrightarrow m_2$, $\delta\leftrightarrow-\delta$ and $q\leftrightarrow 1/q$.

We re-expand the right-hand-side of Eq. (4.51), and truncate the expansion for ϖ and $\vec{\Omega}_{1,2}$ at the same power of x *beyond the leading order*. We refer to the order of the last retained terms as the *precession PN order*. For the majority of comparisons presented in this chapter, we truncate at 3.5PN; truncation at lower PN order is only used in Sec. 4.4.3. Note that spin-squared interactions imply the lack of circular orbits for generic orientations of the spins. We neglect these complications in the present work.

4.6.2 Useful quaternion formulas

We refer the reader to other sources [68, **?**] for general introductions to quaternions. Here, we simply give a few formulas that are particularly important in this chapter. First, we introduce some basic notation to be used for the four components of a general quaternion Q:

$$Q = (q_0, q_1, q_2, q_3) = q_0 + \vec{q}\,. \tag{4.53}$$

In this notation, the quaternion conjugate is just $\bar{Q} = q_0 - \vec{q}$, and we note that the product of quaternions is given by

$$P\,Q = p_0\,q_0 - \vec{p}\cdot\vec{q} + p_0\vec{q} + q_0\vec{p} + \vec{p}\times\vec{q}\,. \tag{4.54}$$

The norm of a quaternion Q is defined by $|Q|^2 = Q\,\bar{Q}$. The inverse of a quaternion is $Q^{-1} = \bar{Q}/|Q|^2$, which means that the inverse of a unit quaternion is simply its conjugate. The components of a unit quaternion $R = r_0 + \vec{r}$ satisfy $R\,\bar{R} = r_0^2 + \vec{r}\cdot\vec{r} = 1$. Unit quaternions are usually referred to as "rotors". Any rotation can be expressed as a rotor, where the rotor acts on a vector $\vec{v}$ according to the transformation law

$$\vec{v}\,' = R\,\vec{v}\,\bar{R}\ . \tag{4.55}$$

The form of this expression ensures that $\vec{v}\,'$ is a pure vector; it has zero scalar part. To see this, we note that a quaternion has zero scalar part if and only if its conjugate equals its negative, which is true of the right-hand side above. We can use this fact, along with $\vec{p}\cdot\vec{q} = -\frac{1}{2}(\vec{p}\,\vec{q} + \vec{q}\,\vec{p})$ and the unit-norm property $R\,\bar{R} = 1$, to see that the right-hand side above is indeed an isometry. Finally, simple arguments using the cross product can show that such a transformation preserves orientation, and since the origin is fixed, it is therefore a simple rotation for any rotor R.

Exponential, logarithms, and square roots

The quaternions are closely analogous to complex numbers, except that quaternions do not commute in general. One striking example of this analogy is Euler's formula, which generalizes quite directly. If we define the exponential of a quaternion by the usual power series, we get for a unit vector $\hat{u}$

$$\exp[\theta\,\hat{u}] = \cos\theta + \hat{u}\sin\theta\ , \tag{4.56}$$

which is precisely Euler's formula with i replaced by $\hat{u}$. Every rotor $R = r_0 + \vec{r}$ can be expressed in this form, so it is easy to see that the logarithm of any rotor has zero scalar part and is given by

$$\vec{\mathfrak{r}} \coloneqq \log R = \frac{\vec{r}}{|\vec{r}|}\,\arctan\frac{|\vec{r}|}{r_0}\ . \tag{4.57}$$

It is useful to note that the logarithm of a rotor is parallel to the vector part of the rotor. Finding the magnitude of $\vec{r}$, of course, is just the usual square root of the sum of the squares of its components. And the arctan function is applied to real values, so we can use standard implementations of the `atan2` function to evaluate it. So we see that both the exponential and logarithm of quaternions are extremely simple and numerically robust to calculate.

These formulas can also be used to define general powers of quaternions. For the purposes of this chapter, however, we only need one particular power of a quaternion:

the square root. More specifically, given two unit vectors $\hat{u}$ and $\hat{w}$, we need the rotor that takes $\hat{w}$ to $\hat{u}$ by the smallest rotation possible, which is a rotation in their common plane. This rotor is given [**?**] by

$$R_{\hat{w}\to\hat{u}} = \sqrt{-\hat{u}\,\hat{w}} = \pm\frac{1-\hat{u}\,\hat{w}}{\sqrt{2[1-(\hat{u}\,\hat{w})_0]}}\ . \tag{4.58}$$

In this expression, $\hat{u}\,\hat{w}$ represents the result of quaternion multiplication of the quaternions $\hat{u}$ and $\hat{w}$. $(\hat{u}\,\hat{w})_0$ represents the scalar part of this product, so that the square root in the denominator is acting on a real number. The sign ambiguity is generally irrelevant because of the double-sided transformation law for vectors, Eq. (4.55). However, in certain special applications such as rotor interpolation, the sign must be chosen carefully to be continuous [**?**].

Deriving the frame rotor from $\hat{\ell}$ and $\hat{n}$

For both numerical relativity simulations and Post-Newtonian evolutions we have data about the positions and velocities of the black holes, that can be used to derive the frame rotor $R_{\rm f}$, cf. Fig. 4.2. Given positions of the black holes as functions of time, it's a simple matter to calculate their unit separation vector $\hat{n}$, and then to calculate $\hat{\ell}$ using

$$\Omega\,\hat{\ell} = \hat{n}\times\dot{\hat{n}}\ . \tag{4.59}$$

Going from $\hat{\ell}$ and $\hat{n}$ to the frame rotor $R_{\rm f}$, the idea is to first rotate $\hat{z}$ onto $\hat{\ell}$. This will also rotate $\hat{x}$ onto some $\hat{x}'$. We then need to rotate $\hat{x}'$ onto $\hat{n}$, while leaving $\hat{\ell}$ in place. Of course, the $\hat{n}$-$\hat{x}'$ is orthogonal to $\hat{\ell}$, so we just perform a rotation in that plane. This is easily accomplished by the following formula:

$$R_i = \sqrt{-\hat{\ell}\,\hat{z}}\ , \tag{4.60a}$$

$$R_{\rm f} = \sqrt{-\hat{n}\,(R_i\,\hat{x}\,\bar{R}_i)}\ R_i\ . \tag{4.60b}$$

Again, the square roots are to be evaluated using Eq. (4.58).

Comparing frame rotors

Reference [**?**] introduced a simple, geometrically invariant measure R_Δ that encodes the difference between two precessing systems as a function of time, easily reduced to a single real number Φ_Δ expressing the magnitude of that difference. These quantities were

mentioned in Sec. 4.3.3 without much motivation, here we briefly review that motivation.

In general, we assume that there are two (analytical or numerical) descriptions of the same physical system, and that we have two corresponding frames R_{fA} and R_{fB}. To understand the difference between the frames, we can simply take the rotation that takes one frame onto the other. In this case, the rotor taking frame A onto frame B is

$$R_\Delta \coloneqq R_{\mathrm{fB}}\, \bar{R}_{\mathrm{fA}}. \tag{4.61}$$

Rotors compose by left multiplication, so it is not hard to see that this does indeed take R_{fA} onto R_{fB} because the inverse of R_{fA} is just its conjugate, so $R_\Delta\, R_{\mathrm{fA}} = R_{\mathrm{fB}}$.

A particularly nice feature of R_Δ is that it is completely independent of the inertial basis frame $(\hat{x}, \hat{y}, \hat{z})$ with respect to which we define the moving frames. That is, if we have another basis frame $(\hat{x}', \hat{y}', \hat{z}')$, there is some R_δ such that $\hat{x}' = R_\delta\, \hat{x}\, \bar{R}_\delta$, etc. The frame rotors would transform as $R_{\mathrm{fA}} \mapsto R'_{\mathrm{fA}} = R_{\mathrm{fA}}\, \bar{R}_\delta$, in which case we obtain

$$R'_{\mathrm{fB}}\, \bar{R}'_{\mathrm{fA}} = R_{\mathrm{fB}}\, \bar{R}_\delta\, R_\delta\, \bar{R}_{\mathrm{fA}} = R_{\mathrm{fB}}\, \bar{R}_{\mathrm{fA}}. \tag{4.62}$$

That is, R_Δ is invariant.

Now, we seek a relevant measure of the magnitude of the rotation R_Δ. We know that it may be written as a rotation through an angle ϕ about an axis $\hat{v}$. Clearly, ϕ is the measure we seek. The rotor corresponding to such a rotation is given by $R = \exp[\phi\, \hat{v}/2]$. Thus, to find the angle, we just use the logarithm: $\phi = 2|\log R|$, where the norm is the usual vector norm. Again, the formula for the logarithm of a rotor is a simple combination of standard trigonometric functions applied to real numbers, as shown above. Using this interpretation with our difference rotor, we see that the appropriate definition is

$$\Phi_\Delta \coloneqq 2\left|\log\left[R_{\mathrm{fB}}\, \bar{R}_{\mathrm{fA}}\right]\right| \ . \tag{4.63}$$

There is information contained in the direction of the logarithm. For example, the component along $\hat{\ell}$ is related to the difference in orbital phase for non-precessing systems, while the component orthogonal to $\hat{\ell}$ is related to the direction and magnitude of the difference in $\hat{\ell}$ itself. For the sake of simplicity, however, we focus on the magnitude of the logarithm, as given above.

Inadequacy of $\Phi_A - \Phi_B$ for comparisons of precessing systems

In this Appendix we show that it is impossible—when analyzing precessing systems—to compare two rotations R_A and R_B in a non-degenerate and geometrically invariant way

by defining some phases Φ_A and Φ_B for them separately, and then comparing them as $\Phi_A - \Phi_B$. This conclusion motivates our use of the Φ_Δ quantity defined above, which is both non-degenerate and geometrically invariant. Here, "non-degenerate" means that the phase difference is zero if and only if R_A and R_B represent the same rotation, and "geometrically invariant" means that the result is not affected by an overall rotation of the basis used to define R_A and R_B.

The basic idea will not come as a surprise. Essentially, the conclusion stems from the simple fact that—even locally—the three-dimensional rotation group does not look like a (one-dimensional) phase. Any map from the former to the latter cannot be one-to-one, even in an infinitesimal neighborhood of a point. In practical terms, this means that any prescription for $\Phi_A - \Phi_B$ can be "fooled", and there will exist a two-dimensional space of distinct rotations for which the corresponding values of $\Phi_A - \Phi_B$ will be identical.

The basic result does not depend in any way on the topology of the groups involved; it is a purely algebraic argument. As long as R_A and R_B could be non-commuting, the conclusion will still hold. The phase function Φ need not be continuous; indeed, even that very most basic topological notion—the open set—is superfluous. The inadequacy of $\Phi_A - \Phi_B$ is also independent of time; it holds at each instant of time, and for any extended period of time. It does *not* rule out the possibility of using multiple measures of the difference between the rotations simultaneously, one of which may take the form $\Phi_A - \Phi_B$ (though constructing a geometrically invariant measure in this way is not trivial). Rather, it is simply the statement that $\Phi_A - \Phi_B$ alone would be degenerate, and is therefore inadequate for measuring the difference between general rotations. Moreover, this inadequacy will be a problem for *every* system with nonzero precession, no matter how small that precession may be. This conclusion has been the source of some contention, but is an important point in guiding the analysis of precessing systems, so we take this opportunity to present a careful explication and proof.

We begin by defining a function Φ such that $\Phi(R_A) = \Phi_A$ and $\Phi(R_B) = \Phi_B$. The domain of this function is a rotation group, which could be the one-dimensional group U(1) for non-precessing systems, but must be the full three-dimensional group[8] SU(2) for general precessing systems. The range of Φ is the usual range of phases, the additive group of real numbers modulo 2π. It will be useful to note that this is isomorphic to U(1). Finally, non-degeneracy is the condition that $\Phi_A - \Phi_B = 0$ [or equivalently $\Phi(R_A) = \Phi(R_B)$] if and only if $R_A = \pm R_B$.

[8]Even though it is a double cover of the physical rotation group SO(3), we use SU(2) here for consistency of notation, because it is the group of unit quaternions. The proof would actually be slightly simpler for SO(3); we would have $\Phi(R_A) = \Phi(R_B)$, if and only if $R_A = R_B$, and $\ker \Phi' = \{1\}$.

The condition of geometric invariance can be written as a condition on Φ itself. If, for example, we measure everything with respect to some basis $(\hat{x}, \hat{y}, \hat{z})$, and then measure again with respect to some other basis $(\hat{x}', \hat{y}', \hat{z}')$, we should get the same answer. Now, there is some rotor R_δ that takes the first basis into the second. If R_A is defined with respect to the first basis, then the equivalent quantity will be $R_A\, R_\delta$ with respect to the second. Geometric invariance is then the statement

$$\Phi(R_A\, R_\delta) - \Phi(R_B\, R_\delta) = \Phi(R_A) - \Phi(R_B), \tag{4.64}$$

for *any* choice of R_δ in SU(2). We will show that there is no such Φ because the rotation group SU(2) is not isomorphic to U(1).

Since Eq. (4.64) is true for *any* rotor R_δ, we can choose $R_\delta = R_B^{-1}$, and find that

$$\Phi(R_A\, R_B^{-1}) - \Phi(1) = \Phi(R_A) - \Phi(R_B). \tag{4.65}$$

Now, we define another function $\Phi'(R) = \Phi(R) - \Phi(1)$. The last equation becomes

$$\Phi'(R_A\, R_B^{-1}) = \Phi'(R_A) - \Phi'(R_B). \tag{4.66}$$

In exactly the same way, we can see that

$$\Phi'(R_B\, R_A^{-1}) = \Phi'(R_B) - \Phi'(R_A) = -\Phi'(R_A\, R_B^{-1}). \tag{4.67}$$

This must be true for *all* values of R_A and R_B, so we have shown that

$$\Phi'(R^{-1}) = -\Phi'(R), \tag{4.68}$$

for arbitrary R. Therefore, we can also see from Eq. (4.66) that

$$\Phi'(R_1\, R_2) = \Phi'(R_1) + \Phi'(R_2), \tag{4.69}$$

for arbitrary R_1 and R_2. This is precisely the statement that Φ' is a group homomorphism [from SU(2) to the additive group of real numbers modulo 2π].[9]

However, now we can impose the condition that $\Phi_A - \Phi_B = 0$ if and only if $R_A = \pm R_B$. Using the properties of homomorphism, it is clear that this is equivalent to the statement that the set of all elements that map to 0 under Φ' (the kernel) is just $\ker \Phi' = \{-1, 1\}$.

[9]Note that this means only that Φ' is a group homomorphism, rather than a *topological* group homomorphism; Φ' (equivalently Φ) is not required to be continuous.

Then, the First Group Isomorphism Theorem [69] says that the image of Φ' is isomorphic to SU(2) modulo this kernel, which of course is just SO(3). But the image of Φ' is (possibly a subgroup of) the group U(1), which is obviously not isomorphic to SO(3). Therefore, it is impossible to construct a function Φ fulfilling our requirements for precessing systems.

This conclusion holds whenever R_A and R_B come from a non-commutative group. Topological structures associated with SU(2), SO(3), and U(1) are completely unused in this proof. However, if we now consider the standard topology of SO(3), we know that it is possible to find non-commuting elements inside any neighborhood of any point—and in particular, inside any neighborhood of the identity. But precessing systems will necessarily explore some such neighborhood, which means that their orientations may be described by non-commuting rotors R_A and R_B. Thus, $\Phi_A - \Phi_B$ would be an inadequate measure of rotations for *any* system with *any* nonzero amount of precession.

It is, however, interesting to note that if we could restrict our rotations (including the allowed coordinate rotations R_δ) to some subgroup of SU(2) isomorphic to U(1), there would be no contradiction. This is why it *is* possible to construct a useful measure of the form $\Phi_A - \Phi_B$ for *non*-precessing systems—because the rotations can be restricted to rotations about the orbital axis, which results in precisely the group U(1). On the other hand, for precessing systems, the measure Φ_Δ described in Secs. 4.3.3 and 4.6.2 is able to satisfy both key features of a useful measure (non-degeneracy and geometric invariance) because it simply does not attempt to define a homomorphism from the rotation group; rather, it defines a (non-homomorphic, but non-degenerate and rotationally invariant) function from *two copies of* the rotation group onto the phase group, $\mathrm{SU}(2) \times \mathrm{SU}(2) \to \mathrm{U}(1)$.

Chapter 5

Modelling transitional precession

5.1 Chapter Overview

In this chapter, we introduce the notion of transitional precession in binary black hole systems. During transitional precession, the total angular momentum of the binary changes direction drastically, causing the orbital and angular momentum vectors to also undergo a sudden change. This makes the dynamics of the binary much richer than usual. Transitional precession has long been known in Post-Newtonian theory [11], but has never been simulated in full numerical relativity. We outline the conditions necessary for transitional precession to occur and examine a case of transitional precession in numerical relativity.

5.2 Conditions for transitional precession

When the spins of the black holes and the orbital angular momentum are mis-aligned, the spin-orbit interaction causes both the orbital plane and the spins to precess. Quite generally, the dynamics is complicated, but for most configurations, the orbital angular momentum $\vec{L}$ and the spins $\vec{S}_{1,2}$ precess around the total angular momentum $\vec{J}$, which approximately retains its direction during the entire inspiral. Such a system is said to be undergoing *simple* precession [11]. However, when the spins are nearly anti-aligned with angular momentum, and the total spin vector is equal in magnitude to the orbital angular momentum, i.e., $\vec{S} \equiv \vec{S}_1 + \vec{S}_2 \simeq -\vec{L}$, then the total angular momentum $\vec{J}$ undergoes a drastic change of direction, migrating towards $\vec{S}$. This is the regime of *transitional* precession [11] that will be the focus of this chapter. Figure 5.1 shows an example of of the dynamics for simple and transitional precession. The "migration" of

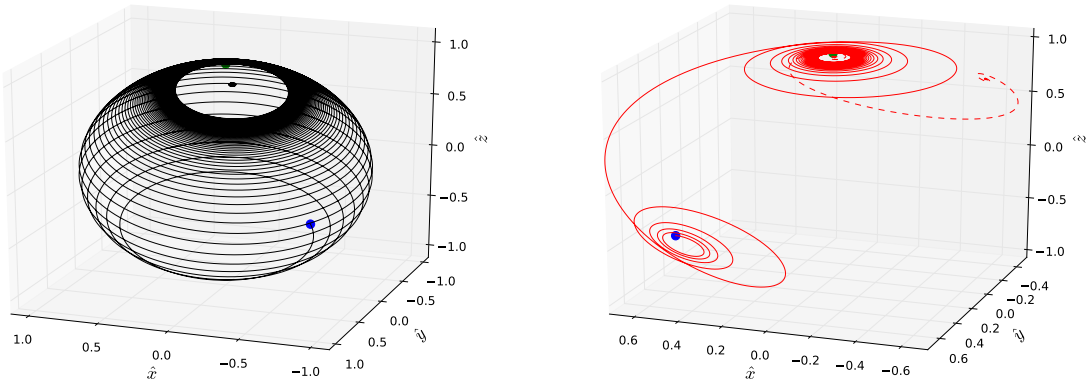

Figure 5.1: Examples of simple (left) and transitional (right) precession. Shown are $\hat{L}$ (solid) and $\hat{J}$ (dashed). The green and blue dots indicate the initial and final positions respectively. Note that in the left plot, $\hat{J}$ is confined to a very small region. The binary has $q = 9$, $\chi_1 = 0.9$, $\chi_2 = 0$. For the left panel, the misalignment angle is 145°; for the right, 175°.The evolution was done with leading order PN equations [11].

$\hat{J}$ and $\hat{L}$ between the 2 periods of simple precession around virtually fixed axes is the hallmark of transitional precession.

Suppose the binary starts in the regime $L = |\vec{L}| > S = |\vec{S}|$ with $\vec{L}$ and $\vec{S}$ nearly anti-aligned. As the orbit shrinks due to the emission of gravitational waves, a stage is reached when $L < S$ so that J must have a minimum, and the system may undergo transitional precession. In practice, the black holes might first merge.

Therefore, in order for transitional precession to occur before coalescence, the orbital frequency of transitional precession $\omega_{\rm trans}$ must be less than the orbital frequency at merger. As an estimate for orbital frequency at merger, we take the ISCO frequency:

$$\omega_{\rm ISCO} = \frac{1}{6^{3/2}} \frac{1}{m}. \tag{5.1}$$

Thus, transitional precession occurs when

$$\omega_{\rm trans} \lesssim \omega_{\rm ISCO}. \tag{5.2}$$

The simplest estimate for $\omega_{\rm trans}$ is to find the orbital frequency when

$$\vec{L} \simeq -\vec{S}. \tag{5.3}$$

Eqs. (5.2) and (5.3) have been used in literature to estimate the mass ratios that are necessary for transitional precession to occur. Buonanno et al [41] take maximally

spinning bodies and assume complete misalignment between the spins and the orbital angular momentum ($\vec{S}_1 = -m_1^2\hat{L}$, $\vec{S}_2 = -m_2^2\hat{L}$). Taking to lowest order $\vec{L} = \vec{L}_N = \mu m^{2/3}\omega^{-1/3}\hat{\ell}$, where $\hat{\ell}$ is the normal to the orbital plane, gives

$$\mu m^{2/3}\omega^{-1/3} = m_1^2 + m_2^2 = \frac{m^2(1+q^2)}{(1+q)^2} = (1-2\nu)m^2. \tag{5.4}$$

Solving for $\omega_{\rm trans}$:

$$\omega_{\rm trans} = \frac{\nu^3}{m(1-2\nu)^3}. \tag{5.5}$$

Applying the condition Eq. (5.2) yields [1]:

$$\frac{\nu^3}{m(1-2\nu)^3} \lesssim \frac{1}{6^{3/2}}\frac{1}{m} \implies \nu \lesssim 0.22,\ q \gtrsim 2. \tag{5.6}$$

Thus, no transitional precession can occur for equal-mass binaries.

Lousto and Zlochower [115] put a bound on the minimum mass ratio by taking the test-particle limit and setting the magnitude of the orbital angular momentum at the ISCO equal to the total spin vector (once again, perfect misalignment is assumed and the spins are maximal). This gives

$$L_{\rm ISCO} = \frac{22}{3\sqrt{3}}\frac{q}{(1+q)^2}m^2 = S = m^2\frac{(1+q^2)}{(1+q)^2}. \tag{5.7}$$

Solving the resulting quadratic yields $q \gtrsim 4$, giving a more conservative estimate.

So far, we have assumed complete misalignment of the spin angular momentum with the orbital angular momentum. Of course, no precession occurs if the spin vector $\vec{S}$ is completely misaligned with $\vec{L}$. Using Eq. (5.3), we can write to lowest order:

$$L = L_N = -\vec{S}\cdot\hat{\ell} \implies \mu m^{2/3}\omega_{\rm trans}^{-1/3} = -S\kappa, \tag{5.8}$$

where $\kappa \equiv \cos\hat{S}\cdot\hat{\ell}$. This gives the estimate:

$$\omega_{\rm trans} = \left(-\frac{\mu m^{2/3}}{S\kappa}\right)^3. \tag{5.9}$$

For a single spinning binary, Eq. (5.9) reduces to

$$\omega = -\frac{1}{m}\left(\frac{1}{q\chi\kappa}\right)^3, \tag{5.10}$$

[1] Reference [41] contains a typo in its Eq.(58) which reverses the sign of the inequality.

where χ is the magnitude of the dimensionless spin of the spinning body.

The estimates Eqs. (5.6), (5.7) and (5.10) demonstrate that, even for high spin, we require moderate mass ratios and close to complete misalignment between the total spin and orbital angular momentum for transitional precession to occur before merger.

Following the discussion in Apostolatos et al [11], we define the dimensionless quantity ϵ:

$$\epsilon \equiv \frac{L}{J}\frac{\dot{L}/L}{\Omega_p}, \tag{5.11}$$

where Ω_p is the precession frequency of the orbital angular momentum, and only the more massive body (m_1) carries spin. To lowest order, Ω_p is given by:

$$\Omega_p = \left(2 + \frac{3}{2}\frac{m_2}{m_1}\right)\frac{J}{r^3}. \tag{5.12}$$

We can rewrite ϵ as

$$\epsilon = \frac{16}{5}\frac{1}{\left(1+\frac{3}{4}\frac{1}{q}\right)}\left(\frac{M}{r}\right)^{3/2}\frac{1}{\gamma^2+2\kappa\gamma+1}, \tag{5.13}$$

where $M = m_1 + m_2$, $q = \frac{m_1}{m_2}$, and $\gamma(t) \equiv \frac{S}{L(t)} \propto \frac{S}{\sqrt{r}}$. It can be shown [11, 99] that

$$\hat{J} = \hat{J}_0 + \epsilon \hat{J}_0 \times \hat{\ell} + \mathcal{O}(\epsilon^2). \tag{5.14}$$

This demonstrates that when $\epsilon \ll 1$, the direction of $\hat{J}$ is approximately fixed to a constant direction $\hat{J}_0$. On the other hand, if ϵ becomes large, $\hat{J}$ will depart from $\hat{J}_0$ during the inspiral. Thus, one can formulate the condition to distinguish simple precession from transitional precession based on ϵ: if ϵ is small then the binary undergoes simple precession, and if $\epsilon \gtrsim 0.5$ then transitional precession is taking place [11].

The typical behaviour of ϵ is shown in Figure 5.2 for a range of misalignment angles. Depending on the misalignment angle, ϵ can have either one or two critical points. Systems that undergo the sequence simple-transitional-simple must have 2 critical points. This is because in this sequence, $\epsilon \gtrsim 0.5$ at the start of transitional precession and $\epsilon \lesssim 0.5$ at the end, so that ϵ must have a local maximum before merger. But $\epsilon \to \infty$ as $r \to 0$, so by continuity, ϵ must also have a local minimum.

For completeness, we note that there is no universally accepted notion of what constitutes transitional precession. Various authors have adapted different criteria, all of them based on some aspect of behaviour of $\hat{J}$; see e.g. [41], where transitional precession is broadly defined to have taken place if

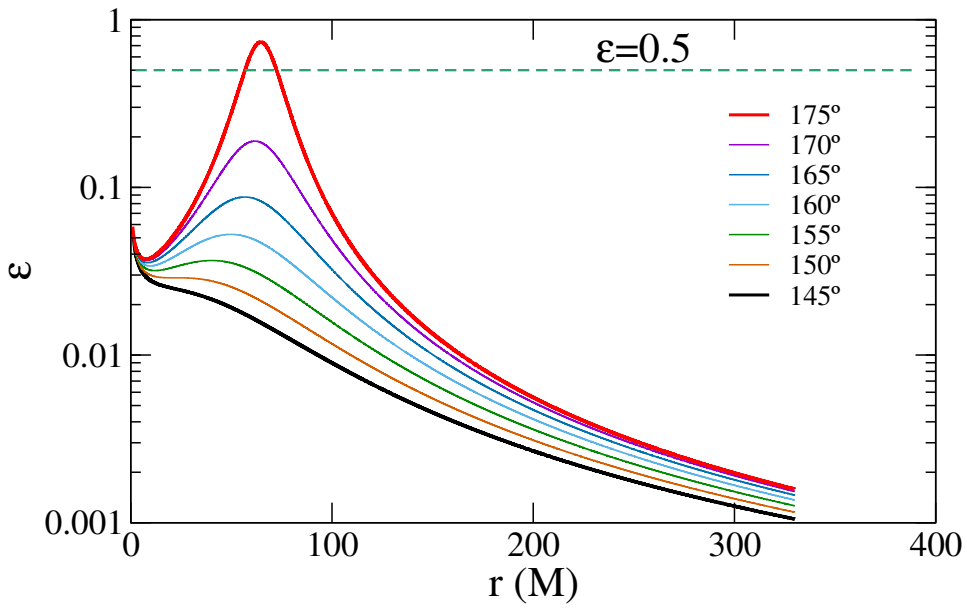

Figure 5.2: ϵ as a function of r for several values of the misalignment angle for a $q = 9$, $\chi_1 = 0.9$, $\chi_2 = 0$ binary.

$$\min_t \hat{J}(t) \cdot \hat{J}_0 < 1 - \epsilon_J, \tag{5.15}$$

where $\epsilon_J = 0.05,\ 0.1$. Thus, this criterion checks how much $\hat{J}$ has changed from its initial direction.

An important feature of transitional precession is the number of orbits spent "tumbling". To lowest order, this can be taken to be [99]

$$N = \frac{\Phi}{2\pi} = \frac{1}{64\nu\pi}((m\omega_i)^{-5/3} - (m\omega_f)^{-5/3}), \tag{5.16}$$

where ω_i and ω_f are the starting and ending orbital frequencies respectively. For the example shown in the right panel of Figure 5.1, this yields $\simeq 180$ orbits from the start of transitional precession ($\epsilon \gtrsim 0.5$) to the end ($\epsilon \lesssim 0.5$). The total number of orbits from the start of transitional precession to merger is $\simeq 2000$.

Apostolatos et al [11] point out that, in order for the entire simple-transitional-simple sequence to occur, the binary must start with $L_i/S \gtrsim 2$ and have $L_f/S \lesssim \frac{1}{2}$ before merger. Since $L \propto \sqrt{r}$ and $\sqrt{r} \propto \omega^{-1/3}$, it follows that

$$\frac{L_i}{L_f} = 4 \implies \frac{\omega_f}{\omega_i} = 4^3 = 64. \tag{5.17}$$

Therefore, the orbital frequency must change by a factor of 64 during inspiral. This is

q	$\vec{\chi}$	κ	$M\Omega$	D_0/M	$N_{\rm orbits}$	Ecc.
6	(0.0, 0.0679, -0.646)	0.9947	0.0148	15.76	28	1.2×10^{-3}

Table 5.1: The parameters of the numerical relativity transitional precession candidate. Here q is the mass ratio, $\vec{\chi}$ is the dimensionless spin, $\kappa = \cos(\hat{\ell} \cdot \hat{S})$ at the initial time, $M\omega$ is the dimensionless orbital frequency, and D_0/M is the coordinate separation.

indeed the case for the transitionally precessing example of Figure 5.1, where $L/S \sim 2.25$ at the start of the simulation and $L/S \sim 0.3$ at ISCO. Taking the ending frequency to be $\omega_f = \omega_{\rm ISCO}$, we obtain $\omega_i \simeq 0.001$. Then, considering as a lower bound the case of an equal-mass binary, Eq. (5.16) above gives $\simeq 1500$ orbits. This is presently outside the reach of full numerical relativity. A more complete analysis taking into account the full PN evolution to highest available order is the subject of future work.

5.3 Transitional precession in numerical relativity

As shown in the previous section, transitional precession requires a fine-tuning of initial conditions to take place before the black holes merge. In particular, we found that moderate mass ratios and high spins are needed; therefore, simulating the sequence simple-transitional-simple in full numerical relativity is outside our current computational abilities. Instead, we attempt to capture only the highly dynamical transitional part. The parameters of the system under study are outlined in Table 5.3. For simplicity, we chose a system with only one black hole spinning.

The coordinate trajectories of the black holes in the inertial frame are shown Figure 5.3. One can see that the orbital plane is precessing and that the coordinate centre of mass is slowly drifting linearly along x and z directions. This motion is due to the residual linear momentum in the initial data [2]. For the analysis here, we ignore this effect.

To establish that the binary is undergoing transitional precession, we compute the total angular momentum $\vec{J}$ as

$$\vec{J} \equiv \vec{J}_{\rm ADM} - \vec{J}_{\rm rad}, \tag{5.18}$$

where $\vec{J}_{\rm ADM}$ is ADM angular momentum evaluated in initial data and $\vec{J}_{\rm rad}$ is the angular momentum emitted by the binary, which is computed from the gravitational waves [157].

The properties of the total angular momentum $\vec{J}$ are shown in Figure 5.4. Several

[2] See Chapter 2 for a more detailed description of this effect

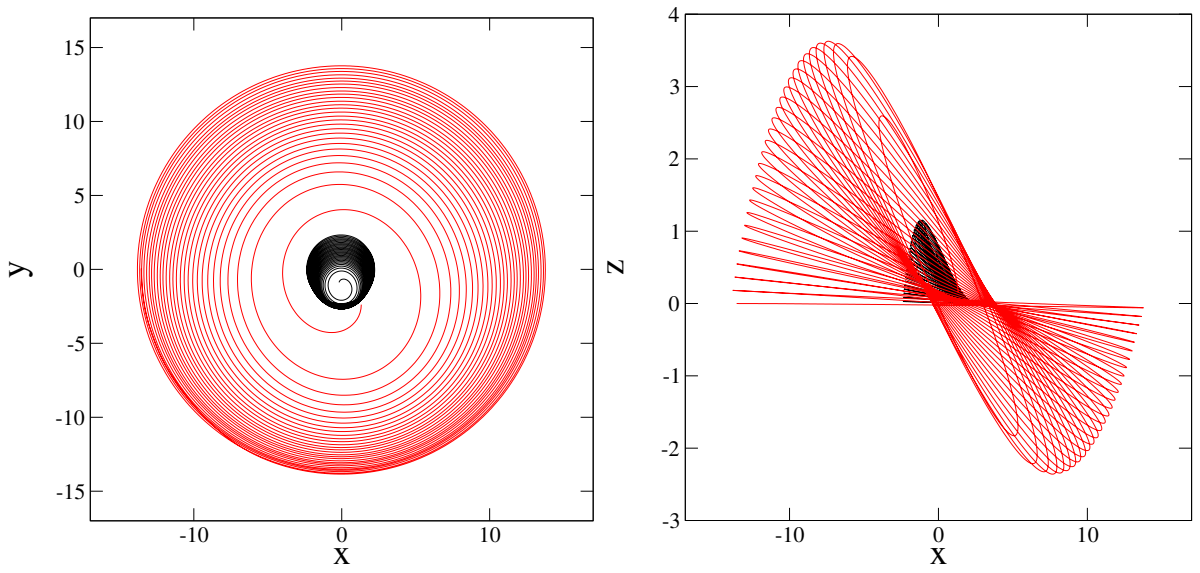

Figure 5.3: Trajectories of the apparent horizons in inertial coordinates projected onto the x–y plane(left) and x–z plane (right).

important features are obvious. Firstly, the total angular momentum changes direction drastically during the evolution, essentially reversing its z component. The angle $\alpha(t) \equiv \hat{J}_i \cdot \hat{J}(t)$ grows to $\simeq 1.8$ radians at merger, which is much larger than observed in any previous simulations. Computing the angle between $\vec{J}_{\rm ADM}$ and the final spin of the black hole $\vec{S}_f$, and comparing this angle to the final value of α, we find the fractional difference in the angles to be $\simeq 0.3\%$, confirming the validity of our use of Eq. (5.18) and the determination of $\vec{J}_{rad}$. Secondly, the magnitude of total angular momentum goes through a minimum shortly before merger, decreasing by about 60% before growing again. Both of these observations are consistent with the binary undergoing transitional precession. In this case, the period of transitional precession started *before* the numerical relativity simulation began and ended due to the black holes merging.

We also monitor the spin of the black holes during the evolution using quasi-local measures [118, 139], and compute the orbital angular momentum $\vec{L}$:

$$\vec{L} = \vec{J} - \vec{S}. \tag{5.19}$$

There is an ambiguity in this definition: $\vec{S}$ is measured as a function of coordinate time, whereas $\vec{J}$ is evaluated at a retarded time $t - r^*$ as defined in Eqs.(14a,14b) of [34]. This ambiguity would be present in any comparison of quantities evaluated in the wave zone with quantities from the near zone. For simplicity, we disregard this ambiguity and assume that the retarded and coordinate times are the same.

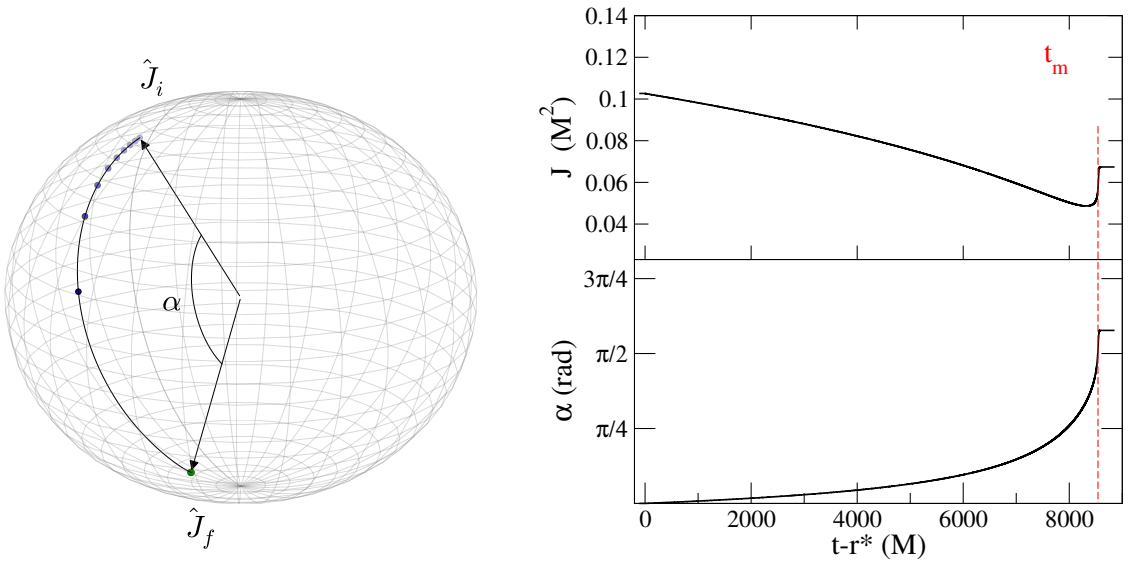

Figure 5.4: The behaviour of the total angular momentum $\vec{J}$ during the evolution. **Left**: $\hat{J}$ projected on the unit sphere. The blue dots show time intervals of 1000 M, and the green dot denotes the final position of $\hat{J}$. **Right**: Top panel gives the magnitude $J = \|\vec{J}\|$; bottom, the angular change from the initial direction: $\alpha = \cos^{-1}(\hat{J}(t) \cdot \hat{J}_i)$. The dashed vertical line is the approximate time of merger.

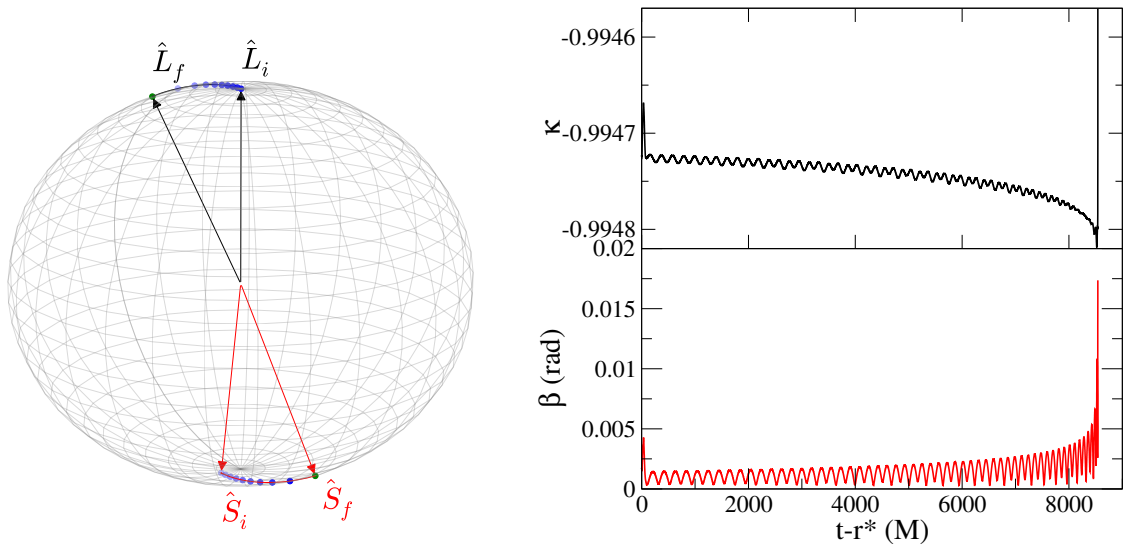

Figure 5.5: Characteristics of motion for $\vec{L}$ and $\vec{S}$. **Left**: $\hat{L}$ and $\hat{S}$ projected on the unit sphere. The blue dots show time intervals of 1000 M, and the green dots denote the final positions of $\hat{L}$ and $\hat{S}$. **Right**: Top panel shows the evolution of κ. The bottom panel shows the angle $\beta = \cos^{-1}(\hat{L} \cdot \hat{\ell})$ by which the direction of the total *orbital* angular momentum differs from the direction of the the *Newtonian* angular momentum.

Figure 5.5 shows the motion of the spin $\vec{S}$ and the orbital angular momentum $\vec{L}$. They start with a misalignment angle of 174 degrees and travel in opposite directions on the unit sphere. This motion is very different from typical precession and does not correspond to precession cones (see Chapter 4 for examples). Instead, we observe a secular "migration", when spins and orbital angular momentum are "precessing" around the transiting total angular momentum, coupled with nutations that take place on the orbital timescale. The top panel of Figure 5.5 shows that κ is conserved to a very good approximation ($\simeq 2\%$) throughout the inspiral. This means that the angle between $\vec{L}$ and $\vec{S}$ is nearly constant during the period of transitional precession. Finally, we examine the difference between the direction of *total* orbital angular momentum $\hat{L}$ and the normal to the orbital plane $\hat{\ell}$. From Figure 5.5, we see that $\beta = \cos^{-1} \hat{\ell} \cdot \hat{L}$ is smaller than 0.005 radians throughout the inspiral, which means that $\hat{\ell}$ and $\hat{L}$ evidently have the same secular evolution but differ in their instantaneous nutations. All of these observations are consistent with expectations from PN theory.

We make a direct comparison with Post-Newtonian theory by applying the formalism developed in Chapter 4. The matching is performed at orbital frequencies $M\omega = 0.0171203,\ 0.0172804,\ 0.0174404$, and with four different window widths. We evolve both the orbital frequency and the precession equations at 3.5 PN order.

Figure 5.6 shows angle $\angle L$ between the normals to the orbital plane; and $\angle\chi$, the angle between the spins. Both angles are $\lesssim 0.03$ radians throughout the inspiral, regardless of the Taylor approximant used. This suggests that PN precession equations are fairly accurate, even for transitionally precessing binaries.

We illustrate the motion of $\hat{\ell}$ and $\hat{S}$ on the unit sphere in Figure 5.7. As one can see, there is fairly good agreement between PN and NR.

Turning our attention now to the orbital phasing, we examine the phase differences between PN and NR for different Taylor approximants, using the rotationally invariant quantity Φ_Δ introduced in Chapter 4. The results follow the same trend found previously for comparably high mass ratios ($q \geq 5$): Taylor T1 and T5 agree better with NR than T4, as seen in Figure 5.8. However, even for the best performing Taylor approximant, the phasing error is over a radian close to merger, which is again consistent with previous results for non-spinning binaries of similar mass ratios.

Finally, we compare the PN prediction for the total angular momentum $\vec{J}_{PN}$ to the NR results. We find good agreement both in direction and magnitude up until close to merger, as shown in Figure 5.9. The angle $\angle J$ between the PN and NR predictions stays below 0.1 radians throughout the inspiral, and the magnitude of $\vec{J}$ is accurate to within $\simeq 1\%$.

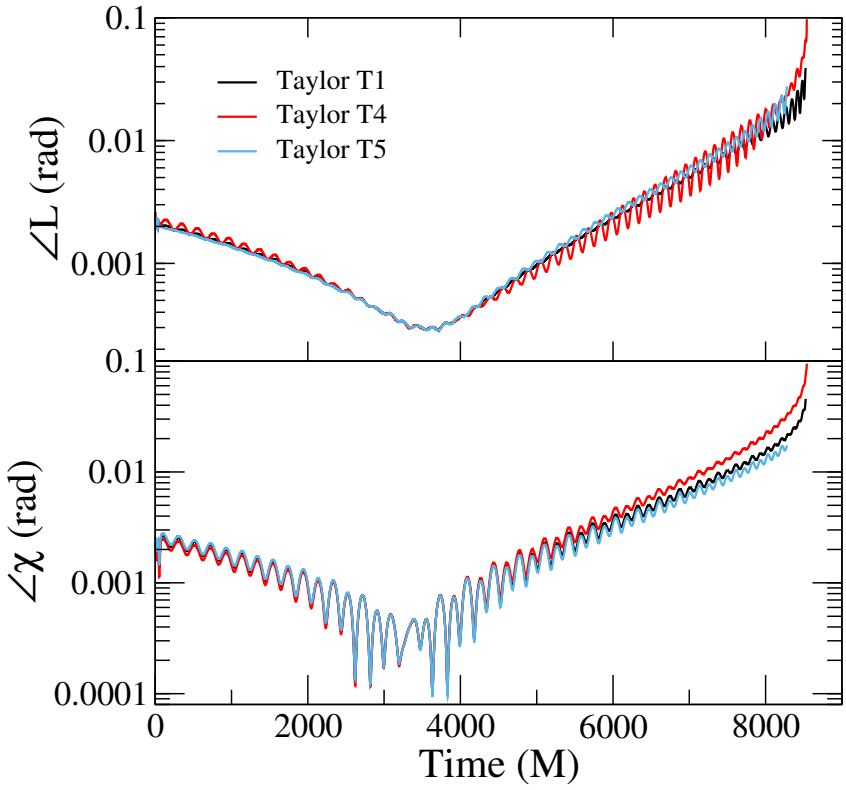

Figure 5.6: **Top**: angle $\angle L$ between the normals to the orbital plane $\hat{\ell}^{NR}, \hat{\ell}^{PN}$ in NR and PN. **Bottom**: angle χ between the PN and NR spins. Both angles are less than 0.03 radians until very close to merger.

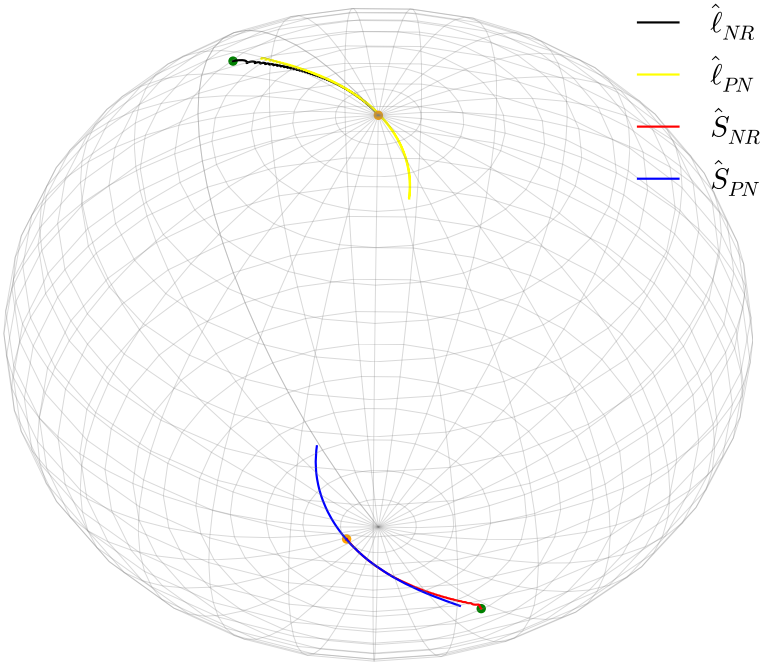

Figure 5.7: The motion of the normal to the orbital plane $\hat{\ell}$ and the spin direction $\hat{S}$ in numerical relativity (black, red) and Post-Newtonian theory (yellow,blue). The orange and green dots indicate the starting and ending positions of the NR vectors. The PN quantities were evolved backward in time for an additional ~ 15000 M.

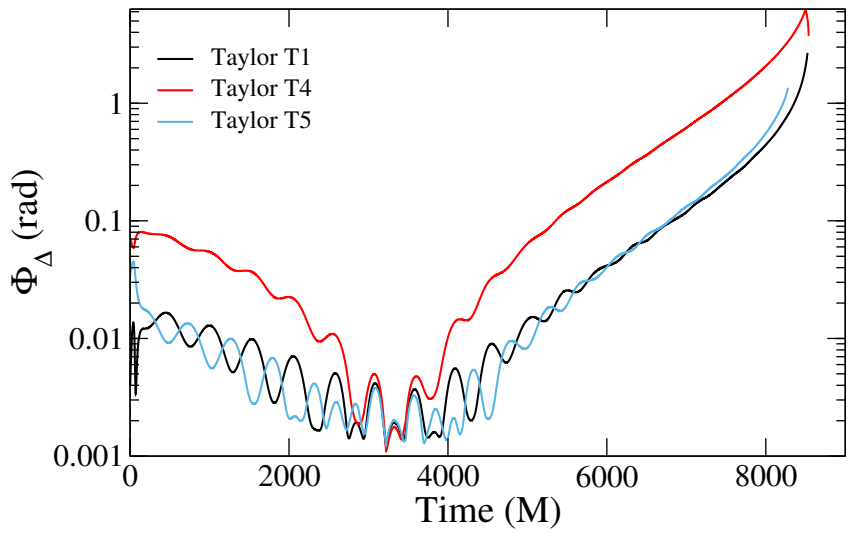

Figure 5.8: Phasing error as a function of time for three different Taylor approximants. Taylor T1 has the smallest phasing errors and Taylor T4 the largest.

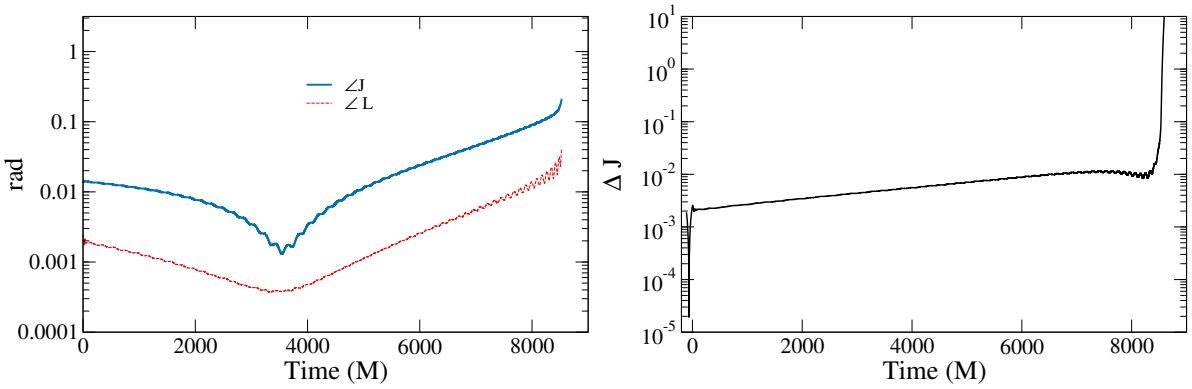

Figure 5.9: **Left**: The angle $\angle J$ between the PN and NR total angular momentum for the binary matched at $M\omega_{\rm match} = 0.0171203$ with window width $12\% M\omega_{\rm match}$. **Right**: $\Delta J \equiv (J^{NR} - J^{PN})/J^{NR}$, the fractional difference in the magnitude.

In the future, we plan to extend the scope of the study in three ways: by examining in detail the behaviour of the waveforms with the goal of constructing hybrids, by including a comparison with the precessing EOB model (SEOBNRv3 described in [141]), and by performing more numerical relativity simulations to explore parameter space dependence of the dynamics, utilizing Post-Newtonian theory results to pick appropriate candidates.

5.4 Summary

We have characterized the conditions necessary for transitional precession to occur and analyzed a full numerical relativity simulation that displays transitional precession. We have found that Post-Newtonian precession equations fairly accurately describe the motion of the angular momentum and spin vectors during this highly dynamical phase.

Chapter 6

Conclusions and future work

It is a very exciting time to be part of the gravitational physics community. With the advent of advanced gravitational wave detectors, and more accurate long-term observations of pulsars by pulsar timing arrays, the possibility of detection of gravitational waves is very likely. This will open up an entirely new branch of astronomy that will allow us to glean new information about many interesting systems and about the universe itself. The prospect of combining gravitational wave observations with their electromagnetic and neutrino counterparts for astrophysical phenomena, such as neutron star - neutron star mergers, is a particularly enticing one.

One of the more promising sources of gravitational waves are black hole binaries. Very little is known observationally about such systems; gravitational wave astronomy will allow us to probe them for the first time. Of special interest are precessing binaries, as they exhibit rich dynamics that lead to complicated modulations of the gravitational waveform. For ground-based interferometric detectors, extremely accurate models of the gravitational wave signal are required for reliable signal detection and for parameter estimation. Many different approaches to this problem have been developed. Enormous progress has been made in the semi-analytic approximation domain, including successful methods such as Post-Newtonian theory, Effective One Body model and self-force expansion. Meanwhile, advances in numerical relativity have allowed direct numerical integration of the two-body problem.

While much has been accomplished, many challenges remain. Chief among them are the numerical exploration of precessing BBH parameter space and construction of fast analytical models that can be used as templates for GW searches.

In this dissertation, we have explored various aspects of modelling precessing binary black hole systems. In Chapters 2 and 3, we have examined new techniques to enhance and extend the abilities of `SpEC` to simulate generically precessing binaries, especially at

high mass ratio and high spin. In particular, we first presented a new version of the initial data solver which featured enhanced robustness in a much larger region of parameter space. An updated method to control linear momentum in initial data was also shown to eliminate spurious gravitational wave mixing due to the drift of the centre of mass during the evolution. We then discussed a novel parametrization of rotations via quaternions that allowed for generically precessing binaries to be simulated in `SpEC`. Chapters 4 and 5 used results of numerical simulations of precessing binaries to explore their dynamics and to perform a comparison to post-Newtonian predictions. After developing a matching procedure to associate physical parameters between numerical relativity and post-Newtonian theory in Chapter 4, we performed a systematic comparison of precession dynamics. We found good agreement for the precession of the orbital planes and the spins. We also found that the nutation features of the spin dynamics do not match between numerical relativity and post-Newtonian theory. Examining the orbital phasing, we found that different Taylor approximants match numerical relativity best in different regions of parameter space, in line with previous investigations. Finally, the convergence of the post-Newtonian precession equations and of the Taylor T4 approximant were investigated. The precession equations were found to converge essentially monotonically with PN order, in sharp contrast to the convergence of the orbital phase, which experienced sharp features at some PN orders. Chapter 5 explored a particularly interesting regime of precession, in which the direction of total angular momentum changes significantly during the inspiral. This *transitional precession* has been predicted in Post-Newtonian theory but has not been simulated in numerical relativity. We reviewed features of transitional precession and then presented a numerical relativity simulation exhibiting the characteristics of transitional precession. Applying the formalism developed in Chapter 4, we again found good agreement with post-Newtonian theory.

The above projects have several interesting extensions. On the numerical side, the new initial data code has opened up the possibility of simulating high-mass ratio and/or high spin *precessing* binaries. While the evolution itself remains computationally very demanding, simulations starting close to merger are of interest for determining the physical properties of the remnant black hole (i.e. mass, spin, and velocity) for calibration of fitting formulae and analytical waveform models (for the former, see e.g. [91, 116]; for the latter, see [62] and references therein). With the new code, hyperbolic encounters between black holes and dynamical capture binaries can also be explored. These simulations can serve as models for strong-field interactions in dense stellar environments. They also provide interesting new regimes for calibrating semi-analytic approximations [63]. Finally, we can simulate more transitionally precessing binaries to explore this phenomenon

in the fully non-linear regime. On the analytic side, the work of Chapters 4 and 5 can be extended to use the precessing EOB model (SEOBNRv3 [141]). Further, creating precessing hybrid waveforms is of great interest for data analysis purposes.

Bibliography

[1] `http://www.black-holes.org/SpEC.html`.

[2] J. Aasi et al. Prospects for Localization of Gravitational Wave Transients by the Advanced LIGO and Advanced Virgo Observatories. 2013.

[3] J. Aasi et al. Advanced LIGO. *Class. Quant. Grav.*, 32:074001, 2015.

[4] J. Abadie et al. Predictions for the Rates of Compact Binary Coalescences Observable by Ground-based Gravitational-wave Detectors. *Class. Quant. Grav.*, 27:173001, 2010.

[5] B. Abbott et al. LIGO: The Laser interferometer gravitational-wave observatory. *Rept. Prog. Phys.*, 72:076901, 2009.

[6] P. Ajith. Addressing the spin question in gravitational-wave searches: Waveform templates for inspiralling compact binaries with nonprecessing spins. *Phys. Rev. D*, 84:084037, 2011.

[7] P. Ajith, Michael Boyle, Duncan A. Brown, Bernd Brugmann, Luisa T. Buchman, et al. The NINJA-2 catalog of hybrid post-Newtonian/numerical-relativity waveforms for non-precessing black-hole binaries. *Class. Quantum Grav.*, 29(12):124001, 2012.

[8] P. Ajith, Michael Boyle, Duncan A. Brown, Bernd Brugmann, Luisa T. Buchman, et al. Addendum to 'The NINJA-2 catalog of hybrid post-Newtonian/numerical-relativity waveforms for non-precessing black-hole binaries'. *Class. Quantum Grav.*, 30(19):199401, 2013.

[9] Miguel Alcubierre. *Introduction to 3+1 Numerical Relativity*. Oxford University Press, New York, 2008.

[10] Simon Altmann. *Rotations, quaternions, and double groups*. Dover Publications, Mineola, N.Y, 2005.

[11] Theocharis A. Apostolatos, Curt Cutler, Gerald J. Sussman, and Kip S. Thorne. Spin-induced orbital precession and its modulation of the gravitational waveforms from merging binaries. *Phys. Rev. D*, 49:6274 – 6297, 1994.

[12] R. Arnowitt, S. Deser, and Charles W. Misner. The dynamics of general relativity. In L. Witten, editor, *Gravitation: An Introduction to Current Research*, pages 227–265. Wiley, New York, 1962.

[13] M. Arribas, A. Elipe, and M. Palacios. Quaternions and the rotation of a rigid body. *Celestial Mechanics and Dynamical Astronomy*, 96(3-4):239–251, October 2006.

[14] K. G. Arun, Alessandra Buonanno, Guillaume Faye, and Evan Ochsner. Higher-order spin effects in the amplitude and phase of gravitational waveforms emitted by inspiraling compact binaries: Ready-to-use gravitational waveforms. *Phys. Rev. D*, 79:104023, 2009.

[15] B. Aylott, J. G. Baker, W. D. Boggs, M. Boyle, P. R. Brady, D. A. Brown, B. Brügmann, L. T. Buchman, A. Buonanno, L. Cadonati, J. Camp, M. Campanelli, J. Centrella, S. Chatterji, N. Christensen, T. Chu, P. Diener, N. Dorband, Z. B. Etienne, J. Faber, S. Fairhurst, B. Farr, S. Fischetti, G. Guidi, L. M. Goggin, M. Hannam, F. Herrmann, I. Hinder, S. Husa, V. Kalogera, D. Keppel, L. E. Kidder, B. J. Kelly, B. Krishnan, P. Laguna, C. O. Lousto, I. Mandel, P. Marronetti, R. Matzner, S. T. McWilliams, K. D. Matthews, R. A. Mercer, S. R. P. Mohapatra, A. H. Mroué, H. Nakano, E. Ochsner, Y. Pan, L. Pekowsky, H. P. Pfeiffer, D. Pollney, F. Pretorius, V. Raymond, C. Reisswig, L. Rezzolla, O. Rinne, C. Robinson, C. Röver, L. Santamaría, B. Sathyaprakash, M. A. Scheel, E. Schnetter, J. Seiler, S. L. Shapiro, D. Shoemaker, U. Sperhake, A. Stroeer, R. Sturani, W. Tichy, Y. T. Liu, M. van der Sluys, J. R. van Meter, R. Vaulin, A. Vecchio, J. Veitch, A. Viceré, J. T. Whelan, and Y. Zlochower. Testing gravitational-wave searches with numerical relativity waveforms: Results from the first Numerical INJection Analysis (NINJA) project. *Class. Quantum Grav.*, 26(16):165008, 2009.

[16] Maria Babiuc, Béla Szilágyi, Ian Hawke, and Yosef Zlochower. Gravitational wave extraction based on Cauchy-characteristic extraction and characteristic evolution. *Class. Quantum Grav.*, 22(23):5089–5107, 2005.

[17] John G. Baker, Joan Centrella, Dae-Il Choi, Michael Koppitz, and James van Meter. Gravitational wave extraction from an inspiraling configuration of merging black holes. *Phys. Rev. Lett.*, 96:111102, 2006.

[18] John G. Baker, James R. van Meter, Sean T. McWilliams, Joan Centrella, and Bernard J. Kelly. Consistency of post-Newtonian waveforms with numerical relativity. *Phys. Rev. Lett.*, 99(18):181101, 2007.

[19] B. M. Barker and R. F. O'Connell. Gravitational Two-Body Problem with Arbitrary Masses, Spins, and Quadrupole Moments. *Phys. Rev.*, D12:329–335, 1975.

[20] D. Baskaran, S.R. Lau, and A.N. Petrov. Center-of-mass integral in canonical general relativity. *Annals Phys.*, 307:90–131, 2003.

[21] T. W. Baumgarte and S. L. Shapiro. On the numerical integration of Einstein's field equations. *Phys. Rev. D*, 59:024007, 1999. gr-qc/9810065.

[22] Thomas W. Baumgarte and Stuart L. Shapiro. *Numerical Relativity: Solving Einstein's Equations on the Computer*. Cambridge University Press, New York, 2010.

[23] Nigel T. Bishop, Roberto Gómez, Luis Lehner, and Jeffrey Winicour. Cauchy-characteristic extraction in numerical relativity. *Phys. Rev. D*, 54(10):6153–6165, Nov 1996.

[24] Luc Blanchet. Post-Newtonian theory and the two-body problem. *Fundam.Theor.Phys.*, 162:125–166, 2011.

[25] Luc Blanchet. Gravitational radiation from post-Newtonian sources and inspiralling compact binaries. *Living Rev.Rel.*, 17:2, 2014.

[26] Alejandro Bohé, Guillaume Faye, Sylvain Marsat, and Edward K Porter. Quadratic-in-spin effects in the orbital dynamics and gravitational-wave energy flux of compact binaries at the 3PN order. 2015.

[27] Alejandro Bohé, Sylvain Marsat, Guillaume Faye, and Luc Blanchet. Next-to-next-to-leading order spin-orbit effects in the near-zone metric and precession equations of compact binaries. *Class. Quant. Grav.*, 30(7):075017, April 2013.

[28] Jeffrey M. Bowen and James W. York, Jr. Time-asymmetric initial data for black holes and black-hole collisions. *Phys. Rev. D*, 21(8):2047–2056, 1980.

[29] John P. Boyd. *Chebyshev and Fourier Spectral Methods*. Dover Publications, second edition, 1999.

[30] M. Boyle, L. E. Kidder, S. Ossokine, and H. P. Pfeiffer. Gravitational-wave modes from precessing black-hole binaries. 2014. arXiv:1409.4431.

[31] Michael Boyle. Uncertainty in hybrid gravitational waveforms: Optimizing initial orbital frequencies for binary black-hole simulations. *Phys. Rev. D*, 84:064013, Sep 2011.

[32] Michael Boyle. Transformations of asymptotic gravitational-wave data. Not yet published, 2015.

[33] Michael Boyle, Duncan A. Brown, Lawrence E. Kidder, Abdul H. Mroué, Harald P. Pfeiffer, Mark A. Scheel, Gregory B. Cook, and Saul A. Teukolsky. High-accuracy comparison of numerical relativity simulations with post-Newtonian expansions. *Phys. Rev. D*, 76(12):124038, 2007.

[34] Michael Boyle and Abdul H. Mroué. Extrapolating gravitational-wave data from numerical simulations. *Phys. Rev. D*, 80(12):124045–14, December 2009.

[35] Michael Boyle, Robert Owen, and Harald P. Pfeiffer. A geometric approach to the precession of compact binaries. *Phys. Rev. D*, 84:124011, 2011.

[36] Steve Brandt and Bernd Brügmann. A simple construction of initial data for multiple black holes. *Phys. Rev. Lett.*, 78(19):3606–3609, 1997.

[37] L. T. Buchman and O. C. A. Sarbach. Improved outer boundary conditions for Einstein's field equations. *Class. Quantum Grav.*, 24:S307–S326, 2007.

[38] Luisa T. Buchman, Harald P. Pfeiffer, Mark A. Scheel, and Béla Szilágyi. Simulations of unequal mass binary black holes with spectral methods. *Phys. Rev. D*, 86:084033, 2012.

[39] A. Buonanno and T. Damour. Effective one-body approach to general relativistic two-body dynamics. *Phys. Rev. D*, 59:084006, 1999.

[40] Alessandra Buonanno, Yanbei Chen, Yi Pan, and Michele Vallisneri. Quasiphysical family of gravity-wave templates for precessing binaries of spinning compact objects: Application to double-spin precessing binaries. *Phys. Rev. D*, 70:104003, 2004.

[41] Alessandra Buonanno, Yanbei Chen, and Michele Vallisneri. Detecting gravitational waves from precessing binaries of spinning compact objects: Adiabatic limit. *Phys. Rev. D*, 67:104025, 2003.

[42] Alessandra Buonanno, Gregory B. Cook, and Frans Pretorius. Inspiral, merger and ring-down of equal-mass black-hole binaries. *Phys. Rev. D*, 75:124018, 2007.

[43] Alessandra Buonanno, Lawrence E. Kidder, Abdul H. Mroué, Harald P. Pfeiffer, and Andrea Taracchini. Reducing orbital eccentricity of precessing black-hole binaries. *Phys. Rev. D*, 83:104034, 2011.

[44] Alessandra Buonanno, Yi Pan, Harald P. Pfeiffer, Mark A. Scheel, Luisa T. Buchman, and Lawrence E. Kidder. Effective-one-body waveforms calibrated to numerical relativity simulations: Coalescence of non-spinning, equal-mass black holes. *Phys. Rev. D*, 79:124028, 2009.

[45] Juan Calderón Bustillo, Alejandro Bohé, Sascha Husa, Alicia M. Sintes, Mark Hannam, et al. Comparison of subdominant gravitational wave harmonics between post-Newtonian and numerical relativity calculations and construction of multimode hybrids. 2015.

[46] M. Campanelli, C. O. Lousto, H. Nakano, and Yosef Zlochower. Comparison of numerical and post-Newtonian waveforms for generic precessing black-hole binaries. *Phys. Rev. D*, 79:084010, 2009.

[47] Manuela Campanelli, Carlos O. Lousto, Yosef Zlochower, Badri Krishnan, and David Merritt. Spin flips and precession in black-hole binary mergers. *Phys. Rev. D*, 75:064030, 2007.

[48] Manuela Campanelli, C.O. Lousto, P. Marronetti, and Y. Zlochower. Accurate evolutions of orbiting black-hole binaries without excision. *Phys. Rev. Lett.*, 96:111101, 2006.

[49] Matthew Caudill, Greg B. Cook, Jason D. Grigsby, and Harald P. Pfeiffer. Circular orbits and spin in black-hole initial data. *Phys. Rev. D*, 74(6):064011, 2006.

[50] Katerina Chatziioannou, Neil Cornish, Antoine Klein, and Nicolás Yunes. Detection and Parameter Estimation of Gravitational Waves from Compact Binary Inspirals with Analytical Double-Precessing Templates. *Phys. Rev.*, D89(10):104023, 2014.

[51] Matthew W. Choptuik and Frans Pretorius. Ultra Relativistic Particle Collisions. *Phys. Rev. Lett.*, 104:111101, 2010.

[52] Tony Chu, Harald P. Pfeiffer, and Mark A. Scheel. High accuracy simulations of black hole binaries: Spins anti-aligned with the orbital angular momentum. *Phys. Rev. D*, 80:124051, 2009.

[53] M. Coleman Miller and E. J. M. Colbert. Intermediate-Mass Black Holes. *Int. J. Mod. Phys. D*, 13:1–64, 2004.

[54] LIGO Scientific Collaboration. LSC Algorithm Library software packages LAL, LALWRAPPER, and LALAPPS.

[55] Greg Cook. Initial data for numerical relativity. *Living Rev. Rel.*, 3, November 2000. 5.

[56] Gregory B. Cook. Corotating and irrotational binary black holes in quasicircular orbits. *Phys. Rev. D*, 65(8):084003, Mar 2002.

[57] Gregory B. Cook and Harald P. Pfeiffer. Excision boundary conditions for black-hole initial data. *Phys. Rev. D*, 70(10):104016, Nov 2004.

[58] Gregory B. Cook and Bernard F. Whiting. Approximate Killing vectors on S^2. *Phys. Rev. D*, 76(4):041501(R), 2007.

[59] Tito Dal Canton, Andrew P. Lundgren, and Alex B. Nielsen. Impact of precession on aligned-spin searches for neutron-star–black-hole binaries. *Phys. Rev.*, D91(6):062010, 2015.

[60] T. Damour, A. Nagar, and M. Trias. Accuracy and effectualness of closed-form, frequency-domain waveforms for nonspinning black hole binaries. *Phys. Rev. D*, 83(2):024006, January 2011.

[61] Thibault Damour. Coalescence of two spinning black holes: an effective one-body approach. *Phys. Rev. D*, 64:124013, 2001.

[62] Thibault Damour. The General Relativistic Two Body Problem and the Effective One Body Formalism. 2012.

[63] Thibault Damour, Federico Guercilena, Ian Hinder, Seth Hopper, Alessandro Nagar, et al. Strong-Field Scattering of Two Black Holes: Numerics Versus Analytics. *Phys.Rev.*, D89(8):081503, 2014.

[64] Thibault Damour, Bala R. Iyer, and Alessandro Nagar. Improved resummation of post-Newtonian multipolar waveforms from circularized compact binaries. *Phys. Rev. D*, 79:064004, 2009.

[65] Thibault Damour, Bala R. Iyer, and B.S. Sathyaprakash. A Comparison of search templates for gravitational waves from binary inspiral. *Phys.Rev.*, D63:044023, 2001.

[66] Thibault Damour and Alessandro Nagar. Comparing Effective-One-Body gravitational waveforms to accurate numerical data. *Phys. Rev. D*, 77:024043, 2008.

[67] Thibault Damour and Alessandro Nagar. An Improved analytical description of inspiralling and coalescing black-hole binaries. *Phys. Rev. D*, 79:081503, 2009.

[68] Chris Doran and Anthony Lasenby. *Geometric algebra for physicists*. Cambridge University Press, third edition, 2003.

[69] David S. Dummit and Richard M. Foote. *Abstract algebra*. Prentice Hall, Hoboken, NJ, second edition, 1999.

[70] A. Einstein. Über Gravitationswellen. In *Sitzber. Preuss. Akad. Wiss.*, page 154, Jan 1918.

[71] Lee S. Finn. Detection, measurement, and gravitational radiation. *Phys. Rev. D*, 46(12):5236, December 1992.

[72] Lee Samuel Finn and David F. Chernoff. Observing binary inspiral in gravitational radiation: One interferometer. *Phys. Rev. D*, 47:2198–2219, 1993.

[73] F. Foucart, L. Buchman, M. D. Duez, M. Grudich, L. E. Kidder, I. MacDonald, A. Mroue, H. P. Pfeiffer, M. A. Scheel, and B. Szilagyi. First direct comparison of nondisrupting neutron star-black hole and binary black hole merger simulations. *Phys. Rev. D*, 88(6):064017, September 2013.

[74] F. Foucart, M. B. Deaton, M. D. Duez, L. E. Kidder, I. MacDonald, C. D. Ott, H. P. Pfeiffer, M. A. Scheel, B. Szilagyi, and S. A. Teukolsky. Black hole-neutron star mergers at realistic mass ratios: Equation of state and spin orientation effects. *Phys. Rev. D*, 87:084006, March 2013.

[75] Francois Foucart, Matthew D. Duez, Lawrence E. Kidder, and Saul A. Teukolsky. Black hole-neutron star mergers: Effects of the orientation of the black hole spin. *Phys. Rev. D*, 83:024005, 2011.

[76] Francois Foucart, Lawrence E. Kidder, Harald P. Pfeiffer, and Saul A. Teukolsky. Initial data for black hole-neutron star binaries: a flexible, high-accuracy spectral method. *Phys. Rev. D*, 77:124051, 2008.

[77] Helmut Friedrich. On the hyperbolicity of Einstein's and other gauge field equations. *Commun. Math. Phys.*, 100(4):525–543, 1985.

[78] Helmut Friedrich and Alan Rendall. *The Cauchy Problem for the Einstein Equations*, volume 540 of *Lecture Notes in Physics*. Springer Berlin Heidelberg, 2000.

[79] David Garfinkle. Harmonic coordinate method for simulating generic singularities. *Phys. Rev. D*, 65(4):044029, 2002.

[80] E. Gourgoulhon. 3+1 formalism and bases of numerical relativity, March 2007.

[81] C. J. Handmer, B. Szilágyi, and J. Winicour. Gauge invariant spectral characteristic extraction.

[82] M. Hannam, S. Husa, F. Ohme, and P. Ajith. Length requirements for numerical-relativity waveforms. *Phys. Rev. D*, 82(12):124052, December 2010.

[83] Mark Hannam. Status of black-hole-binary simulations for gravitational- wave detection. *Class. Quant. Grav.*, 26:114001, 2009.

[84] Mark Hannam, Sacha Husa, Franke Ohme, Doreen Müller, and Bernd Brügmann. Simulations of black-hole binaries with unequal masses or nonprecessing spins: Accuracy, physical properties, and comparison with post-Newtonian results. *Phys. Rev. D*, 82:124008, 2010.

[85] Mark Hannam, Sascha Husa, José A. González, Ulrich Sperhake, and Bernd Brügmann. Where post-Newtonian and numerical-relativity waveforms meet. *Phys. Rev. D*, 77:044020, 2008.

[86] Mark Hannam, Patricia Schmidt, Alejandro Bohé, Leila Haegel, Sascha Husa, et al. A simple model of complete precessing black-hole-binary gravitational waveforms. *Phys.Rev.Lett.*, 113:151101, 2014.

[87] Gregory M. Harry. Advanced LIGO: The next generation of gravitational wave detectors. *Class.Quant.Grav.*, 27:084006, 2010.

[88] I.W. Harry, A.H. Nitz, Duncan A. Brown, A. Lundgren, Evan Ochsner, et al. Investigating the effect of precession on searches for neutron-star-black-hole binaries with Advanced LIGO. *Phys.Rev.*, D89:024010, 2014.

[89] J. Hartung and J. Steinhoff. Next-to-next-to-leading order post-Newtonian spin-orbit Hamiltonian for self-gravitating binaries. *Annalen der Physik*, 523:783–790, October 2011.

[90] James Healy, Frank Herrmann, Ian Hinder, Deirdre M. Shoemaker, Pablo Laguna, and Richard A. Matzner. Superkicks in hyperbolic encounters of binary black holes. *Phys. Rev. Lett.*, 102:041101, 2009.

[91] Daniel A. Hemberger, Geoffrey Lovelace, Thomas J. Loredo, Lawrence E. Kidder, Mark A. Scheel, Béla Szilágyi, Nicholas W. Taylor, and Saul A. Teukolsky. Final spin and radiated energy in numerical simulations of binary black holes with equal masses and equal, aligned or antialigned spins. *Phys. Rev. D*, 88:064014, Sep 2013.

[92] Daniel A. Hemberger, Mark A. Scheel, Lawrence E. Kidder, Béla Szilágyi, Geoffrey Lovelace, Nicholas W. Taylor, and Saul A. Teukolsky. Dynamical excision boundaries in spectral evolutions of binary black hole spacetimes. *Class. Quantum Grav.*, 30(11):115001, 2013.

[93] Katherine Henriksson, FranÃ§ois Foucart, Lawrence E. Kidder, and Saul A. Teukolsky. Initial data for high-compactness black hole-neutron star binaries. 2014.

[94] Ian Hinder. The Current Status of Binary Black Hole Simulations in Numerical Relativity. *Class. Quant. Grav.*, 27:114004, 2010.

[95] Ian Hinder et al. Error-analysis and comparison to analytical models of numerical waveforms produced by the NRAR Collaboration. *Classical and Quantum Gravity*, 31(2):025012, 2014.

[96] G. Hobbs, A. Archibald, Z. Arzoumanian, D. Backer, M. Bailes, et al. The international pulsar timing array project: using pulsars as a gravitational wave detector. *Class.Quant.Grav.*, 27:084013, 2010.

[97] Michael Holst, Lee Lindblom, Robert Owen, Harald P. Pfeiffer, Mark A. Scheel, and Lawrence E. Kidder. Optimal constraint projection for hyperbolic evolution systems. *Phys. Rev. D*, 70:084017, 2004.

[98] Lawrence E. Kidder. Coalescing binary systems of compact objects to (post)$^{5/2}$-Newtonian order. V. Spin effects. *Phys. Rev. D*, 52(2):821–847, Jul 1995.

[99] Lawrence E. Kidder. Coalescing binary systems of compact objects to postNewtonian 5/2 order. 5. Spin effects. *Phys. Rev.*, D52:821–847, 1995.

[100] Lawrence E. Kidder, Clifford M. Will, and Alan G. Wiseman. Coalescing binary systems of compact objects to (post)$^{5/2}$-Newtonian order. III. Transition from inspiral to plunge. *Phys. Rev. D*, 47(8):3281–3291, Apr 1993.

[101] Dieter Kraft. A software package for sequential quadratic programming. *Deutsche Forschungs- und Versuchsanstalt für Luft- und Raumfahrt*, 88, 1988.

[102] J. B. Kuipers. *Quaternions and Rotation Sequences: A Primer with Applications to Orbits, Aerospace and Virtual Reality*. Princeton University Press, 2002.

[103] L. Lehner and F. Pretorius. Numerical Relativity and Astrophysics. *Ann.Rev.of Astron. & Astroph.*, 52:661–694, August 2014.

[104] Michele Levi. Binary dynamics from spin1-spin2 coupling at fourth post-Newtonian order. 2011.

[105] Michele Levi and Jan Steinhoff. Equivalence of ADM Hamiltonian and Effective Field Theory approaches at next-to-next-to-leading order spin1-spin2 coupling of binary inspirals. *JCAP*, 1412(12):003, 2014.

[106] Michele Levi and Jan Steinhoff. Leading order finite size effects with spins for inspiralling compact binaries. 2014.

[107] Michele Levi and Jan Steinhoff. An effective field theory for gravitating spinning objects in the post-Newtonian scheme. 2015.

[108] Lee Lindblom, Mark A. Scheel, Lawrence E. Kidder, Robert Owen, and Oliver Rinne. A new generalized harmonic evolution system. *Class. Quantum Grav.*, 23:S447–S462, 2006.

[109] Lee Lindblom and Béla Szilágyi. An improved gauge driver for the GH Einstein system. *Phys. Rev. D*, 80:084019, 2009.

[110] Chris Loken, Daniel Gruner, Leslie Groer, Richard Peltier, Neil Bunn, Michael Craig, Teresa Henriques, Jillian Dempsey, Ching-Hsing Yu, Joseph Chen, L Jonathan Dursi, Jason Chong, Scott Northrup, Jaime Pinto, Neil Knecht, and

Ramses Van Zon. SciNet: Lessons Learned from Building a Power-efficient Top-20 System and Data Centre. *J. Phys.: Conf. Ser.*, 256:012026, 2010.

[111] Carlos O. Lousto and James Healy. Flip-flopping binary black holes. *Phys.Rev.Lett.*, 114(14):141101, 2015.

[112] Carlos O. Lousto and Yosef Zlochower. Hangup Kicks: Still Larger Recoils by Partial Spin/Orbit Alignment of Black-Hole Binaries. *Phys. Rev. Lett.*, 107:231102, 2011.

[113] Carlos O. Lousto and Yosef Zlochower. Orbital evolution of extreme-mass-ratio black-hole binaries with numerical relativity. *Phys. Rev. Lett.*, 106:041101, January 2011.

[114] Carlos O. Lousto and Yosef Zlochower. Nonlinear Gravitational Recoil from the Mergers of Precessing Black-Hole Binaries. *Phys.Rev.*, D87(8):084027, 2013.

[115] Carlos O. Lousto and Yosef Zlochower. Where angular momentum goes in a precessing black hole binary. *Phys. Rev. D 89, 021501 (2014)*, 2013.

[116] Carlos O. Lousto and Yosef Zlochower. Black-Hole Binary Remnant Mass and Spin Revisited: A New Phenomenological Formula. *Phys. Rev. D*, 89:104052, 2014.

[117] Geoffrey Lovelace, Michael Boyle, Mark A. Scheel, and Béla Szilágyi. High-accuracy gravitational waveforms for binary-black-hole mergers with nearly extremal spins. *Class. Quant. Grav.*, 29:045003, 2012.

[118] Geoffrey Lovelace, Robert Owen, Harald P. Pfeiffer, and Tony Chu. Binary-black-hole initial data with nearly-extremal spins. *Phys. Rev. D*, 78:084017, 2008.

[119] Geoffrey Lovelace, Mark. A. Scheel, and Béla Szilágyi. Simulating merging binary black holes with nearly extremal spins. *Phys. Rev. D*, 83:024010, 2011.

[120] A. Lundgren and R. O'Shaughnessy. Single-spin precessing gravitational waveform in closed form. *Phys.Rev.*, D89(4):044021, 2014.

[121] M. A. Scheel, M. Boyle, T. Chu, L. E. Kidder, K. D. Matthews and H. P. Pfeiffer. High-accuracy waveforms for binary black hole inspiral, merger, and ringdown. *Phys. Rev. D*, 79:024003, 2009.

[122] Ilana MacDonald, Abdul H. Mroué, Harald P. Pfeiffer, Michael Boyle, Lawrence E. Kidder, Mark A. Scheel, Béla Szilágyi, and Nicholas W. Taylor. Suitability of hybrid gravitational waveforms for unequal-mass binaries. *Phys. Rev. D*, 87:024009, 2013.

[123] Ilana MacDonald, Samaya Nissanke, and Harald P. Pfeiffer. Suitability of post-Newtonian/numerical-relativity hybrid waveforms for gravitational wave detectors. *Class. Quantum Grav.*, 28(13):134002, July 2011.

[124] Sylvain Marsat. Cubic order spin effects in the dynamics and gravitational wave energy flux of compact object binaries. *Class.Quant.Grav.*, 32(8):085008, 2015.

[125] Sylvain Marsat, Alejandro Bohé, Luc Blanchet, and Alessandra Buonanno. Next-to-leading tail-induced spin–orbit effects in the gravitational radiation flux of compact binaries. *Class. Quantum Grav.*, 31(2):025023, 2014.

[126] Sean T. McWilliams. The status of black-hole binary merger simulations with numerical relativity. *Class. Quantum Grav.*, 28:134001, 2011.

[127] M. Mezcua, T. P. Roberts, A. P. Lobanov, and A. D. Sutton. The powerful jet of an off-nuclear intermediate-mass black hole in the spiral galaxy ngc 2276. *Monthly Notices of the Royal Astronomical Society*, 448(2):1893–1899, 2015.

[128] Charles W. Misner, Kip S. Thorne, and John Archibald Wheeler. *Gravitation*. Freeman, New York, New York, 1973.

[129] Abdul H. Mroué and Harald P. Pfeiffer. Precessing Binary Black Holes Simulations: Quasicircular Initial Data. 2012.

[130] Abdul H. Mroue, Mark A. Scheel, Bela Szilagyi, Harald P. Pfeiffer, Michael Boyle, Daniel A. Hemberger, Lawrence E. Kidder, Geoffrey Lovelace, Sergei Ossokine, Nicholas W. Taylor, Anil Zenginoglu, Luisa T. Buchman, Tony Chu, Evan Foley, Matthew Giesler, Robert Owen, and Saul A. Teukolsky. A catalog of 174 binary black hole simulations for gravitational wave astronomy. *Phys. Rev. Lett.*, 111:241104, 2013.

[131] T. Nakamura, K. Oohara, and Y. Kojima. General relativistic collapse to black holes and gravitational waves from black holes. *Prog. Theor. Phys.*, 90, 1987.

[132] Ezra Newman and Roger Penrose. An approach to gravitational radiation by a method of spin coefficients. *J. Math. Phys.*, 3(3):566–578, 1962.

[133] Alexander H. Nitz, Andrew Lundgren, Duncan A. Brown, Evan Ochsner, Drew Keppel, et al. Accuracy of gravitational waveform models for observing neutron-star–black-hole binaries in Advanced LIGO. *Phys.Rev.*, D88:124039, 2013.

[134] Frank Ohme. Analytical meets numerical relativity - status of complete gravitational waveform models for binary black holes. *Class. Quant. Grav.*, 29:124002, 2012.

[135] Frank Ohme, Mark Hannam, and Sascha Husa. Reliability of complete gravitational waveform models for compact binary coalescences. *Phys. Rev. D*, 84:064029, September 2011.

[136] Serguei Ossokine, Michael Boyle, Lawrence E. Kidder, Harald P. Pfeiffer, Mark A. Scheel, and Béla Szilágyi. Comparing post-Newtonian and numerical-relativity precession dynamics. 2015.

[137] Serguei Ossokine, Francois F. Foucart, Harald P. Pfeiffer, Michael Boyle, and Béla Szilágyi. Improvements to the construction of binary black hole initial data. 2015. Submitted to CQG.

[138] Serguei Ossokine, Lawrence E. Kidder, and Harald P. Pfeiffer. Precession-tracking coordinates for simulations of compact-object-binaries. *Phys. Rev. D*, 88:084031, 2013.

[139] Robert Owen. *Topics in Numerical Relativity: The periodic standing-wave approximation, the stability of constraints in free evolution, and the spin of dynamical black holes*. PhD thesis, California Institute of Technology, 2007.

[140] L. D. Paarmann. *Design and analysis of analog filters a signal processing perspective*. Kluwer Academic Publishers, Boston, 2001.

[141] Yi Pan, Alessandra Buonanno, Andrea Taracchini, Lawrence E. Kidder, Abdul H. Mroue, et al. Inspiral-merger-ringdown waveforms of spinning, precessing black-hole binaries in the effective-one-body formalism. *Phys. Rev. D*, 89:084006, 2013.

[142] Dheeraj R. Pasham, Tod E. Strohmayer, and Richard F. Mushotzky. A 400-solar-mass black hole in the galaxy m82. *Nature*, 513(7516):74–76, Sep 2014. Letter.

[143] Larne Pekowsky, Richard O'Shaughnessy, Jim Healy, and Deirdre Shoemaker. Comparing gravitational waves from nonprecessing and precessing black hole binaries in the corotating frame. *Phys. Rev. D*, 88:024040, 2013.

[144] Ruben E. Perez, Peter W. Jansen, and Joaquim R. R. A. Martins. pyOpt: A Python-based object-oriented framework for nonlinear constrained optimization. *Structures and Multidisciplinary Optimization*, 45(1):101–118, 2012.

[145] H. P. Pfeiffer, L. E. Kidder, M. A. Scheel, and S. A. Teukolsky. A multidomain spectral method for solving elliptic equations. *Comput. Phys. Commun.*, 152:253–273, 2003.

[146] Harald P. Pfeiffer. The initial value problem in numerical relativity. *J. Hyperbol. Differ. Eq.*, 2(2):497–520, 2005.

[147] Harald P. Pfeiffer. Numerical simulations of compact object binaries. *Class. Quant. Grav.*, 29:124004, 2012.

[148] Harald P. Pfeiffer, Duncan A. Brown, Lawrence E. Kidder, Lee Lindblom, Geoffrey Lovelace, and Mark A. Scheel. Reducing orbital eccentricity in binary black hole simulations. *Class. Quantum Grav.*, 24(12):S59–S81, 2007.

[149] Harald P. Pfeiffer, Gregory B. Cook, and Saul A. Teukolsky. Comparing initial-data sets for binary black holes. *Phys. Rev. D*, 66:024047, 2002.

[150] Harald P. Pfeiffer and James W. York. Extrinsic curvature and the Einstein constraints. *Phys. Rev. D*, 67(4):044022, Feb 2003.

[151] Rafael A Porto and Ira Z. Rothstein. Next to Leading Order Spin(1)Spin(1) Effects in the Motion of Inspiralling Compact Binaries. *Phys. Rev. D*, 78:044013, 2008.

[152] W. H. Press, S. A. Teukolsky, W. T. Vetterling, and B. P. Flannery. *Numerical Recipes: The Art of Scientific Computing (3rd Ed.)*. Cambridge University Press, New York, 2007.

[153] Frans Pretorius. Evolution of binary black hole spacetimes. *Phys. Rev. Lett.*, 95:121101, 2005.

[154] Frans Pretorius. Numerical relativity using a generalized harmonic decomposition. *Class. Quantum Grav.*, 22(2):425–451, 2005.

[155] Oliver Rinne, Luisa T. Buchman, Mark A. Scheel, and Harald P. Pfeiffer. Implementation of absorbing boundary conditions for the Einstein equations. In *Proceedings of Spanish Relativity Meeting*, volume 1122, pages 384–387. AIP Conference Proceedings, 2008.

[156] Oliver Rinne, Luisa T. Buchman, Mark A. Scheel, and Harald P. Pfeiffer. Implementation of higher-order absorbing boundary conditions for the Einstein equations. *Class. Quantum Grav.*, 26:075009, 2009.

[157] M. Ruiz, R. Takahashi, M. Alcubierre, and D. Núñez. Multipole expansions for energy and momenta carried by gravitational waves. *Gen. Relativ. Gravit.*, 40:1705–1729, 2008.

[158] R. K. Sachs. Gravitational waves in general relativity. VIII. waves in asymptotically flat space-time. *Proc. R. Soc. Lond. A*, 270(1340):103–126, October 1962.

[159] L. Santamaría, F. Ohme, P. Ajith, B. Brügmann, N. Dorband, M. Hannam, S. Husa, P. Mösta, D. Pollney, C. Reisswig, E. L. Robinson, J. Seiler, and B. Krishnan. Matching post-newtonian and numerical relativity waveforms: Systematic errors and a new phenomenological model for non-precessing black hole binaries. *Phys. Rev. D*, 82:064016, 2010.

[160] Olivier Sarbach, Gioel Calabrese, Jorge Pullin, and Manuel Tiglio. Hyperbolicity of the BSSN system of Einstein evolution equations. *Phys.Rev.*, D66:064002, 2002.

[161] B.S. Sathyaprakash and B.F. Schutz. Physics, Astrophysics and Cosmology with Gravitational Waves. *Living Rev.Rel.*, 12:2, 2009.

[162] M. A. Scheel, M. Giesler, D. A. Hemberger, G. Lovelace, K. Kuper, M. Boyle, B. Szilágyi, and L. E. Kidder. Improved methods for simulating nearly extremal binary black holes. *Classical and Quantum Gravity*, 32(10):105009, May 2015.

[163] Mark A. Scheel, Harald P. Pfeiffer, Lee Lindblom, Lawrence E. Kidder, Oliver Rinne, and Saul A. Teukolsky. Solving Einstein's equations with dual coordinate frames. *Phys. Rev. D*, 74:104006, 2006.

[164] Patricia Schmidt, Mark Hannam, Sascha Husa, and P. Ajith. Tracking the precession of compact binaries from their gravitational-wave signal. *Phys. Rev. D*, 84:024046, 2011.

[165] M. Shibata and T. Nakamura. Evolution of three-dimensional gravitational waves: Harmonic slicing case. *Phys. Rev. D*, 52:5428–5444, 1995.

[166] Deirdre Shoemaker, Karan Jani, Lionel London, and Larne Pekowsky. Connecting Numerical Relativity and Data Analysis of Gravitational Wave Detectors. *Astrophys.Space Sci.Proc.*, 40:245–258, 2015.

[167] J. M. Silverman and A. V. Filippenko. On IC 10 X-1, the Most Massive Known Stellar-Mass Black Hole. *Astrophys. J. Lett.*, 678:L17–L20, 2008.

[168] U. Sperhake, B. Bruegmann, D. Muller, and C.F. Sopuerta. 11-orbit inspiral of a mass ratio 4:1 black-hole binary. *Class. Quant. Grav.*, 28:134004, 2011.

[169] U. Sperhake, V. Cardoso, F. Pretorius, E. Berti, T. Hinderer, and N. Yunes. Cross section, final spin and zoom-whirl behavior in high-energy black hole collisions. *Phys. Rev. Lett.*, 2009. in press.

[170] Ulrich Sperhake, Vitor Cardoso, Christian D. Ott, Erik Schnetter, and Helvi Witek. Extreme black hole simulations: collisions of unequal mass black holes and the point particle limit. 2011.

[171] R. Sturani, S. Fischetti, L. Cadonati, G.M. Guidi, J. Healy, et al. Complete phenomenological gravitational waveforms from spinning coalescing binaries. *J.Phys.Conf.Ser.*, 243:012007, 2010.

[172] R. Sturani, S. Fischetti, L. Cadonati, G.M. Guidi, J. Healy, et al. Phenomenological gravitational waveforms from spinning coalescing binaries. 2010.

[173] Béla Szilágyi. Key Elements of Robustness in Binary Black Hole Evolutions using Spectral Methods. *Int.J.Mod.Phys.*, D23(7):1430014, 2014.

[174] Bela Szilagyi, Jonathan Blackman, Alessandra Buonanno, Andrea Taracchini, Harald P. Pfeiffer, et al. Numerical relativity reaching into post-Newtonian territory: a compact-object binary simulation spanning 350 gravitational-wave cycles. 2015.

[175] Béla Szilágyi, Lee Lindblom, and Mark A. Scheel. Simulations of binary black hole mergers using spectral methods. *Phys. Rev. D*, 80:124010, 2009.

[176] A. Taracchini, Y. Pan, A. Buonanno, E. Barausse, M. Boyle, T. Chu, G. Lovelace, H. P. Pfeiffer, and M. A. Scheel. Prototype effective-one-body model for nonprecessing spinning inspiral-merger-ringdown waveforms. *Phys. Rev. D*, 86(2):024011, July 2012.

[177] Andrea Taracchini, Alessandra Buonanno, Yi Pan, Tanja Hinderer, Michael Boyle, Daniel A. Hemberger, Lawrence E. Kidder, Geoffrey Lovelace, Abdul H. Mroue, Harald P. Pfeiffer, Mark A. Scheel, Bela Szilagyi, and Anil Zenginoglu. Effective-one-body model for black-hole binaries with generic mass ratios and spins. *Phys.Rev.*, D89 (R)(6):061502, 2014.

[178] J H Taylor and J M Weisberg. A new test of general relativity: gravitational waves from the binary pulsar psr 1913+16. *The Astrophysical Journal*, 253:908, 1982.

[179] Nicholas W. Taylor, Michael Boyle, Christian Reisswig, Mark A. Scheel, Tony Chu, Lawrence E. Kidder, and Béla Szilágyi. Comparing gravitational waveform extrapolation to Cauchy-characteristic extraction in binary black hole simulations. *Phys. Rev. D*, 88:124010, Dec 2013.

[180] The LIGO Scientific Collaboration. Advanced LIGO. *ArXiv:1411.4547*, 2014.

[181] The Virgo Collaboration. Advanced Virgo Baseline Design, 2010. VIR–027A–09.

[182] The Virgo Collaboration. Advanced Virgo Technical Design Report, 2012. [VIR-0128A-12].

[183] Vijay Varma, Parameswaran Ajith, Sascha Husa, Juan Calderon Bustillo, Mark Hannam, and Michael Puerrer. Gravitational-wave observations of binary black holes: Effect of non-quadrupole modes. 2014. arXiv:1409.2349.

[184] J. M. Weisberg, J. H. Taylor, and L. A. Fowler. Gravitational waves from an orbiting pulsar. *Scientific American*, 245:74–82, October 1981.

[185] Clifford M. Will. The Confrontation between General Relativity and Experiment. *Living Rev.Rel.*, 17:4, 2014.

[186] J. W. York, Jr. Kinematics and dynamics of general relativity. In L. L. Smarr, editor, *Sources of Gravitational Radiation*, pages 83–126, 1979.

[187] James W. York. Conformally invariant orthogonal decomposition of symmetric tensors on Riemannian manifolds and the initial-value problem of general relavity. *J. Math. Phys.*, 14:456–464, 1973.

[188] James W. York. Conformal "thin-sandwich" data for the initial-value problem of general relativity. *Phys. Rev. Lett.*, 82(7):1350–1353, Feb 1999.

[189] Yosef Zlochower, Manuela Campanelli, and Carlos O. Lousto. Modeling Gravitational Recoil Using Numerical Relativity. *Class.Quant.Grav.*, 28:114015, 2011.